UNIVERSITA' DEGLI STUDI DI CATANIA

DOTTORATO DI RICERCA IN FISICA

SONJA ELENA AGATA ORRIGO

Experimental and theoretical study of ^{15}C via the (^{7}Li,^{7}Be) reaction and QRPA microscopic approach

TESI PER IL CONSEGUIMENTO DEL TITOLO

XVII CICLO 2001-2004

UNIVERSITA' DEGLI STUDI DI CATANIA

DOTTORATO DI RICERCA IN FISICA

SONJA ELENA AGATA ORRIGO

Experimental and theoretical study of ^{15}C via the (^{7}Li,^{7}Be) reaction and QRPA microscopic approach

Tutor: Ch.mo Prof. A. Cunsolo

Coordinatore: Ch.mo Prof. A. Insolia

TESI PER IL CONSEGUIMENTO DEL TITOLO

XVII CICLO 2001-2004

The most beautiful thing we can experience is the mysterious.
It is the source of all true art and science.

Albert Einstein, *What I Believe.*

Alla mia famiglia

CONTENTS

CHAPTER 4

CHAPTER 5

CHAPTER 6

CHAPTER 7

CHAPTER 8

INTRODUCTION

In recent years the study of the structure and the reaction mechanisms involving light exotic nuclei has given a new interesting scenario of the nuclear physics, leading to the development of new theoretical models and experimental techniques. Various unexpected phenomena have been observed at the drip lines which cannot be explained within the traditional models used for the stable nuclei, indicating a shift away from the mean field dynamics towards a new type of dynamics in which the many-body correlations play a fundamental role.

The systematic comparison of data for light neutron-rich nuclei with slightly different neutron emission thresholds may provide important information on the evolution of their structural properties and related phenomena when more and more extreme conditions of charge asymmetry and low density are reached. An interesting case is the ^{15}C nucleus because its characteristics seem to be intermediate between those of well-bound nuclei, such as ^{12}C, and more exotic isotopes. Indeed, ^{15}C exhibits in the same time properties typical of both stable and drip-line nuclei. This contradictory behaviour, together with the uncertain presence of a halo in the ^{15}C ground state, make this nucleus particularly intriguing.

The aim of the present work is the investigation of weakly-bound neutron-rich nuclei, such as ^{15}C, from both experimental and theoretical point of views. In particular, ^{15}C was studied via the (^{7}Li,^{7}Be) Charge EXchange (CEX) reaction at 55 MeV incident energy. This experiment, performed at the IPN-Orsay (France), is part of a research program which will be continued with the large-acceptance magnetic spectrometer MAGNEX at the LNS-INFN, Catania (Italy). The purpose is the systematic exploration of both structural properties and CEX mechanism in light neutron-rich nuclei where three external neutrons are coupled with an integer number of α particles. Particular attention is paid to experimental signatures of the core excitations, such as the Bound States Embedded in the Continuum (BSEC), which are expected to be an important phenomenon in the low-energy continuum of such nuclei due to the easily polarizable core.

The first two Chapters of this thesis give an overview of the physical background of interest, constituted by the drip-line phenomena and the experimental studies of ^{15}C. Next, various questions concerning the dynamics of the (^{7}Li,^{7}Be) CEX reaction and the interesting information that can be extracted from this reaction are discussed. The two following Chapters are devoted to the experimental phases. A high-purity ^{15}N gas target was designed and constructed on purpose at the LNS-INFN; it was crucial to overcome the difficulties that originated from a ^{15}N enriched solid target in a previous experiment. The use of a high-resolution magnetic spectrometer to detect ^{7}Be make the measurement in coincidence of the deexcitation γ-rays not necessary. The experimental results are presented and discussed. In

particular, an interference effect is experimentally observed for the first time in a CEX reaction (see Sections 5.2.3).

The last three Chapters describe the theoretical analysis. The $^{15}N(^{7}Li,^{7}Be)^{15}C$ reaction is analyzed in the CEX-Quasiparticle Random Phase Approximation (CEX-QRPA) theoretical framework, where the ^{15}C bound states are described in terms of correlated one particle-one hole (1p-1h) excitations with respect to the ^{15}N ground state. Microscopic CEX-QRPA calculations are performed. The results of the structure calculations are compared to the experimental spectra and used to calculate the cross sections and G-factor (defined in Section 3.4.1) distributions, to compare to the measured angular distributions and G-factor values. Important information is obtained on the nuclear structure and reaction dynamics.

The Dynamical Core Polarization (DCP) effects have to be taken into account in order to give a proper description of the ^{15}C continuum. QRPA-DCP calculations are performed according to the Quasiparticle-Core Coupling (QPC) model. In this model the dynamical many-body correlations in odd-mass nuclei are described by coupling a quasiparticle to configurations with excitation of the even-even core, given by the QRPA theory. The results obtained allow a better understanding of the structure of the ^{15}C nucleus.

The line shape calculations presented in the last Chapter, which are also based on the QPC model, take their origin from the new experimental observation discussed in Chapter 5. The effects of the BSEC phenomenon in weakly-bound neutron-rich nuclei are considered for the first time. With the purpose of a systematic study of such effects in the C-isotopes, results for the ^{15}C, ^{17}C and ^{19}C nuclei are presented. In particular, the results obtained for ^{15}C are compared with the experimental spectra, showing a very good qualitative agreement.

CHAPTER 1

NUCLEAR PHYSICS AT THE DRIP LINES

The phenomena observed when approaching the drip lines constitute the new frontier of the modern nuclear physics. This new and interesting field has become accessible through the development of appropriate experimental techniques and theoretical models. A pictorial overview of the physics phenomena appearing at the drip lines is given in Figure 1.1 [Naz96].

Very peculiar conditions affect the structure and the reaction mechanisms involving light exotic nuclei: the large charge asymmetry and the low separation energy of the valence nucleon (or nucleons). In such a picture, even the small energy contribution of residual interactions strongly influences the properties of the nuclei far off stability. Unusual phenomena can be observed, especially for light neutron-rich nuclei, such as the formation of a thick superficial layer of neutron (skin) or the development of a low density region (halo) with increasing of the neutron excess ([Tan90, Tan91, Rii92, Han95] and refs. therein), the latter corresponding to narrower momentum distribution [Kob88].

The nuclei at the drip lines are characterized by large isospin and weak binding. A strong enhancement of the isospin effects makes the density distributions of neutrons and protons very different in such nuclei. In fact, the nucleon-nucleon isovector interactions are strongly repulsive for the excess neutrons, reducing their separation energy and pushing them towards the continuum threshold [Len98b, Len01]. On the contrary, such interactions are attractive for the missing nucleons, giving them a stronger binding. For example, in the neutron-rich ^{15}C nucleus the last neutron is bound by only 1.218 MeV, while the last proton is bound by 21.080 MeV. This situation is schematised in Figure 1.2, compared to those in the stable ^{15}N nucleus, where the separation energies of the last proton and neutron are very close.

The dynamics of weakly-bound nuclei shows new features not observed in the stable nuclei [Len98b, Len01]. The decrease of binding energy enhances considerably the coupling between bound and unbound configurations. As a result, nuclei change gradually from well-bound to open quantum systems. The enhanced role of the isovector interactions and the coupling with the continuum lead to the dissolution of shell structures in these systems. In fact there is evidence of correlation effects, for which the mean field dynamics is no longer appropriate. The single particle energies and residual interactions act on comparable scales resulting in a strong mutual influence. Thus the structure of such nuclei cannot be explained within the traditional models based on the mean field assumption and more detailed descriptions within the general framework of the many-body theory are needed.

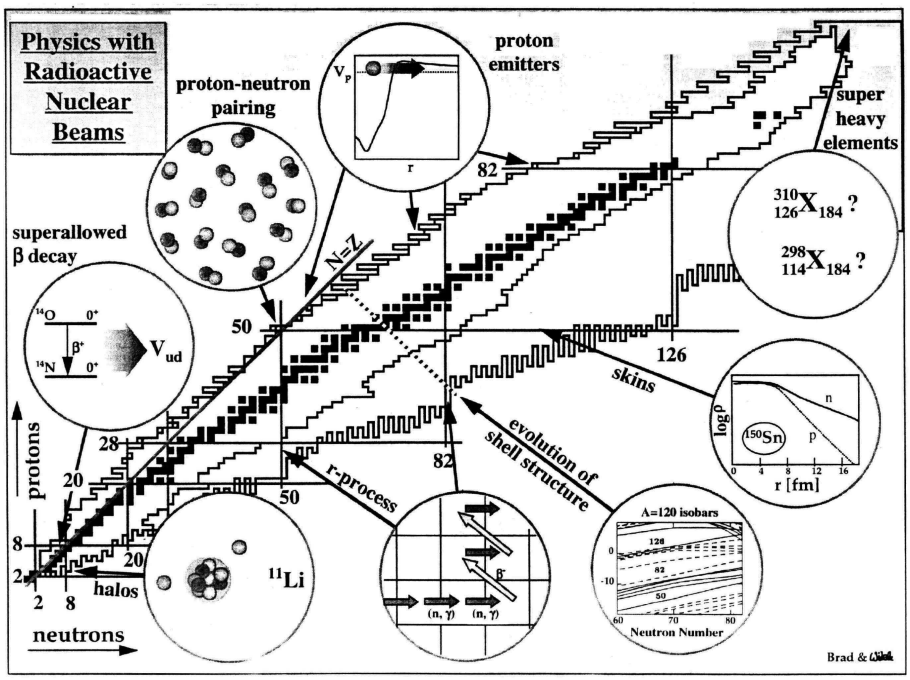

Figure 1.1. Chart of nuclides or Segré plot. The black squares in the central region (stability valley) represent the stable nuclei, while the external lines denote the nuclear drip lines. The phenomena expected or experimentally observed near the proton and neutron drip lines are indicated schematically [Naz96].

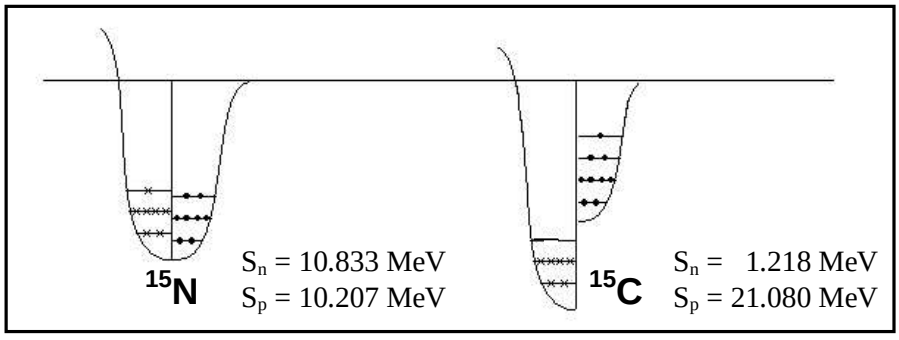

Figure 1.2. Schematic picture of the potential and single particle levels in the stable ^{15}N and neutron-rich ^{15}C nuclei. The separation energies of the last neutron and proton are also indicated.

Nuclear astrophysics is closely related to the physics of the exotic systems. Nucleosynthesis consists mainly of reactions involving exotic nuclei. The cross sections of these processes are fundamental parameters for the stellar models and at present are almost completely unmeasured. The neutron-rich elements to be explored are an essential part: in this region the formation of the heavier elements has occurred during the r-process (rapid neutron capture in the (n,γ) reactions before β-decay back to the stable region [Cla68, Rol88]).

This Chapter is organized as follow: the experimental evidence which led to the discovery of the halo structure are described in Section 1.1. Section 1.2 concerns the properties of the transfer reactions involving exotic nuclei. Finally, Section 1.3 discusses the effects of the pairing correlations (1.3.1) and the dynamical core polarization (1.3.2).

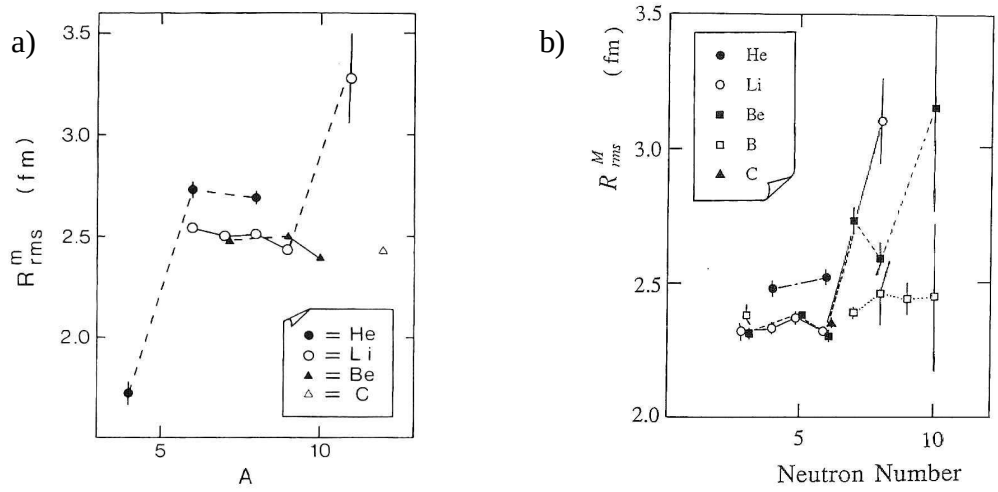

Figure 1.3. R^m_{rms} matter radii in function of the a) mass number A [Tan85] and b) neutron number N [Tan88].

1.1 Halo nuclei

The experimental studies carried out in the last twenty years have lead to the discovery of unexpected and intriguing phenomena. In particular, for light drip-line nuclei, low angular momenta states characterized by very extended density profile distribution (halo) have been observed in the ground and states at very low excitation energy. Here we consider especially experimental observations concerning the neutron-rich region of the mass table. However, the major difference between the neutron and proton halos is the presence of the Coulomb barrier, which makes the proton wave function less extended than the neutron one.

The first "exotic" effects were observed in ^{11}Be. In 1970 the inversion between the $1p_{1/2}$ and $2s_{1/2}$ levels was observed experimentally in the first two states of ^{11}Be by Auton [Aut70] (see Section 2.3.1 for the shell inversion phenomenon). In 1983 Millener et al. measured the E1 transition probability connecting the first excited state of ^{11}Be (E_x = 0.32 MeV, $J^\pi = 1/2^-$) and the ground ($J^\pi = 1/2^+$) [Mil83]. This is the fastest E1 transition known, corresponding to 0.36 ± 0.03 Weisskopf units. Although initially not interpreted in this sense, such a strong transition may be explained only by assuming an unusual spatial extension of the wave function of the last neutron in both states, in a similar manner as the matrix element of the dipole operator gives contribution also for larger radii.

These two observations in ^{11}Be cannot be reproduced by using a mean field approach and they represent the starting point for the development of a new branch of the nuclear physics: the exotic physics. In its first years, the study was limited essentially to the ground state properties (masses, spin, charge radii) and some information about the low lying excited states were obtained by studying the decays. A new era has been started by the advent of the Radioactive Ion Beams (RIBs) produced in the new facilities. New kinds of investigations have been extensively performed in order to study the structural properties and reaction mechanisms in unstable nuclei.

A first signature of the halo states was observed by Tanihata and al. [Tan85]. The RIBs produced by projectile fragmentation in high-energy heavy-ion reactions were used to measure the interaction cross section σ_I in light drip-line nuclei by bombarding thick targets

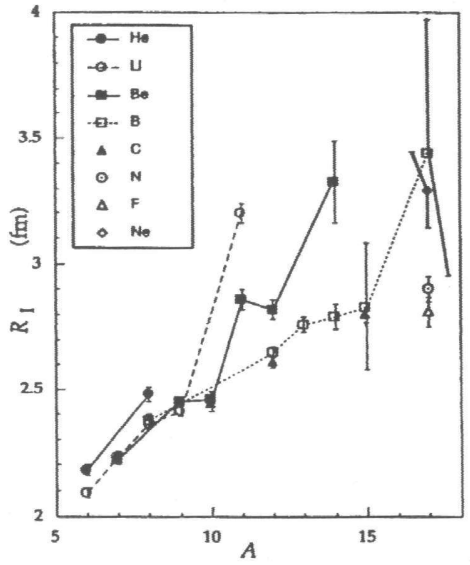

Figure 1.4. Interaction radii R_I for light nuclei determined from the measured interaction cross sections. The data are taken from refs. [Tan88, Tan88b, Tan92, Oza94].

at E_{inc} = 790 MeV/u. The root mean square (rms) interaction radii R_{rms} were extracted from σ_I by a Glauber model analysis with the assumption of a static density distribution. It was a surprising result to observe significantly larger matter radii in nuclei like ^{6,8}He and, above all, ^{11}Li (R^m_{rms} = 3.27 ± 0.24 fm) (see Fig. 1.3a) in comparison with the matter radii for the standard p-shell nuclei (R^m_{rms} ~ 2.5 fm). These results suggested a large deformation and/or a long tail (halo) in the matter distribution owing to the weakly-bound nucleons of ^{11}Li. In subsequent experiments (see, e.g., refs. [Mit87, Tan88, Sai89]) the interaction radii were measured for other light nuclei. High matter radii were found for ^{11}Be and ^{14}Be also [Tan88] (see Fig. 1.3b). The interaction radii measured for several light nuclei are shown in Figure 1.4; considerable increases are seen for a number of nuclei near the neutron drip line. The lines in Figs. 1.3 and 1.4 are only guides for the eye.

A measurement of the magnetic moment of ^{11}Li suggested that ^{11}Li is a spherical nucleus [Arn86] (see also ref. [Tan90]). In 1987 Arnold et al. [Arn87] showed that the charge distribution inside ^{11}Li is almost identical to the charge distributions in ^{9}Li. Thus the large matter radius was not due to the existence of deformations, but to some unexpected behaviour of the last two neutrons in ^{11}Li, in agreement with the hypothesis of a two-neutron halo structure around the ^{9}Li core.

Another important halo probe has come from dissociation experiments at high energies, in which the valence neutron is removed from the projectile and the momentum of the recoiling core is measured. In the sudden (or Serber) approximation [Ser47], the Momentum Distribution (MD) of the core fragments from one-neutron removal reactions reflects the momentum distribution of the removed nucleon [Kob88]. Thus it provides a direct measurement of the square of the Fourier transform of the internal wave function. Qualitatively, from the uncertainty principle it is expected that the width of the distribution of the valence neutron in momentum space is inversely proportional to its width in spatial coordinates. Thus narrow MD of the core fragments are signatures of the large spatial

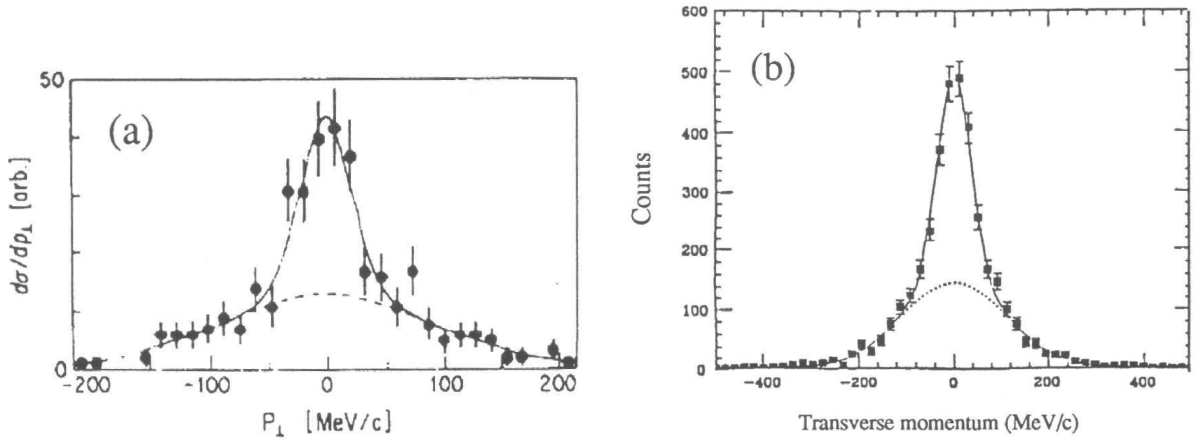

Figure 1.5. Transverse longitudinal momentum distribution of the core fragments after one-neutron removal from a) ^{11}Li [Kob88] and b) ^{11}Be [Tan90] on a carbon target. The lines correspond to Gaussian fit of the observed broad and narrow components.

extension of the valence nucleons in halo nuclei. However, this is a simplified picture, actually the reaction mechanism and final state interactions have to be taken into account.

The Transverse MD (TMD) of the ^{9}Li fragments from breakup of ^{11}Li on a carbon target was measured at E_{inc} = 790 MeV/u by Kobayashi et al [Kob88]. As shown in Figure 1.5a, a structure with two components was found: a broad bump (σ = 95 ± 12 MeV/c, obtained by Gaussian fit), similar to the results from ^{12}C fragmentation, and a narrow peak (σ = 23 ± 5 MeV/c), which reflects the removal of the valence nucleons. This observation indicates the existence of a long neutron tail in ^{11}Li. Analogous results were found for the breakup of ^{11}Be on C at E_{inc} = 800 MeV/u [Tan90], with σ = 109 ± 7 and 25 ± 4 MeV/c for the large and the narrow component, respectively (see Fig. 1.5b).

Also in atomic physics the MD is used in a similar way to probe the wave function of valence electrons [Loh81]. However, in heavier nuclei the simple picture previously discussed is modified because of the strongly absorbing nuclear core. This happens most strongly for the transverse component of the neutron momentum, which essentially reflects diffraction dissociation [Ann90]. The Longitudinal MD (LMD) of the charged fragment (and presumably the neutron) is expected to be less affected [Ber92]. Later, many experiments were devoted to the measurement of the LMD (see for instance refs. [Orr92, Kel96, Baz95]). In particular, the LMD of the ^{9}Li fragments from breakup of ^{11}Li on different target was measured by Orr et al. [Orr92]. By assuming a Lorentzian function for the shape of the distribution, they extracted a width of only 37 MeV/c, confirming the large spatial extension of the valence neutrons. Many complementary and more recent experiments are reviewed in refs. [Han93, Jon95, Han95, Tan96]. Other experiments concerning measurements of interaction radii and LMD for ^{15}C will be discussed in the next Chapter.

As already seen for the E1 transition between the first two ^{11}Be states, strong electromagnetic transitions may reflect states with extended wave functions. In particular, the higher order electric transitions are expected to be effective probes mainly for the proton halo, while the magnetic transition operators are less affected by the tail of the wave function than the electric ones because of the $r^{\lambda-1}$ factor [Rii92].

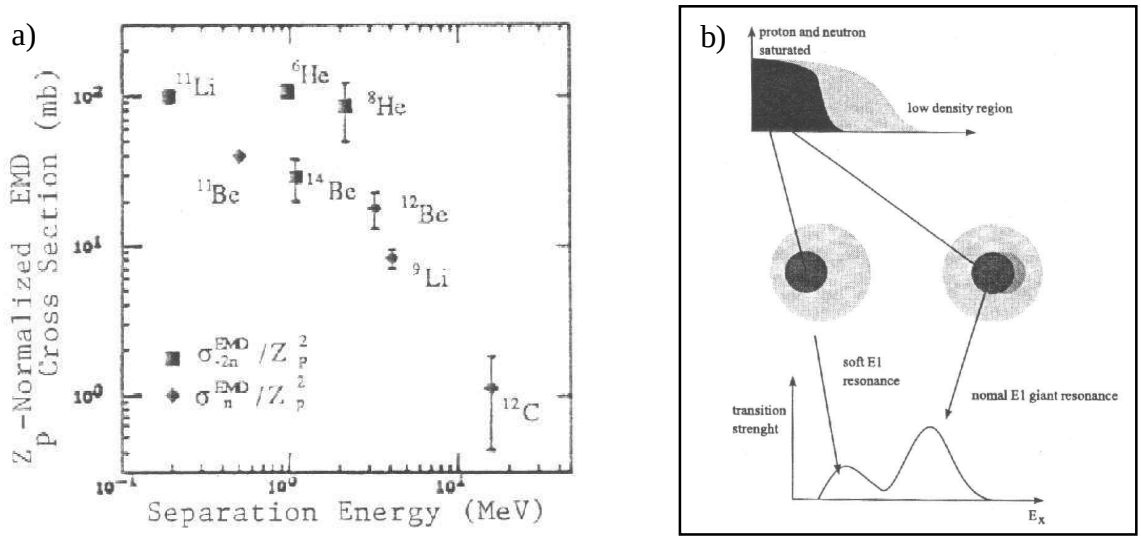

Figure 1.6. a) EMD cross sections (after normalization by projectile Z) versus the neutron separation energy [Tan90]. b) Schematic picture of the soft and hard E1 modes in halo nuclei (taken from ref. [Tan96]).

Further experimental probes are available for the halo states. Among these, the ElectroMagnetic Dissociation (EMD) provides important information. The EMD cross section depends on the electromagnetic transition probability B(Eλ). The large separation between the external neutron and the core in halo nuclei implies a large electric dipole polarizability, which corresponds to an enhanced EMD cross section. The increase of σ_{EMD}, already predicted by Hansen and Jonson in their di-neutron model of ^{11}Li [Han87], was experimentally observed in various neutron-rich nuclei (see Figure 1.6a, taken from ref. [Tan90]) by Coulomb breakup with one-neutron removal.

The existence of large electric dipole strength at low excitation energy is related to the increased σ_{EMD}. Ikeda [Ike92] suggested that the normal Giant Dipole Resonance (GDR) could split into two components, the first one (hard mode) corresponding to the oscillation of the core protons against the core neutrons and the second one (soft mode) to the oscillation of the halo neutron (or neutrons) with respect to the core, as schematized in Figure 1.6b.

The same effects may be seen in photodisintegration, where the virtual photons of the Coulomb field are replaced by real photons, and in the inverse process, the radiative capture. From the experimental point of view, the Coulomb dissociation is the favoured method [Bau86], but it can be applied only for ground state halos, whereas the radiative capture also can provide information on the excited states. Finally, without exhausting the list of all the possible probes for nuclear structure, in addition the processes that simply depend on the spatial overlap between the initial and final states can be useful tools. This is the case for β-decay and charge exchange reactions.

As knowledge of the nuclei far from stability deepened, it became more evident that the nuclear halos are a general feature of loosely bound nuclei. These systems in general can be represented as one or two weakly bound nucleons interacting with both an inert or excited core. A first simple theoretical model of halo nuclei was described in ref. [Han87]; it is essentially a two-body model where the two valence neutrons of ^{11}Li are treated as an unique particle without considering their intrinsic degree of freedoms. The weak binding leads to a

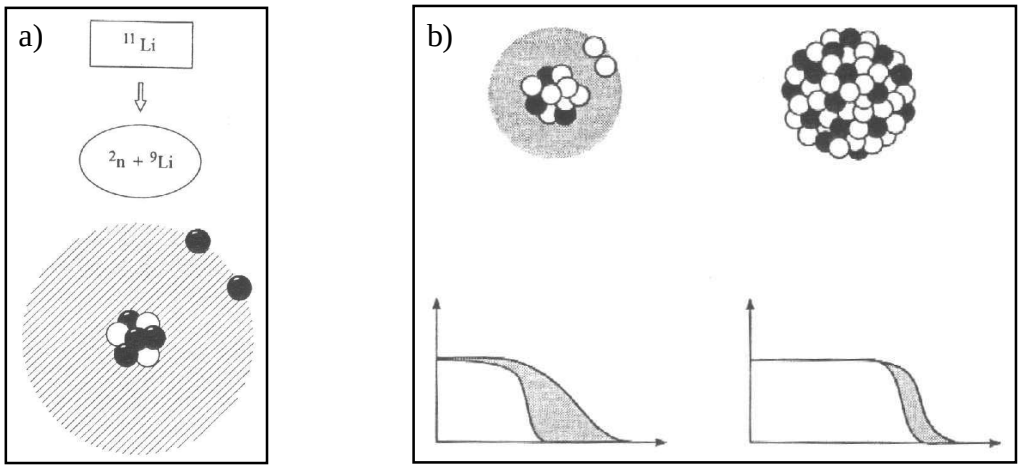

Figure 1.7. a) Pictorial illustration of the two-neutron halo in ^{11}Li. b) Schematic comparison between a halo nucleus (left) and a nucleus with a neutron skin (right). Taken from ref. [Hey99].

low density region: the valence nucleons tunnel out of the central potential, enhancing the diffuseness of the nuclear surface. Eventually, this leads to a delocalization of the valence nucleons, which can be pictured as a halo surrounding the core of the nucleus (see Figure 1.7a). The appearance of the halo is determined by the height of the potential barrier, which itself depends on the binding energy, momentum and, for protons, the Coulomb potential. A schematic comparison between the halo and skin phenomena is shown in Fig. 1.7b. The main difference is in the radial extension of the neutron distribution. The neutron skin appears for separation energies higher than in neutron halo: e.g., in ^{8}He (S_{2n} = 2.137 MeV, R_I = 2.48 fm).

Extensive discussions of halo nuclei are given, e.g., in refs. [Han93, Jon95, Han95, Tan96]. Further in-depth theoretical studies were carried out [Rii92, Fed93, Rii00, Jen00]. For a two-body system, consisting of core plus a valence particle, a loose definition of a halo state was given in ref. [Rii92] such as a state where the probability that the valence nucleons is in the classical forbidden region is more than 50 %. The influence of a long-range repulsive potential on the halo state was examined also [Rii92], both for neutron and proton halos.

Conditions for the halo occurrence were given [Rii92, Fed93, Jen00]. A reasonable estimate in terms of the radial extension is that $\langle r^2_{cn}\rangle/R^2 \gtrsim 2$, where $\langle r^2_{cn}\rangle$ is the average distance between the neutron and the core and R is the range of the particle-core potential. This corresponds to an upper limit of the binding energy S around 5-10 MeV·fm^2. More precisely, two-body halos only may appear for single particle states with l = 0, 1 and $S \cdot A^{2/3} \lesssim 2$ MeV. In particular, the appearance of the proton halo is possible for small charge of the core (Z_c < 10). Three-body halos (i.e., two-neutron halos) can only occur for similarly small binding energies and hyperspherical quantum number K = 0, 1. Again, single particle s- or p-states are needed to construct the K = 0, 1 states. The ratio $\langle r^2\rangle/R^2$ is shown in Figure 1.8 versus the scaled separation energy; the radial extent of the halo is found by subtracting the core contribution from the total mean-square radius [Rii00]. The well established s-wave halos $^{11}Be_{GS}$ and deuteron lie on the l = 0 curve. According to the previous relation, $^{15}C_{GS}$ (S_n = 1.218 MeV) might be an s-wave halo. However, such theoretical constraints are obtained from average properties and thus the detailed picture for a given nucleus might be different.

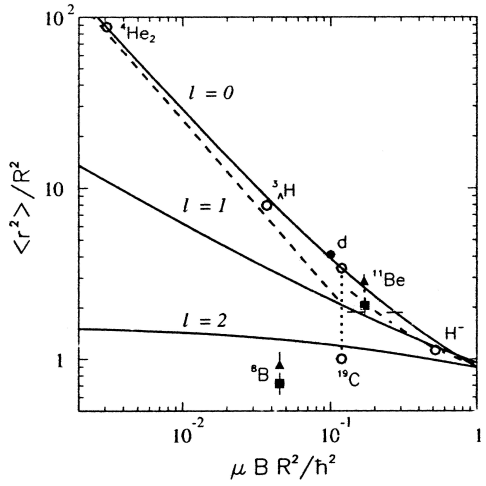

Figure 1.8. Scaling plot for two-body halo systems [Rii00]. The solid lines are results for s-, p- and d-wave in a square-well potential. The thin horizontal line indicates where the 50% of the wave function is outside the potential. The dash-dotted lines are results for r^{-2} potential. Filled symbols are derived from experimental data [Fed94, Jen00, Tan85]; open symbols are from theoretical calculation [Nie98, Cob97, Rid97] and are plotted at the calculated binding energy. For ^{19}C the two given points corresponds to spin equal to 1/2 and 3/2.

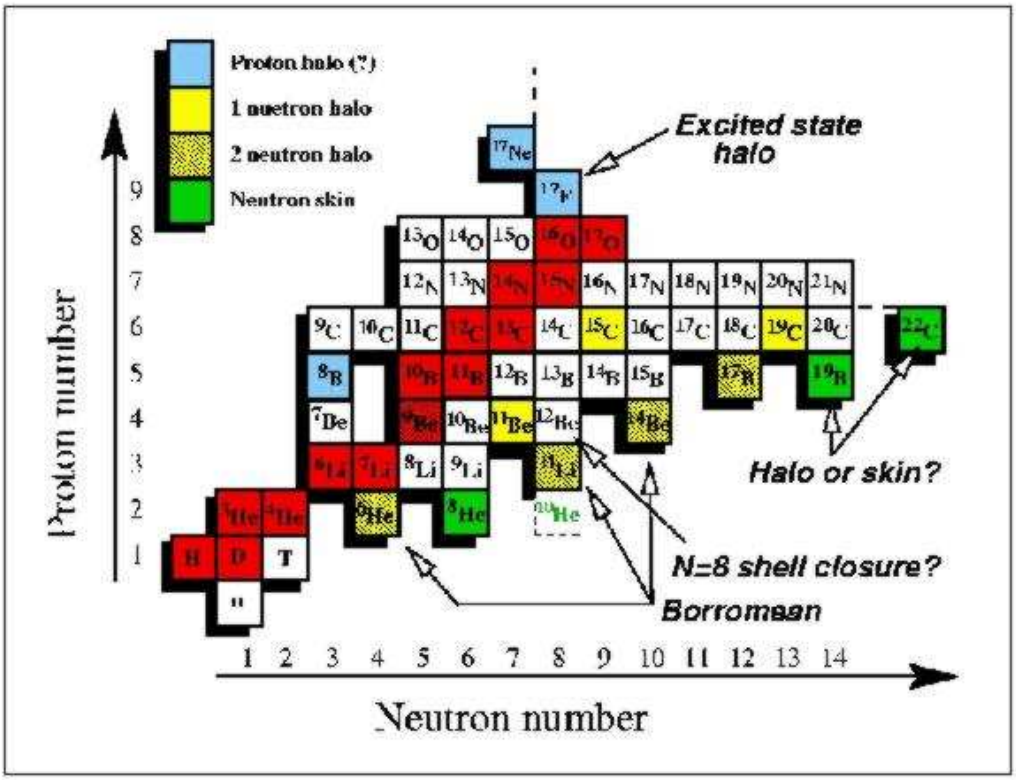

Figure 1.9. Nuclear mass table for light nuclei [Alk02]. Two- and one-neutron halo nuclei and candidates for the proton halo are indicated.

Besides, any realistic mean field model may account for the single particle states, but essential uncertainties remain in the extrapolation towards the drip lines, which are model dependent. The known halo nuclei are shown in the nuclear mass table of Figure 1.9.

1.2 Transfer reactions with exotic nuclei

In the past, transfer reactions with light and heavy ions have given much spectroscopic information concerning stable nuclei: e.g., spin and parity assignments to the nuclear levels, occupation probabilities and wave functions and so on (see, e.g., [Sat83]). The recent developments of exotic beam facilities open new perspectives. The use of the low-energy single nucleon transfer reactions to investigate the structure of drip-lines nuclei is discussed in detail in ref. [Len98]. In fact, the peculiar structural properties of the exotic nuclei (e.g., the low continuum threshold and the extended valence wave function) influence the excitation functions and angular distributions.

The energy-momentum dependence is closely related to the special properties of the wave function of weakly bound states. A new important feature is the prevalence of small momentum components in the form factor. In general, for a transfer reaction from an incident channel α = (b+x, B) to the exit channel β = (b, B+x) the form factor in momentum space is:

$$F(\mathbf{k}_\beta, \mathbf{k}_\alpha) = \int d\mathbf{p}\ \Phi_\beta^+\left(\frac{B}{A}\mathbf{k}_\beta - \mathbf{k}_\alpha - s\,\mathbf{p}\right)\ U_{\beta\alpha}(\mathbf{p})\ \Phi_\alpha\left(\mathbf{k}_\beta - \frac{b}{a}\mathbf{k}_\alpha + t\,\mathbf{p}\right) \qquad (1.1)$$

where $\Phi_{\beta,\alpha}$ and $\mathbf{k}_{\beta,\alpha}$ are, respectively, wave functions and momenta in the center of mass system (CM) in the entrance and exit channel, $U_{\beta\alpha}$ is the interaction and $\mathbf{p}$ is the recoil momentum. In the post (prior) representation the weight factors are s = 1 (s = 0) and t = 0 (t = 1). By using a zero-range approximation, as, e.g., usually done for (d,p) reactions, equation (1.1) becomes proportional to the Fourier transform of the wave function of the final state B+x. The Fourier transform of a bound state in general is peaked at momenta around the inverse of the rms radius of the populated state. Considering a halo state in the final system B+x, its larger rms radius leads to a narrower momentum distribution peaked at smaller momenta than for stable nuclei. Thus far off stability the properties of the final state Φ_β will determine the momentum dependence of the transfer form factor and, as a consequence, the energy dependence of the cross section. Φ_β reacts strongly on small variations of the incident energy (i.e., $\mathbf{k}_\alpha$) and the momentum transfer. The momentum structure of Φ_β implies a maximum in the cross section at low bombarding energies.

Calculations were performed for the $^{18\text{-}36}$Mg and $^{100\text{-}140}$Sn isotopes by Lenske and Schrieder [Len98]. The theoretical total transfer cross sections for the (^{36}Mg,^{37}Mg$_{GS}$) reaction on different targets are shown in Figure 1.10a. A different dependence on the incident energy is seen for the different targets. In particular, a small cross section is obtained for the ^{12}C and ^{24}Mg targets. In general, for heavier targets the combined effect of the increased absorption and Coulomb barrier leads to a smaller cross section. However, also the Q-value mismatching has an important role. Indeed, in reactions involving stable nuclei in both the incident and exit channel, the large separation energies compensate them selves giving an overall low Q-value. On the contrary, if the reaction involves an exotic nucleus and a very bound target such as ^{12}C, such a cancellation does not occur and the high Q-value obtained (typically from –14 to –16 MeV) leads to a small cross section. Instead, for a weakly-bound target the overall Q-value becomes small. Moreover, the damping effects due to the Coulomb force and absorption are reduced.

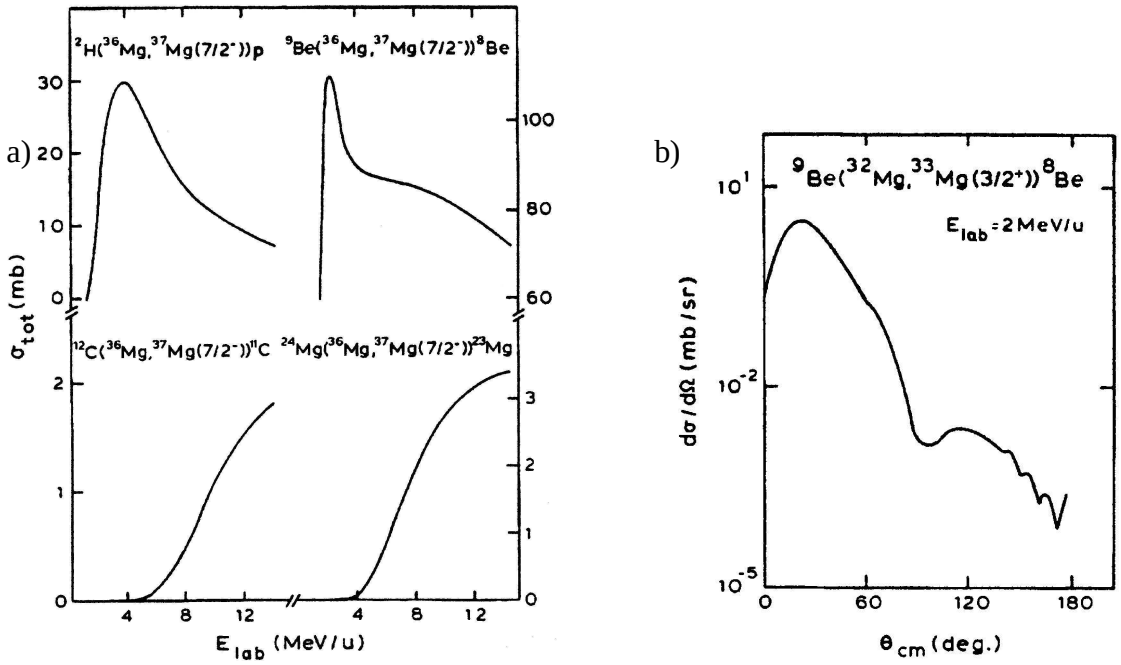

Figure 1.10. a) Dependence on the incident energy of the total transfer cross sections for the (^{36}Mg,^{37}Mg$_{GS}$) reaction on different targets [Len98]. b) Angular distribution for the ^{9}Be(^{32}Mg,^{33}Mg$_{GS}$) reaction at E_{inc} = 2 MeV/u [Len98].

This explains why weakly-bound targets such as, e.g., deuterium and ^{9}Be are preferential to perform transfer reaction involving exotic nuclei.

In these conditions $|\mathbf{k}_\beta| \cong |\mathbf{k}_\alpha| \cong [E_{CM}/N]^{1/2}$, the transfer of low momenta is no longer hindered and the cross section has a maximum at small incident energies. In Figure 1.10a the maximum is observed at $E_{inc} \sim 1.8$ MeV/u for the ^{9}Be target and at $E_{inc} \sim 3$ MeV/u for the deuterium one. Thus the cross section maximum is predicted by calculations at energies much lower than for stable nuclei where, e.g., the maximum is at $E_{inc} \sim$ 15-20 MeV/u for (d,p) reaction [Sat83]. Since the momentum transfer varies from $|k_\alpha - k_\beta|$ at 0° to $|k_\alpha + k_\beta|$ at 180°, a good momentum matching is obtained only at small angles and thus the angular distributions are peaked at forward angles (see, e.g., Figure 1.10b).

From an experimental point of view, the main differences for reactions performed with exotic beams are the use of inverse kinematics and the low beam intensities. Indeed, since the exotic beams are produced as secondary beams, their intensities are reduced by several orders of magnitude with respect to those of the primary beam. As a consequence, only transfer reactions with a rather large cross section may be studied. The cross sections obtained by calculations are from about 10 to 100 mb.

1.3 Correlation effects at the drip lines

In nuclear theory the separation between single particle and many-body degrees of freedom is a very successful concept. In first approximation, the nucleus is described as a self-bound system in which the nucleons move as independent particles in a static mean field. The independent particle model in its various formulations accounts quite well for average

variations of the nuclear properties over the mass table. However, the limits of such a model are evident in describing the details of the spectra. This is seen clearly in drip-line nuclei, in which many-body correlations play a fundamental role.

1.3.1 Pairing correlations

The pairing force usually is not important to describe the bulk properties of the stable nuclei and may be treated perturbatively for nucleons close to the Fermi surface. However, approaching the drip lines the situation is different. In fact, let us consider the approximate Hartree-Fock-Bogoliubov (HFB) relation $S \cong -\lambda - \Delta$. It connects the particle separation energy S with the Fermi-level energy λ and the pairing-gap energy Δ, where the values λ and Δ are determined by the particle-hole and particle-particle components of the effective interaction, respectively. In absence of pairing correlations $S \cong -\lambda$, thus the separation energy would be equal to the Fermi-energy of the removed nucleon, characterizing mean field properties. The effect of the pairing field is to increase (decrease) this number by an amount Δ for even-even (odd-mass) nuclei. For drip-line nuclei $S \rightarrow 0$, thus the single particle and the pairing field are almost equal and Δ cannot longer be considered a perturbation [Dob96].

In particular, the existence of nuclei such as ^{6}He and ^{11}Li as bound systems is strongly related to the pairing correlations. Indeed, the removal of one neutron from these two-neutron halo nuclei leads to the particle unstable ^{5}He and ^{10}Li nuclei, respectively. The binding of ^{6}He and ^{11}Li comes mainly from the paring interactions of the last two neutrons among themselves. The strong correlation in the Singlet Even particle-particle channel (S = 0, L = 0, T = 1) favours the formation of neutron pairs in the $^{1}S_{0}$ configuration. The di-neutron is very close to forming a bound state (only 100 keV away). This quasi-bound state does not exist in the free two-neutron system, thus the interactions between neutrons and core are also important [Len98b]. To describe well a 3-body system such as ^{11}Li it is necessary to take into account the correlations both between the valence neutrons and between each of them and the core.

A mean field description of the ^{11}Li, not accounting for pairing, leads to an unbound system with the last two neutrons arranged in a sharp $1/2^{-}$ resonance (p-wave) at around 250 keV. The conventional approaches, such as the Bardeen-Cooper-Schrieffer (BCS) or the Hartree-Fock-Bogoliubov (HFB) ones, are not appropriate for a detailed description of the ^{11}Li continuum because both methods neglect important high order contributions to its valence wave function [Len98b]. The direct solution of the Gorkov equations

$$(h - e_{+})\phi_{+} - \Delta\phi_{-} = 0 \qquad (h - e_{-})\phi_{-} - \Delta^{\dagger}\phi_{+} = 0 \qquad (1.2)$$

as a coupled channel problem for the particle ϕ_{+} and hole ϕ_{-} components [Len98b, Len01] gives good results. In equations (1.2) h and Δ denote the mean field Hamiltonian and the pairing field, respectively. The ^{11}Li ground state wave function, calculated by solving system (1.2) with a density dependent pairing interaction [Hof98], is mainly made by s- and p-wave components with occupation probabilities of 12 % and 80 %, respectively [Len98b].

The low excitation energy response function of ^{11}Li was measured at GSI, obtaining two prominent structures at E_x = 1.3 and 2.2 MeV [Zin97, Eml98]. The QRPA dipole (1^{-})

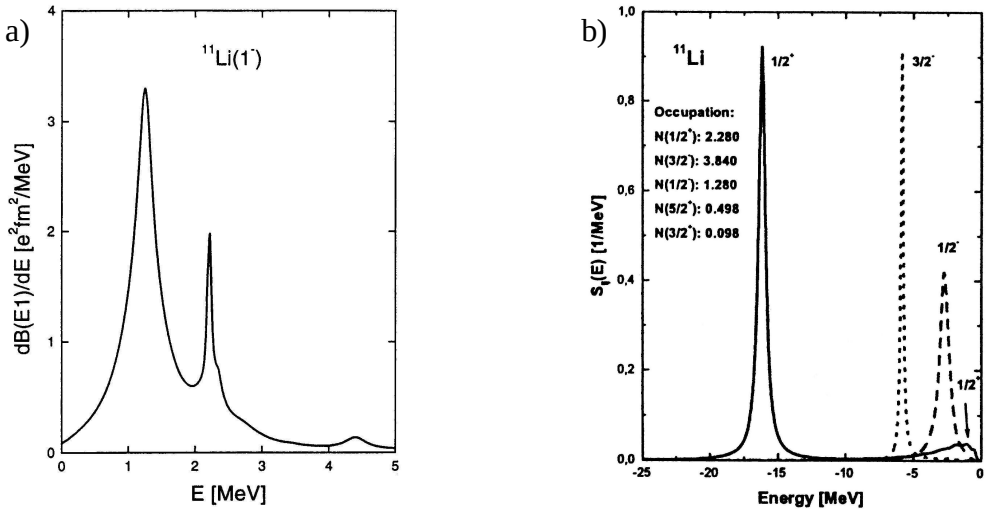

Figure 1.11. a) Dipole response function for ^{11}Li obtained by QRPA calculations [Len98b]. The energy is taken with respect to the continuum threshold of ^{11}Li. b) Single-particle spectral function for s- and p-wave neutron states in ^{11}Li [Len01]. The finite width of the states is due to continuum coupling. The partial occupation numbers N(J^π) are also shown, including the d-wave contributions.

response function for ^{11}Li [Len98b] is given in Figure 1.11a, showing the same features. A close agreement is obtained by comparing the sum rules: both the data and the calculations predict that only the 10 % of the Thomas-Reiche-Kuhn (TRK) sum rule is contained in the measured energy interval. This value does not support an interpretation in terms of a collective soft dipole resonance. The low-energy dipole strength is produced by non-collective states, predominantly given by excitations of the weakly bound s- and p-wave holes into the p- and s-wave continua, respectively. The structure around 4.5 MeV is due to core excitations into the $5/2^+$ continuum.

In Figure 1.11b the theoretical single particle spectral function for s- and p-wave neutron states in ^{11}Li is shown [Len01]. Besides the expected s- and p-wave components, also the $d_{5/2}$ and $d_{3/2}$ strengths are lowered into the bound state region. The mean field supports neither bound $2s_{1/2}$ nor $1d_{5/2}$ and $1d_{3/2}$ single particle levels; their appearance is only because of pairing. The presence of the admixture of the $(2s_{1/2})^2$ and $(1p_{1/2})^2$ configurations in the ground state wave function of ^{11}Li was experimentally obtained at the GSI by using a 287 MeV/u ^{11}Li beam [Sim99].

The proton and neutron ground state densities for ^{11}Li are shown in Figure 1.12a [Len01]. The strong neutron halo component formed by s-, p- and d-states is clearly visible.

1.3.2 Dynamical core polarization

Deviations from the shell model results for odd-mass nuclei may be interpreted in terms of Dynamical Core Polarization (DCP). These nuclei can be described as a single nucleon moving outside an even-mass core; the system may gain energy by exciting the core. The DCP is a well known effect in the stable even-odd nuclei [Eck89, Eck90] and it becomes particularly important for drip-line nuclei [Len98b]. In fact, far off stability the core is rather

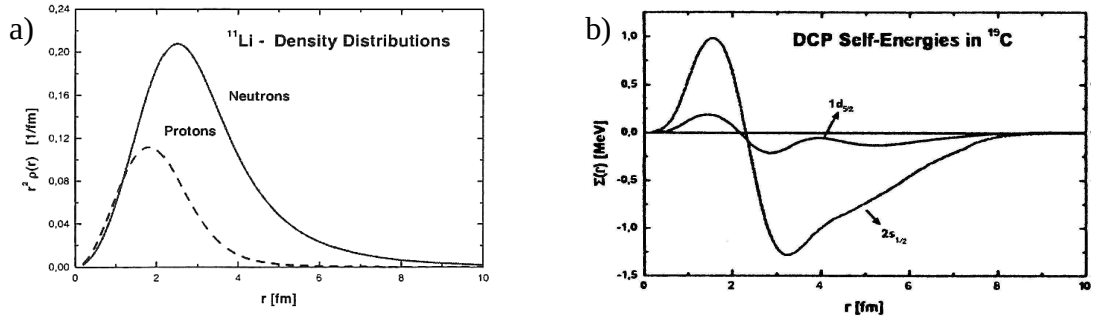

Figure 1.12. a) Proton and neutron ground state density distributions (weighted by r^2) for ^{11}Li [Len01]. b) DCP self-energies [Len01] for the low-energy $2s_{1/2}$ and $1d_{5/2}$ states in ^{19}C (see section 1.3.2). Only the local part ($r = r_1 = r_2$) is shown.

soft because of the isovector repulsion enhanced by the charge asymmetry. Thus the core is more easily polarizable and the DCP effects are expected to be strongly enhanced. In particular, one-nucleon halo nuclei such as ^{8}B, ^{11}Be and ^{19}C are well suited to study the interaction of a weakly-bound valence nucleon with the core nucleus. Here the binding is not longer obtained from pairing such as in ^{11}Li, simply because of the lack of the second valence particle, but from dynamical valence-core interactions [Len01]. The particle-core coupling leads to fragmentation of the single particle strength over many eigenstates, reflecting the importance of the residual interaction (i.e., of the many body correlations).

^{19}C is the heaviest halo nucleus discovered so far. However, its halo structure is less prominent than in ^{11}Be [Bau98]. A narrow longitudinal momentum distribution of the ^{18}C fragments was measured from the breakup of the ^{19}C nucleus on a Be target at 100 MeV/u incident energy [Baz98]. Concerning ^{17}C, shell model calculations predict a very close proximity between the s- and d-orbital in this nucleus. Relativistic mean field calculations for the carbon isotopes [Zho97] foresee the ground state spin and parity equals to $1/2^+$, $3/2^+$ and $1/2^+$ for ^{15}C, ^{17}C and ^{19}C, respectively. The dipole polarizability does not change very much over the $^{10\text{-}22}$C isotopic chain (10 % only), while the quadrupole polarizability is maximum for ^{16}C and ^{18}C, which have low-lying 2^+ states. The energy of the 2^+ states decreases in the carbon isotopes with increasing mass.

The existence of 2^+ core states at low excitation energy is a good indicator of systems in which sizeable DCP effects are expected [Len98b]. The systematics of the 2^+ states is well reproduced by continuum QRPA calculations with a residual interaction derived in the Landau-Fermi liquid theory from the D3Y in-medium interaction. This shows that such states are prevalently of vibrational nature, rather than due to static deformation as assumed, e.g., in ref. [Nun96]. In the DCP approach used in refs. [Len87, Len98b, Len01] the valence particle obeys a non-static Schrödinger equation

$$[H_{MF} + \Sigma_{pol}(\varepsilon) - \varepsilon]\Psi = 0 \qquad (1.3)$$

where H_{MF} is the static mean field Hamiltonian and $\Sigma_{pol}(\varepsilon)$ is the non-local and energy dependent polarization self-energy. The latter describes the rescattering of the nucleon by

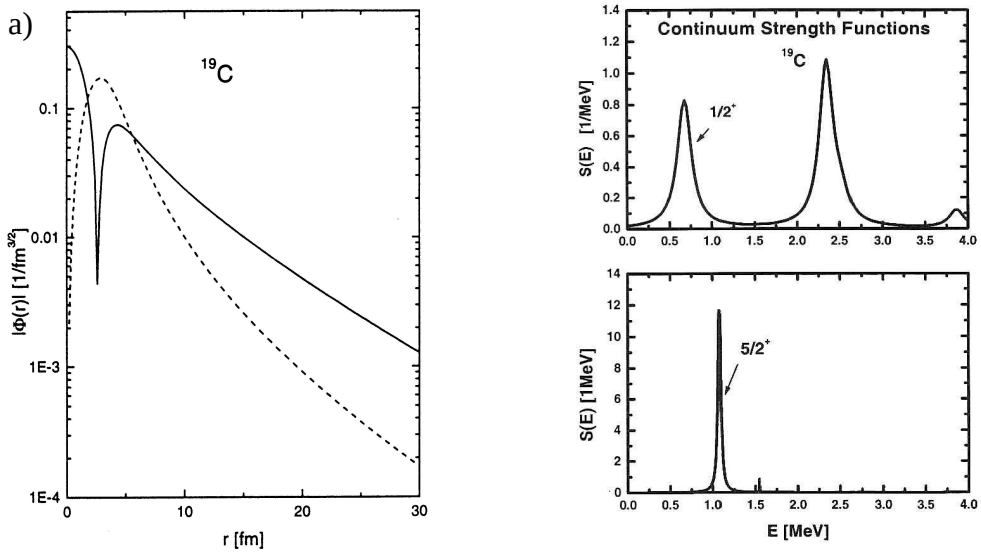

Figure 1.13. a) Radial wave function obtained in the DCP calculation for ^{19}C [Len98b]. The solid and dashed curves represent, respectively, the $^{18}C_{GS}(0^+) \otimes 2s_{1/2}$ (ground state) and $^{18}C(2^+) \otimes 1d_{5/2}$ configurations. b) Continuum strength functions for the ^{19}C $1/2^+$ (upper panel) and $5/2^+$ (lower panel) channels [Len01].

interaction with the core which, after being excited into states of various multipolarities and energies, deexcites back to the ground state. During these processes the particle can be scattered virtually into high-lying orbitals, with the only constraint that the global J^π are conserved in the intermediate 2p-1h or 1p-2h configurations. The dynamical single particle self-energy Σ_{pol} affects the separation energies and wave functions. This model will be discussed in detail in Chapter 7, where it is applied to the ^{15}C nucleus.

In the DCP calculations for ^{19}C [Len98b, Len01] the density dependent G-matrix interaction of ref. [Hof98] is used, which has been applied in the ^{11}Li calculations described in Section 1.3.1 also. The core excitations are calculated with the QRPA theory. Σ_{pol} is found to be state-dependent in drip-line nuclei, as shown in Figure 1.12b for the lowest $1/2^+$ and $5/2^+$ ^{19}C states. The $1/2^+$ component experiences an additional attractive self-energy at the surface, which is the main source of binding for the ^{19}C ground state ($J^\pi = 1/2^+$). The $5/2^+$ strength is small and the lowest state is predicted at about 300 keV, just above the particle threshold. The theoretical separation energy is $S_n = 183$ keV, against the experimental value $S_n = 160 \pm 110$ keV [Aud97]. However, other experiments give different values (see, e.g., refs. [Mar96, Mad01]), showing that this is still an open question.

Core polarization is important in order to explain the ground state wave function of ^{19}C. Indeed, a spectroscopic factor of only 0.4 is obtained for the $^{18}C_{GS}(0^+) \otimes 2s_{1/2}$ configuration, while the major part of the remaining 60 % is given by the $5/2^+$ and $3/2^+$ neutron state coupled to the first 2^+ core-excited state [Len98b]. The ^{19}C wave functions calculated for the $^{18}C_{GS}(0^+) \otimes 2s_{1/2}$ and $^{18}C(2^+) \otimes 1d_{5/2}$ configurations are shown in Figure 1.13a. The s-wave function shows an extended tail compatible with a halo state. By contrast, d-wave decays more rapidly.

Corresponding calculations for ^{11}Be also results in a $1/2^+$ ground state but with a much larger spectroscopic factor (S = 0.74), explaining the more developed halo with respect to ^{19}C [Len01]. Moreover, the core polarization explains the inversion of the $1/2^+$ and $1/2^-$ states in ^{11}Be as due to an additional attractive self-energy in the $1/2^+$ channel [Len01].

The DCP also affects the low-energy continuum of drip-line nuclei. The continuum strength functions for the $1/2^+$ and $5/2^+$ components in ^{19}C are shown in Figure 1.13b. Narrow resonances in the continuum are observed. They correspond to core-excited configurations where neither of the involved nucleons is in a state above the threshold although the total energy is well above the particle threshold. Such states are called Bound States Embedded in the Continuum (BSEC) and will discussed in Section 2.2.

CHAPTER 2

INVESTIGATIONS OF THE NEUTRON-RICH ^{15}C NUCLEUS

Important information on the evolution of the phenomena involving drip-line nuclei (described in Chapter 1) going towards more extreme conditions of charge asymmetry and low density may be obtained by the systematic comparison of data for neutron-rich nuclei with slightly different neutron separation energy S_n. In particular, an interesting case is ^{15}C which, with the small separation energy of the valence neutron (S_n = 1.218 MeV), is intermediate between the well-bound ^{12,13,14}C nuclei and the more exotic ^{17}C (S_n = 0.73 MeV) and ^{19}C (S_n = 0.16 MeV). The present Chapter focuses attention on the ^{15}C nucleus.

Over the last few years the interest in ^{15}C has been manyfold and different kinds of experiments have been performed in order to explore its various properties (see Sections 2.1 and 2.3). As discussed in Section 2.3, an intriguing characteristic of this nucleus has been the uncertain presence of a halo in its ground state. In fact, for a long time there have been contrasting results. Even though the measured matter radius of ^{15}C (R^m_{rms} = 2.40 ± 0.05 fm) does not differ much from those of the near stable nuclei [Aud93, Oza96, Oza01], nevertheless some "exotic" features have been found, such as: the inversion between the $1d_{5/2}$ and $2s_{1/2}$ neutron orbitals [Ajz86] and the narrow longitudinal momentum distribution of the ^{14}C core fragments, observed in one-neutron removal experiments, which suggests a strong spatial delocalization of the valence neutron [Baz98, Par00, Sau00, Mad01]. However, other recent results seem to deny the existence of a halo state in $^{15}C_{GS}$ [Chu00].

The spectroscopic investigation of ^{15}C via the (^{7}Li,^{7}Be) Charge EXchange (CEX) reaction, which is the object of the present work, should be regarded into a more general context. Indeed, this experiment is inserted in a research program which will be performed by the use of the large-acceptance magnetic spectrometer MAGNEX at the LNS-INFN laboratories, Catania (Italy) [Cun02a, b, c]. As described in Section 2.2, the purpose is the systematic study of both the CEX mechanism and the structural properties of the light neutron-rich nuclei with structure given by an integer number *n* of α particles coupled with a system of three neutrons. Since the α clusters may be considered rather compact, most likely they form an inert core. Thus similar features are expected both in structure and reaction mechanism for nuclei which differs by *n* α particles. In Sect. 2.2 particular attention is paid to the presence in the energy spectra of narrow resonances well beyond the neutron emission threshold S_n, which is also expected in ^{15}C, in connection with the BSEC phenomenon.

2.1 Spectroscopy of the ^{15}C nucleus

The ^{15}C nucleus (S_n = 1.218 MeV) possesses only two weakly-bound states, the $1/2^+$ ground state and the $5/2^+$ first excited one at E_x = 0.74 MeV. The spin and parity of the ^{15}C ground state have been assigned to be $J^\pi_{GS} = 1/2^+$ by neutron stripping reactions, which were the first experiments devoted to the spectroscopic study of ^{15}C (see Section 2.1.1). All these experiments agree on the J^π values of the ^{15}C ground and first excited state. The ground state wave function is given mainly by the $^{14}C_{GS}(0^+) \otimes (2s_{1/2})$ configuration with a spectroscopic factor S = 0.88, while the wave function of the 0.74 MeV excited state is given by $^{14}C_{GS}(0^+) \otimes (1d_{5/2})$ with S = 0.69 [Gos75]. However, relevant contributions from the excited states of the ^{14}C core were found by nuclear breakup of ^{15}C [Baz98]. In ^{15}C the $1d_{5/2}$ and $2s_{1/2}$ neutron orbitals are inverted with respect to the independent-particle model levels (see Sect. 2.3.1).

The simplest levels possible for the ^{15}C nucleus are the one particle-two hole (1p-2h) states, obtained by coupling a (sd)-shell neutron to the ground state of the ^{14}C core. These states have positive parity and the predicted J^π values are $1/2^+$, $3/2^+$ and $5/2^+$. The ^{15}C ground and first excited state are almost entirely 1p-2h states ([Mur94] and refs. therein). Next in complexity are the negative-parity 2p-3h states, with J^π from $1/2^-$ to $9/2^-$, which consist of two (sd)-shell neutrons coupled to three p-shell holes. Single-neutron transfer reactions can populate the 1p-2h ^{15}C states, but not the 2p-3h ones, except via core-excited components of the $^{14}C_{GS}$. On the contrary, two-neutron transfers can populate 2p-3h states.

The main reactions used in the various years to study ^{15}C and the results obtained are described in the present Section.

2.1.1 The ^{14}C(d,p)^{15}C stripping reaction

The ^{14}C(d,p)^{15}C stripping reaction was first studied in 1959 by Moore and Mc Gruer [Moo59] in the angular range between 2° and 90°, populating the ^{15}C ground and excited states at E_x = 0.75, 3.09, 4.21, 5.94, 6.38 and 7.32 MeV. In 1973 Goss et al. [Gos73] studied the same reaction at 12, 13 and 14 MeV incident energies and θ_{lab} = 60°, 90° and 120°. A magnetic spectrograph was used, allowing for a high experimental resolution (~ 14 keV). In Figure 2.1 a proton spectrum, measured at the bombarding energy of 14 MeV and 60°, is shown, where the excitation energy of the populated ^{15}C states are indicated. Nine excited states were found, starting from the ground to the 7.35 MeV state, with a better determination of the excitation energies. Two wider levels were found at 3.1053 MeV (Γ ~ 42 keV) and 6.4281 MeV (Γ ~ 61 keV). The presence of a large continuum background in the spectrum made it impossible to observe weakly populated states with Γ > 100 keV.

A second experiment was performed by the same authors [Gos75] using a polarized deuteron beam at E_{inc} = 14 MeV. The angular distributions were obtained for 10 final states up to E_x ~ 7 MeV. Vector Analyzing Powers (VAP) were measured for deuteron elastic scattering and for the (d,p) reaction leading to the two ^{15}C bound states. Distorted Wave Born Approximation (DWBA) calculations were performed with two different set of optical-model parameters, in order to test the sensitivity of the results to the used parameterisation. The deuteron parameters of the first set were obtained by fitting the cross section of the

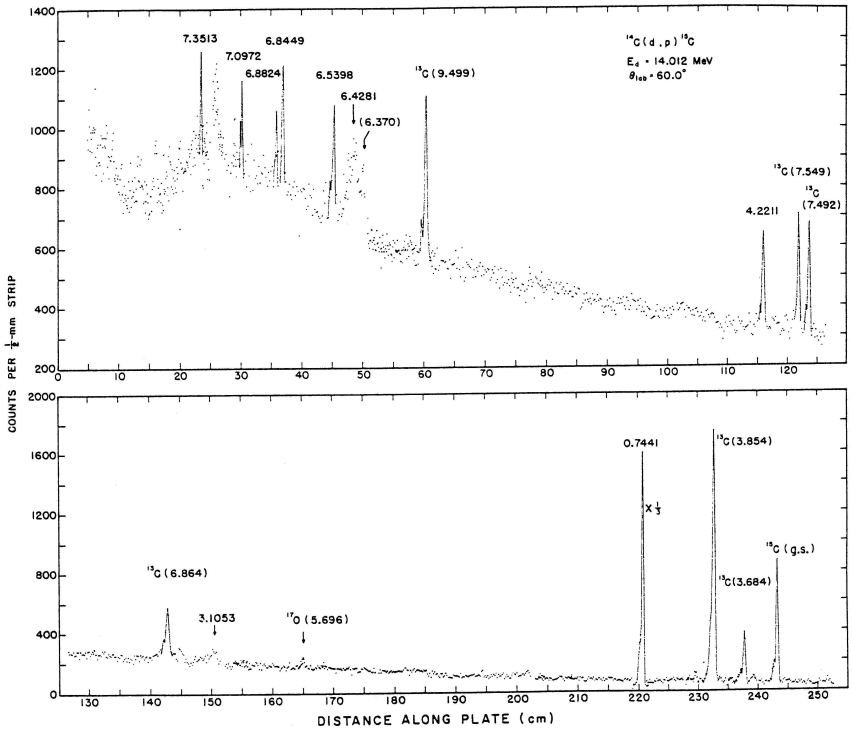

Figure 2.1. Proton spectrum from the ^{14}C(d,p)^{15}C reaction measured at 14 MeV bombarding energy and θ_{lab} = 60° [Gos73]. Proton groups leading to the ^{15}C states are labeled with the excitation energy. The contaminants groups are also labeled with the symbol for the residual nucleus and related excitation energy.

^{4}C($\vec{d}$,d)^{14}C reaction and then slightly varied according to the VAP results for the two bound state. The DWBA analysis of angular distributions allowed to assign spin and parity to the ^{15}C ground and first excited state together with the related spectroscopic factors S = 0.88 and 0.69, respectively. These were obtained from the set of optical parameters giving the best fit to the respective angular distributions, as shown in Figure 2.2. While the single particle $d_{5/2}$ state was located at E_x = 6.428 MeV, no evidence for the $3/2^+$ state was found. Besides, many states with high spin (from $7/2^+$ to $13/2^+$) were found in the region between 6 and 7 MeV excitation energy, however the authors underlined that these assignments may be erroneous if indeed the state are populated predominantly by two-step processes.

Ten years after, another (d,p) experiment was performed with a 16 MeV polarized deuteron beam [Dar85] in order to search for the $d_{3/2}$ strength in the particle-unbound region of ^{15}C, where the 1p-2h $J^\pi = 3/2^+$ state is expected to lie. Proton spectra were obtained over the angular range θ_{lab} = 15° to 110° in 5° steps. The experimental results are shown in Figure 2.3. Two $3/2^+$ levels (indicated by arrows in Fig. 2.3a), one broad ($\Gamma = 1.74 \pm 0.40$ MeV) and one relatively narrow ($\Gamma \sim 64$ keV), were observed at E_x = 4.78 and 5.81 MeV, respectively. The J^π value of the broad state was proposed on the basis of DWBA calculations (see Figs. 2.3b and 2.3c) as in ref. [Gos75]. Since this state interferes with the narrow one, they must have the same spin and parity. The authors identified these states with the 1p-2h and 3p-4h $3/2^+$ levels predicted by shell model calculations. The two states exhaust approximately the 50 % of the single particle strength. However, considerable fluctuations were present in the data

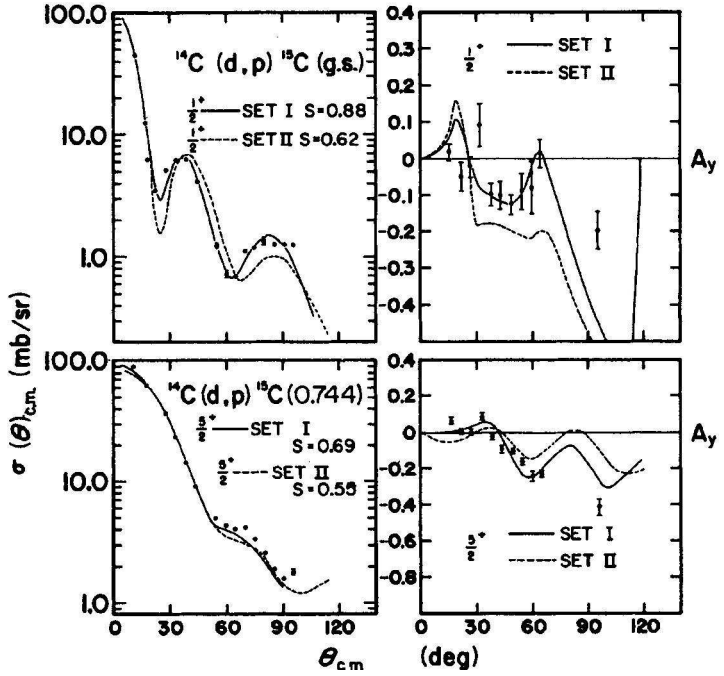

Figure 2.2. Cross sections and analyzing powers for the two bound states of ^{15}C [Gos75]. The lines are the results of DWBA calculations with two different sets of optical-model parameters.

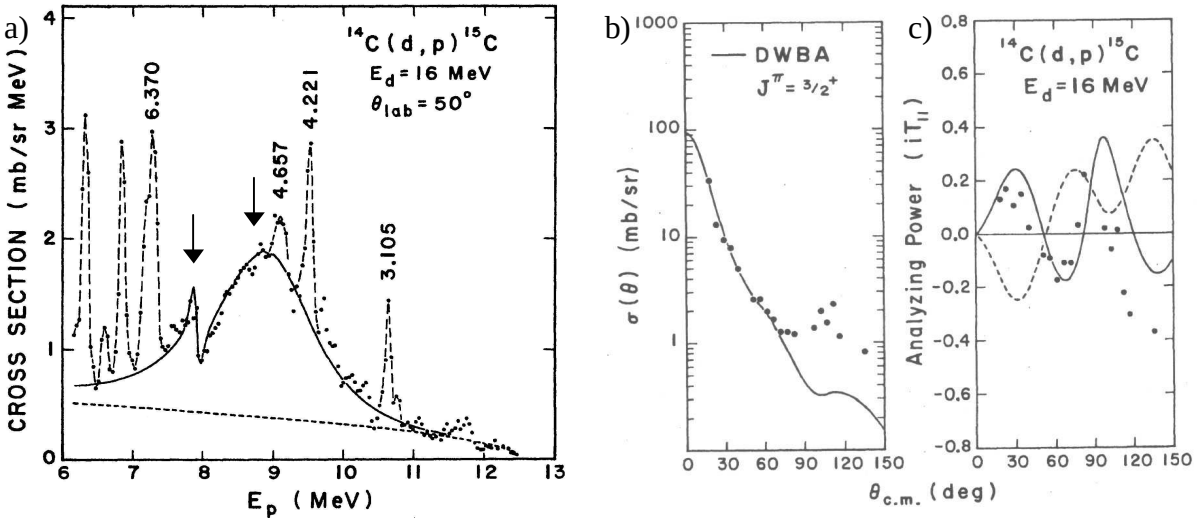

Figure 2.3. Results for the ^{14}C(d,p)^{15}C reaction at 16 MeV incident energy [Dar85]. a) Neutron-unbound portion of the proton spectrum measured at θ_{lab} = 50°. Dashed curves are drawn through proton groups corresponding to the known levels of ^{15}C. The arrows indicate the levels that are candidates to have $J^\pi = 3/2^+$. The smooth dashed curve shows the phase-space contribution due to the deuteron breakup. The solid curve represents a fit to the spectrum. b) Angular distribution and c) VAP results for the broad state at 4.78 MeV. The solid curves are the DWBA predictions for $J^\pi = 3/2^+$, while the dashed one corresponds to $J^\pi = 5/2^+$.

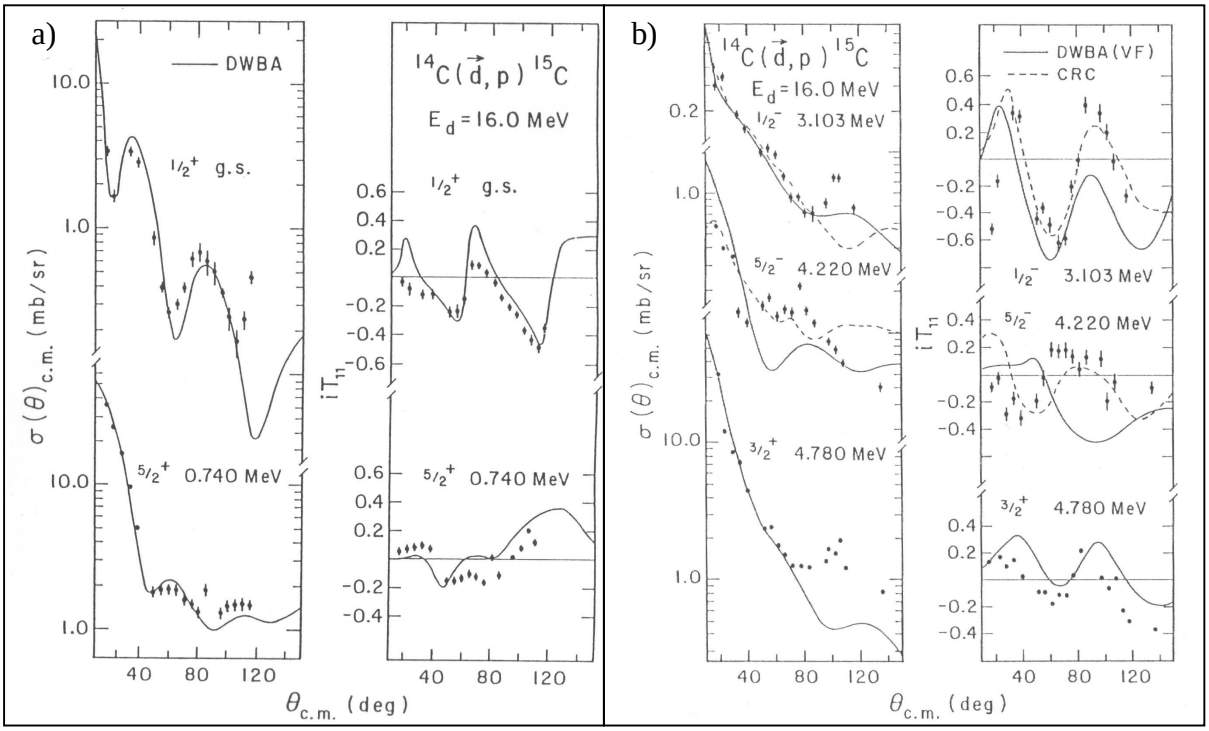

Figure 2.4. Results for the ^{14}C(d,p)^{15}C reaction at 16 MeV incident energy [Mur94]. Cross sections and vector analyzing powers for a) the two bound states of ^{15}C and b) the unbound states of ^{15}C at E_x = 3.103, 4.22 and 4.78 MeV. The solid and dashed curves represent the results of DWBA and CRC calculations, respectively.

due to background from the ^{12}C(d,p)^{13}C reaction. The interference observed between the two $3/2^+$ overlapping resonances is visible at all but the largest angles and lead to an asymmetric line shape in the proton spectra. Similar phenomena were before observed in refs. [Bau75, Bau77] (see Section 8.1) and are connected with the BSEC states (Section 2.2).

Subsequently, the same authors [Mur94] analyzed the angular distributions and the VAP data for various ^{15}C states by DWBA calculations for bound and unbound states. The importance of two-step processes was investigated via Coupled Reaction Channels (CRC) calculations. The results are shown in Figure 2.4. The ground and the states at E_x = 0.74, 3.103 and 4.78 MeV appear populated primarily by a one-step process, with a small two-step contribution in the case of the 3.103 MeV state. On the contrary, the 4.22 MeV state seems populated predominantly by two-step processes.

2.1.2 The ^{9}Be(^{7}Li,p)^{15}C compound nuclear reaction

In the past, the ^{14}C(d,p) and ^{9}Be(^{7}Li,p) reactions were widely used in order to investigate ^{15}C, because they are the most easily realizable in terms of available target and material. However, the ^{9}Be(^{7}Li,p)^{15}C reaction (see ref. [Gar74] and refs. therein) proceeds through an intermediate compound system and therefore is less selective than the ^{14}C(d,p)^{15}C stripping reaction.

In ref. [Gar74] the ^{9}Be(^{7}Li,p)^{15}C reaction was studied at 20 MeV bombarding energy. The authors identified 27 states in ^{15}C: all the levels reported from the ^{14}C(d,p) reaction plus five additional states at E_x = 4.55, 5.84, 5.86 and 6.64 MeV. A proton spectrum measured

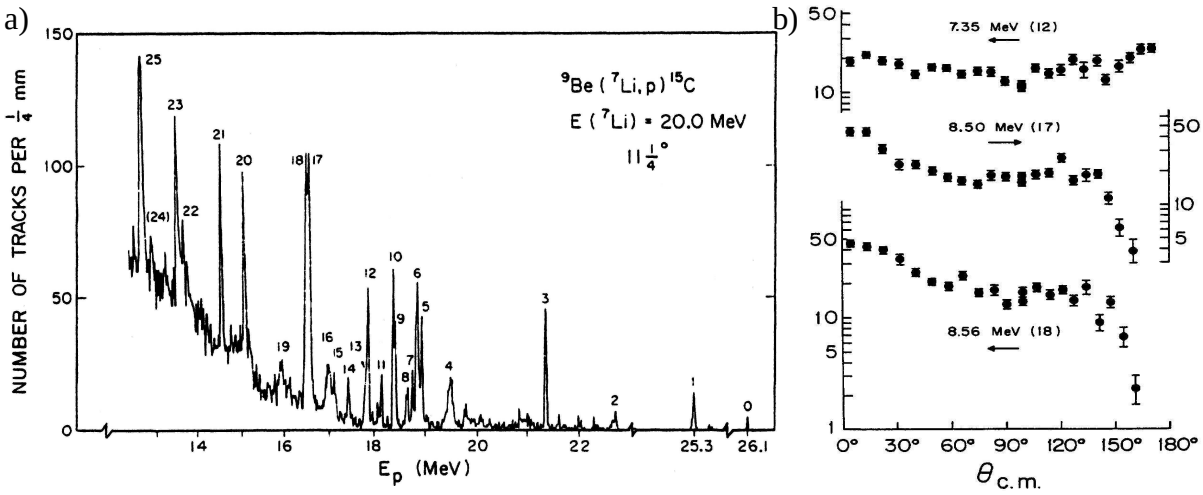

Figure 2.5. a) Proton spectrum from the ^{9}Be(^{7}Li,p)^{15}C reaction at E_{inc} = 20 MeV and θ_{lab} = 11.25°. The numbers identify the peaks corresponding to the populated ^{15}C states (see Table I in ref. [Gar74]), among which 0 and 1 are the two ^{15}C bound states (ground and first excited at E_x = 0.74 MeV, respectively). b) Angular distributions for the ^{15}C unbound states at E_x = 7.35, 8.50 and 8.56 MeV [Gar74].

at θ_{lab} = 11.25° is shown in Figure 2.5a. Several narrow resonances in the continuum were observed. Angular distributions were measured for many of the ^{15}C levels. Consistent with the compound reaction mechanism, they are almost shapeless and approximately symmetric at 90°, except for the two narrow levels ($\Gamma \sim 40$ keV) at E_x = 8.50 and 8.56 MeV (see Fig. 2.5b).

For a compound system populated at sufficient excitation energy and with a distribution of large angular momenta, the total cross section is proportional to $(2 J_f + 1)$, where J_f is the angular momentum of the final state. According to this statistical assumption, the total cross sections extracted from the angular distributions were used to suggest spin and parity for many of the populated states (see Table III in ref. [Gar74]). High spins were proposed for some of the ^{15}C resonances lying in the single particle continuum (see the values in Table 5.2). Their narrow widths indicate hindrance for the neutron emission, for which either a reduced penetrability due to the high angular momentum of the decaying system, or a nuclear wave function with small overlap with a single particle configuration (n $\otimes$ $^{14}C_{GS}$) may be responsible. The authors incline for the first hypothesis.

Both the ^{15}C and ^{17}O nuclei have nine neutrons and ground state configurations with an unpaired neutron outside the filled p-shell. However, the neutron emission threshold is considerably lower in ^{15}C than in ^{17}O (S_n = 4.143 MeV). According to the shell model, configurations with the valence neutron in the $s_{1/2}$, $d_{5/2}$ and $d_{3/2}$ orbitals are expected in the low-lying spectra of both nuclei. Such states should be populated strongly in the ^{14}C(d,p) and ^{16}O(d,p) reactions. A comparison between the low-lying levels of ^{15}C and ^{17}O is shown in Figure 2.6. The states for which a similar configuration is suggested are connected by dashed lines. It is seen that in ^{15}C the $5/2^+$ and $1/2^+$ levels are reversed with respect those of ^{17}O. The authors explained the different number of states observed above E_x = 5 MeV as due to the presence of levels based on three unpaired particles, which should be different for ^{15}C and ^{17}O. Besides, some states that are narrow in ^{17}O may be broad in ^{15}C and thus may have been escaped detection.

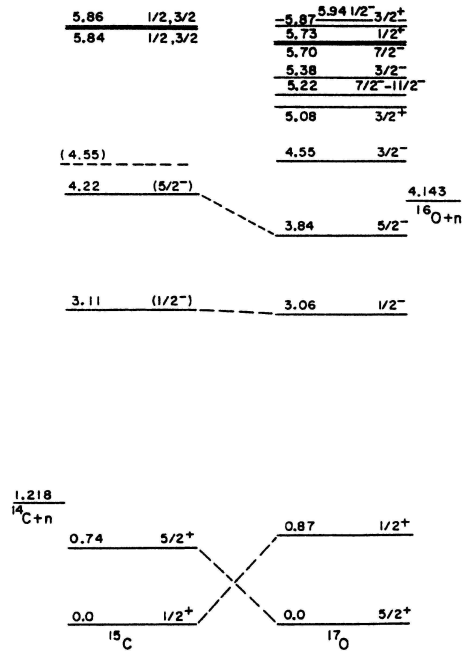

Figure 2.6. Comparison of the low-lying level schemes of the ^{15}C and ^{17}O nuclei.

2.1.3 The transfer reactions

The main features of the transfer reactions involving exotic nuclei are described in Section 1.2. Here we discuss some transfer reactions specifically used in order to study ^{15}C. While one-neutron transfer reactions, such as the ^{14}C(d,p) described in Section 2.1.1, excite mainly the 1p-2h strength, two-neutron transfers may excite both the 1p-2h and 2p-3h ones.

In 1978 Jahn et al. studied the (α,^{2}He) reaction at 55 and 65 MeV bombarding energies on several targets, among which ^{13}C, in the angular range θ_{lab} from 12° to 35° [Jah78]. The unbound reaction product ^{2}He can be identified by measuring its two breakup protons in coincidence. In general, preferential population of two-neutron states with dominant $(d_{5/2})^2_4$, $(d_{3/2}\ f_{7/2})_5$ and $(f_{7/2})^2_6$ configurations was found. In particular, the ^{13}C(α,^{2}He)^{15}C reaction allowed the observation of the 0.74 MeV state ($J^\pi = 5/2^+$) and two levels at E_x = 6.74 and 7.35 MeV, which the authors interpreted as the $(d_{5/2})^2_{4^+}$ two-neutron configuration coupled with a $^{13}C_{GS}$ ($J^\pi = 1/2^-$) core, suggesting for such states $J^\pi = 7/2^-$ and $9/2^-$, respectively.

Later, Truong and Fortune [Tru83] used the ^{13}C(t,p)^{15}C reaction at 18 MeV incident energy in order to study the 1p-2h and 2p-3h states in ^{15}C up to E_x = 7.5 MeV. A proton spectrum measured at 11.25° is shown in Figure 2.7. The energy resolution was about 15 keV. All the $(sd)^2(1p)^{-3}$ states expected to be strongly populated in the (t,p) reaction were observed, together with two of the three $(sd)(1p)^{-2}$ states. The 1p-2h $3/2^+$ state was missing.

The three-neutron transfer reaction ^{12}C(^{12}C,^{9}C)^{15}C at E_{inc} = 230.7 MeV was studied recently by Bohlen et al. [Boh03]. The detected ^{9}C ejectile is particle stable only in its ground states, all the excited states being unstable against proton emission (S_p = 1.296 MeV). Thus the measured ^{15}C spectrum (see Fig. 2.8) shows only states in combination with $^9C_{GS}$. The ^{15}C

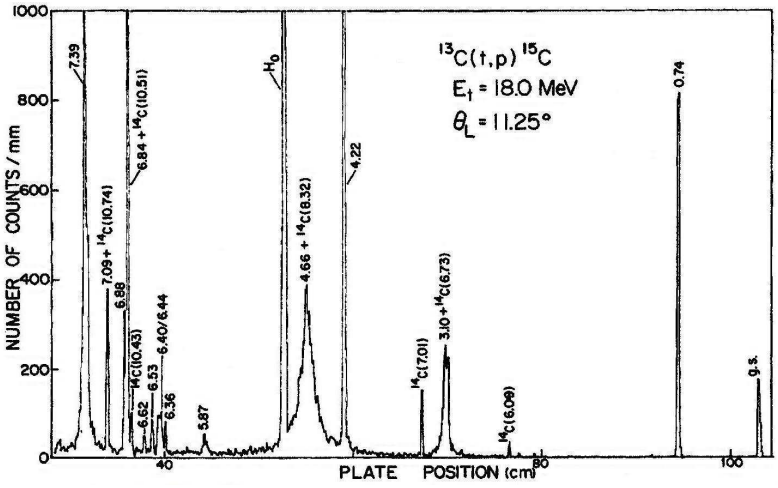

Figure 2.7. Proton spectrum from the ^{13}C(t,p)^{15}C reaction measured at E_{inc} = 18 MeV and θ_{lab} = 11.25° [Tru83]. The ^{15}C states are labeled with their excitation energies. The peaks from ^{12}C and hydrogen impurities present in the target are also indicated.

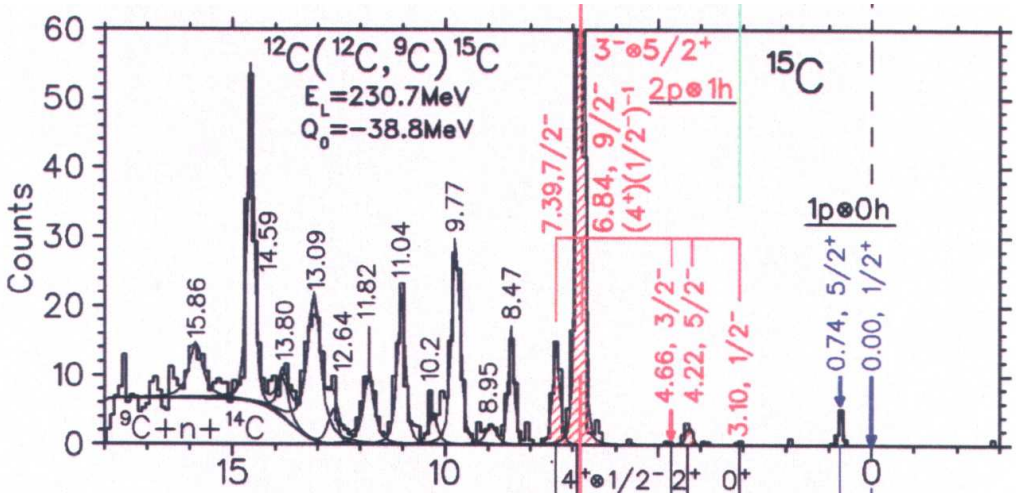

Figure 2.8. Excitation energy spectrum from the ^{12}C(^{12}C,^{9}C)^{15}C reaction measured at E_{inc} = 230.7 MeV [Boh03].

excited state at E_x = 6.84 MeV is the strongest observed state in that spectrum. The $d_{3/2}$ single particle resonance at E_x = 4.8 MeV is presumably too weak and broad to be seen. The spins and parities of the ^{15}C states measured at E_x = 6.84, 7.39 MeV were proposed to be $J^\pi = 9/2^-$ and $7/2^-$, respectively, on the basis of a comparison with the particle-hole structure of the related ^{14}C states. Precisely, this doublet was considered due to a dominant 2p-1h structure with a $1p_{1/2}$ neutron-hole, which couples to a $^{14}C_{4+}$ core. It was further discussed that the above mentioned ^{15}C states may be populated, starting from ^{14}C, in two different ways: either to add a $1d_{5/2}$ neutron to the particle component of the 1p-1h doublet of ^{14}C ($E_x(J^\pi)$ = 6.73(3^-) and 7.34(2^-) MeV) or to fill a hole in the $1p_{1/2}$ shell of the 2p-2h positive-parity multiplet, i.e., in the 4^+ state at E_x = 10.74 MeV, obtaining in both cases the $4^+\otimes 1/2^-$ coupling.

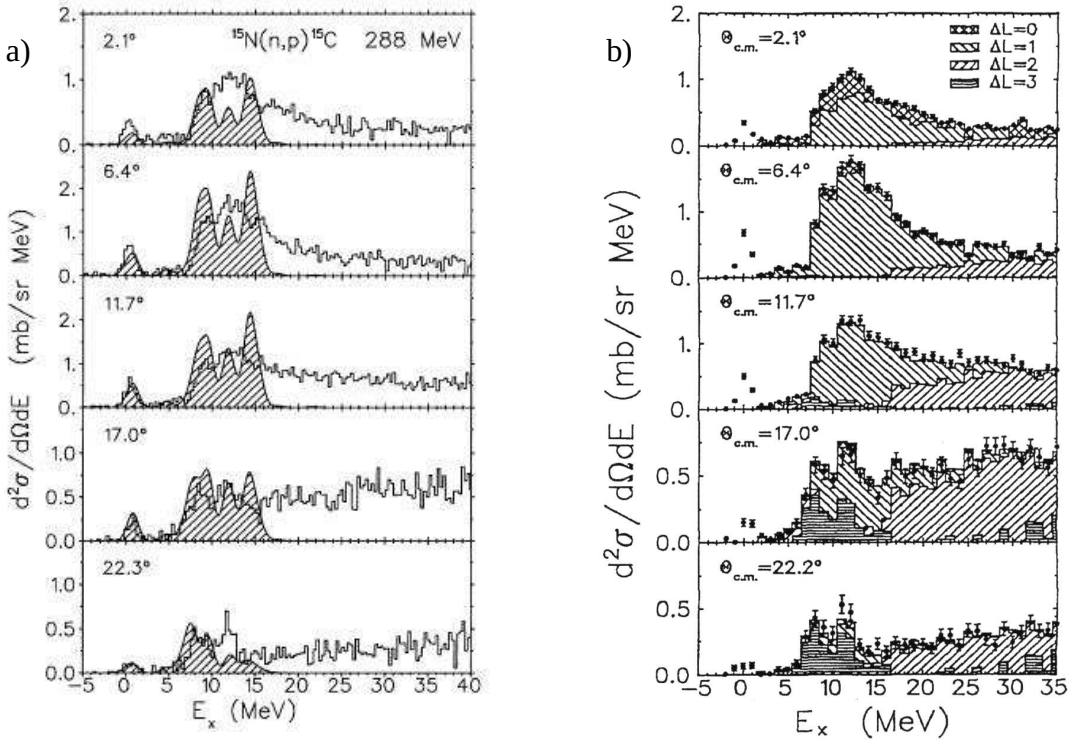

Figure 2.9. Results from the ^{15}N(n,p)^{15}C reaction at E_{inc} = 288 MeV [Cel91]. a) Comparison between the experimental spectra at different angles and the corresponding theoretical strength distributions (shared areas) for excitation of positive-parity states. The calculated cross sections are folded with gaussian functions and scaled by a factor 0.7. b) Multipole decomposition analysis for excitation energies above 2 MeV and ΔL = 0, 1, 2 and 3 components.

2.1.4 The ^{15}N(n,p)^{15}C CEX reaction

Compared with the transfer reactions, which mainly transfer neutrons into open shells, the (n,p)-like CEX reactions excite the one-neutron-particle–one-proton-hole strength of the nucleus considered. Thus only a partial overlap is expected with the states excited in the transfer reactions. The (n,p)-like CEX reactions proceed with isospin transfer ΔT_z = + 1. The response of the ^{15}C nucleus to such an isovector probe was, until recently, little known primarily because of difficulties to realize a high-purity ^{15}N target.

The only previous data in this field were the ^{15}N(n,p)^{15}C reaction, studied using a 288 MeV neutron beam and a high-pressure ^{15}N gas target at the TRIUMF facility [Cel91]. The protons were analysed by the TRIUMF medium-resolution spectrometer. Proton spectra were measured at different angles in the range θ_{lab} from 0° to 20°. The overall resolution was about 1.4 MeV at 0° and this value increases at larger angles. In Figure 2.9a the experimental spectra are shown in comparison with the calculated ones.

The authors were interested in the study of the strength distribution of the Spin Dipole (SD) transitions (ΔL = 1, ΔS = 1), in connection with the problem of the missing Gamow-Teller (GT) strength (ΔL = 0, ΔS = 1). An attempt to estimate the SD contributions was made by a multipole decomposition analysis (Fig. 2.9b).

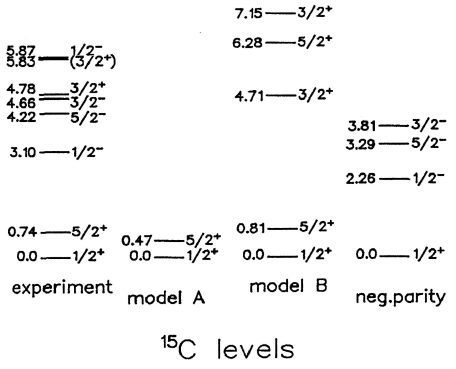

Figure 2.10. ^{15}C energy levels, experimental [Ajz86] and from shell model calculations [Cel91].

As a check of the reliability of such calculations, it is important to have experimental data in cases where the $\Delta L = 1$ transitions can be clearly resolved and the nuclear structure is simple enough to permit realistic model calculations. Since for the $^{15}N(n,p)^{15}C$ reaction from $^{15}N_{GS}$ ($J^\pi = 1/2^-$) to the first two ^{15}C states, the ground ($J^\pi = 1/2^+$) and first excited state at 0.74 MeV ($J^\pi = 5/2^+$), the $\Delta L = 0$ GT transitions are forbidden in first order, the $\Delta L = 1$ strength can be measured for these two states. The energy resolution does not allow to separate them (see Fig. 2.9a), however, they are separated by more than 2 MeV from the ^{15}C states at higher excitation energy. Thus the authors divided the spectra in three different energy ranges, integrating each of them separately and obtaining the respective angular distributions. In the first region only the two lowest ^{15}C states are included.

In Figure 2.10 the ^{15}C energy levels obtained from shell model calculations [Cel91] are compared with the experimental ones taken from ref. [Ajz86]. The ^{15}N ground state is described by the shell model mainly as a single-hole $(1p_{1/2})^{-1}$ state coupled to an inert ^{16}O core, while the two ^{15}C bound states can be described as $\nu(2s_{1/2}\ 1d_{5/2})^1\ \pi(1p_{1/2})^{-2}$ (levels predicted by the model A in Fig. 2.10). More complicated configurations are included in the model B by allowing two holes anywhere in the full 1p-shell and one particle anywhere in the full 2s1d-shell: $(sd)^1(p)^{-2}$. This allows a description of low-lying positive-parity states with spin J from 1/2 to 9/2 (model B levels in Fig. 2.10). This model predicts, starting from $^{15}N_{GS}$, transitions involving $\Delta J \leq 4$ with a change of parity, which can be excited by spin-flip transitions with $\Delta L = 1$ and 3. Finally, the ^{15}C negative-parity states with $E_x < 5$ MeV may be described in terms of 2p-3h configurations. The GT transitions to these states are forbidden in the approximation that $^{15}N_{GS}$ is a pure one-proton-hole state. However, the results of $^{15}N(e,e')$ experiments [Sin83, Dev88] indicate substantial admixture of 1h and 2p-3h states in the ground state wave function of ^{15}N.

The theoretical spectra (shaded areas in Fig.2.9a) were calculated for transitions to the states with $J^\pi \leq 9/2^+$ predicted by the model B. For each state, the theoretical cross section was then folded with a Gaussian distributions of assumed Full Width at Half Maximum (FWHM) $\Gamma_{FWHM} = 1.5$ MeV and renormalized by a factor 0.7 in order to describe the magnitude of the experimental SD cross section, which is maximum at around 7°. However, significant discrepancies were found between the predicted SD angular distribution for the two ^{15}C bound states and the data extracted from the corresponding energy region. Since the GT strength

depends sensitively on the detailed shape of the spectrum, the fit to the angular distribution is not sufficient to determine it. The multipole decomposition analysis (Fig. 2.9b) was made assuming contributions from the $\Delta L = 0$, 1, 2 and 3 transitions, also accounting for transitions to negative-parity states in ^{15}C. At small angles the main contribution to the cross section below $E_x = 20$ MeV is given by the $\Delta L = 1$ SD excitations, in agreement with the shell model predictions concerning several excited states in this energy region. The $\Delta L = 2$ component appears above $E_x = 15$ MeV at 2.1° and becomes dominant at larger angles. A considerable $\Delta L = 3$ component is found at angles above 15°.

The CEX reactions are discussed in more detail in Chapter 3. The main advantage of the (n,p) reactions is the relative simplicity of the n-p vertex, however, the production of the neutron beam leads to a poor energy resolution. The (^{7}Li,^{7}Be) CEX reaction, which we have used to study ^{15}C, has different advantages in comparison with the (n,p) one (see Section 3.3).

2.2 Exploring the structure of the light neutron-rich nuclei: the BSEC phenomenon

A systematic investigation of the light neutron-rich nuclei via the (^{7}Li,^{7}Be) CEX reaction has been started by our Group (MAGNEX), in order to study both the structural properties of the nuclei under consideration and the CEX mechanism. In this Section the attention is concentrated on the aspects involving nuclear structure, postponing unto Chapter 3 the motivations for the choice of this particular CEX reaction and the important information obtainable by analysing the reaction dynamics. In particular, we are interested in a systematic exploration of nuclei for which an integer number *n* of α particles is coupled to three extra neutrons, such as: ^{7}He, ^{11}Be, ^{15}C, ^{19}O, ^{23}Ne, ^{27}Mg and heavier systems. For these nuclei one can assume that the single particle excitations at low energy are mainly due to the three valence neutrons, while the α particles form a rather compact core. Thus, if the transition operators have a large overlap with the single particle wave functions (as, e.g., for CEX reactions), the measured energy spectra give information on the three neutron dynamics in the nuclear medium.

Experimental signatures of the DCP correlations (see Section 1.3.2) may be obtained by studying transfer or CEX reactions involving weakly-bound nuclei. In fact, close to the neutron drip line, the core system itself is already neutron-rich and thus more easily polarizable. For the ($n\alpha \otimes 3n$) nuclei, the pairing of two of the three neutrons to the inner core gives an softer core, which can be dynamically polarized by the interaction with the remaining neutron even at low excitation energy. Consequently, the energy available in the reaction can be directly transferred to the core, which becomes excited, while the valence neutron is weakly influenced. The important observable connected with the core excitations is the presence of Bound States Embedded in the Continuum (BSEC) in the experimental spectra. These states appear as very narrow resonances lying at energies well beyond the neutron emission threshold. For these structures the mean-field dynamics is no longer appropriate. A natural explanation [Bau77, Len01, Cor01] is that they are quasi-bound core-excited configurations, where the weakly-bound valence nucleon couples to the excited states of the core, as described, e.g., by the DCP model.

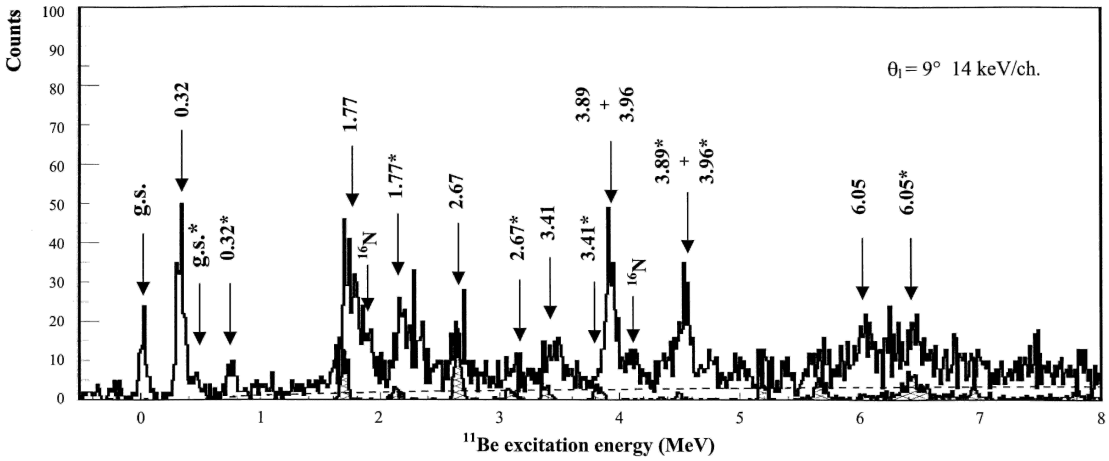

Figure 2.11. Excitation energy spectrum from the ^{11}B(^{7}Li,^{7}Be)^{11}Be reaction at E_{inc} = 57 MeV and θ_{lab} = 9° [Cap01]. Peaks marked with an asterisk are associated to the excitation of ^{7}Be at 0.429 MeV. The shaded histogram represents the normalized background from the ^{12}C(^{7}Li,^{7}Be)^{12}B reaction. The dashed line represents the ^{11}B(^{7}Li,n^{7}Be)^{10}Be 3-body phase space.

The BSEC phenomenon was predicted theoretically some time ago by Mahaux and Weidenmüller [Mah69]. In ref. [Bau77] it was investigated theoretically in stable nuclei. A BSEC was observed for the first time in the stable ^{13}C nucleus: the excited state at E_x = 7.677 MeV ($J^{\pi} = 3/2^{+}$) [Fuc80]. Here, we consider the BSEC excitations in loosely-bound neutron-rich systems. In such nuclei an enhancement of the BSEC phenomenon is expected due to the larger polarizability of the neutron-rich core. The increased polarizability of the system is related, e.g., to the presence of low-energy 2^{+} core states, whose energy decreases with increasing mass. A good example is given by the carbon isotopes, which show this feature with increasing neutron number and for which the BSEC structures might be an important phenomenon in the low-energy continuum [Len01, Cor01]. In addition, the weak binding of the valence particles in the exotic nuclei increases the interactions among bound and unbound configurations, thus giving such nuclei the characteristics of an open quantum system. Altogether, we expect a strong enhancement of the BSEC excitations in the low-energy continuum of the neutron-rich nuclei.

The first (^{7}Li,^{7}Be) experiments, involving the study of the ^{7}He, ^{11}Be [Cap01, Cap04b] and ^{15}C (see Chapters 4 and 5) nuclei and a preliminary test concerning ^{19}O, have been performed at the Tandem facility of the IPN-Orsay laboratory, while the next ones will be done at the LNS-INFN laboratories by using the large-acceptance magnetic spectrometer MAGNEX. While the analysis of the ^{7}He data is at the beginning, interesting results has been found in the ^{11}Be spectrum, shown in Figure 2.11. Two weakly-bound states, the ground and first excited at E_x = 0.32 MeV, are populated, together with several narrow resonances in the continuum (S_n = 0.504 MeV in ^{11}Be) and a structure at E_x = 9.4 MeV with Γ_{FWHM} ~ 7 MeV compatible with the Spin Dipole Resonance (SDR) (not shown in Fig. 2.11, see ref. [Cap04b] for further details). QRPA calculations reproduce only the two bound states, thus the sharp resonances seen at $E_x > S_n$ cannot be simply connected to single particle excitations, which supports the BSEC interpretation. A microscopic treatment of the DCP effects is considered crucial in order to describe correctly the ^{11}Be spectrum above E_x = 2 MeV [Cap04b].

Considering the ^{11}Be results (indeed, ^{15}C differs from ^{11}Be only by an α particle) and the previous discussions, the ^{15}C nucleus seems a good candidate to observe BSEC excitations. We made a first attempt to study ^{15}C in 2001 but, due to various difficulties (see Chapter 4), it was only possible to observe the two ^{15}C bound states and a narrow state at E_x = 8.5 MeV [Noc03]. However, the presence of this state is encouraging. Moreover, microscopic calculations in the framework of the DCP model foresee a strong fragmentation of the ^{15}C strength between 8 and 14 MeV excitation energy [Noc03], thus narrow resonances above the particle threshold are indeed expected in the energy spectrum of ^{15}C.

2.3 Probing the existence of the halo in $^{15}C_{GS}$

Until now, the presence of halo states has been clearly seen in experiments involving some light nuclei, such as ^{11}Be, ^{11}Li, ^{14}Be, ^{17}B and ^{19}C, which represent the last bound nuclei in the N = 7, 8, 10, 12 and 13 isotones, respectively [Zho97]. In ref. [Zho97] it is predicted that also the last bound isotones with N = 9, ^{14}B and ^{15}C, are halo nuclei (see 2.3.1) and it is suggested to study the neutron halo as a common phenomenon along the chain of the isotones at the drip lines. However, as we will see, the experimental evidence concerning the ^{15}C nucleus are contrasting and a definitive conclusion about the existence of the one-neutron halo in its ground state has not been achieved. Other spectroscopic tools for ^{15}C and their contrary results are described in the present Section, which is devoted to the investigation of the halo phenomenon in $^{15}C_{GS}$.

2.3.1 The shell inversion in ^{15}C

A well-known "exotic" characteristic in ^{15}C is the inversion between the $1d_{5/2}$ and $2s_{1/2}$ neutron levels with respect to the standard shell model prediction, giving $J^\pi = 1/2^+$ in the ground state [Ajz86]. This phenomenon, usually called "shell inversion", is typical of weakly-bound light neutron rich nuclei. In fact, the $2s_{1/2}$ orbital is known to lower in excitation for lighter nuclei [Boh69]. In the well known one-neutron halo nucleus ^{11}Be (S_n = 0.504 MeV) the $2s_{1/2}$ neutron level is even below the $1p_{1/2}$ shell model orbit [Ajz68, Aut70]. Another example is ^{14}B, where the $1d_{5/2}$–$2s_{1/2}$ inversion is found [Ajz86], strengthening the analogy with ^{15}C. The neutron shell structure of $^{14}B_{GS}(J^\pi = 2^-)$ is similar to that of $^{15}C_{GS}$: $\nu(2s_{1/2})^1$ $\pi(1p_{3/2})^{-1}$ with spectroscopic factor S = 0.95. Besides, the neutron separation energy is about 1 MeV in both nuclei (S_n = 0.97 MeV in ^{14}B) and ^{14}B has only two bound states: the ground and the first excited state at 0.74 MeV, as in ^{15}C. However, the main difference is that ^{14}B is an odd-odd nucleus. It has been already studied by the (^{7}Li,^{7}Be) reaction [Bal73, Orr01], but new spectroscopic studies would be useful in order to extend the knowledge of the its structure.

The level inversion may be caused by both the isospin dependence of the mean field and the decrease of the neutron spin-orbit splitting with increasing neutron excess [Zho97]. On the contrary, average quantities such as binding energies and nuclear radii are not significantly influenced because they arise from contributions of all the nucleons. The inversion of the orbitals in ^{15}C is reproduced by shell model calculations in which the WBP interaction is used [War92]; they give mainly a $^{14}C_{GS}(0^+) \otimes (2s_{1/2})$ configuration for the ground state wave function. Nevertheless, the contributions from the core-excited states are important [Baz98].

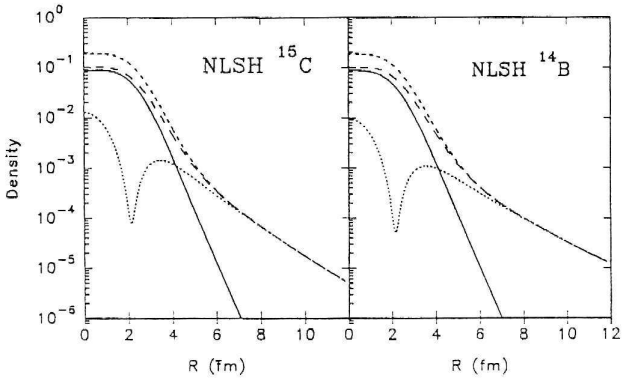

Figure 2.12. Density distributions [fm^{-3}] for the ground state of ^{15}C and ^{14}B [Zho97]. Solid, long-dashed, short-dashed and dotted curves are, respectively, the density distributions of proton, neutron, matter and last neutron.

The ground state properties of the N = 9 isotones were studied in ref. [Zho97] with the non-linear Relativistic Mean Field (RMF) theory. The energy difference calculated between the $1d_{5/2}$ and $2s_{1/2}$ levels in the N = 9 isotones decreases with increasing neutron excess from ^{17}C to ^{13}Be. In particular, the inversion is reproduced for the ground state of ^{15}C and ^{14}B. The density distributions calculated for these states are shown in Figure 2.12. In both nuclei a large spatial extension is predicted for the neutron wave function (halo). The inclusion of the tensor coupling produced by the ρ meson in the RMF calculations improves the $2s_{1/2}$–$1d_{5/2}$ spacing: e.g., from 10 to 540 keV for ^{15}C, against the experimental value of 740 keV.

2.3.2 Results from one-neutron removal experiments

A characteristic halo signature is the Longitudinal Momentum Distribution (LMD) of the core fragments (see Sect. 1.1), which is measured in one-neutron removal experiments. The first experimental results concerning ^{15}C are reported in ref. [Baz98]. The 83 MeV/u secondary beam of ^{15}C was produced by fragmentation of a primary ^{18}O beam on a thick (790 mg/cm^2) Be target at E_{inc} = 100 MeV/u. The LMD of the ^{14}C fragments are shown in Figure 2.13a and b, respectively for breakup of ^{15}C on Be and Ta target.

When the breakup happens on light target, such as Be, it is due mainly to the nuclear interaction. The nuclear breakup data were compared with a Hankel function calculation with l = 0 (last neutron in $2s_{1/2}$) and the inclusion of the localization effect (Fig. 2.13a). Discrepancies were found with the predicted shape, mainly in the tails of the LMD (corresponding to smaller radii in spatial coordinates). On the contrary, no discrepancies were observed in the ^{11}Be case between the LMD data and the calculations performed by the same approach [Han96]. A calculation with a Woods-Saxon potential gives a distribution very similar to the Hankel one and a radius R_{rms} = 5.62 fm for ^{15}C. The authors attributed the disagreement to contributions from the core. As the binding energy increases, the size of the halo decreases and breakup reactions where the core gets excited become possible. The LMD data related to the ^{15}C nuclear breakup were fitted by a modified Lorentzian shape, giving a width Γ_{FWHM} = 67 ± 3 MeV/c. This narrow LMD indicates a spatial delocalisation of the valence neutron, similar to the ^{11}Be case. The one-neutron removal cross section, obtained by integrating the LMD, is σ_{-1n} = 33 mb for ^{15}C, against the theoretical value of 120 mb.

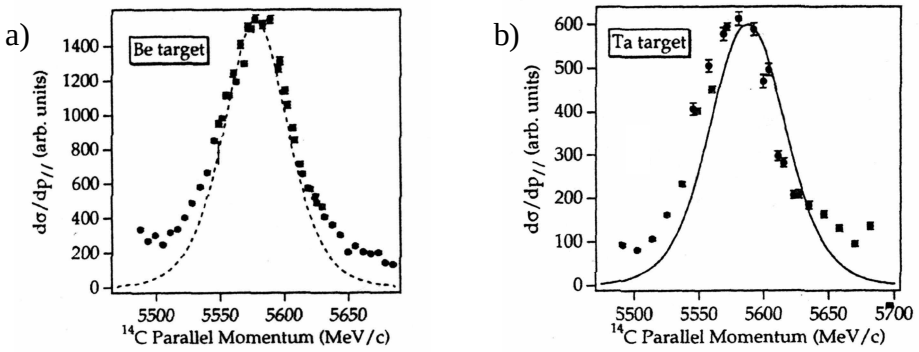

Figure 2.13. Longitudinal momentum distributions of ^{14}C after the breakup of ^{15}C [Baz98]. a) Breakup on a Be target. The dashed line corresponds to an $l = 0$ Hankel function calculation accounting for the localization effect. b) Breakup on a Ta target. The solid line comes from a Coulomb breakup calculation with a Yukawa potential.

The LMD data from ^{15}C breakup on Ta give $\Gamma_{FWHM} = 67 \pm 1$ MeV/c. Since for heavy targets the Coulomb process is dominant, these data are compared to a Coulomb breakup calculation (Fig. 2.13b). The observed discrepancies again suggest that reactions removing a neutron from the core rather than the valence one account for a significant part of the cross section. The integration of the LMD gives a Coulomb dissociation cross section $\sigma_{EMD} = 75$ mb. This value is considerably smaller than the calculated values with Yukawa and Woods-Saxon potentials, 447 and 676 mb, respectively, while the agreement was very good for the ^{11}Be case. The authors considered that this may be in part due to the neglected nuclear dissociation, which clearly must contribute also for the Ta target. Besides, they supposed that the smaller σ_{EMD} primarily reflects the quenching of the low-energy E1 strength with increasing separation energy of the last neutron. This indicates a return towards the normal nuclei, for which the major part of the electric dipole strength is shifted to the region of the Giant Dipole Resonance (GDR). However, a possible experimental problem due to the restricted angular acceptance of the A1200 spectrometer was acknowledged.

The narrow LMD is typical of spatially extended wave functions, nevertheless low values are obtained for σ_{-1n} and σ_{EMD}, which instead should enhance for halo states. The ^{15}C results indicate that a possible neutron halo is not as prominent in this nucleus as in ^{11}Be (for which $\Gamma_{FWHM} = 47.5 \pm 0.6$ MeV/c and $\sigma_{-1n} = 203 \pm 31$ mb [Aum00]), and that core excitations start playing a role in the breakup mechanism. Similar results are obtained in the same work for ^{14}B [Baz98].

The removal of the s-wave valence neutron from ^{15}C leads to production of core fragments in their ground state ($J^{\pi} = 0^{+}$), while the removal of a p-wave neutron produces core fragments in the 1^{-} and 0^{-} excited states [Par00]. Since the p-wave neutrons are more bound and thus more localised, their removal corresponds to enhance the high-momentum region of the LMD. The $^{14}C_{GS}$ contributions to the LMD can be separated from the components due to core-excited states by measuring the deexcitation γ-rays in coincidence with the ^{14}C fragments. In ref. [Nav99] the ^{9}Be(^{15}C,^{14}C + γ) reaction at $E_{inc} = 65$ MeV/u was performed to measure the LMD for removal of p-wave neutrons. It was concluded that the removal of core neutrons can give significant yields and affect the momentum distribution.

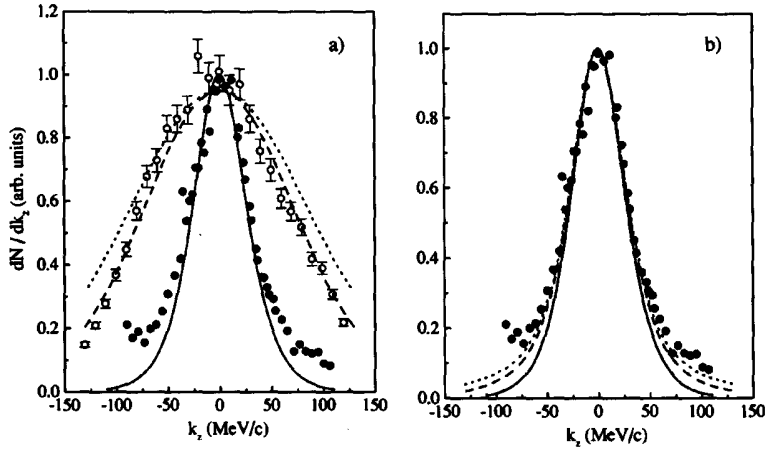

Figure 2.14. Longitudinal momentum distribution of ^{14}C fragments from one-neutron removal. Dots are the experimental data from ref. [Baz98] without identification of the ^{14}C state. Open circles correspond to excited fragment states [Nav99]. The solid lines are calculated LMD [Par00] for $2s_{1/2}$ neutron removal with production of fragments in the ground state. In a) the dashed and dotted lines are LMD for $1p_{1/2}$ neutron removal (with production of fragments in 1^- and 0^- states) obtained, respectively, with black disk and realistic profile function approximations. In b) the dashed and dotted lines are LMD from removal of neutron with production of fragments in all the final states obtained, respectively, with black disk and realistic profile functions.

In Figure 2.14 the LMD data from refs. [Baz98, Nav99] are compared to theoretical calculations [Par00] of the neutron removal cross section for s-wave, p-wave (assuming excitation of the core in the 1^- and 0^- states) and total. Agreement between the theoretical results and the experimental data is found, especially in the central region of the LMD (Fig. 2.14a). The agreement improves by including the one-neutron removal from the core (Fig. 2.14b), but the calculations are sensitive to the type of profile function, which corresponds to the nucleon and core interaction with the target. According to the data from ref. [Baz98], the cross section leading to ^{14}C excited states is ~ 25 % of the total one-neutron removal cross section.

A systematic study of one-neutron removal reactions on 23 neutron-rich (psd)-shell nuclei was carried out by Sauvan et al. [Sau00]. The core LMD obtained for reactions on a carbon target are shown in Figure 2.15a, in comparison with theoretical distributions. These are calculated by the Glauber model with spectroscopic factors extracted by the shell model, and are normalized to the peak number of counts to facilitate the comparison among different isotopes. A marked reduction of the LMD width is found after the sub-shell closures at N = 8 and N = 14. In particular, the reduction is more pronounced for ^{15}C (Γ_{FWHM} = 63.5 ± 0.7 MeV/c) and ^{14}B (Γ_{FWHM} = 56.5 ± 0.5 MeV/c). Moreover, these two nuclei exhibit enhanced one-neutron removal cross section: σ_{-1n} = 159 ± 15 mb for ^{15}C and σ_{-1n} = 153 ± 15 mb for ^{14}B. The enhancement of σ_{-1n} for ^{15}C with respect to the other C isotopes is evident in Fig. 2.15b. While the measured Γ_{FWHM} agrees with the value of ref. [Baz98], σ_{-1n} is considerably bigger, supporting the supposition that the previous low value was because of the limited acceptance.

Recently, the ^{9}Be(^{15}C,^{14}C + γ) reaction was studied at E_{inc} = 54 MeV/u [Mad01]. The γ-ray spectrum, detected in coincidence, suggests important contributions from the core states at

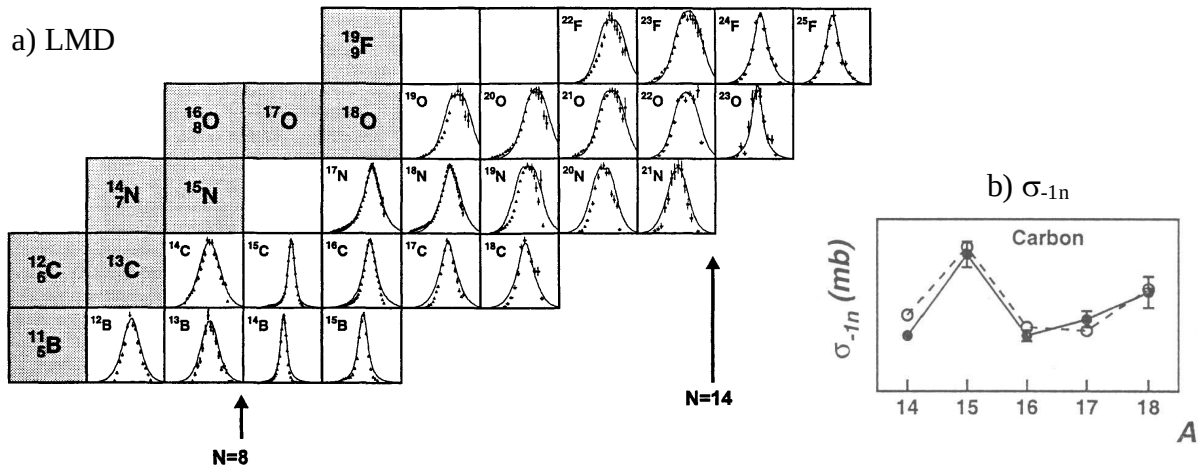

Figure 2.15. a) Longitudinal momentum distribution from one-neutron removal on a C target [Sau00]. The solid lines correspond to Glauber model calculations. b) Measured (solid points and lines) and calculated (open points and dashed lines) one-neutron removal cross-sections for carbon isotopes [Sau00].

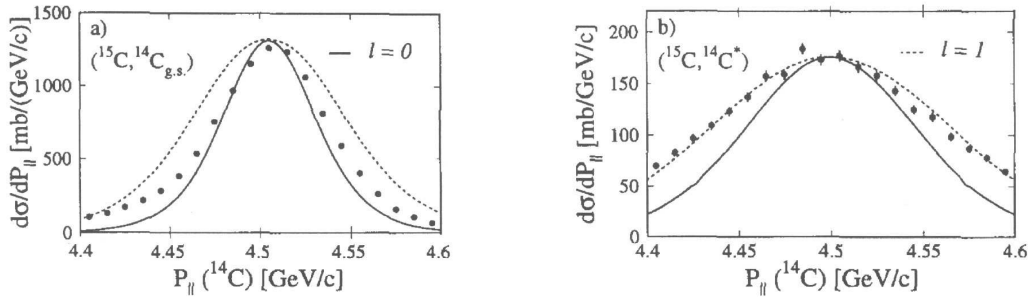

Figure 2.16. Experimental LMD from the ^{9}Be(^{15}C,^{14}C+γ) reaction [Mad01] with the residues of ^{14}C in the a) ground state and b) excited states. Solid and dashed lines are for l = 0 and l = 1 calculations, respectively.

E_x = 6.09 MeV ($J^\pi = 1^-$), which decays directly to the ground state, and E_x = 6.90 MeV (0^-), decaying through the 1^- with two γ-rays in cascade. The 7.01 MeV (2^+) state is also included in the fit, although its predicted spectroscopic is very small; note that the 6.73 MeV (3^-) state is forbidden by selection rules. In Figures 2.16a and b the experimental LMD are shown relatively to $^{14}C_{GS}$ and ^{14}C excited fragments, respectively. The comparison with calculated eikonal model curves for l = 0 and 1 indicates the s-wave character of the ground state distribution and the p-wave one of the excited states. A good agreement is found in the l = 1 case, while small deviations are present in the shape of the ground state LMD, especially at low energy. In fact, the eikonal model does not reproduce the observed asymmetry of the LMD, which instead is well reproduced by Coupled Discretized Continuum Channels (CDCC) calculations [Tos02]. The measured one-neutron removal cross sections for ^{15}C are 137 ± 16 mb (total) and 109 ± 14 mb (for $^{14}C_{GS}$ fragments).

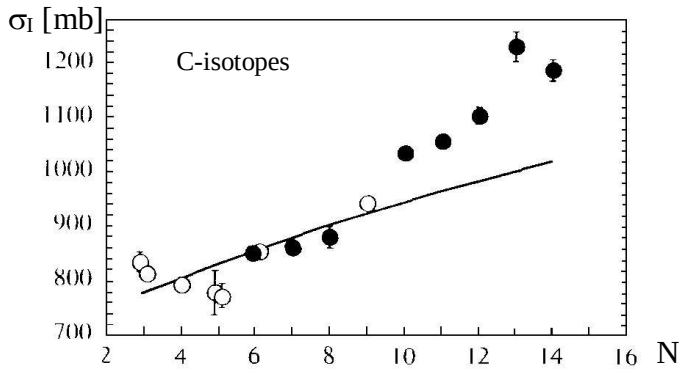

Figure 2.17. Interaction cross sections for the carbon isotopes. The full circles are data taken from ref. [Oza01], the open circles are from ref. [Oza06]. The solid line is calculated as described in the text.

2.3.3 Measurements of interaction cross sections and radii

The ^{15}C nucleus has not been recognized as halo nucleus until now, mainly because its matter radium (R^{m}_{rms} = 2.40 ± 0.05 fm) does not show a considerable deviation from the systematic increase with mass number, $R = r_0 A^{1/3}$, which is valid for stable nuclei [Aud93]. However, the situation is unclear, with measurements of the total cross section exhibiting no effect and others with small enhancements (see ref. [Sau00] and refs. therein).

The interaction cross sections σ_I and radii of several weakly-bound nuclei, among which ^{15}C, were measured at E_{inc} = 730 and 950 MeV/u by Ozawa et al. [Oza96, Oza01] by means of a transmission method with Be, C and Al targets. The interaction cross sections obtained for the carbon isotopes are shown in Fig. 2.17. The solid line represents a calculation of σ_I according to the formula for the stable nuclei, $\sigma_I = \pi [R_I(^{12}C) + r_0 A^{1/3}]^2$, where r_0 is chosen in order to reproduce $\sigma_I(^{12}C)$. The ^{15}C point (N = 9, σ_I = 945 ± 10 mb for a carbon target) lies close to this line, showing that the formula $r_0 A^{1/3}$ gives a reasonable prediction for the ^{15}C radius. σ_I increase with increasing neutron number, with a maximum for ^{19}C.

The effective rms radii were deduced from the σ_I by Glauber model calculations. The dependences of the radii on the mass number A and on the isospin are shown in Figures 2.18a and b, respectively. The data are compared with the matter radii deduced from the measured charge radii [Dev87] and with results of Relativistic Mean Field (RMF) calculations, which reproduce qualitatively the global tendency. From Fig. 2.18a it is noted that the ^{12}C radius is larger than the neighbours, this is due to the α-cluster formation and occours also for ^{16}O (see ref. [Oza96]), which is a known α-cluster nucleus. The observed ^{15}C radius deviates from the calculated one, but, since the radii of the neighbour nuclei are not well known this is not enough to conclude that this nucleus has an anomalous structure. Concerning the isospin dependence (Fig. 2.18b), nuclei with larger isospin show larger radii. The ^{15}C radius is smaller than the calculated one, but it is consistent with the observed radii for ^{15}O and ^{15}N.

A comparison of the radii obtained at relativistic energies with those at intermediate ones provides information about the existence of tail component in the density distributions. Indeed, great discrepancies have been found. The Glauber model calculation, as those of ref. [Ozw96], underestimate systematically the cross section at intermediate energies. This difference varies particularly between the stable and halo nuclei (e.g., between ^{12}C and

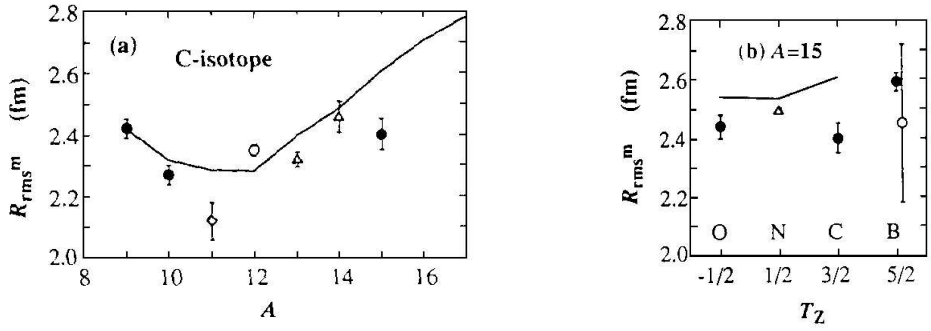

Figure 2.18. Rms matter radius a) for carbon isotopes versus the mass number and b) for A = 15 versus the isospin. The closed circles are data from ref. [Oza96], the open circles from ref. [Tan88] and the open rhombus from ref. [Oza95]. The open triangles are the radii calculated from the observed rms charge radii [Dev87]. The solid lines are from RMF calculations.

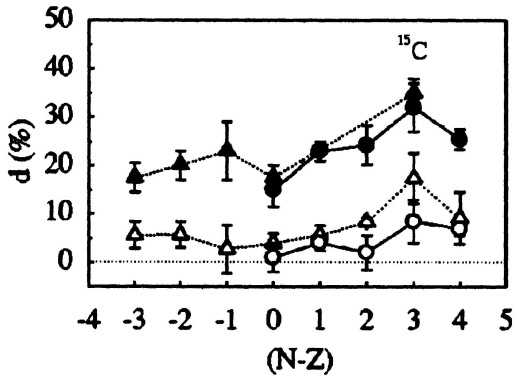

Figure 2.19. Neutron excess dependences of the difference factor d for carbon isotopes. The solid (open) triangles are data from ref. [Oza96] calculated with the Glauber model (BUU model). The solid (open) circles are data from ref. [Fan00] obtained by Glauber calculation (BUU calculation).

^{11}Be) and an its enhancement likely reflects an enhancement of the tail component in the density distribution. A difference factor d is defined as $d = [\sigma_I(int) - \sigma_I(Gla)]/\sigma_I(Gla)$, where $\sigma_I(int)$ is the experimental reaction cross section at intermediate energy and $\sigma_I(Gla)$ is the Glauber calculated one at the same energy by fitting the experimental σ_I at relativistic energy. The d value is about from 10 to 20 % for stable nuclei and from 30 to 40 % for nuclei with anomalous structure; e.g., for ^{11}Be d > 30 % (see ref. [Oza96]). The isospin dependence of the difference d is shown in Figure 2.19 for the C isotopes. High-energy data [Oza96] are compared with data at intermediate energy [Fan00]. The results of Glauber calculations (full circles) and Boltzmann-Uehling-Uhlenbeck (BUU) calculations (open circles) are also shown; the latter reproduce σ_I at intermediate energy better than the former. The d value for ^{15}C is considerably larger than for the other isotopes; the same happens for ^{14}B. This suggests that also ^{15}C and ^{14}B should have an anomalous neutron density distribution, of halo- or skin-type.

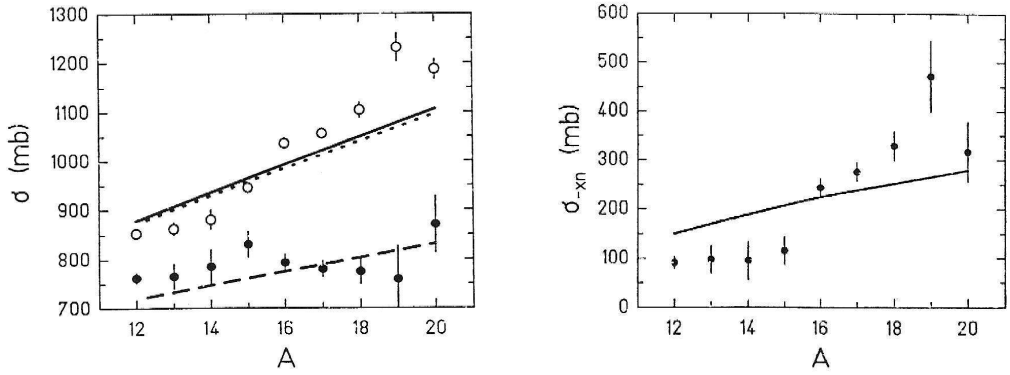

Figure 2.20. a) Experimental charge-changing (filled circles) [Chu00] and interaction (open circles) [Oza96] cross sections for C isotopes, in comparison with theoretical calculations [Chu00]. The solid line is the result of the IntraNuclear-Cascade (INC) model. The dotted line is σ_I calculated by the Kox semiempirical formulae. The dashed line is σ_{CC} from the INC calculation. b) One-neutron removal cross sections for C isotopes ($\sigma_I - \sigma_{CC}$). The solid line is the INC calculation with fragment deexcitation [Chu00].

Nevertheless, other recent results seem to deny an extended neutron distribution in ^{15}C [Chu00]. The measured charge-changing cross sections σ_{CC} for carbon isotopes [Chu00] are shown in Figure 2.20a, together with the σ_I data [Oza01]. For ^{15}C the measured value is σ_{CC} = 830 ± 26 mb. The one-neutron removal cross sections σ_{-1n}, obtained from the difference between σ_I and σ_{CC}, are shown in Fig. 2.20b. Since no peculiarity is found in σ_{-1n} for ^{15}C, the authors conclude that no evidence can be seen for a one-neutron halo structure in this nucleus.

2.3.4 Concluding remarks

The various results discussed from Section 2.3.1 to 2.3.3 indicate that the ^{15}C nucleus exhibits contradictory behaviours: its properties seem intermediate between those of the stable and drip line nuclei, showing characteristics typical of both normal and exotic nuclei. The global picture suggests a quite extended density distribution of the valence neutron, although the higher $S_n \sim 1$ MeV suppresses the development of a distribution as large as that found in the more weakly-bound ^{11}Be, ^{19}C and ^{11}Li halo nuclei. Entering into further details is beyond the aim of this thesis, however for a conclusive statement further experiments and more sophisticated theoretical approaches appear to be necessary.

CHAPTER 3

THE (^{7}LI,^{7}BE) CHARGE EXCHANGE REACTION

Direct reactions constitute, in general, an important source of information on the nuclear structure. In particular, heavy-ion Charge EXchange reactions (CEX) are a powerful tool for spectroscopic studies, especially in exotic nuclei, in which they may populate states not easily excited by elementary projectiles (nucleon and light ions), such as high spin states. By an appropriate choice of the projectile-target system and incident energy, the heavy-ion reactions can be used as a very precise probe of specific charge exchange excitations modes of nuclei [Oer88]. Single CEX reactions – (n,p) and (p,n) type transitions – allow one to investigate the isovector response of nuclei because of their selectivity [Ost92, Alf98]. New spectroscopic information can be expected from heavy-ion CEX reactions, e.g., concerning the interesting and still-open question of the quenching of the Gamow-Teller strength distributions in nuclei. Besides the interest in spectroscopic work, CEX reactions makes it possible to study the contributions of the spin and isovector interactions to heavy-ion scattering [Len88]. Moreover, the existing models of the nuclear forces may be tested under the extreme conditions of high charge asymmetry, low nuclear density and low binding energy through CEX reactions involving exotic nuclei.

In particular, the (^{7}Li,^{7}Be) reaction has been widely used [Coo84, Dod85, Etc88, Nak90, Sak93, Win96, Jän96, Orr01, Cap01] to extract information about nuclear structure and the CEX mechanism. In refs. [Cap01, Cap04b] we used the same technique as present to explore the ^{11}Be spectrum up to 15 MeV excitation energy. The good resolution obtained (about 50 keV) allowed identification of the single particle excitations below 2 MeV and several narrow resonances in the continuum. The aim of the work here described is to apply a similar technique to ^{15}C, using the (^{7}Li,^{7}Be) CEX reaction. In fact, ^{15}C differs from ^{11}Be only by an α particle and so similar features are expected in structure and the reaction mechanism.

3.1 The CEX reaction mechanism

CEX scattering has become a very useful spectroscopic tool to investigate both (n,p) and (p,n) type transitions in nuclei. The reaction mechanism is simpler compared to other reaction channels because only effective isovector interactions are allowed, however some complication arises into the interpretation of the experimental data due to the presence of two

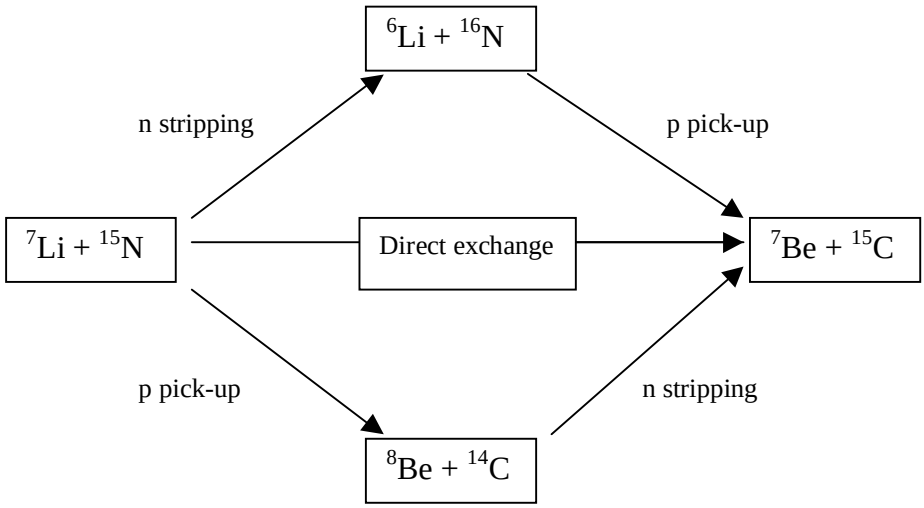

Figure 3.1. Scheme of the one- and two-step processes in the ^{15}N(^{7}Li,^{7}Be)^{15}C CEX reaction.

competitive processes. In fact, CEX reactions can proceed via two fundamental processes, which populate the same final channel and which we call direct and transfer charge exchange. In the direct process the final states are excited by the one-step exchange of charged mesons as described by the isovector nucleon-nucleon (NN) interaction. The transfer charge exchange mechanism is at least a second order process in which the same final states are populated by sequential proton-pickup neutron-stripping, or vice versa (see the scheme of Figure 3.1).

These two reaction mechanisms have an quite different origin: the first one is a typical NN-collision process leading to mutual excitation of projectile and target, while the second one corresponds to mean field processes. The two mechanisms contribute coherently to the cross section. Since the desired nuclear structure information is most directly available from the direct process because no intermediate channels are involved, it is of particular importance to know under which experimental conditions the direct mechanism is dominant. As we will see, the dominance of the first or second process depends on incident energy, scattering angle and on nuclear structure effects. In particular, as discussed in Section 3.1.3 in relation to the analysis of the reaction ^{12}C(^{12}C,^{12}N)^{12}B, the very different dependence on the incident energy gives the possibility to study the transition from the mean field dynamics to the NN-collision regime in correspondence of the passage from the two-step to the direct mechanism.

The theory of the CEX reactions presented in the following Sections is taken from refs. [Len88, Len89, Len89b] and it is valid for a range of incident energy between 10 and 100 MeV/u. A generic CEX reaction A(a,b)B can be schematised as:

$$\underbrace{a(N_a, Z_a) + A(N_A, Z_A)}_{\alpha} \rightarrow \underbrace{b(N_a \pm 1, Z_a \mp 1) + B(N_A \mp 1, Z_A \pm 1)}_{\beta} \qquad (3.1)$$

where α and β represent the entrance and exit channels, respectively, while N and Z indicate the number of neutrons and protons. The reaction happens with a transfer of the third isospin component $\Delta T_z = \pm 1$.

3.1.1 The one-step process

The direct charge exchange is in the lowest order a one-step process, mediated by the exchange of virtual isovector mesons. The relation to nuclear structure is very transparent. The matrix element of the transition operator between the states α = (a, A) and β = (b, B) can be written in the first order Distorted Wave Born Approximation (DWBA) as:

$$T_{\beta\alpha}^{DWBA}(one) = \left\langle \chi_{\beta}^{(-)} \middle| F_{\beta\alpha}^{(\tau)} \middle| \chi_{\alpha}^{(+)} \right\rangle = \int \chi_{\beta}^{(-)} F_{\beta\alpha}^{(\tau)} \chi_{\alpha}^{(+)} d\mathbf{R} \tag{3.2}$$

where $\chi_\alpha^{(+)}(k_\alpha,r)$ and $\chi_\beta^{(-)}(k_\beta,r)$ represent the distorted waves in the incident and final channels, respectively, and **R** is the coordinate of the center of mass. The CEX form factor

$$F_{\beta\alpha}^{(\tau)} = \left\langle bB \middle| V^{(\tau)} \middle| aA \right\rangle \tag{3.3}$$

is obtained in the double-folding model by folding the charge exchange transition densities with the isovector component of the effective NN-interaction $V^{(\tau)}$:

$$F_{\beta\alpha}^{(\tau)} = \int d\xi_a \, d\xi_A \; \rho_{ab}(\xi_a) \; V^{(\tau)}(\mathbf{R}, \xi_a, \xi_A) \; \rho_{AB}(\xi_A) \tag{3.4}$$

Nuclear structure enters into the form factor via the CEX transition densities ρ_{ab} and ρ_{AB}, describing the projectile (a $\rightarrow$ b) and target (A $\rightarrow$ B) transitions, respectively. These quantities contain the information on the structural overlap between the nuclei in the entrance and exit channels. They depend on the internal nuclear coordinates ξ, which include spatial, spin and isospin degrees of freedom. The transition densities can be expressed in terms of the proton and neutron single particle wave functions Φ_p, Φ_n. For example, for a ΔT_z = + 1 transition (e.g., ^{12}C $\rightarrow$ ^{12}B or ^{7}Li $\rightarrow$ ^{7}Be) with orbital, spin and total angular momentum transfer (L, S, J), we obtain:

$$\rho_{LSJ}^{(+)} = \sum_{np} \left\langle b \middle\| \left[a_n^+ a_p \right]_{LSJ} \middle\| a \right\rangle \left[\Phi_p^* \Phi_n \right]_{LSJ} \tag{3.5}$$

where a^+ and a are creation and annihilation operators for a single nucleon. Corresponding expressions are obtained for ΔT_z = –1 transitions. The β-decay matrix elements depend on the same transition densities, so these last can be tested independently in other processes, too. When exotic nuclei such as ^{15}C are involved, the transition densities are calculated in a more complex way (see Section 6.2.2).

In the direct form factors the proton and neutron creation and annihilation operators are coupled:

$$a_n^+ a_p \; a_{p'}^+ a_{n'} \tag{3.6}$$

This leads to a discontinuous evolution of the charge distribution, that may be interpreted as a mean field fluctuation originating from NN-collisions, which in this case are due to $V^{(\tau)}$.

The isovector NN-interaction $V^{(\tau)}$, which induces the direct isospin-flip in the one-step process, is given by:

$$V^{(\tau)} = \left(V_\tau + V_{\sigma\tau}\,\sigma_a \cdot \sigma_A + V_{T\tau} S_{12}\right) \tau_a \cdot \tau_A \tag{3.7}$$

where the spin scalar V_τ and vector $V_{\sigma\tau}$ central parts and the rank-2 tensor interaction $V_{T\tau}$ are included and S_{12} is the tensor operator

$$S_{12} = \left(3/r^2\right)\left(\sigma_a \cdot \mathbf{r}_a + \sigma_A \cdot \mathbf{r}_A\right) - \sigma_a \cdot \sigma_A \tag{3.8}$$

As we will see, in general the one-step process is dominant at high incident energies (E_{inc} ~ 100 MeV/u) and forward angles.

3.1.2 The two-step process

In the two-step process the same final states as the one-step process are populated by transfer reactions. This mechanism includes intermediate transitions to neighbouring (A ± 1)-systems. The sequential proton-pickup neutron-stripping and neutron-stripping proton-pickup contribute coherently to the two-step process, which generally dominate at low incident energies (E_{inc} ~ 10 MeV/u) and large angles. The T-matrix element of the CEX transfer process can be written in the second order Exact Finite Range (EFR) DWBA as:

$$T_{\beta\alpha}^{DWBA}(\text{two}) = \sum_\gamma \left\langle \chi_\beta^{(-)} \middle| F_{\beta\gamma}\; G_\gamma^{(+)} F_{\gamma\alpha} \middle| \chi_\alpha^{(+)} \right\rangle \tag{3.9}$$

where the summation is restricted to intermediate transfer channels $\gamma = (c_\gamma, C_\gamma)$ in which either the particle or the hole component of the final configurations are populated. The optical model Green's function $G_\gamma^{(+)}$ describes the propagation in the intermediate channels. The EFR form factors are determined by the overlap of the initial and final nuclear wave function at each step and, e.g., for a neutron-stripping single process, can be expressed in terms of spectroscopic amplitudes and pure single particle form factors as:

$$F_{\gamma\alpha}\;(r_\gamma, r_\alpha) = \sum_{j_n s_n} \left\langle C_\gamma \middle\| a_{s_n}^+ \middle\| a \right\rangle \left\langle C_\gamma \middle\| a_{j_n} \middle\| A \right\rangle\; F_{\gamma\alpha}^{j_n s_n}(r_\gamma, r_\alpha) \tag{3.10}$$

The need for a finite range approximation, such as EFR, is because the elementary transfer processes in general occur at several fm of distance.

The two-step transition densities have a microscopic structure

$$a_n^+ a_{n'},\; a_{p'}^+ a_p \tag{3.11}$$

in which, for each single step, the proton and neutron creation and annihilation operators are decoupled. This corresponds to a continuous evolution of the charge density and thus of the mean field.

3.1.3 The CEX cross section: the ^{12}C(^{12}C,^{12}N)^{12}B reaction

From an experimental point of view, it is not possible to distinguish whether a given event is due to a one-step process or to a two-step one. Therefore, the cross section for a charge exchange reaction is determined by the coherent superposition of the direct and transfer contributions:

$$\sigma_{\beta\alpha} \sim |T_{\beta\alpha}(\text{one}) + T_{\beta\alpha}(\text{two})|^2 \tag{3.12}$$

However, the analysis of the excitation functions and angular distributions gives more information about the processes considered. In fact the two mechanisms depend in a different way on the incident energy due to the very different physical origins. The direct amplitude depends mainly on the momentum transfer of the reaction, i.e., on excitation energy and scattering angle. Instead, the transfer amplitudes for each step depend mainly on the linear momenta (i.e., kinetic energy) of the transferred nucleons, which have to be absorbed by the binding mean field. Since the high momentum components are strongly suppressed in the mean field dynamics, the transfer cross section will decrease with the incident energy. On the contrary, in general the one-step contribution to the cross section increases with the incident energy, dominating at higher energies. This different behaviour gives the possibility to observe the transition from mean field interactions at low incident energies to NN-reaction mechanisms in the Fermi-energy regime.

This was done in particular for the ^{12}C(^{12}C,^{12}N)^{12}B reaction [Len89, Len89b], which was among the first studied heavy-ion CEX reactions, giving a quite complete impression of the CEX mechanism. Since only the ^{12}N ground state ($J^\pi = 1^+$) is bound and the ^{12}C ground state has $J^\pi = 0^+$, this reaction is well suited to study vector-isovector transitions in the target. In Figure 3.2 the calculated excitation functions and angular distributions are compared to the experimental data of refs. [Boh88, Win86]. The two-step process dominate clearly at low incident energies, being maximum at about 30 MeV/u and then decreasing. At E_{inc} = 70 MeV/u the data at small scattering angles are quite well described by the one-step calculations, but the transfer contributions at larger angles are still of comparable strength. In fact, at small angles the direct components are dominant but they decrease steeply, so that the cross sections at the larger angles are determined almost completely by the transfer contributions.

Thus at intermediate energies (10 MeV/u $\leq E_{inc} \leq$ 100 MeV/u) a transition from the two-step to the one-step processes is observed. For the reaction considered, the direct mechanism begins to dominate only for energies well above 50 MeV/u. However, nuclear structure effects make the precise transition point depending on the populated final states (see Fig. 3.2b). This dependence is mainly due to the different angular and linear momentum transfers involved.

Another interesting question concerns the role of the tensor interaction. In Figure 3.3 the one-step calculation at E_{inc} = 70 MeV/u is shown, with the contributions of the central and rank-2 tensor isovector interactions plotted separately. The central part gives a strongly oscillatory angular pattern (pure L = 0) in disagreement with the data. The experimental angular distribution can be described by including the tensor contribution, which allows L = 2 transfer.

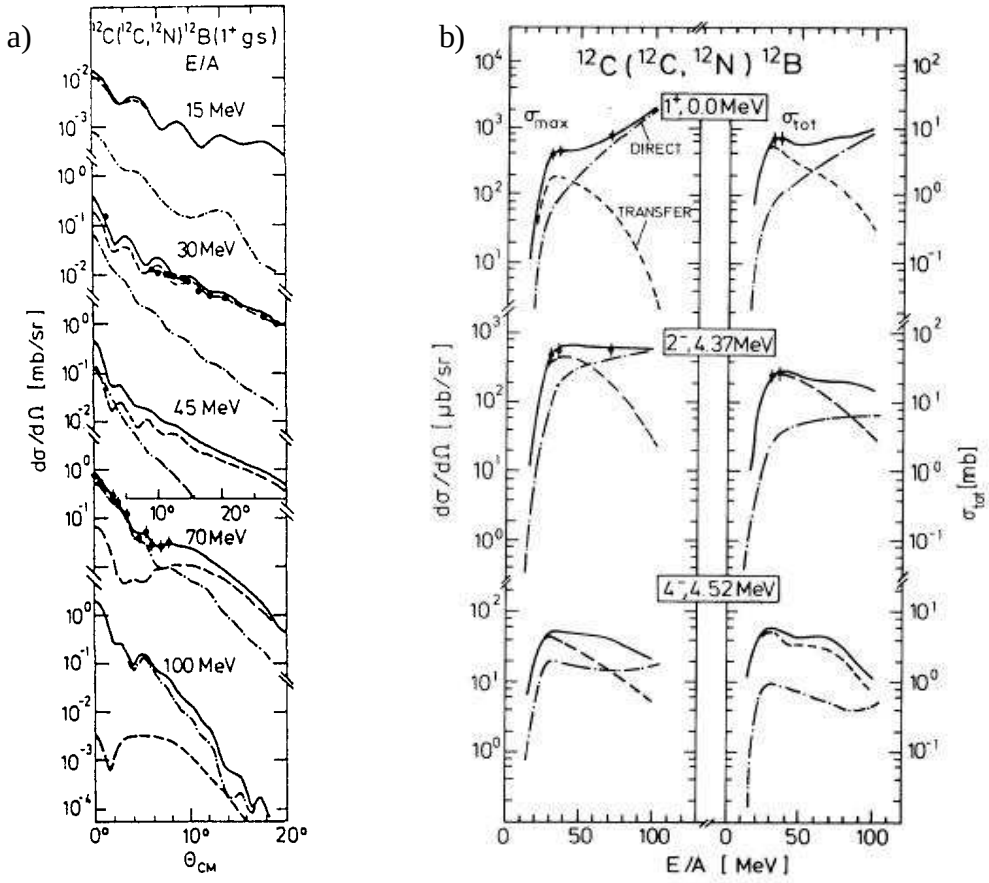

Figure 3.2. a) Angular distributions for the ^{12}C(^{12}C,^{12}N)^{12}B$_{GS}$ reaction as a function of the incident energy. b) Incident energy dependence of the maximum differential cross section (left) and total cross section (right) for the ^{12}C(^{12}C,^{12}N)^{12}B reaction. In both a) and b) the direct (dashed-dotted) and transfer (dashed) contributions and their coherent sum (full) are shown [Len89, Len89b], in comparison with the experimental data at E_{inc} = 30 and 70 MeV/u [Boh88] and E_{inc} = 35 MeV/u [Win86].

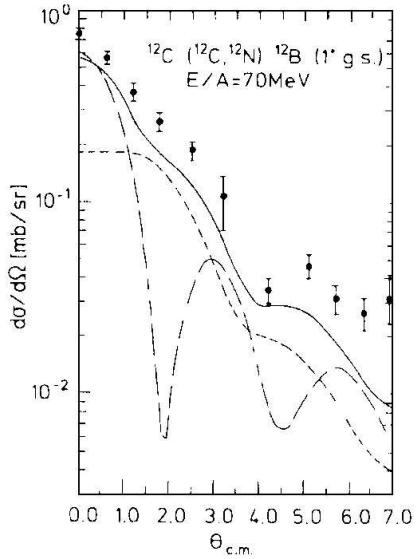

Figure 3.3. Angular distributions for the ^{12}C(^{12}C,^{12}N)^{12}B$_{GS}$ reaction at E_{inc} = 70 MeV/u. Direct charge exchange central (dashed) and tensor (dashed-dotted) contributions and their coherent sum (full) are shown [Len89, Len89b] in comparison with experimental data [Boh88].

3.2 Analogy with the inelastic scattering

In CEX reactions the same excitation operators as inelastic scattering are involved. A general analogy can be established between the isospin-flip (i.e., one-step CEX), spin-flip and inelastic scattering transition amplitudes [Oer88]. This analogy is defined only in the NN-collision regime, in which the previously-mentioned processes may be interpreted as single nucleon excitation produced by exchange of different mesons. The connection among the effective potentials of the three processes derives from the symmetry properties of the NN-interaction, essentially from the separation of the spin and isospin degrees of freedom from the spatial ones. Thus, under certain conditions, also the spin-flip and isospin-flip potentials may be expanded in terms of multipole operators and to excite collective modes. However, the analogy is no longer valid if multi-step processes are involved in the reaction. Besides, the inelastic scattering is characterized by a $\Delta T = 0$ transfer, while the spin-flip and isospin-flip by $\Delta S = 1$ and $\Delta T = 1$, respectively. Thus CEX reactions have the propriety of probing selectively the isovector nuclear response.

Independent of the reaction mechanism, in a CEX reaction the momentum transfer due to the (asymptotic) incoming and outgoing momenta k_α and k_β is:

$$\mathbf{q} = \mathbf{k}_\alpha - \mathbf{k}_\beta \tag{3.13}$$

For all the inelastic processes without nucleon transfer the momentum transfer at 0° (minimum transfer) is given mainly by the Q-value of the reaction:

$$q\,[\mathrm{fm}^{-1}] = 0.11\frac{Q}{\sqrt{E_{inc}/A}} \tag{3.14}$$

Formula (3.14) will be valid also for a direct CEX reaction because there is not nucleon transfer. Inserting the values for the ^{15}N(^{7}Li,^{7}Be)^{15}C reaction, we obtain $q = 0.42$ fm^{-1}. If q is transferred to the whole nucleus, the maximum angular momentum transfer is:

$$L_{max} = q \cdot R_{int} \tag{3.15}$$

and, with an interaction radius $R_{int} = r_0 \cdot (A_P^{1/3} + A_T^{1/3}) \sim 5$ fm for $r_0 = 1.2$ fm and A_P, A_T the mass number of projectile and target, $L_{max} = 2$. Really, a distributions of L-values $\leq L_{max}$ is transferred because the transfer happens in a diffuse region around the nuclear surface.

The momentum transfer q increases with the scattering angle. Higher q values give larger $L \neq 0$ contributions, as also the influence of the tensor component of the interaction (which results in strong $L = 2$ contributions). Besides, as q increases, the one-step cross section decreases. Thus the direct CEX process, directly related to the nuclear structure information, may be observed only at very forward angles. This explain the necessity to measure at forward angles. Especially the measurements around 0° are very important in order to minimize the momentum transfer. In the case of the (^{7}Li,^{7}Be) CEX reaction, as we will see in Section 3.4, there are also other reasons which makes fundamental to measure at $\theta_{lab} = 0°$.

3.3 The (^{7}Li,^{7}Be) reaction

In this Section, particular attention is paid to the (^{7}Li,^{7}Be) CEX reaction, which was used in the present work in order to explore the ^{15}C excitation energy spectrum.

Among the CEX reactions with isospin transfer $\Delta T_z = +1$, the (n,p) and (^{7}Li,^{7}Be) reactions are well suited for the study of isovector transitions because they have strong overlaps between the involved states and thus large cross sections. Advantages of (^{7}Li,^{7}Be) over (n,p) are the high beam intensity (^{7}Li is an easy beam from both Tandem and Cyclotron) and the better energy resolution with respect to the neutron (secondary) beam.The selective character of (^{7}Li,^{7}Be) with respect to isospin has long been recognized and used in experiments [Coo84, Dod85, Etc88, Nak90, Nak90b, Sak93, Nak99, Win96, Jän96, Orr01, Cap01, Cap04b]. In contrast to the nucleon reactions, where the transferred angular momentum is small (L = 0, 1), (^{7}Li,^{7}Be) can excite states with higher multipolarity.

The (^{7}Li,^{7}Be) reaction populates the two bound ^{7}Be states, the $3/2^-$ ground state and the $1/2^-$ first excited state at 0.429 MeV, which we will indicate as $^7Be_{GS}$ and $^7Be_{exc}$, respectively. In relation to this, the measured spectra will show a doublet of states for each target transition, corresponding to $^7Be_{GS}$ and $^7Be_{exc}$. The two contributions may be separated either by detecting the γ-rays due to the in-flight decay of $^7Be_{exc}$, or by using a high resolution magnetic spectrometer (present case). Since the ^{7}Li ground state has $J^\pi = 3/2^-$, the ($^7Li_{GS}$,$^7Be_{GS}$) reaction proceeds via $\Delta J^\pi = 0^+$, 1^+, 2^+ and 3^+ couplings, while the ($^7Li_{GS}$,$^7Be_{exc}$) via $\Delta J^\pi = 1^+$, 2^+. Because of the number of possible spin transfers, the interpretation of the angular distributions is more difficult than, for example, for (^{12}C,^{12}N). Nevertheless, as discussed in the next Section, the existence of such a doublet gives the possibility to measure both spin transfer and not spin transfer transitions.

In principle, at low bombarding energy the (^{7}Li,^{7}Be) reaction includes contributions from both the sequential transfer and direct charge exchange. It is important to know in which energy range the one-step mechanism dominates. Generally, this happens for high incident energies, however it depends on the reaction considered very much. In fact, the final state interaction may substantially change the limiting energy value: as we will see, this value varies even in the same (^{7}Li,^{7}Be) reaction depending on the target. Besides, if the final nucleus is exotic, such as ^{15}C, the one-step threshold is expected to be lower than for a well-bound nucleus. Indeed, for direct reaction involving a weakly-bound nucleus in the exit channel, the momentum dependence of the transfer form factor is due principally to the wave function of the final channel ([Len98], Section 1.2). The larger extension of the halo wave function corresponds to a narrower momentum distribution, peaked at smaller momenta than usually. Therefore the transfer excitation functions are peaked at lower energy and fall off rapidly thereafter, thus the one-step dominance is expected at a lower energy with respect to CEX reactions involving stable nuclei.

In particular for (^{7}Li,^{7}Be) other reasons makes one expect the direct mechanism to dominate at low energy. ^{7}Li and ^{7}Be are mirror nuclei, thus the necessary minor rearrangement could make the meson exchange preferable with respect to the sequential transfer. Besides, the Q-values of the (^{7}Li,^{7}Be) reactions are usually smaller than other CEX reactions, such as, e.g., (^{12}C,^{12}N), leading to a minor momentum transfer. Finally, the transfer process is strongly suppressed in (^{7}Li,^{7}Be), even at low bombarding energy, because the most

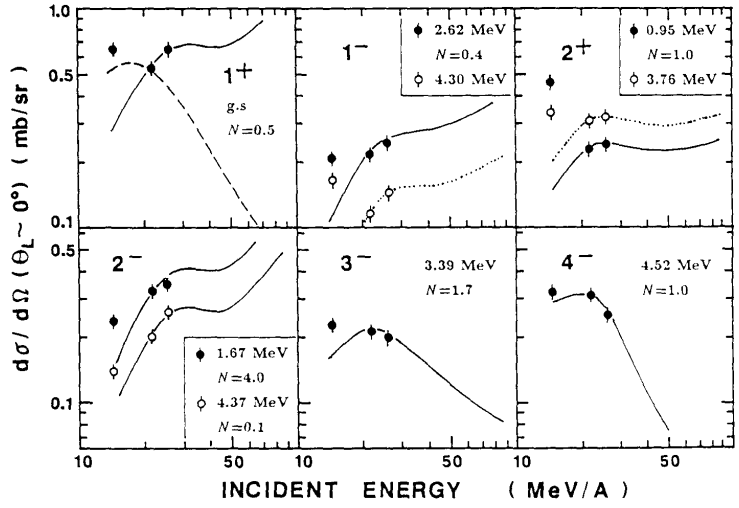

Figure 3.4. Cross sections for different transitions induced by the ^{12}C(^{7}Li,^{7}Be)^{12}B reaction at θ_{lab} = 0° [Nak90b]. The results of one-step calculations (solid and dotted lines), normalized by a factor N, are compared to experimental data taken at E_{inc} = 14, 21 and 26 MeV/u. The result of a two-step calculation (dashed line) is shown for the $0^+ \rightarrow 1^+$ ground state transition.

important intermediate routes of the two-step process – populating the ^{8}Be states – are hindered from the weak single particle components of ^{8}Be states at low excitation energy [Etc88]. In any case, the angular distributions of the one- and two-step processes are expected to have rather different shapes even at low incident energy and, thus, separable at forward angles [Sak93]. A useful consequence of all this is that for (^{7}Li,^{7}Be) we can have a one-step process also at very low incident energies, while normally for other CEX reactions $E_{inc} \sim 50$ MeV/u.

The ^{12}C(^{7}Li,^{7}Be)^{12}B reaction was studied in detail at different incident energies by Nakayama et al. [Nak90, Nak90b, Nak99]. In Figure 3.4 the θ_{lab} = 0° cross sections measured at E_{inc} = 14, 21 and 26 MeV/u are shown, in comparison with microscopic DWBA calculations for the direct process. Two-step calculations were performed only for the $0^+ \rightarrow 1^+$ transition to $^{12}B_{GS}$. The cross sections increase with the bombarding energy, except in the 3^- and 4^- transitions. This is because of the reduced momentum transfer which, decreasing with the energy, hinders the transfer of high angular momenta. Normalization coefficients N, different for each ^{12}B state, were used to scale the one-step cross sections in order to reproduce the measured values at 21 MeV/u. After this scaling, the experimental data taken at E_{inc} = 21 and 26 MeV/u lie on the one-step curves, while the point at 14 MeV/u is systematically underestimated. This indicates not negligible transfer contributions at the energy considered. Besides, the two-step calculation fails to reproduce the rise of the cross section observed between 21 and 26 MeV/u. Therefore the authors concluded that at θ_{lab} = 0° the one-step mechanism is dominant for $E_{inc} \geq 21$ MeV/u.

However, in the previous analysis the use of scaling factors, together with the presence of only three measured points, does not allow to give a clear conclusion. An interesting result is shown in Figure 3.5, where the point at 8.1 MeV/u, recently obtained by the ^{12}C(^{7}Li,^{7}Be)^{12}B at 57 MeV [Cap01], is added to the previous ones. For transition to the unnatural parity states 1^+ and 2^-, these new points lie close to the low energy extrapolation of

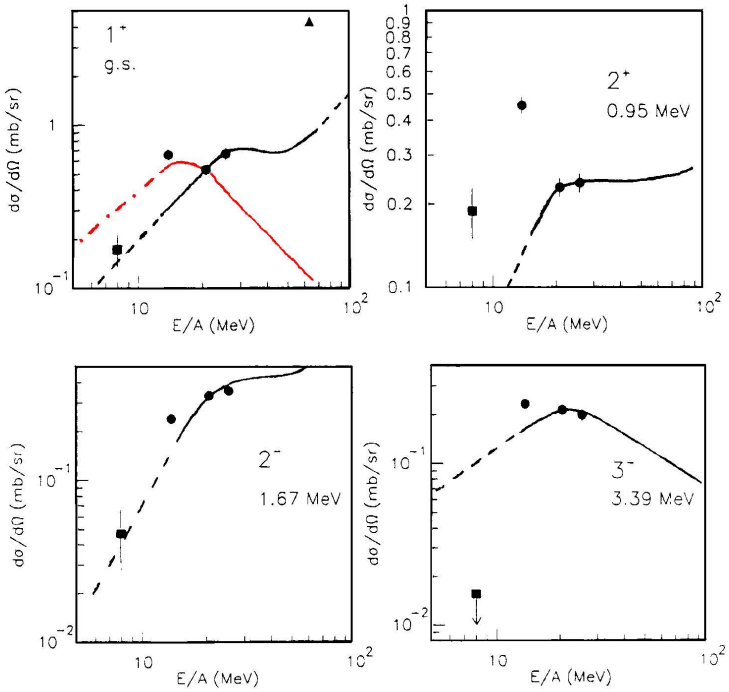

Figure 3.5. Cross sections for different transitions induced by the ^{12}C(^{7}Li,^{7}Be)^{12}B reaction at θ_{lab} = 0°. The full circles are data taken from ref. [Nak90b], the squares from [Cap01] and the triangle from [Nak99]. The black curves are the results of one-step calculations, while the red one of a two-step calculation (performed only for the 1^{+} state). The dashed parts represent the extrapolation of the curves at low energies.

the one-step curves. Considering the transitions to natural parity states, the one-step calculations underestimate the new point in the case of the 2^{+} state and, on the contrary, overestimate it for the 3^{-} state. The further point measured at 65 MeV/u for the 1^{+} transition [Nak99] is in clear disagreement with the one-step predictions. Thus, due to the uncertainty in absolute normalization of the calculated cross sections, the energy threshold of the direct mechanism in the ^{12}C(^{7}Li,^{7}Be)^{12}B reaction is a still open question.

A dominance of the one-step process has been reported in the (^{7}Li,^{7}Be) reaction also at lower incident energy; e.g., in the ^{28}Si(^{7}Li,^{7}Be)^{28}Al reaction at E_{inc} = 10 MeV/u [Dod85] and in the ^{6}Li(^{7}Li,^{7}Be)^{6}He at E_{inc} = 11 MeV/u [Sak93], although in the last case the approximation of vanishing tensor contributions to calculate the cross sections is questionable.

In another experiment [Etc88] the ^{10}B(^{7}Li,^{7}Be)^{10}Be reaction was studied at 5.6 MeV/u. As already said, in ref. [Etc88] it was speculated that the two-step routes are strongly hindered due to kinematical reasons. Indeed, e.g., the 2^{+} excited states of ^{8}Be, (which constitute the most important intermediate routes) are blocked by the isospin-mixing effects and Q-optimum mismatching for all the ^{10}Be final states. However, the authors remark that it had been not proved that the two-step mechanism is not important for the reaction considered.

The extracted angular distributions were analysed in the DWBA approach, performing one-step microscopic calculations in the One Body Transition Density (OBTD) approximation. The results obtained using four different find of residual interactions were compared. For a satisfactory description of the measured cross sections, the necessity to include in the calculations both the central and tensor interactions is emphasized. In Figure

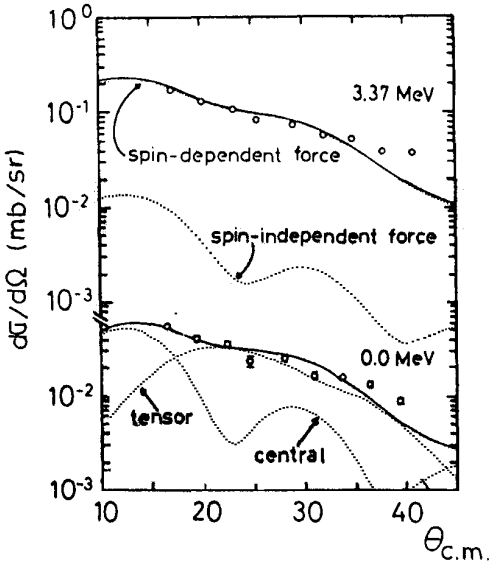

Figure 3.6. Comparison between the experimental and calculated cross sections for the ^{10}B(^{7}Li,^{7}Be)^{10}Be reaction [Etc88]. The theoretical cross section was microscopically calculated for the direct process in the DWBA approach. In the lower part, the contributions of the central and tensor interactions are separately shown for the transition to the ^{10}Be ground state. In the upper part, the spin-dependent and independent components of the interaction are shown for the ^{10}Be excited state at E_x = 3.37 MeV.

3.6 (lower part) the central and tensor components are separately shown for the cross section corresponding to the ^{10}Be ground state ($J^\pi = 0^+$). The sum of the two contributions reproduces the experimental angular distribution, except at very large angles, where the transfer process is not negligible. In the upper part of Fig. 3.6 the partial contribution of the spin-dependent and spin-independent forces are also displayed for the ^{10}Be excited state at E_x = 3.37 MeV ($J^\pi = 2^+$). The spin-independent component does not give appreciable contributions. This indicates a dominance of spin transfer processes in the transition considered. The suppression of the two-step mechanism is supported by the agreement between the calculated one-step cross sections and the data. The authors conclude that the role of one-step process is considerable even at E_{inc} = 5.6 MeV/u. The importance of this result is enhanced by the fact that in this case the normalization coefficients used are close to one.

More recently, the ^{11}B(^{7}Li,^{7}Be)^{11}Be reaction was studied at E_{inc} = 8.1 MeV/u [Cap01, Cap04b], using the IPN-Orsay Split-Pole magnetic spectrometer to detect ^{7}Be. The high resolution obtained (~ 50 keV) allowed to separate the ^{7}Be$_{GS}$ and ^{7}Be$_{exc}$ doublet, without the need to use a coincidence technique to measure the γ-rays emitted from ^{7}Be$_{exc}$. Theoretical angular distributions were calculated for the ^{11}Be ground and first excited state in the DWBA approach. The one-step microscopic calculations performed include both the central and tensor component of the NN-interaction. The comparison with the data shows that the ^{11}B(^{7}Li,^{7}Be)^{11}Be reaction preferentially proceeds via direct dynamics at the incident energy considered and at very forward angles. Indeed, the experimental cross sections are well reproduced especially at small angles, while at backward scattering angles – as observed also in the ^{10}B(^{7}Li,^{7}Be)^{10}Be reaction [Etc88] – the systematic underestimate of the strength indicates the importance of transfer dynamics.

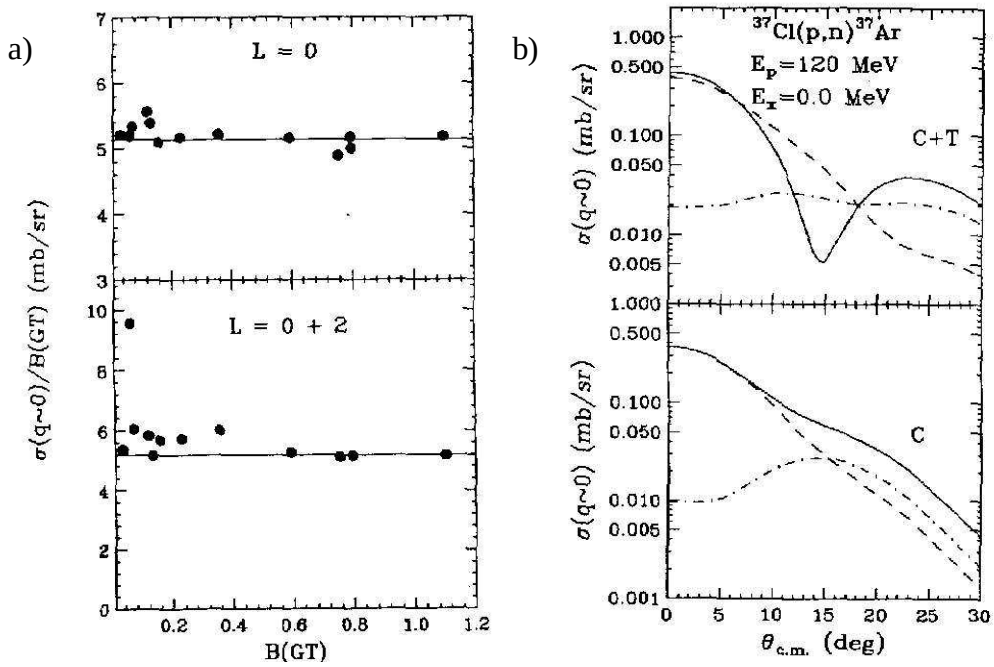

Figure 3.7. a) Calculated $\sigma(q\sim0)/B(GT)$ for the $^{37}Cl(p,n)^{37}Ar$ reaction with $\Delta J=1$, with and without the inclusion of the L = 2 component [Aus94]. The full lines represent the mean values obtained considering the five strongest β-decay transitions. b) Calculated $\sigma(q\sim0)$ cross section for $^{37}Cl(p,n)^{37}Ar$, considering only the central forces (C) and including also the tensor contribution (C + T) [Aus94]. The dashed and dot-dashed lines represent the L = 0 and L = 2 components, respectively, and the solid one their coherent sum.

3.4 Analogy with the β-decay

A general and very important characteristic of the CEX reactions is that, assuming the same initial and final nuclear systems, the form factor of the direct process has a mathematical structure very similar to the β-decay one. This leads to establish a further analogy: between the one-step mechanisms and the β-decay. However, substantial differences exist between the two processes. The main difference is that the β-decay is mediated by the electro-weak coupling constants, while the direct CEX reaction is mediated by the isovector meson-nucleon coupling constants. Besides, the β-decay happens with lepton emission (e^- and the coupled $\overline{\nu}_e$ for β^--decay, e^+ and ν_e for β^+-decay), thus the recoil of the emitting system is very small and, due to this, the linear and angular momentum transfers are very low. Oppositely, there is not lepton emission in a CEX process, so the linear and angular momentum transfers may also be rather high. Nevertheless, the analogy between the two processes is valid when the effects of the lepton emission are neglected and if only low momentum transfers are considered.

To test the validity of this assumption, the CEX cross section obtained for low momentum transfer, $\sigma_{CEX}(q \sim 0)$, has to be compared with the reduced transition probability B for β-decay, as done in ref. [Aus94] for the $^{37}Cl(p,n)^{37}Ar$ CEX reaction. The spin-flip ($\Delta S = 1$) and non spin-flip ($\Delta S = 0$) transitions of the CEX reaction have to be separately compared with the corresponding β-decay transitions: the Gamow-Teller ($\Delta L = 0$, $\Delta S = 1$) and Fermi

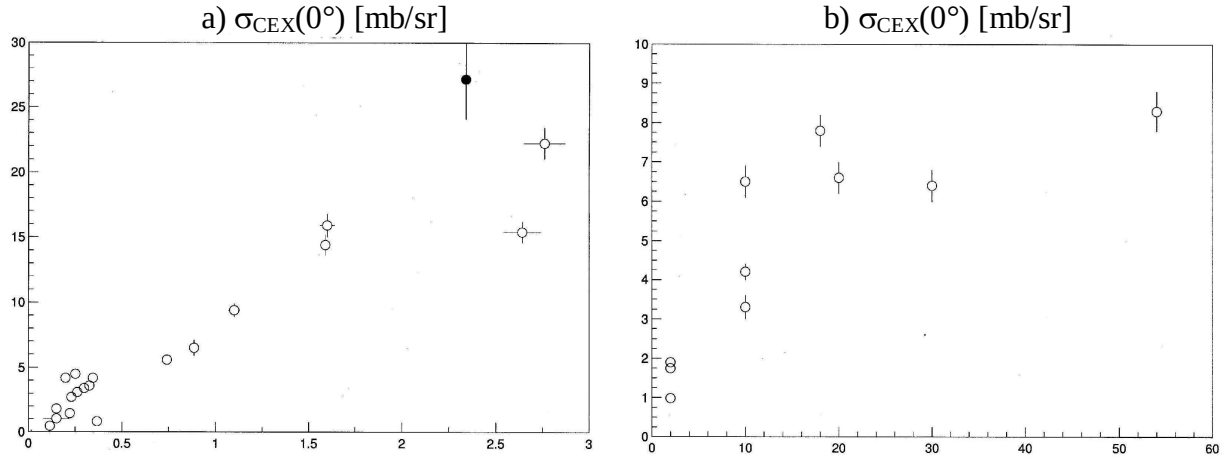

Figure 3.8. Cross section measured at 0° for the (p,n) reaction at 160 MeV on different target [Tad87]. a) Mixed Gamow-Teller and Fermi transitions (data taken from Table 4 of ref. [Tad87]). The full circle corresponds to the ^{7}Li target. b) Pure Fermi transitions (from Table 5 of ref. [Tad87]).

($\Delta L = 0$, $\Delta S = 0$) transitions, respectively. In Figure 3.7a the ratio $R \equiv \sigma_{CEX}(q \sim 0) / B(GT)$ is shown for the spin-flip CEX transition [Aus94]. The DWBA cross section was calculated at very forward angles to minimize the momentum transfer and compared with the tabulated B(GT) values for the $^{37}Cl \rightarrow {}^{37}Ar$ β-decay. The considered $\Delta S = 1$, $\Delta J = 1$ transition may transfer $\Delta L = 0, 1, 2$. While for an allowed β-decay only the $\Delta L = 0$ transfer is important, in general for a CEX reaction the L = 0 and 2 amplitudes can contribute. Since for this reaction L = 1 is negligible at 0°, the calculations were performed only for L = 0, 2 (see Fig. 3.7a). If the ratio assumes a constant value, the CEX reaction provides an accurate measurement of the Gamow-Teller strength. For B(GT) > 0.4 the ratio R stays almost constant both with and without taking into account the L = 2 contributions. For less favourite transitions (B(GT) < 0.4) deviations of also a factor 2 are observed between the calculations with and without L = 2. Thus for the strong transitions the L = 2 amplitude is negligible, while for the weak ones L = 2 contributes significantly to the cross section.

A multipolar decomposition to isolate the L = 0 contribution is possible when only central forces are involved. Indeed, the tensor forces induce an interference between the L = 0 and L = 2 amplitudes, which cannot be isolated, and causes the deviation of R from a constant value. The contribution of the tensor interaction is evidenced in Figure 3.7b. Its effects are negligible at small angles, but become stronger at larger angles, where the tensor components have to be considered even for more favoured transitions.

The important conclusion is that at very forward angles, for small momentum transfer and for super-allowed transitions (high B strength) the analogy between the one-step CEX dynamics and the β-decay keeps its validity.

The existence of a proportionality relationship between the cross section of the (p,n) CEX reaction at 0° and the corresponding Gamow-Teller and Fermi transition strengths B of β-decay was examined in details in ref. [Tad87]. Figure 3.8 shows the 0° cross sections measured for the (p,n) reaction at 160 MeV on different target. The data corresponding to

mixed (GT and F) transitions and to pure F transitions are shown separately (Fig. 3.8a and b) versus the B(GT) and B(F) strengths, respectively. The authors found a good correspondence between β-decay strengths and (p,n) cross sections for transition carrying as little as 3 % of single particle strength. A single proportionality constant can serve to relate all the GT transitions originating from the same target nucleus. Besides, an empirical and model-independent relationship relates the GT and F cross sections at 0°. However, the target dependence is considerable. The extrapolation or interpolation of the proportionality constants from one target nucleus to another has an uncertainty of about 20 % - 50 %. In general, proportionality holds only if the previously-mentioned conditions are satisfied.

3.4.1 Spin transfer in the (^{7}Li,^{7}Be) reaction: the G factor

In connection with the analogy with β-decay, the measurement of the (^{7}Li,^{7}Be) cross section at 0° supplies important information on the spin transfer dynamics. In the past it was already noted that the two cross sections related to $^7Be_{GS}$ and $^7Be_{exc}$ depends in a different way on the V_τ and $V_{\sigma\tau}$ components of the effective NN-interaction [And70]. This feature provides a very interesting opportunity to extract information on the nuclear spin-isospin response function, and probably on the role of tensor interaction in the CEX dynamics.

The relative strength (ΔS = 1)/[(ΔS = 0) + (ΔS = 1)] of the spin transfer excitations is defined as [Nak91]:

$$P_{sf} = N\frac{\sigma(\Delta S = 1)}{\sigma(\Delta S = 0) + \sigma(\Delta S = 1)} \tag{3.16}$$

where σ(ΔS = 0) and σ(ΔS = 1) denote the cross sections resulting from ΔS = 0 and ΔS = 1 spin transfers in nuclei, respectively. The factor N indicates the probability that a spin transfer process will produce spin-flip in the nuclear system. In fact, spin-flip and spin transfer are slightly different: the latter is a necessary, but not sufficient, condition for the former. Measurements of P_{sf} provide information on the contribution of the spin-vector component of the interaction from the selection of the Fermi and Gamow-Teller transitions. P_{sf} is related to the spin-flip probability S_{NN} [Gla87]:

$$P_{sf} = S_{NN}/\alpha \tag{3.17}$$

where α represents the spin-flip probability for ΔS = 1 transitions. In the case of isovector excitations, P_{sf} has been investigated through S_{NN}, measured by using polarized protons especially in the $(\vec{p},\vec{n})$ reaction [Tad84]. The last reaction has been a good spectroscopic tool with $\Delta T_z = -1$ for well resolved states and isolated resonances, however it is not so adapted when high energy resolution is required in order to separate overlapping resonances. In this case, the (^{7}Li,^{7}Be) reaction is superior, providing the relative strength P_{sf} also for the continuum and overlapping resonances by γ-coincidence technique [Nak91].

The two routes of the the (^{7}Li,^{7}Be) reaction turns out to be an important aspect of this CEX process. In fact, the (^{7}Li,$^7Be_{GS}$) and (^{7}Li,$^7Be_{exc}$) branches are characterized by different nucleonic spin transfer. Indeed, in the (^{7}Li,$^7Be_{GS}$) transition the $3/2^- \rightarrow 3/2^-$ angular

momentum coupling selects the $\Delta J^\pi = 0^+$, 1^+, 2^+ and 3^+ transfers, with $\Delta L = 0$, 2 and $\Delta S = 0$, 1. Instead, for the (^{7}Li,^{7}Be$_{exc}$) transition the angular momentum coupling is $3/2^- \rightarrow 1/2^-$, selecting $\Delta J^\pi = 1^+$, 2^+ with $\Delta L = 0$, 2 and $\Delta S = 0$, 1. For $\Delta L = 0$, the $\Delta S = 0$ and 1 are related, respectively, to the well known Fermi and Gamow-Teller transitions of the β-decay involving the target and projectile nuclei. The relative importance of the $\Delta L = 2$ transfer depends on the rank-2 tensor strength of the CEX operator and on the momentum transfer.

Both the transitions (^{7}Li,^{7}Be$_{GS}$) and (^{7}Li,^{7}Be$_{exc}$) correspond to super-allowed β-decay with log(ft) = 3.3 and 3.53, respectively [Cho93]. As a consequence, at very forward angles the tensor strength vanishes [Aus94, Etc88] and thus, at least in this limit, it is possible to correlate the CEX and β-decay dynamics. In such conditions the $\Delta J^\pi = 0^+$, 1^+ (with $\Delta L = 0$ and $\Delta S = 0$, 1) components accounts for the major part of the (^{7}Li,^{7}Be$_{GS}$) reaction, while $\Delta J^\pi = 1^+$ (with $\Delta L = 0$ and $\Delta S = 1$) for (^{7}Li,^{7}Be$_{exc}$). Therefore, the first reaction is constituted by mixed Fermi and Gamow-Teller transitions, while the second one consists of pure Gamow-Teller transition. In detail, the cross sections for the above transition can be written as [Nak91]:

$$\sigma\left(^7\mathrm{Be}_{GS}\right) \equiv \sigma_0 \approx B_0(F,q)\ \sigma(\Delta S = 0) + B_0(GT,q)\ \sigma(\Delta S = 1) \tag{3.18a}$$

$$\sigma\left(^7\mathrm{Be}_{exc}\right) \equiv \sigma_1 \approx B_1(GT,q)\ \sigma(\Delta S = 1) \tag{3.18b}$$

where q is the linear momentum transfer, $B_0(F,q)$ and $B_0(GT,q)$ are the nuclear structure factors for non spin-flip and spin-flip transitions in (^{7}Li,^{7}Be$_{GS}$), respectively, and $B_1(GT,q)$ is the nuclear structure factor for spin-flip transition in (^{7}Li,^{7}Be$_{exc}$). In particular, in (3.18a) the cross section σ_0 is expressed as an incoherent sum of the $\Delta S = 0$ and 1 cross sections for the transition to ^{7}Be$_{GS}$. Extracting the ratio $\sigma(\Delta S = 1)/\sigma(\Delta S = 0)$ from (3.18) and substituting it in (3.16) one obtains:

$$P_{sf} = N\frac{\sigma(\Delta s = 1)}{\sigma(\Delta s = 1)+\sigma(\Delta s = 0)} = N\frac{\sigma_1/\sigma_0}{\sigma_1/\sigma_0\left(1-\dfrac{B_0(GT,q)}{B_0(F,q)}\right)+\dfrac{B_1(GT,q)}{B_0(F,q)}} \tag{3.19}$$

In the limit of negligible momentum transfer (q ~ 0), the structure factors are given by the reduced probabilities $B_0^\beta(F)$, $B_0^\beta(GT)$ and $B_1^\beta(GT)$ for the analogous β-decay transitions and we can set N = 1 in (3.19). In this limit the B-ratios of (3.19) are given by:

$$\frac{B_0(GT,0)}{B_0(F,0)} = \frac{B_0^\beta(GT)}{B_0^\beta(F)} = 1.25 \tag{3.20a}$$

$$\frac{B_1(GT,0)}{B_0(F,0)} = \frac{B_1^\beta(GT)}{B_0^\beta(F)} = 1.11 \tag{3.20b}$$

where the values of the ratios come from β-decay data [Cho93], and (3.19) becomes:

$$P_{sf} = \frac{\frac{\sigma_1}{\sigma_0}}{1.11 - 0.25\frac{\sigma_1}{\sigma_0}} = \begin{cases} 1 & \text{if } \sigma(\Delta S = 0) = 0 \quad \Rightarrow \frac{\sigma_1}{\sigma_0} = 0.888 \\ 0 & \text{if } \sigma(\Delta S = 1) = 0 \quad \Rightarrow \frac{\sigma_1}{\sigma_0} = 0 \end{cases} \tag{3.21}$$

Thus, under the assumption of dominance of the one-step process, the relative strength of the isovector $\Delta S = 1$ and $\Delta S = 0$ excitations can be directly connected to the cross section ratio $\sigma(^7Be_{exc})/\sigma(^7Be_{GS}) \equiv \sigma_1/\sigma_0$. So this important spin observable can be determined independently on the nuclear structure models by a measurement of the two cross sections at very forward angles. In practice, it is useful to define the ratio G, which is equal to zero for pure $\Delta S = 0$ transitions and to 0.46 for pure $\Delta S = 1$ transitions [Jän96]:

$$G \equiv \frac{\frac{\sigma_1}{\sigma_0}}{1+\frac{\sigma_1}{\sigma_0}} = \begin{cases} 0.46 & \text{for} \Delta S = 1 \\ 0 & \text{for} \Delta S = 0 \end{cases} \tag{3.22}$$

Of course, the physical meaning of G and P_{sf} is very similar. The G factor provides important information on the reaction dynamics, both on the spin transfer contribution and on the validity of the analogy with the β-decay. The value of G is expected to remain constant in the conditions in which the analogy is valid, i.e., for prevalence of the one-step mechanism, low momentum transfer and negligible contribution of the tensor component of the NN-interaction. In other words, a flat angular distribution of the G factor is a good indication of the validity of these hypotheses. They are typically true at very forward angles, but are less reliable for backward angles. Thus the assignments of $\Delta S = 0$ or 1 to a given transition may be based on the measured G factor and cross section ratios at $\theta_{lab} \sim 0°$ [Nak91, Jän96]. Besides, the measurement of the cross sections at larger angles gives information about the influence of the tensor forces, whose strength may be empirically adjust to fit the data.

3.4.2 Some results

In this Section some results for the strength P_{sf} of the spin transfer excitations and for the G factor are discussed. The cross section ratios σ_1/σ_0 obtained by Nakayama et al. [Nak90b] for the $^{12}C(^7Li,^7Be)^{12}B$ reaction are reported in Figure 3.9a as a function of the incident energy and for different transitions. A different behaviour is observed for natural (1^-, 2^+) and unnatural (1^+, 2^-) parity states. The ratios for the unnatural parity transitions are nearly independent on the incident energy because in this case both σ_0 and σ_1 involve the spin transfer component ($\Delta S = 1$) only, thus the cross section ratio cancels out every energy dependence of the spin transfer parts in the effective NN-interaction. On the other hand, the ratios for the natural parity transitions vary with the incident energy, reflecting an energy dependence of the ratio of spin transfer to not spin transfer parts of the effective NN-interaction. As observed in Section 3.3, the point at 14 MeV/u systematically deviates from the one-step predictions.

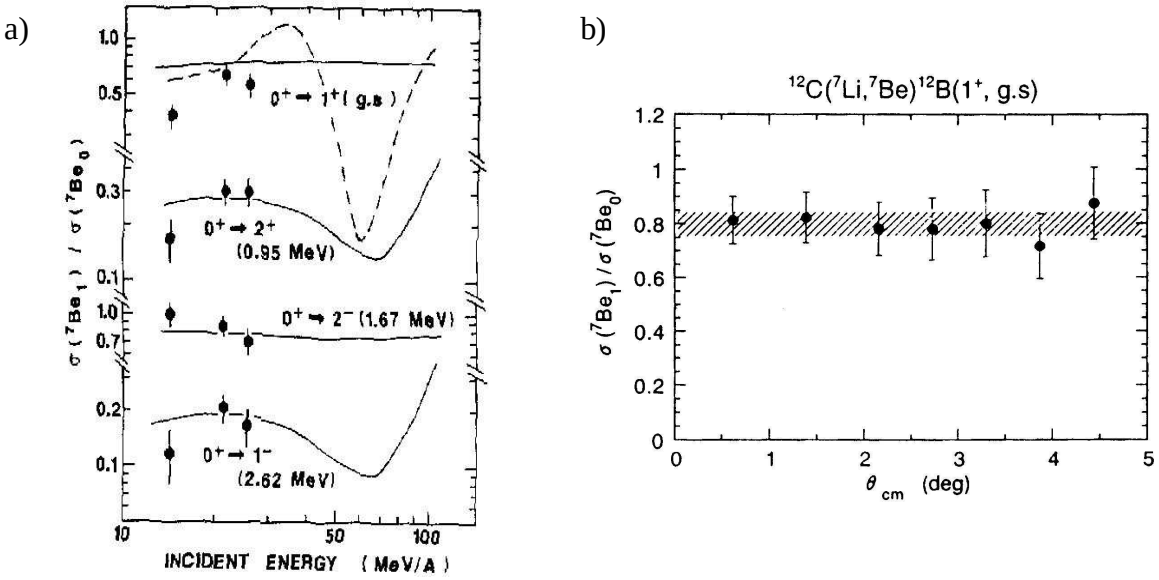

Figure 3.9. a) Cross section ratios for different transitions induced by ^{12}C(^{7}Li,^{7}Be)^{12}B at θ_{lab} = 0° [Nak90b]. The measured quantities refer to E_{inc} = 14, 21 and 26 MeV/u. Solid lines denote the calculations for the one-step process, while the dashed line corresponds to a two-step calculation for the $0^+ \rightarrow 1^+$ ground state transition. b) Angular dependence of the ratio σ_1/σ_0 for the 1^+ transition to $^{12}B_{GS}$ at E_{inc} = 65 MeV/u [Nak99].

The angular dependence of the ratio σ_1/σ_0 for the 1^+ Gamow-Teller transition to $^{12}B_{GS}$ at E_{inc} = 65 MeV/u is shown in Fig. 3.9b [Nak99]. This ratio is found to be independent on the scattering angle, indicating that the reaction proceeds via direct mechanism. The mean value (hatched area) obtained for the ratio is 0.80 ± 0.05, or equivalently G = 0.44 ± 0.05. However the ratio corresponding to the β-decay of ^{7}Be is 0.89. This slight discrepancy may be due to a linear momentum transfer different from zero. On the basis of the shape of the tensor component obtained in the same angular range of Fig. 3.9b, the author considered the ratio independent from the tensor contribution.

The relative strength of the isovector spin excitations P_{sf} at E_{inc} = 26 MeV/u is shown in Figure 3.10 [Nak91]. P_{sf} was derived up to 18 MeV of ^{12}B excitation energy by measuring separately the (^{7}Li,^{7}Be$_{GS}$) and (^{7}Li,^{7}Be$_{exc}$) reaction channels at θ_{lab} = 0° with the ^{7}Be-γ coincidence technique [Nak91]. Under these conditions the linear momentum transfer is q ~ 0.3 fm^{-1}. P_{sf} was normalized to 1 using the ratio σ_1/σ_0 for the 1^+ and 2^- transitions to ^{12}B ground and 1.76 MeV excited state, finding N ~ 1.3. Also here a different behaviour between natural and unnatural parity transitions is observed. For unnatural parity states P_{sf} ~ 1, corresponding to G = 0.41. This is in agreement with the result obtained at 65 MeV/u for G of the 1^+ transition (Fig. 3.9b), confirming the prevalence of the one-step mechanism in these cases. In contrast, for natural parity states and for the continuum ($E_x \geq 6$ MeV) P_{sf} ~ 0.5 and G = 0.26. This suggests that the ΔS = 0 and ΔS = 1 isovector excitations have similar magnitudes for natural parity states and for E_x between about 6 and 18 MeV.

The results obtained by Winfield et al. [Win96] for the same reaction at E_{inc} = 70 MeV/u, reported in Fig. 3.11, agree with those of Fig. 3.10 [Nak91]. However, deviations

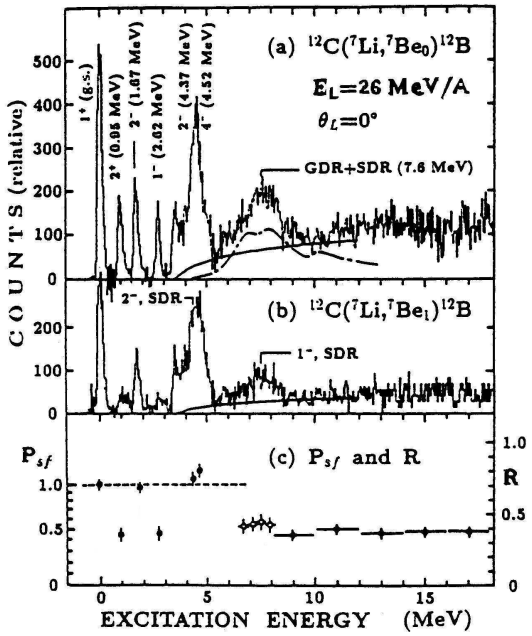

Figure 3.10. Excitation energy spectra for a) ^{12}C(^{7}Li,^{7}Be$_{GS}$)^{12}B and b) ^{12}C(^{7}Li,^{7}Be$_{exc}$)^{12}B reactions at θ_{lab} = 0° and E_{inc} = 26 MeV/u [Nak91]. c) Relative strength of spin excitations P_{sf} and cross section ratio R = σ_1/σ_0 (solid circles). P_{sf} and R are connected by an empirical relation. The open circles correspond to the isovector dipole resonance. The dashed line represents the average value observed for R in the 1^+ and 2^- transitions. [Nak91].

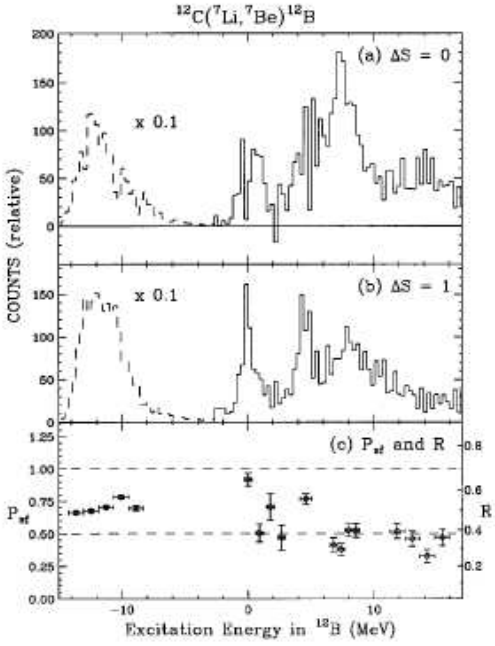

Figure 3.11. Excitation energy spectra for the ^{12}C(^{7}Li,^{7}Be)^{12}B reaction at θ_{lab} = 0° and E_{inc} = 70 MeV/u for a) ΔS = 0 and b) ΔS = 1 channels [Win96]. c) Relative strength of spin excitations P_{sf} and cross section ratio R = σ_1/σ_0 [Win96].

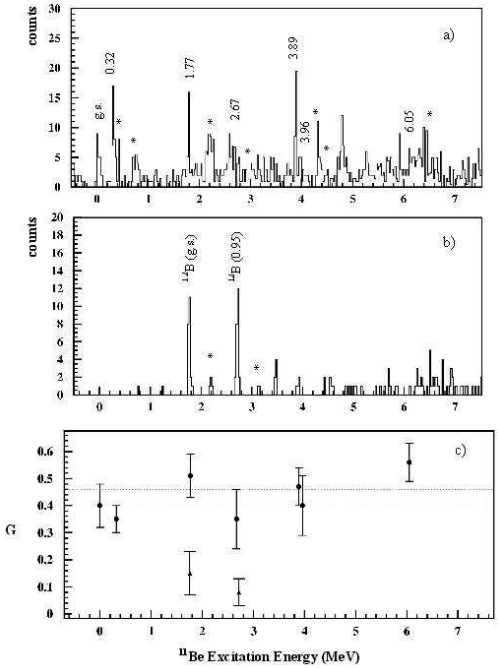

Figure 3.12. Excitation energy spectra for the a) ^{11}B(^{7}Li,^{7}Be)^{11}Be and b) ^{12}C(^{7}Li,^{7}Be)^{12}B reactions at θ_{lab} = 0° and E_{inc} = 8.1 MeV/u [Cap01, Cap04b]. Only 1/5 of the full statistics is shown. The asterisks indicates the peaks associated with the excitation of ^{7}Be. c) Values of the G factor at θ_{lab} = 0° for the populated ^{11}Be (full circles) and ^{12}B (full triangles) states [Cap01, Cap04b].

from these behaviours are present at lower energy, as observed by Cappuzzello et al. [Cap01, Cap04b] at E_{inc} = 8.1 MeV/u. In particular, in Fig. 3.12 the values of the G factor at θ_{lab} = 0° for various ^{11}Be states are compared to those associated with the most excited transitions to ^{12}B: the 1^+ and 2^+ transitions to the ground and first excited (E_x = 0.95 MeV) state, respectively. These values, also reported in Table 3.1, were measured during the same experiment, devoted to the study of the ^{11}B(^{7}Li,^{7}Be)^{11}Be reaction, in which a ^{12}C target was used in order to subtract the background from the ^{12}C(^{7}Li,^{7}Be)^{12}B reaction.

Table 3.1. G factor values measured at θ_{lab} = 0° and E_{inc} = 8.1 MeV/u for the ^{11}B(^{7}Li,^{7}Be)^{11}Be and ^{12}C(^{7}Li,^{7}Be)^{12}B reactions [Cap01, Cap04b].

	^{11}Be							**^{12}B**				
Ex [MeV]	g.s.	0.32	1.77	2.67	3.89	3.96	6.05	g.s.	0.95	1.67	2.62	4.50
G	0.38	0.35	0.46	0.35	0.47	0.40	0.56	0.15	0.17	0.40	0.33	0.34
ΔG	0.04	0.03	0.04	0.04	0.04	0.07	0.03	0.03	0.03	0.06	0.07	0.03

It is interesting to note that some of the G values obtained for the ^{12}B states deviate from the behaviour observed at higher bombarding energies. In particular, the 1^+ transition at higher energy is prevalently Gamow-Teller, while the 2^+ one shows a minor spin transfer contribution. On the contrary, at E_{inc} = 8.1 MeV/u the G factors of the two transitions considered are nearly the same and exhibit a very small value. This indicates an increased role of the two-step mechanisms for the transition to the well bound ^{12}B states. Thus at E_{inc} = 8.1 MeV/u the sequential mechanisms turns out to be important even at small angles (~ 0°).

Contrarily, concerning the transitions to all the ^{11}Be states, the values of the G factor are definitely different from 0 and close to the 0.46 limit of the Gamow-Teller transitions in the projectile. This indicate clearly a one-step dynamics. Moreover, the ^{11}Be angular distributions at forward angles are well reproduced by one-step DWBA calculations [Cap04b]. It is found that the unnatural parity transitions account for the major part of the observed cross sections. In order to describe correctly the angular distributions, a significant role of the tensor force is required, however this tensor component has a minor effect on the G factor at 0°. Therefore the results of ref. [Cap04b] indicate the dominance of spin transfer even though the projectile transitions are not pure Gamow-Teller. Only at larger angles the contribution of the two-step process cannot be neglected.

The experiments of Nakayama et al. [Nak91, Nak99], as also those described, e.g., in refs. [Jän96, Win96], used ^{7}Li Cyclotron beams. In these cases the energy resolution did not allow the separation of the ^{7}Be doublet, so a ^{7}Be-γ coincidence technique was employed to isolate the transition to the excited ^{7}Be state and to separate the $\Delta S = 0$ and 1 contributions. The γ-detection efficiency was the main source of uncertainty in the G measurement. At low incident energy, as in refs. [Etc88, Nak90b, Cap01] and in the present experiment (see Section 4.2 and refs. [Orr03, Cap04]), the separation of the doublet is obtained detecting the ^{7}Be ejectiles by a high-resolution magnetic spectrometer. This makes also possible to measure at very forward angles, including 0°.

On the basis of the actual knowledge, it is not possible to draw certain conclusions on the dynamics of the (^{7}Li,^{7}Be) CEX reactions. The interest in the comprehension of the reaction mechanism and the richness of information that can be extracted from (^{7}Li,^{7}Be), especially when exotic nuclei are involved, make necessary further investigations. Systematic measurements of high resolution energy spectra, cross sections and G factors at very forward angles, together with the development of a sophisticated theoretical model, are needed.

CHAPTER 4

THE $^{15}N(^{7}Li,^{7}Be)^{15}C$ REACTION: EXPERIMENTAL SET-UP AND MEASUREMENTS

This Chapter describes the experimental set-up and measurement strategy for the $^{15}N(^{7}Li,^{7}Be)^{15}C$ CEX reaction at 55 MeV incident energy. The purpose of the experiment was to study the spectroscopy of the ^{15}C nucleus and the CEX mechanism. The experiment was performed at the Tandem laboratory of IPN-Orsay (France) on June 2002, using a 55 MeV $^{7}Li^{+++}$ beam and a high-purity (99.8 %) ^{15}N gas target, designed and constructed on purpose at the LNS-INFN (Catania) [Orr03, Cap04]. The ^{7}Be ejectiles were detected by the IPN-Orsay Split-Pole magnetic spectrometer.

The goal of this experiment was to obtain clearer data on ^{15}C and explore a wider angular range – especially forward angles – compared to our previous experiment, which was performed at the IPN-Orsay on February 2001 in order to explore the ^{15}C [Noc03] and ^{14}B [Orr01] spectra. In that occasion a major damage to the Split-Pole focal plane detector forced us to use a silicon ΔE-E telescope and measure at $\theta_{lab} = 10°$ only.

The gas target (described in Section 4.1) was a crucial factor to overcome the difficulties came up in the analysis of the data taken in the previous experiment with a ^{15}N enriched melamine solid target [Noc03]. The experimental set-up is described in Section 4.2, while Section 4.3 concerns with the realization of the measurements.

4.1 The gas target

^{15}N is a rare nitrogen isotope, which only constitutes the 0.37 % of the whole nitrogen present on the Earth. Nevertheless, highly pure stocks of such a gas can be found in the market. More difficult is to design an efficient shape for the container, which minimizes the energy straggling while maximizing the effective target thickness.

The choice of a gas target, fundamental for the experiment success, was stimulated by the incomplete results obtained in the previous experiment [Noc03] with a ^{15}N enriched melamine $C_3H_6N_6$ (supported by 30 $\mu g/cm^2$ ^{12}C backing) solid target, which gave a large background produced by the ^{12}C impurity in the target. This background, together with the low yield of the ^{15}C peaks, did not allow to draw safe conclusions about ^{15}C.

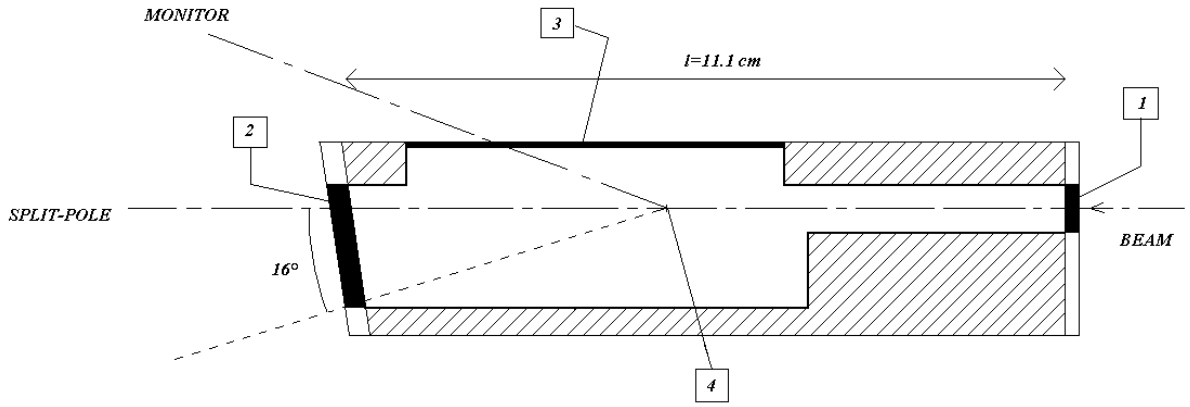

Figure 4.1. Design of the gas target. 1) Beam entry window (nickel). 2) Beam exit window (nickel). 3) Lateral window for monitor (mylar). 4) Optical center.

We used a confined high-purity (0.2 % ^{14}N) ^{15}N gas target (schematised in Figure 4.1), which was designed and constructed at the LNS-INFN (Catania). This target guarantees a high gas purity and may work at high density – dependent on the gas pressure – to increase the effective target thickness, in order to achieve a good statistic amount of data. However the necessity to have simultaneously a good experimental resolution imposes some limitation to the pressure value, especially at forward angles.

In general, the best compromise between different parameters has to be chosen. Unlike a differential pumped gas target, a confined gas target must include appropriate windows for beam inlet and reaction products outlet. These windows have to be thin as much as possible to not straggle the particle energies, but at the same time they have to support the pressure difference with the scattering chamber under vacuum (greater the gas pressure and greater the mechanical force on the windows).

The shape of the gas target is a parallelepiped (~11 cm long) with the beam entry and exit windows made from nickel (0.6 μm thick) to withstand the beam heating; the lateral window for a monitor telescope is made from mylar (1.5 μm thick). The size of the exit window (2 cm large) allows the Split-Pole to explore an angular range between 0° and 16° (limit angle). The nickel is an appropriate material for the beam windows, because it is a good conductor with a high melting point; besides a thin (0.6 μm) nickel foil may support a differential pressure of 100 mbar. The energy straggling of a ^{7}Li beam (55 MeV) through a Ni window 0.6 μm thick is about 44 keV, as calculated by the TRIM code [Sri00], with an average energy loss of 160 keV, tolerable for our purposes.

The target shape is designed in order to reduce scattering background from the window (see Fig. 4.1). The particles produced in the entry window will be stopped on the target walls, while a collimator located at the entrance of the Split-Pole (see Fig. 4.4) reduces the background from the exit window. However these precautions have no effect for the 0° measurements, in which therefore a considerable Ni background is expected.

The window thickness traversed by the outgoing particles varies with the detection angle ($t_{eff} = t / \cos\theta$); thus the exit window has an oblique closure to mediate the thickness differences.

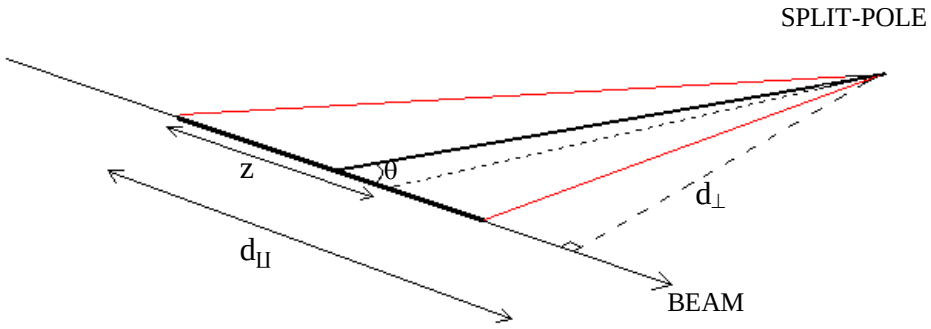

Figure 4.2. Scheme of the detector-target system. The tick line represents the gas target (l = 111 mm). The beam direction is indicated by the arrow.

4.1.1 Calculation of the geometrical factor g(θ)

The collimator at the entrance of the Split-Pole was also used to define the explored collision zone. In fact, another problem which arises when one uses a gas target is that the size of the collision region, the solid angle of detection and the angular spread are defined by the collimating system and vary with the angle of detection.

Let us consider the definition of the yield of a certain nuclear process:

$$N_{RIV}(\theta) = N_{INC}\, N_{TAR}^{Vol} \int_0^{l(\theta)} d\Omega(z)\sigma(\theta, z)\, dz \tag{4.1}$$

where N_{INC} is the number of incident particles, N_{TAR}^{Vol} is the number of target nuclei/cm^3, $\sigma(\theta,z)$ is the laboratory differential cross section and $z = z(\theta)$ represents a generic point of the target, which is supposed to be mono-dimensional for simplicity.

If $\sigma(\theta,z) \equiv \sigma(\theta)$, i.e., the cross section variation with z may be neglected, we obtain:

$$N_{RIV}(\theta) = N_{INC}\, N_{TAR}^{Vol}\, \sigma(\theta) \int_0^{l(\theta)} d\Omega(z)\, dz \tag{4.2}$$

where

$$\frac{g(\theta)}{\sin\theta} = \int_0^{l(\theta)} d\Omega(z)\, dz \tag{4.3}$$

Formula (4.3) defines the detection geometrical factor g(θ), it accounts for the effective target thickness l(θ) and solid angle Ω(z(θ)) which are seen from the detector and are determined by the peculiar geometry of the whole system (target, collimator and detector).

For the measurements at 0° and 2.5°, performed without the collimator (see Sect. 4.3), g(θ)/sinθ may be calculated simply integrating the solid angle element dΩ(z) on the target length because in this case the detector sees the whole target length $l(\theta) \equiv l = 111$ mm. Thus:

$$\frac{g(\theta)}{\sin\theta} = \int_0^{l} \frac{S}{[d(z)]^2}\, dz = \int_0^{l} \frac{S}{(d_{II} - z)^2 + d_\perp^2}\, dz \tag{4.4}$$

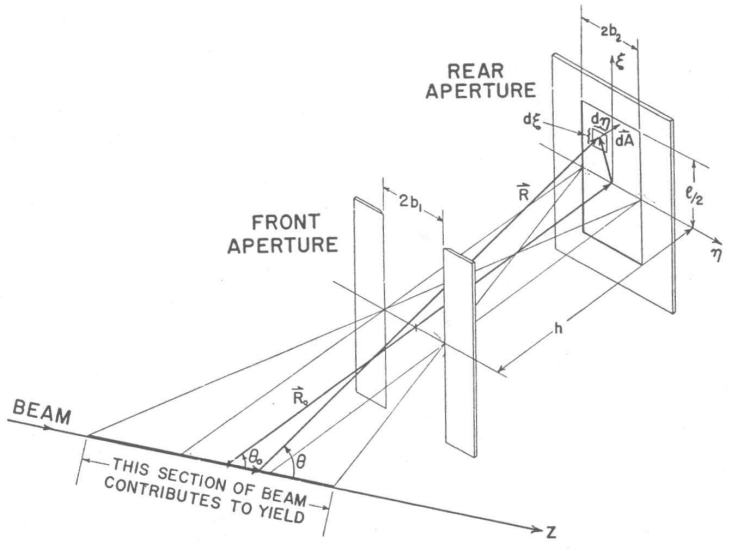

Figure 4.3. Schematic diagram showing the case of a vertical front slit and a rectangular rear aperture, taken from the original paper by Silverstein [Sil59]. It shows the geometric relations between a point on the beam axis from which scattered particles originate, and an area element $d\xi\, d\eta$ of the rear aperture, through which they pass after being scattered through an angle θ. The vector diagram applies to all cases.

where S is the detector sensitive area, determined by the slits span and assumed to be point-like to integrate; $(d_{II} - z)$ and $d_{\perp}$ are the components of the vector distance $\underline{d}(z)$ between target and detector ($d_{\perp} = 0$ at 0°), as shown in Figure 4.2.

At larger angles the calculation of $g(\theta)$ is more complex due to the presence of the two rectangular apertures of the collimator, used to define the collision zone and reduce the background from the exit window. The geometrical factor will also depend on the derivatives of the cross section with respect to the angle, since the effect of the variation of the cross section over the small angular range accepted by the rear aperture cannot always be neglected. In this case $g(\theta)$ was calculated following the Silverstein method [Sil59]. Silverstein's calculations concern geometrical effects only, without taking into account effects due to slit edge or multiple scattering. He treats different types of aperture boundaries, integrating on the area elements $d\xi\, d\eta$ of the rear aperture and considering the contribution from the total length of beam seen by each element.

We are interested in the case of a vertical front slit and a rectangular rear aperture, as schematised in Figure 4.3, and therefore we used the relative formulae of ref. [Sil59] to calculate $g(\theta)$, in which the beam is considered a line beam, i.e., the effects arising from the finite diameter of a real beam are neglected. It is noticed that the Silverstein's formulae are not applicable without a collimator and/or at 0° because some parameters become undefined; besides in every case they give $g(\theta)$, but the needed $g(\theta)/\sin\theta$ value diverges at $\theta = 0°$. Thus in these cases we have to use formula (4.4).

The calculated geometrical factor values, obtained for the different angles of measurement, are reported in Table 4.1.

Table 4.1. Calculated geometrical factor g(θ)/sinθ at different angles. Formula (4.4) was used for θ_{lab} = 0°, 2.5°. For θ_{lab} = 8°, 10°, 14° we used the formulae of ref. [Sil59].

θ [°]	0	2.5	8	10	14
g(θ)/sinθ [mm · sr]	0.182	0.026	0.027	0.021	0.015

4.2 Experimental set-up

A picture of the adopted experimental set-up is shown in Figure 4.4, where the scattering chamber is visible, together with the gas target at the center, the collimator at the entrance of the Split-Pole and the monitor detector located at θ_{mon} = 20°. The beam direction is also indicated. The details of the devices are discussed in this Section.

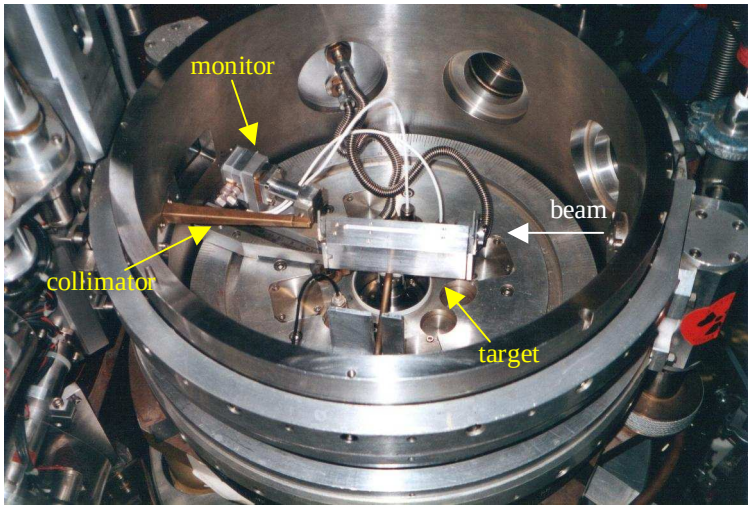

Figure 4.4. Photograph of the scattering chamber. The beam enters from right and goes into the gas target, at the center of the chamber. On the left , we can see the Split-Pole collimator and the monitor detector at θ_{mon} = 20°.

4.2.1 The beam

The $^{7}Li^{+++}$ beam was produced and accelerated at 55 MeV at the Tandem Van de Graaff facility of the IPN-Orsay laboratory, and send to the Split-Pole magnetic spectrometer, located at the end of one beam line. The energy definition of the IPN Tandem is quite good ($\Delta E/E \sim 2 \cdot 10^{-4}$), giving a good matching with the optical properties of the spectrometer. The beam, focused by various optical elements, enters in the scattering chamber and, passing through the gas target, is trapped into a Faraday cup. The beam intensity ranges from 2 nA for the 0° measurements, to 15 nA for the larger angles ones.

4.2.2 The scattering chamber and monitor detector

The reaction takes place into the cylindrical scattering chamber shown in Figure 4.4, with the axis normal to the beam direction and a radius of 20 cm. The chamber is provided with a sliding seal, it allows that the spectrometer rotates under vacuum (~10^{-6} torr), exploring the angular range from –12° to +150° with respect to the beam direction. The gas target is placed at the center of the chamber. The wall of the chamber has a lateral aperture, equipped with movable horizontal and vertical slits, to which the collimator may be connected. The aperture gives a direct connection to the Split-Pole spectrometer.

A ΔE-E telescope composed by two silicon detectors (100 μm and 1000 μm thick, respectively) was used to monitor, e.g., possible gas pressure and beam intensity variations. Disposing the monitor detector at $\theta_{mon} = 30°$ and more is usually necessary to discriminate the various elastic peaks due to the impurities present in the target. In this case we did not expect to have background from impurities (as, e.g., ^{12}C) owing to the use of a high-purity (0.2 % ^{14}N) ^{15}N gas target. Therefore the monitor was mounted in the scattering chamber at $\theta_{mon} = 20°$ to increase the number of counts.

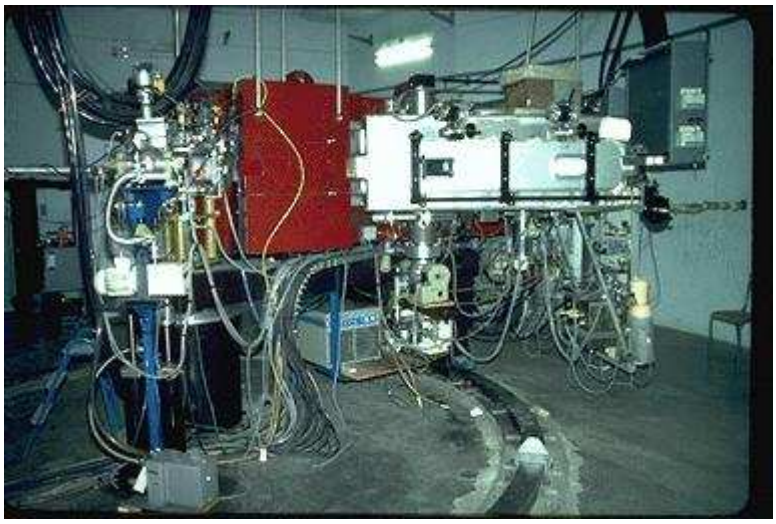

Figure 4.5. Photograph of the Split-Pole magnetic spectrometer. The beam enters from left and goes into the scattering chamber. The reaction products are selected by the magnetic elements (in red) of the spectrometer and identified on the focal plane detector (big silver box).

4.2.3 The Split-Pole magnetic spectrometer

The ^{7}Be ejectiles were detected by the IPN-Orsay Split-Pole magnetic spectrometer [Spe67], shown in Figure 4.5, in order to measure at forward angles and with high energy resolution (ΔE/E ~ 1/2000). The optical elements of the spectrometer consist of two magnetic dipoles – as schematised in Figure 4.6 – which assure an efficient selection of the reaction products. The first dipole focuses on the vertical plane while the second one focuses on the horizontal plane and both disperse the particles on the focal plane according to their magnetic rigidity $B\rho = p/q$.

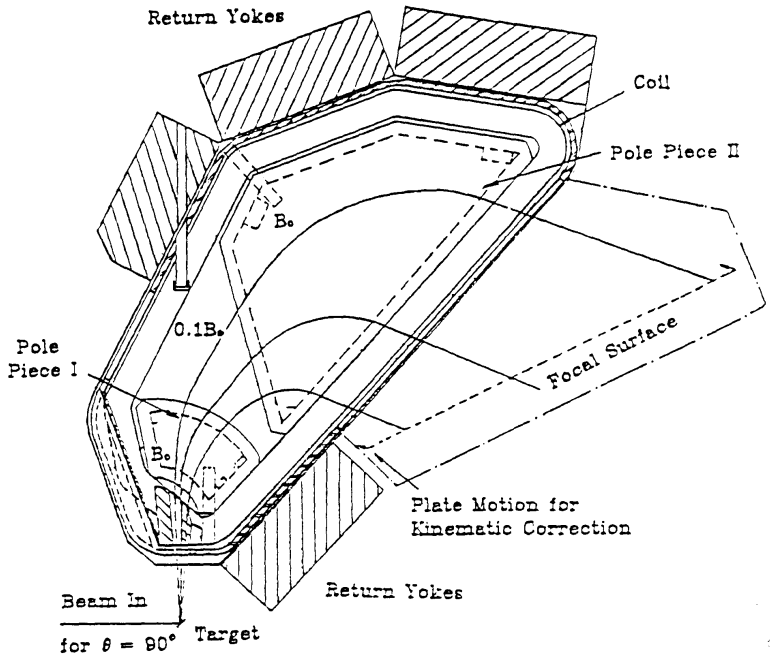

Figure 4.6. Scheme of the Split-Pole magnetic spectrometer. The first dipole focuses on the vertical plane while the second focuses on the horizontal one; they both disperse the particles on the focal plane according to their magnetic rigidity $B\rho = p/q$.

The associated focal plane detector (FPD), shown in Fig. 4.7, consists of a proportional counter with cathode strips read by a delay line, used to measure the energy loss ΔE and the position of the particle, and a stopping Ne102 plastic scintillator foil, which measures the residual energy E_r. The FPD is filled by pure propane gas at a pressure of about 330 mbar.

A particle entering the FPD detector creates a track of ions and electrons drifting at constant velocity along the uniform electric field lines. When the drifting electrons reach the active region (~ 50 μm from the anodic wire), they start a quick and very localised multiplication process, giving an amplified signal only on the underlying cathode strips, which allows to measure the horizontal coordinate by the delay line readout technique. The electron drift times determines the vertical coordinate; the start signal for the drift time measurement is given by the scintillator. Besides, the anodic wire collects the charge produced by the particle, related to the energy loss ΔE. Particles reaching the plastic scintillator produce a signal read by a couple of photo-multipliers positioned on the left and right sides. The sum of the left and right signals is used to reconstruct the residual energy E_r of incident particle. The acquisition system was triggered by the AND logical signal between the left and right fast signals of the plastic scintillator.

As all the optical systems, a spectrometer is affected by optical aberrations. E.g., particles with same $B\rho$ but emitted with different angles may be focused on FPD in different positions. Besides, both the vertical and horizontal extensions of the gas target enhances these effects. The collimator at the entrance of the Split-Pole serves to reduce them also, by limiting the angular acceptance and defining more precisely the collision region.

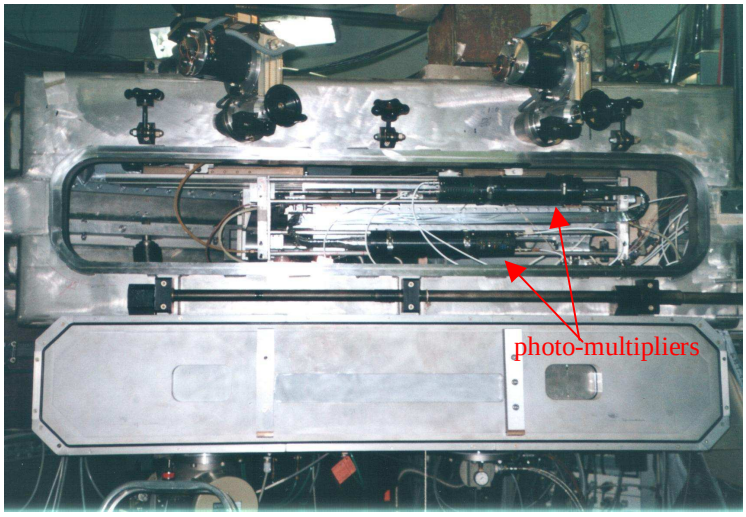

Figure 4.7. Photograph of the focal plane detector.

4.3 Measurements

Preliminary to the measurements, a delicate first step consists of the alignment of the gas target with the beam direction and Split-Pole entrance. The target was lined up using two collimators appositely constructed on its top, by means of an external video camera visualizing the spot beam on a fluorescent material mounted on the top of the gas target.

Caution was used in doing the vacuum into the scattering chamber and in pumping the gas into the target, because the thin target windows might be broken by a high pressure difference. The gas pressure was constantly monitored by a differential manometer between target and chamber, letting us intervene to compensate light leaks varying the aperture of the gas cylinder. In this way there were no relevant pressure variations during several hours of measurements, 1.5 mbar being the maximum bearable variation in order to have the desired experimental resolution. The gas pressure was set to 14 mbar for the 0° and 2.5° runs and to values from 55 mbar to 63 mbar for the larger angle runs.

Another fundamental step of the measurement consists of the search for the optimal matching between the reaction kinematics and the magnetic field setting. In the case of the Split-Pole spectrometer this operation is easy due to the large momentum acceptance $p_{max}/p_{min} \sim 2.8$. In fact considering that

$$\frac{E_{max} - E_{min}}{E_{max}} = 1 - \left(\frac{p_{min}}{p_{max}} \right)^2 \approx 0.87 \qquad (4.5)$$

if the magnetic field is set so that the higher kinetic energy particles associated with a given transition exit at the largest radius side from the second dipole, one can measure simultaneously almost all (87 %) the excitation energy spectrum of the nucleus of interest.

The angular range explored was θ_{lab} = 0°, 2.5°, 8°, 10°, 14°. Especially the 0° measurements were delicate. Because the Faraday cup was utilizable for $\theta_{lab} > 2°$ only, during the 0° measurements particular care was given to stop the beam: the magnetic field was set to stop the beam inside the second dipole. The collimator was not used during the 0° and 2.5° measurements because useless in the first case (at 0° the detector equally sees the whole target length) and banging with the Faraday cup in the second case. Supplementary runs with an empty target were performed at 0° and 2.5° in order to measure the background coming from the nickel windows, which is important at forward angles.

To check the accumulated yield during the measurements it is important to be able to identify on-line the ^{7}Be ejectiles. To do this the two peaks associated with the $p(^{7}Li,^{7}Be)n$ reaction were used. These peaks represent the two solutions of the inverse kinematics equation of this process and, although the hydrogen was present in the target only as an impurity (i.e., in small quantity), they are characterised by a very intense large cross section and result dominant in the spectrum. An important property of the $^{15}N(^{7}Li,^{7}Be)^{15}C$ energy spectra is that the peak associated to the transition to the $^{15}C_{GS}$ lies in an intermediate position between the two previously-mentioned peaks. This, together with their simultaneous presence in the energy spectra at angles lower than 7.2° in the laboratory reference frame, makes these peaks a very useful reference to locate the region of the ^{15}C peaks. In particular, the two peaks disappear for kinematical reasons at angles larger than 7.2°.

However, a simple plot of ΔE versus $B\rho$ is not enough to identify the ^{7}Be region because of a superposition between the positions occupied by the ^{7}Be and ^{7}Li detected ions. To solve this problem the plastic scintillator (left, right and sum of them) residual energy spectra were considered. Putting various graphical cut conditions in the ^{7}Be-^{7}Li region of the ΔE-$B\rho$ and E_r-$B\rho$ matrices, as explained in Section 5.1.1, it is possible to separate the two ions and ^{7}Be may be clearly identified.

CHAPTER 5

THE $^{15}N(^{7}Li,^{7}Be)^{15}C$ REACTION: DATA ANALYSIS AND EXPERIMENTAL RESULTS

The present Chapter concerns the data analysis of the $^{15}N(^{7}Li,^{7}Be)^{15}C$ CEX reaction and the experimental results obtained. Together with the realization of the experiment, the data reduction constitutes a fundamental and critical phase of an experimental work.

The various steps of data analysis, necessary to obtain the ^{15}C excitation energy spectra from the raw data, are described in Section 5.1. The experimental results are shown in the subsequent Sections. In Section 5.2 the ^{15}C final spectra and populated states are shown, from which a new important observation emerges: the interference effect in the peak corresponding to the 8.5 MeV state (see 5.2.3). The measured $^{15}N(^{7}Li,^{7}Be)^{15}C$ experimental cross sections and angular distributions are presented in Section 5.3, while in Section 5.4 the distributions of the G factor – related to the spin-flip probability, see 3.4.1 – are reported.

5.1 Data analysis

We discuss in detail the data reduction procedure used to extract the ^{15}C excitation energy spectra, which consists of several precise steps: the first is the identification and selection of the ^{7}Be ions, then the energy calibration, the background subtraction and so on.

5.1.1 ^{7}Be identification and selection

The first step consists of the identification and selection of the ^{7}Be ejectiles. The reaction products were identified using the energy loss ΔE of the particle in the gas-filled FPD, the energy signal E_r from the scintillator behind it and the $B\rho$ obtained from position measurement of the delay line readout of the proportional counter, i.e., both in the ΔE-$B\rho$ and E_r-$B\rho$ matrices, on the basis of energy loss and kinematical calculations. The identification of ^{7}Be is confirmed by the presence of the strong peak associated to the second kinematical solution of the ($^{7}Li,^{7}Be$) reaction on hydrogen (the peak related to the first solution was out of the spectrometer acceptance). The procedure of Section 4.3 for the on-line ^{7}Be identification was improved in the off-line analysis, in order to achieve the same discrimination confidence

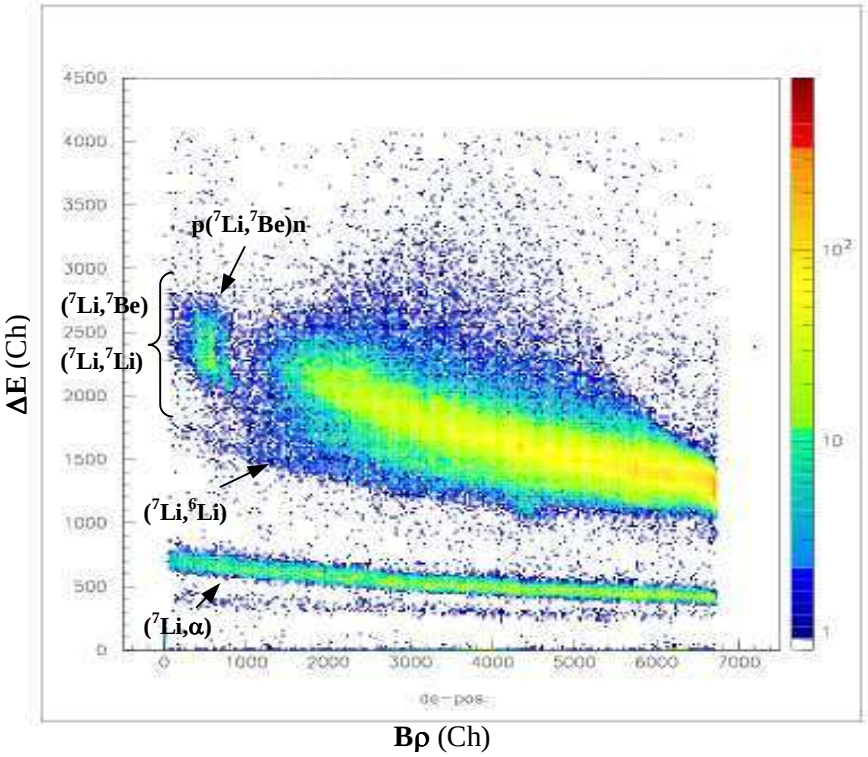

Figure 5.1. ΔE-Bρ matrix at θ_{lab} = 0°. The ^{7}Be, ^{7}Li and ^{6}Li ions lie in the large central region, while α particles lie lower down. The intense peak on the left corresponds to the (^{7}Li,^{7}Be) reaction on protons.

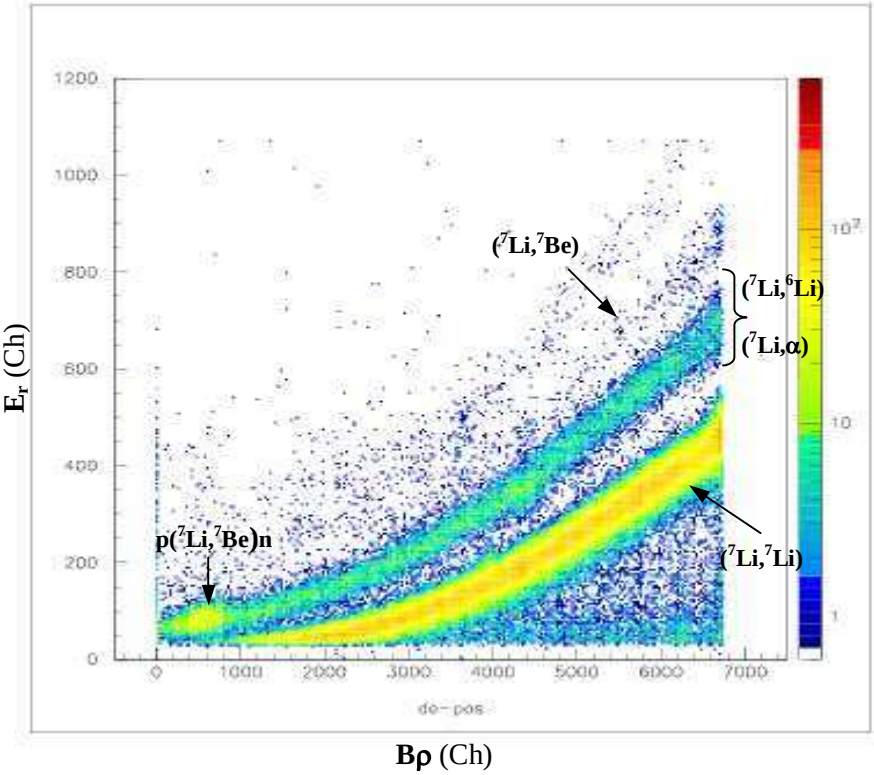

Figure 5.2. E_r-Bρ matrix at θ_{lab} = 0°. The ^{7}Be region is overlapped to the ^{6}Li and α ones, while the ^{7}Li ions are separated. Still the strong peak on the left corresponding to the p(^{7}Li,^{7}Be)n reaction is indicated.

even in absence of the p(^{7}Li,^{7}Be)n transition peaks, i.e., for the spectra at laboratory angles bigger than 7.2°. In these cases the identification was based on the detailed knowledge of the matrices and ^{7}Be spectrum, also determined by the previous experiment analysis [Noc03].

Graphical cut conditions were used to select the ^{7}Be ions. Because of the superposition between the ^{7}Be and ^{7}Li regions in the ΔE-Bρ matrix (see Figure 5.1), we had to use a self-consistent procedure to separate ^{7}Be from ^{7}Li, which consists of many graphical cut conditions imposed on the ΔE-Bρ and E_r-Bρ matrices. In fact, in the ΔE-Bρ matrix the positions of the detected ^{7}Be and ^{7}Li are superimposed, together with the ^{6}Li ions, while the α particles are clearly isolated (Fig. 5.1). On the contrary, in the E_r-Bρ matrix ^{7}Be and ^{7}Li are separated, but the ^{7}Be region is mixed with ^{6}Li and α.

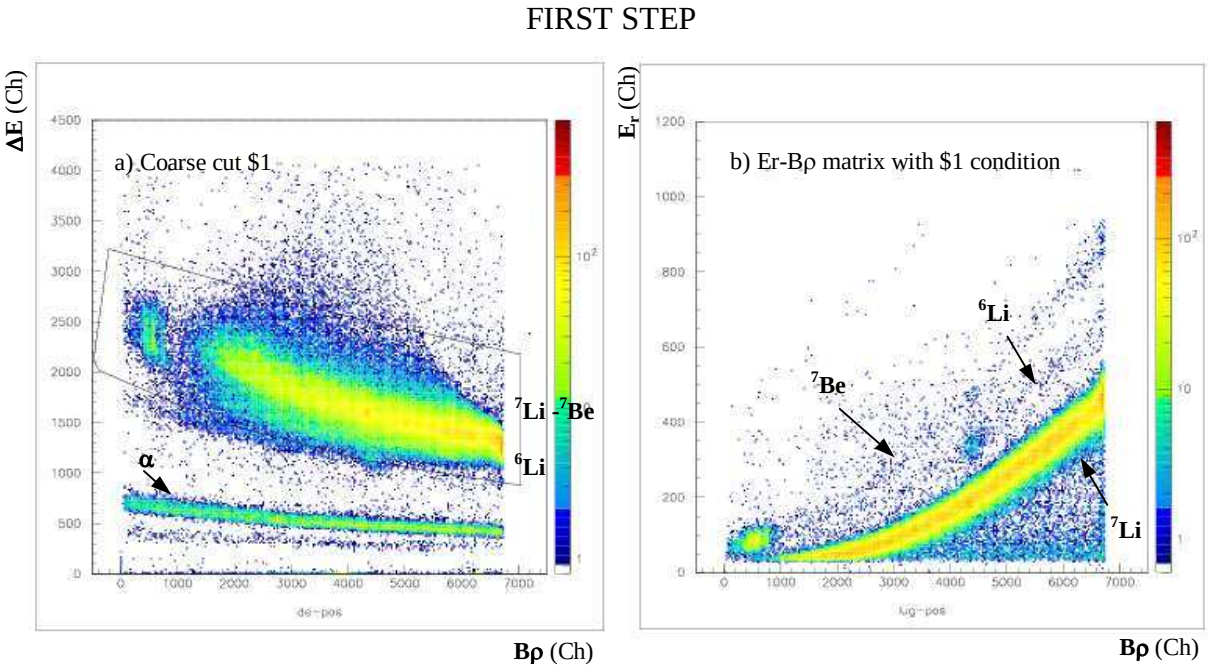

Figure 5.3. a) Coarse graphical cut $1 on the ΔE-Bρ matrix to exclude α particles. b) E_r-Bρ matrix plotted using $1 condition: ^{7}Be is separated from the α particles. $2 \cdot 10^{5}$ events are used.

Thus, for each run we used the following iterative procedure, which allowed a visible improvement of the graphical conditions applied to the matrices. A first coarse graphical cut $1 is drawn on the ΔE-Bρ matrix to exclude the α particles, only including the region of the ^{7}Be-^{7}Li superposition (Fig. 5.3a). This region is clearly identified by the presence of p(^{7}Li,^{7}Be)n transition peak for the spectra at $\theta_{lab} < 7.2°$ and by similarity between the ΔE-Bρ matrices for laboratory angles bigger than 7.2°. Then the E_r-Bρ matrix is plotted with this first condition $1: ^{7}Be is found to be separated from the α particles, besides ^{7}Li is easily separable by cutting, but ^{6}Li is still partially mixed (Fig. 5.3b).

In the second step of the cut procedure a coarse graphical cut $2 is drawn on the last matrix in the ^{7}Be corresponding line, excluding the ^{7}Li ions (Fig. 5.4a). Now the ΔE-Bρ matrix is plotted again with both the defined graphical conditions $1 and $2: this matrix contains ^{7}Be principally and some remaining ^{6}Li (Fig. 5.4b).

SECOND STEP

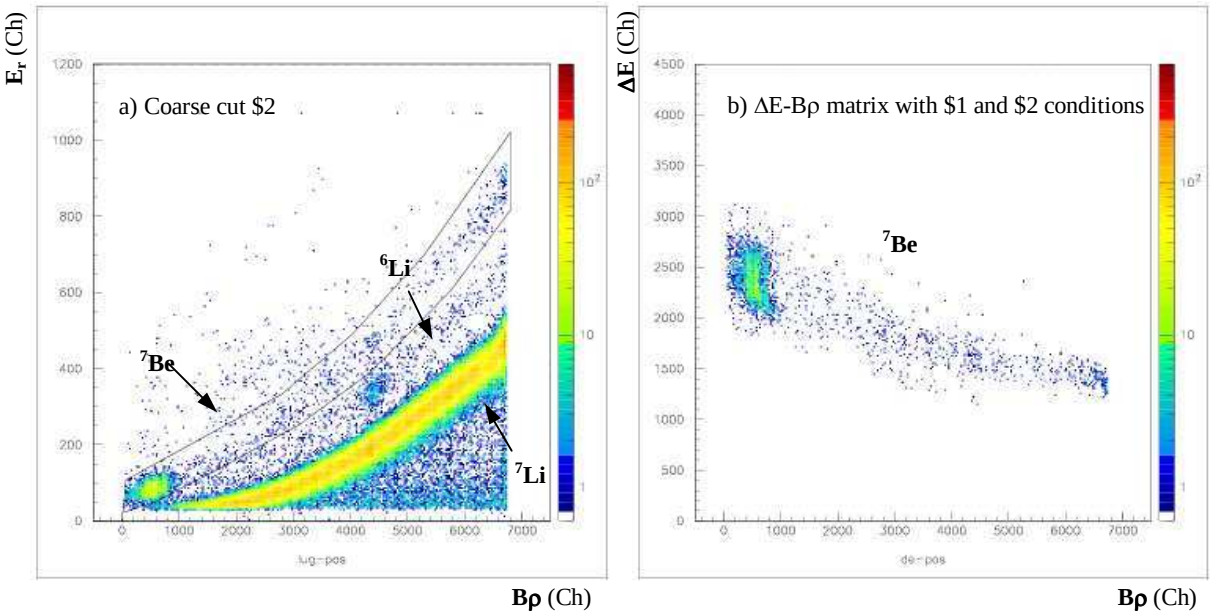

Figure 5.4. a) Second coarse graphical cut $2 on the E_r-Bρ matrix to select ^{7}Be excluding ^{7}Li. b) ΔE-Bρ matrix plotted with $1 and $2 conditions. $2 \cdot 10^5$ events are used.

THIRD STEP

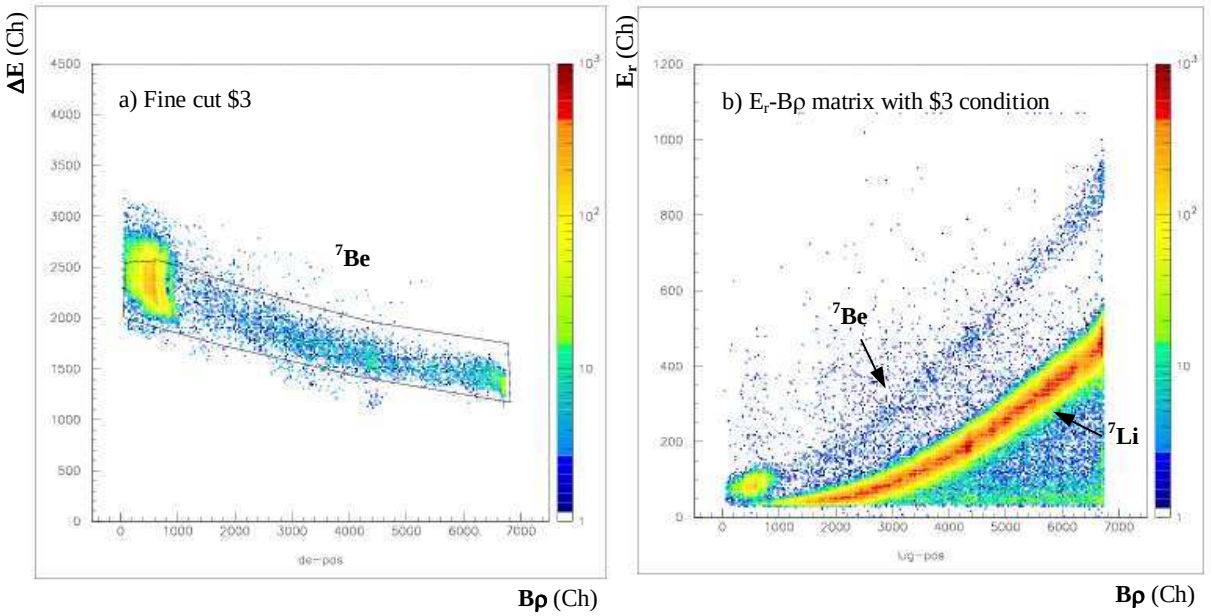

Figure 5.5. a) Fine graphical cut $3 on the ΔE-Bρ matrix to exclude the remaining ^{6}Li. b) E_r-Bρ matrix plotted with $3 condition. $5 \cdot 10^5$ events are used.

At this point the whole procedure is repeated starting from the last matrix and using finer cuts, in order to achieve a greater rejection of unwanted events. A fine graphical cut $3 was drawn on the ΔE-Bρ matrix of Fig. 5.4b, excluding ^{6}Li as well as α particles (Fig. 5.5a).

FOURTH STEP

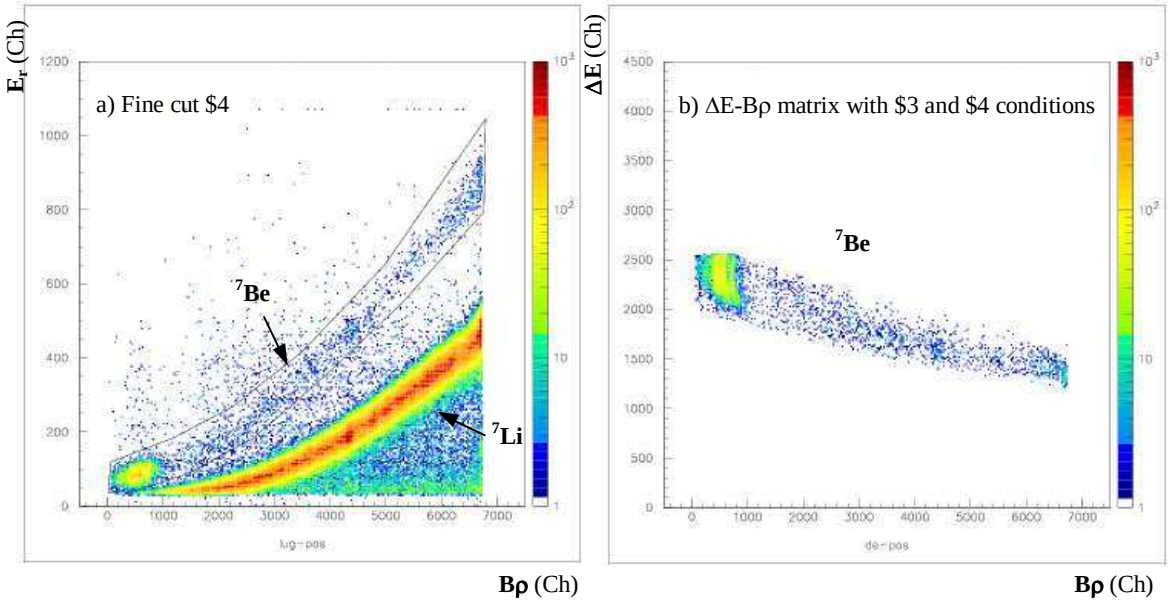

Figure 5.6. a) Fine graphical cut $4 on the E_r-Bρ matrix to select ^{7}Be excluding ^{7}Li. b) ΔE-Bρ matrix plotted with $3 and $4 conditions. The ^{7}Be ions are accurately selected. $5 \cdot 10^{5}$ events are used.

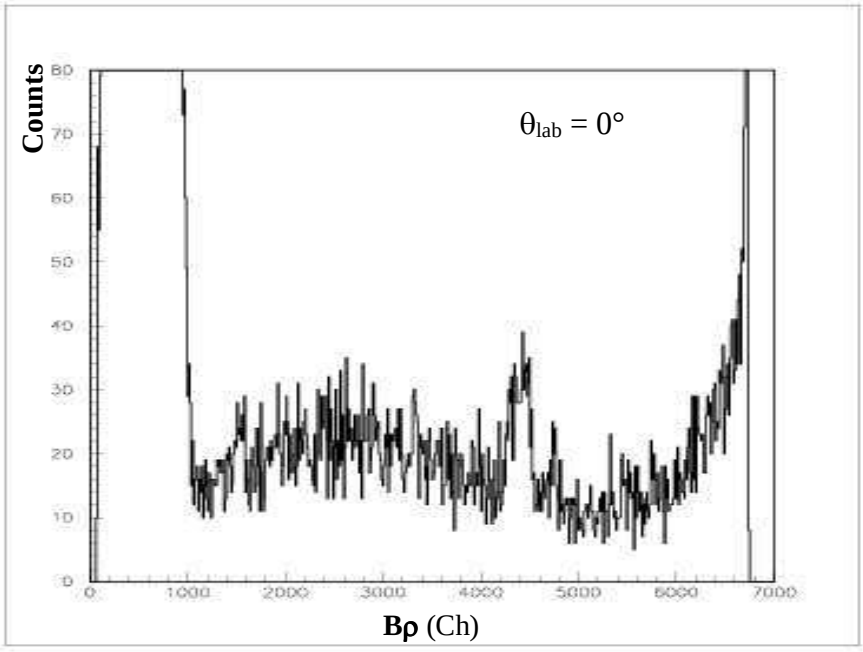

Figure 5.7. Example of raw spectrum, extracted projecting the matrix of Fig. 5.6b on the Bρ axis with the fine conditions $3 and $4. The strong peak on the left corresponds to the second kinematical solution of p(^{7}Li,^{7}Be)n.

Again the E_r-Bρ matrix is plotted with the fine condition $3 (Fig. 5.5b) and a last fine cut $4 is imposed on it to separate ^{7}Be from ^{7}Li (Fig. 5.6a). In the end, the ΔE-Bρ matrix is plotted using the two fine conditions $3 and $4 (Fig. 5.6b). In this way the ^{7}Be ions may be selected accurately. The raw spectra were extracted projecting the last matrix on the Bρ axis with the fine conditions $3 and $4 (an example with all the full statistics is shown in Fig. 5.7).

5.1.2 Excitation energy calibration

The detected ejectile ^{7}Be is particle stable only in his ground state and first excited state. Therefore the ($^{7}Li,^{7}Be$) CEX reaction may populate two bound ^{7}Be states: the $3/2^{-}$ GS and the $1/2^{-}$ first excited state at E_x = 0.429 MeV (see Section 3.3), indicated as $^{7}Be_{GS}$ and $^{7}Be_{exc}$, respectively. Thus the measured spectra show doublets of peaks for each state of the recoil nucleus ^{15}C. At low incident energy, as in the present experiment, these doublets are resolved by detecting the ^{7}Be ejectiles in a high-resolution magnetic spectrometer. In our case, indeed, the energy resolution obtained (on average ~ 250 keV) allows an easy separation of the two ^{7}Be states.

Starting from the raw position spectra (Bρ in channels), the kinetic energy calibration was done by a fit of five well identified peaks of the ^{7}Be spectrum: the four peaks associated to the transitions to the ^{15}C ground state and the known E_x = 0.74 MeV first excited and the peak associated to the second solution of the p($^{7}Li,^{7}Be$)n reaction. For a magnetic spectrometer the relation between kinetic energy T and channel Ch derives from $B\rho = p/q = \sqrt{2mT}/q$, thus the fit was done using a quadratic function: $T = p_1 + p_2\,Ch + p_3\,Ch^2$. In addition, since the ion mass is involved in the Bρ-formula, the energy-channel correspondence is dependent on the relevant ion. Therefore the focal plane calibration has to be done for mass 7.

The calibration was done separately for each spectrum measured at different angles. The peak parameters – peak centroid in channels obtained via the gaussian fit and the kinetic energy calculated by the Catkin code [Cat02] – used for doing the quadratic fit are reported in Table 5.1, concerning, e.g., the θ_{lab} = 0° spectrum. In the 0° case the fit is shown in Figure 5.8. The parabola obtained is almost linear: $T = [30.4 + 3\cdot10^{-3}\,Ch - 6\cdot10^{-9}\,Ch^2]$ MeV.

Table 5.1. Parameters of the peaks used for the 0° focal plane calibration from magnetic rigidity in channels to kinetic energy. The peak centroids (second column) were obtained through gaussian fits; the kinetic energies in the third column were calculated by the Catkin kinematical code.

Peak	Channel	T [MeV]
$^{15}C_{GS} + {}^{7}Be_{GS}$	4747	44.08
$^{15}C_{GS} + {}^{7}Be_{exc}$	4638	43.63
$^{15}C_{0.74} + {}^{7}Be_{GS}$	4441	43.30
$^{15}C_{0.74} + {}^{7}Be_{exc}$	4354	42.84
2^{nd} sol. p($^{7}Li,^{7}Be$)n	738	32.50

The next step concerns with the transformation of the ^{7}Be spectra, which actually are in kinetic energy, into ^{15}C excitation energy. The advantage of this procedure consists of the fact that the same ^{15}C excitation fall at the same channel in spectra at different angles. On the contrary, peaks associated to transitions not involving ^{15}C excitation (i.e., produced by

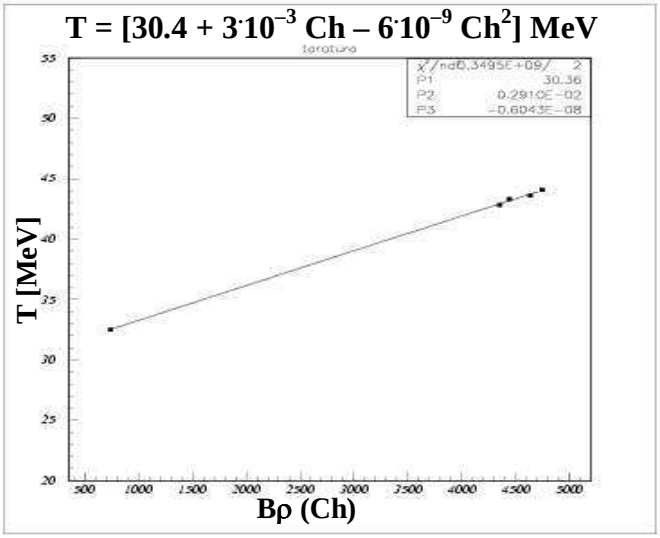

Figure 5.8. Focal plane calibration line at θ_{lab} = 0°: kinetic energy in MeV vs focal plane position in channels. The errors are contained inside the marker key.

target impurities) will have different positions at different angles, because of the different kinematics. By adding spectra at different angles, these latter transitions will produce broad structures, while the ^{15}C peaks will remain sharp. This improves the signal to background ratio and facilitates the identification of the ^{15}C peaks.

The excitation energy transformation was done using the non-relativistic kinematical formula which gives the excitation energy E_x of the residual nucleus, knowing the Q-value of the relevant two body reaction:

$$E_x = Q - T\left(1+\frac{m_3}{m_4}\right) + E_{inc}\left(1-\frac{m_1}{m_4}\right) + 2\frac{\sqrt{m_1 m_3}}{m_4}\sqrt{E_{inc}\,T}\cos\theta_{lab} \qquad (5.1)$$

where: Q = –10.633 MeV for the $^{15}N(^{7}Li,^{7}Be)^{15}C$ reaction; m_1, m_2, m_3 and m_4, are the mass of projectile, target, ejectile and residual nucleus, respectively; T and θ_{lab} are the ^{7}Be kinetic energy and outgoing angle; E_{inc} is the bombarding energy (55 MeV in this case).

The use of kinematical energy values in the calibration does not take into account the energy losses into the gas target and detector. These are compensated by doing a final recalibration, via a linear fit between the peak centroids of the excitation energy spectra and the corresponding known values [Ajz91]. A simulation with the TRIM code [Sri00] confirms that the non-linearity of the energy losses with varying of the ^{7}Be kinetic energy is negligible (a few keV). The complete calibration procedure gives an overall error on the excitation energy estimated less than 50 keV for each spectrum.

At this point the runs from equal angles may be merged in order to reduce the statistical fluctuations.

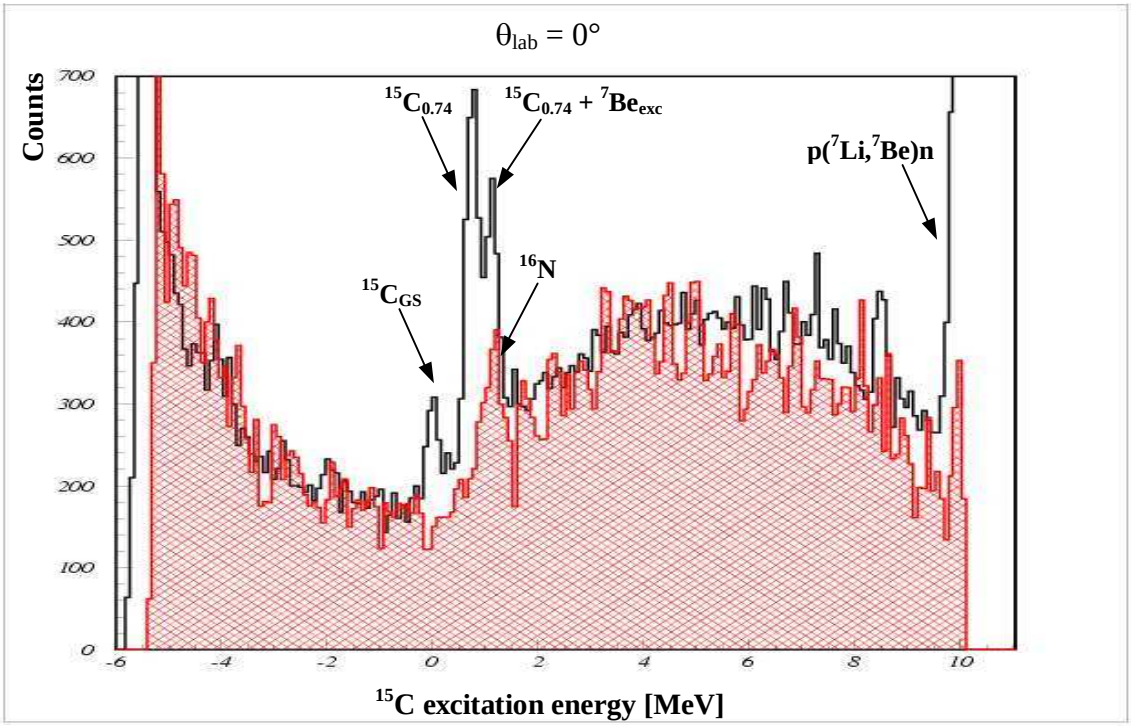

Figure 5.9. Superposition of the ^{15}C spectrum at θ_{lab} = 0° and the corresponding normalized background spectrum (shaded histogram) measured with the empty target. The main background contribution comes from the reaction on the nickel windows. A structure corresponding to the unresolved first four levels of ^{16}N is also present, probably coming from the oxidation of the windows. The strong peak on the right is from the second kinematic solution of the p(^{7}Li,^{7}Be)n reaction. ^{15}C peaks are also indicated.

5.1.3 Background subtraction

The use of the high-purity gas target was fundamental to avoid the presence of the ^{12}C contaminant. As expected (Section 4.3) the main source of background in the 0° and 2.5° spectra was the ^{58}Ni(^{7}Li,^{7}Be)^{58}Co reaction on the target windows. This background was subtracted using normalized spectra measured in runs with an empty target. The background spectra were calibrated with the same curve used for the ^{15}C spectra at the corresponding angle. However, the absence of the gas in the target causes different conditions for the ^{7}Be ions, because of course they do not lose energy in the gas. The ^{7}Be energy loss in the gas was estimated equal to 300 keV by a TRIM [Sri00] calculation, therefore the background spectra were shifted by this quantity. Then, they were normalized using the following procedure: the same portion of spectrum on the left with respect to the ^{15}C ground state was integrated both in the ^{15}C spectrum (let us call the integral value N^{15}_{C}) and in the background spectrum (N_{Back}), giving a normalization coefficient $K = N^{15}_{C} / N_{Back}$. The result of the normalization at θ_{lab} = 0° is shown in Figure 5.9. The continuous background is due to the fact that the reaction on nickel populates the ^{58}Co continuum; the fluctuations in the background spectrum are owing to the low number of counts. Finally the background spectrum, appropriately smoothed to minimize statistical fluctuations, was subtracted from the corresponding ^{15}C spectrum.

In these background spectra, a structure corresponding to the unresolved first four levels (ground and excited states at 0.12, 0.297, 0.397 MeV) of ^{16}N populated in the $^{16}O(^{7}Li,^{7}Be)^{16}N$ reaction was found. Probably, the ^{16}O impurity was present from oxidation of the nickel windows. At forward angles ($\theta_{lab} \leq 7.2°$) there is a strong contribution from the $p(^{7}Li,^{7}Be)n$ reaction. Its subtraction is not effective because, since the high cross section of the ($^{7}Li,^{7}Be$) reaction on protons, it introduces large errors. Fortunately the peak corresponding to the hydrogen impurity is separated from most of the ^{15}C peaks.

A continuous background is present in the spectra from three-body reactions. For the spectra at $\theta_{lab} = 8°$, 10° and 14° the background associated to $^{15}N(^{7}Li,n^{7}Be)^{14}C$ was modelled assuming a non-resonant 3-body phase space in the exit channel [Ohl65]. This assumption is justified from the kinematical selectivity of the ($^{7}Li,^{7}Be$) reaction and because the most important intermediate routes of the two-step process – populating ^{8}Be – are hindered from the weak single particle components of ^{8}Be states at low excitation energy [Etc88]. The phase space function $\rho_{lab}(T)\, dT\, d\Omega$ was calculated analytically in the laboratory frame on the basis of the formulae of ref. [Ohl65]. Then a variable transformation was applied in order to obtain a function of the ^{15}C excitation energy. Finally, a scaling factor was obtained empirically, by normalizing the phase space function to fit the high excitation energy region of each spectrum.

5.2 ^{15}C final spectra

A fit procedure based on the MINUIT [Min92] routines was adopted in order to achieve a correct integration of the ^{15}C peaks. The precision obtainable using a simple gaussian function to fit the peak is limited by the presence of overlapping structures.

5.2.1 The fit procedure

The integration of the ^{15}C peaks was based on a minimization procedure by the MINUIT routines, which allows a use of multigaussian functions. All the fits were done on spectra where the normalized background was subtracted. The fitted gaussian functions were then added to this background and the free parameters (centroid, standard deviation and height) were varied in order to fit the shapes of the peaks. As a general rule the centroids and widths of known transitions were forced to vary in narrow ranges around the values accepted in literature and, at the end of the procedure, they were strongly constrained, allowing only the heights to be free parameters.

To improve the fit, the doublet related to $^{7}Be_{GS}$ and $^{7}Be_{exc}$ was contemporary fitted, generating for each ^{15}C peak a second gaussian having the centroid shifted of 0.43MeV with respect to the centroid of the first one. For the peak associated to $^{7}Be_{exc}$, the Döppler broadening due to the in-flight decay $^{7}Be_{exc} \rightarrow {}^{7}Be_{GS} + \gamma$ has to be taken into account. The maximum spread from the recoil-broadening is given by the base width

$$\delta E_{\gamma} = 2\beta E_{\gamma} \qquad (5.2)$$

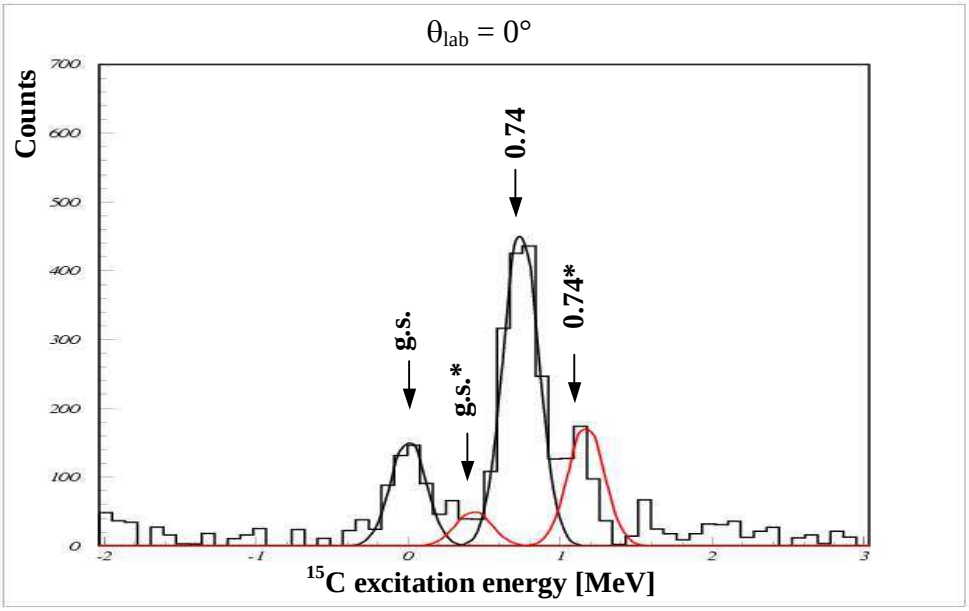

Figure 5.10. Example of the fit procedure. The fit involves two doublets at the same time, precisely: two ^{15}C peaks (the ground and 0.74 MeV state, fitted by the black gaussians) and the correlated partners, associated to ^{7}Be excitation (indicated by an asterisk and fitted using red gaussians). The latter are fitted by strictly adding 0.429 MeV to the centroids obtained from the fit of the former. The calculated Döppler broadening is added to the width (see text for more details).

where $\beta = v/c$ is the average ^{7}Be velocity and $E_\gamma = 0.429$ MeV. Assuming for simplicity an isotropic angular distribution of the emitted γ-rays [Win97, Win01]:

$$\Gamma_{Döppler} = 2/3\ \delta E_\gamma \qquad \Rightarrow \qquad \sigma_{Döppler} = (2/3\ \delta E_\gamma)/2.35 \tag{5.3}$$

Thus the width of the second gaussian is fixed to:

$$\sigma_{Second} = [\sigma_{First}^{\ 2} + \sigma_{Döppler}^{\ 2}]^{1/2} \tag{5.4}$$

where σ_{First} represents the width of the first gaussian. A full treatment of the Döppler broadening effect when the angular distribution of γ-emission is known is given in ref. [Boh78]. The contemporary fit of the two peaks strongly reduced the uncertainties on the procedure itself. For close peaks which are not completely resolved, as are sometimes the ^{15}C ground and first excited state, the fit involves four peaks at the same time: the two ^{15}C peaks and the respective doublet partners. An example of this is shown in Figure 5.10.

5.2.2 The ^{15}C spectra

The ^{15}C experimental spectra were obtained at $\theta_{lab} = 0°$, 2.5°, 8°, 10°, 14°. In Figure 5.11 the ^{15}C spectra measured in the two limit cases $\theta_{lab} = 0°$ and 14° are shown; the small inset shows a detail of the 8° spectrum (see Section 5.2.3).

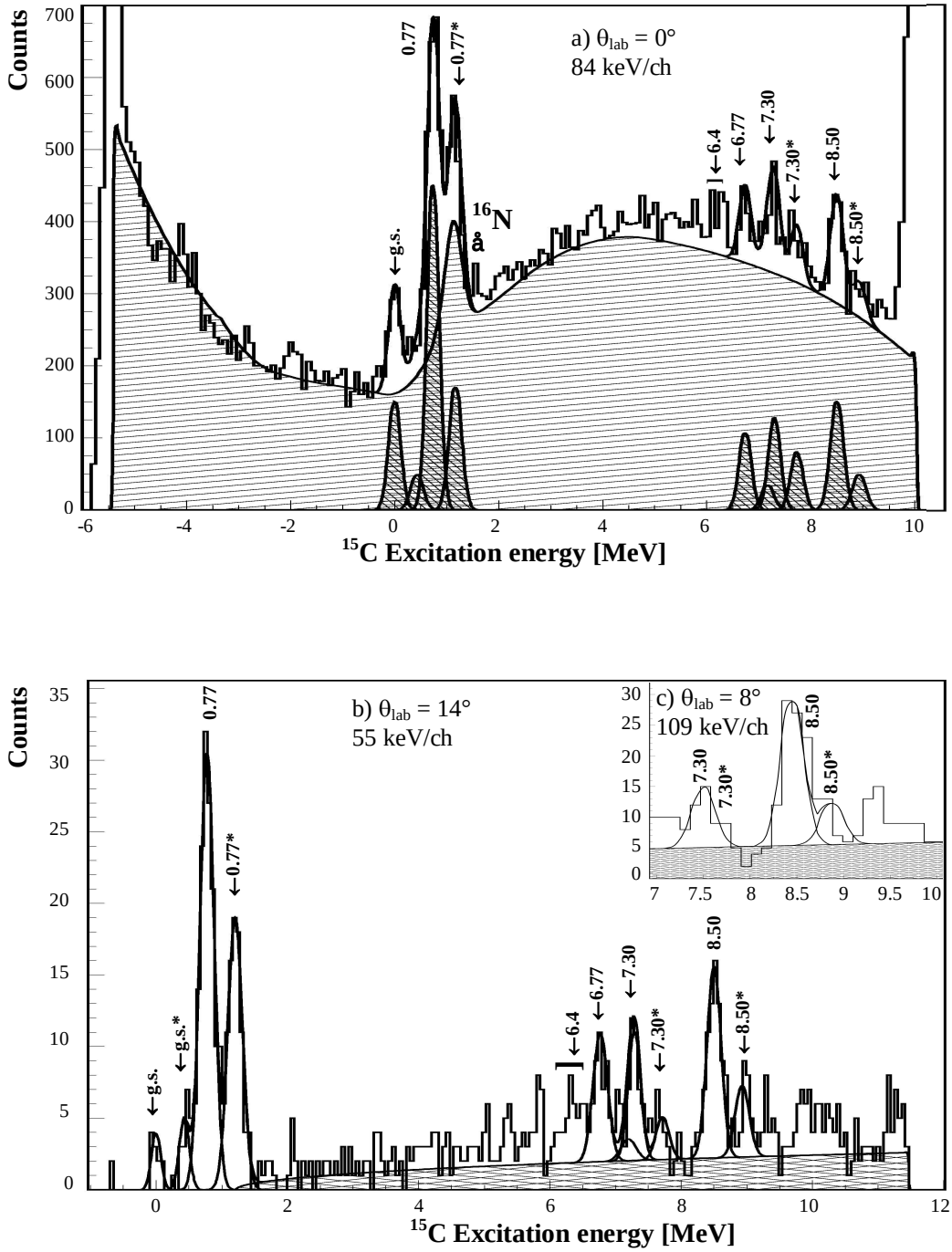

Figure 5.11. Excitation energy spectra for the $^{15}N(^{7}Li,^{7}Be)^{15}C$ reaction. Peaks marked with an asterisk are associated to the excitation of ^{7}Be at 0.429 MeV. a) Spectrum measured at 0°. The shaded histogram represents a smooth of the background measured with the empty target. The continuous line is the sum of the background and the fitted peaks (dark gaussians). b) Spectrum taken at 14°. The shaded histogram represents the non-resonant $^{15}N(^{7}Li,n^{7}Be)^{14}C$ 3-body phase space. The continuous line is the sum of the latter with the fitted gaussians. c) Detail of the spectrum at 8° (see Section 5.2.3).

Table 5.2. States populated in the $^{15}N(^{7}Li,^{7}Be)^{15}C$ reaction at 55 MeV in the present experiment. Values from refs. a)=[Ajz91], c)=[Gar74], d)=[Gos75] are given for comparison; b)=present work.

E_x [MeV]	Γ [keV]	E_x [MeV] [(a)]	J^π	Structure [(d)]
0.00±0.03		GS	$1/2^+$ [(a,b]	$^{14}C(0^+)\otimes(s_{1/2})$ S=0.88
0.77±0.03		0.7400±0.0015	$5/2^+$ [(a,b]	$^{14}C(0^+)\otimes(d_{5/2})$ S=0.69
6.77±0.06	≤160	6.841±0.004	(11/2,13/2)[(c,d]	
7.30±0.06	≤ 70	7.352±0.006	(9/2,11/2) [(c	
8.50±0.06	≤140	8.470±0.015 8.559±0.015	(9/2→13/2) [(c (7/2→13/2) [(c	

The observed energy resolution $\Gamma_{int} \cong 250$ keV was obtained by evaluating at each angle the best width of the fits of the two bound states. This resolution is poorer than in ref. [Cap01], where the same experimental devices were used, because in this case the ions originate in a long angle-dependant segment (the gas target), thus they are generated at different incident energies and have different energy losses in the gas, besides they are detected with $\Delta\theta \cong \pm 1°$ giving kinematical broadening, which is not completely compensated by the spectrometer. However, the resolution obtained is enough to separate the ^{7}Be states.

In the present experiment, the ^{15}C ground and excited states at E_x = 0.77, 6.77, 7.30, 8.50 MeV were observed, as shown in Fig. 5.11. In the spectra a structure at E_x = 6.4 MeV is also evident that could include contributions from several closely spaced ^{15}C levels (see ref. [Ajz91] for more details). In Table 5.2 the values of the centroids and the upper limits of the natural widths of the ^{15}C resonances populated, obtained from gaussian fits of the peaks, are presented. For each angle, the natural width Γ was calculated as:

$$\Gamma = [\Gamma_{exp}^{\ 2} - \Gamma_{int}^{\ 2} - \Gamma_{Döppler}^{\ 2}]^{1/2} \qquad (5.5)$$

where Γ_{exp} represents the fitted width of the peak, Γ_{int} is the energy resolution and $\Gamma_{Döppler}$, given by formula (5.3), accounts for the broadening effect from the in-flight γ-ray emission for transitions associated to $^{7}Be_{exc}$. For each state, the centroid and width were obtained from the mean value and standard deviation for the independent evaluations made at different angles. The error introduced by the fit procedure was negligible. The uncertainties on the excitation energies are dominated by systematic errors, mainly associated to the calibration procedure. In particular a systematic error of ± 30 keV for the peaks corresponding to bound ^{15}C states and ± 60 keV for that in the neutron continuum was assumed. The excitation energies deduced are in agreement with those obtained in the previous experiment [Noc03].

Besides the two ^{15}C bound states, the ground and the first excited (which is the most prominent), three narrow resonances (E_x = 6.77, 7.30, 8.50 MeV) beyond the neutron emission threshold are evident. The observation of narrow states in the continuum confirms our expectations about the ^{15}C nucleus, based on the arguments discussed in Chapter 2. As we

will see in Chapter 7, these states may be interpreted as BSEC excitations (see Sect. 2.2), described in terms of quasi-bound core-excited configurations. The ^{15}C spectra show a parallelism with the ^{11}Be ones ([Cap01], also shown in Sect. 2.2): in both nuclei the ($^{7}Li,^{7}Be$) reaction populates two weakly-bound states (g.s. and first excited), between which there is inversion of the neutron orbitals with respect to the single particle shell model ones, and various narrow resonances in the continuum. The ($^{7}Li,^{7}Be$) reaction is confirmed to be very useful for spectroscopic studies in exotic nuclei.

The ^{15}C structure will be analyzed in detail in the next Chapters, where microscopic calculations based on different theoretical models succeed to explain the full ^{15}C spectrum. The experimental data on the ^{15}C spectroscopy have been published in refs. [Orr03, Cap04].

5.2.3 The interference effect

The 8.5 MeV state was observed also in the previous experiment [Noc03]. Here, a new important feature, not observed before because of the strong ^{12}B background, is the suppression of counts immediately before the 8.5 MeV peak (see Fig. 5.11 and the zoom in the inset). This "hole" is clearly seen in the 0°, 8°, 14° spectra (all the spectra in which the peak is not obscured by background), moving, as expected from the kinematic, to different channels, i.e., to different positions on the spectrometer's focal plane proving that it is not caused by an anomalous behaviour of the focal plane detector. In analogy with the (p,p') inelastic scattering on nuclei, where isolated resonances arising from the coupling of a single particle continuum to a BSEC were found [Bau77], we suggest that this could be an interference between the non-resonant 3-body phase space and the 8.5 MeV BSEC.

In general, the interference effects gives rise to typically asymmetric peaks in the spectra, where the resonant part has a Breit-Wigner form but the total line shape has a more complicated energy dependence [Bau77]. Here we have used a simple model of a gaussian function and the non resonant 3-body phase space of ref. [Ohl65] to fit the 8.5 MeV peak. However, this is incorrect because the peak is asymmetric and the 3-body continuum is deformed by the interference. In order to check the evolution of the line shape as a function of the scattering angle, a qualitative parameter defined as the ratio between the areas of the hole and the peak can be used. We found that this ratio varies with the scattering angle, being 12 ± 2 % at 0°, 7 ± 3 % at 8° and 3 ± 2 % at 14°. This result strengthens our interference hypothesis, because a dependence from the angle is expected in such phenomena.

In Chapter 8 the resonance line shape will be investigated in detail by theoretical calculations, similar to those developed in ref. [Bau77] to describe the interference effect in the spectra of the (p,p') inelastic scattering.

5.3 Cross section and angular distributions

Given a certain nuclear transition, the differential cross section is defined as:

$$\frac{d\sigma}{d\Omega}(\theta) \equiv \frac{N(\theta)}{N_{INC}\, N_{TAR}\, \Delta\Omega\, K} = \frac{N(\theta)}{N_{INC}\, N_{TAR}^{Vol}\, (g(\theta)/\sin\theta)\, K} \qquad (5.6)$$

where $N(\theta)$ represents the number of counts measured at the angle θ for the relevant transition, N_{INC} is the number of incident particles, N_{TAR} is the number of target nuclei per unit surface, $\Delta\Omega$ is the solid angle and K is the dead time coefficient. The last equality in formula (5.6) allows an expression of the cross section in terms of the geometrical factor $g(\theta)$ (see Section 4.1.1). The direct measurements of these parameters usually are not very accurate, giving an error ~ ± 10 % on the cross section value in absolute units (μb/sr). The use of a monitor detector placed at a fixed position θ_M allows a comparison of data acquired in different experimental conditions, as, e.g., measurements at different angles in order to determinate the angular distributions. Let us consider the measurements at two different angles:

$$\frac{d\sigma}{d\Omega}(\theta_1) = \frac{N(\theta_1)}{N_{INC1}\, N_{TAR1}\, \Delta\Omega_1\, K_1} \qquad \frac{d\sigma}{d\Omega}(\theta_2) = \frac{N(\theta_2)}{N_{INC2}\, N_{TAR2}\, \Delta\Omega_2\, K_2} \tag{5.7}$$

The direct comparison between the two cross sections is meaningless because their value depend on the parameters in the denominator. The independent measurements of a monitor

$$\frac{d\sigma}{d\Omega}(\theta_M) = \frac{N_M(\theta_1)}{N_{INC1}\, N_{TAR1}\, \Delta\Omega_M\, K_1} \qquad \frac{d\sigma}{d\Omega}(\theta_M) = \frac{N_M(\theta_2)}{N_{INC2}\, N_{TAR2}\, \Delta\Omega_M\, K_2} \tag{5.8}$$

obtained during the same runs, allow to measure the ratio between the two differential cross sections (5.7) without the need to know the on denominator quantities. In fact, for a given transition, the monitor cross section is the same in all the runs and the monitor solid angle is fixed. Thus, combining the (5.7) and (5.8):

$$\frac{d\sigma}{d\Omega}(\theta_1) = \frac{N(\theta_1)}{\Delta\Omega_1}\frac{\Delta\Omega_M}{N_M(\theta_1)}\frac{d\sigma}{d\Omega}(\theta_M) \qquad \frac{d\sigma}{d\Omega}(\theta_2) = \frac{N(\theta_2)}{\Delta\Omega_2}\frac{\Delta\Omega_M}{N_M(\theta_2)}\frac{d\sigma}{d\Omega}(\theta_M) \tag{5.9}$$

and finally we have:

$$\frac{\frac{d\sigma}{d\Omega}(\theta_1)}{\frac{d\sigma}{d\Omega}(\theta_2)} = \frac{N(\theta_1)}{\Delta\Omega_1\, N_M(\theta_1)}\frac{\Delta\Omega_2\, N_M(\theta_2)}{N(\theta_2)} \tag{5.10}$$

where the only necessary measurements are the integrated counts in the two runs by the spectrometer and monitor, together with the knowledge of the Split-Pole solid angles. From (5.10) the cross sections at different angles are obtained in arbitrary unit (a.u.). The next step is to transform the angular distributions obtained into the center of mass (CM) reference system. Then the absolute normalization of the cross section (μb/sr) is calculated.

Unfortunately, for the runs at θ_{lab} = 8°, 10°, 14° there are no monitor measurements due to damage to the ΔE detector, thus the monitor technique cannot be applied and the cross section has to be calculated directly in absolute units. In particular, for each peak the integrated counts $N(\theta)$ were obtained by integration on the best-fit gaussian function. Besides

the statistic error, the error due to the background subtraction was taken into account at 0° and 2.5°. The number of target nuclei/cm^3 N_{TAR}^{Vol} was calculated using the equation of state for an ideal gas, applicable given the low pressure values of the gas in the target. This gave a precision on the N_{TAR}^{Vol} value (~ 1 %) better then the one obtainable using a solid target. The solid angle covered was calculated in terms of the geometrical factor g(θ) following the Silverstein method (see 4.1.1); the high precision on the measurements of the distances involved in the calculation gave a negligible error on the g(θ) value. The statistic error on the coefficient K is found to be negligible also. The main source of error (~ 10 %) came from the determination of $N_{INC} = n_{beam}\, t$ (beam integration), because of uncertainties in the Faraday cup efficiency. The error on the cross section is due to the combined effect of the different error sources, according to the propagation of errors law:

$$\frac{\Delta\sigma}{\sigma} = \sqrt{\left(\frac{\Delta N(\theta)}{N(\theta)}\right)^2 + \left(\frac{\Delta N_{INC}}{N_{INC}}\right)^2 + \left(\frac{\Delta N_{TAR}}{N_{TAR}}\right)^2} \qquad (5.11)$$

As an example, the error on the cross section associated to the transition to the ^{15}C first excited state is 22 % at 0°, 19 % at 2.5°, 21 % at 10° and 13 % at 14°. The coordinate transformation from the θ_{lab} to the θ_{CM} reference system was obtained multiplying the normalized counts N(θ) by the Jacobian determinant of the transformation, calculated at each angle and energy of interest. The error on the θ_{CM} angles was calculated applying the same coordinate transformation on the total angular range accepted by the spectrometer.

The angular distributions for the cross sections associated to the observed ^{15}C states are presented in Figure 5.12a and 5.12b for transition involving $^{7}Be_{GS}$ and $^{7}Be_{exc}$, respectively. In general they are forward peaked and show no strongly oscillatory patterns, as typical for the CEX reactions involving light nuclei [Coo84, Etc88]. This behaviour is due both to the various angular momenta transferred in the reaction and to the superposition between the one-step process (dominant at forward angles) and the flat two-step contribution at larger angles. Unfortunately we have only few points, however a good agreement with the point of the previous experiment (the ^{15}C first excited state at 10°) is found: the measured cross section values are 110 ± 24 μb/sr (present) and 90 ± 27 μb/sr [Noc03].

In Chapter 6 theoretical angular distributions of the $^{15}N(^{7}Li,^{7}Be)^{15}C$ reaction are obtained for the two ^{15}C bound states by dynamical DWBA calculations, which take into account the effects of the CEX transition operator and the optical potential. The experimental angular distributions were published in ref. [Orr03].

5.4 G factor distributions

The angular distributions for the factor $G = \sigma(^{7}Be_{exc}) / [\sigma(^{7}Be_{GS}) + \sigma(^{7}Be_{exc})]$, defined in Section 3.4.1, were obtained for each ^{15}C state by dividing the cross sections associated to $^{7}Be_{GS}$ and $^{7}Be_{exc}$. By definition, the error on the G value arises from the error on the integrated counts only. Concerning the error on the center of mass angle, the small shift because of the different coordinate transformation was neglected compared to the error estimated in the angular distributions.

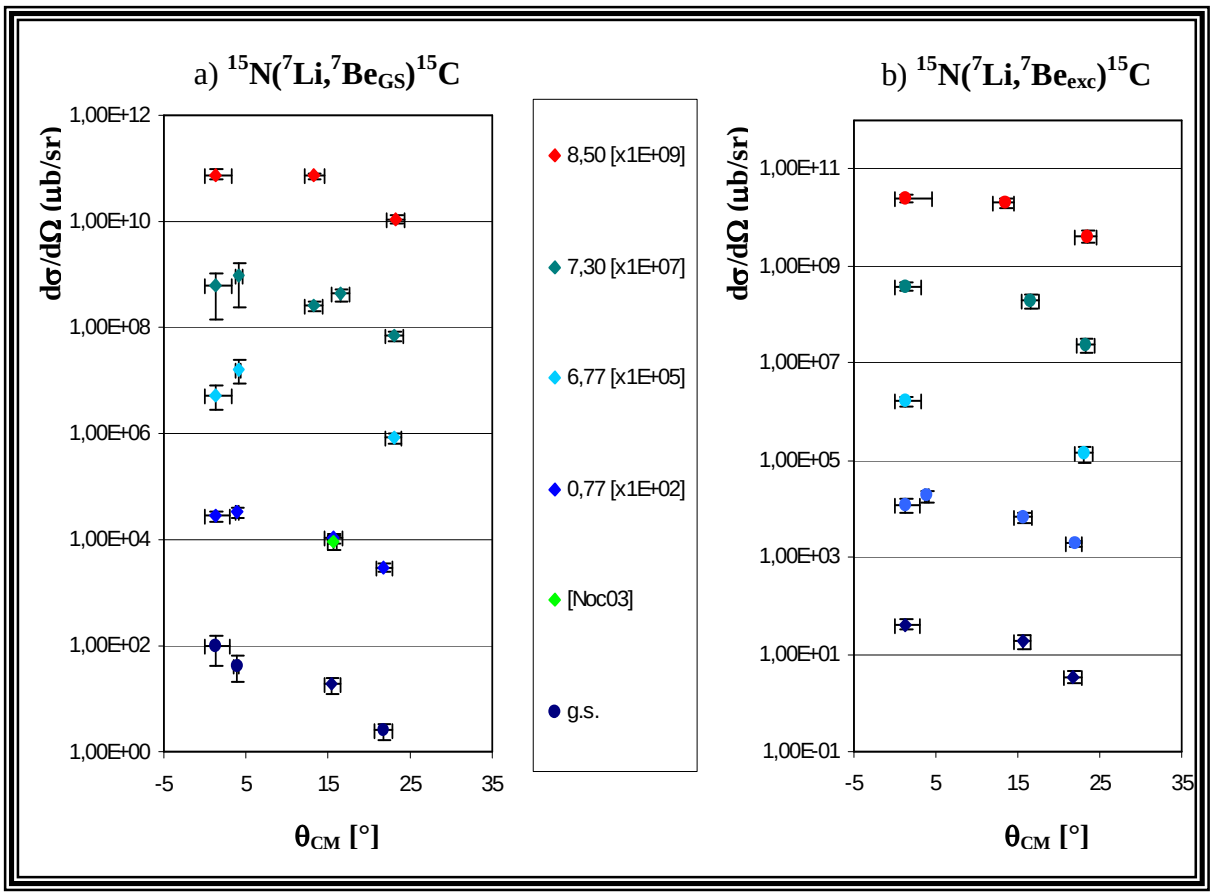

Figure 5.12. Angular distributions for the cross sections associated to the transitions to the ^{15}C ground and the excited states at E_x = 0.77, 6.77, 7.30, 8.50 MeV. a) Transition involving the ^{7}Be ground state. For the 0.77 MeV state a good agreement with the value measured in a previous experiment is obtained. b) Transition involving the ^{7}Be first excited state.

Table 5.3. Values of the G factor measured for the $^{15}N(^{7}Li,^{7}Be)^{15}C$ reaction at θ_{lab} = 0°.

^{15}C state	g.s.	0.77	6.77	7.30	8.50
G	0.30±0.05	0.31±0.02	0.24±0.13	0.39±0.08	0.25±0.08

In Table 5.3 the G-ratios measured at θ_{lab} = 0° are presented, while in Figure 5.13 the extracted angular distributions for G are showed. The values of G at 0° indicate the prominence of nucleonic spin transfer dynamics. The CEX-QRPA calculations of Chapter 6 will give theoretical distributions of G to compare with the experimental ones for the two ^{15}C bound states.

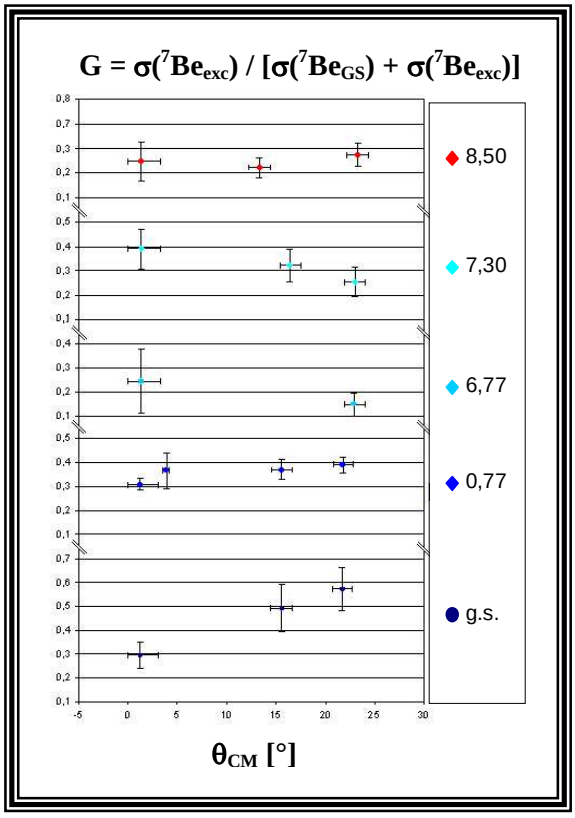

Figure 5.13. Angular distributions for the G-ratios.

5.5 Summary

The $^{15}N(^{7}Li,^{7}Be)^{15}C$ charge exchange reaction at 55 MeV incident energy was studied at forward angles in order to explore the ^{15}C excitation energy spectrum. This reaction is confirmed to be extremely useful for spectroscopic studies in exotic nuclei. The gas target was a crucial factor to overcome the previous difficulties with the solid melamine target. The ^{15}C ground and the states at E_x = 0.77, 6.77, 7.30, 8.50 MeV were populated. The energy resolution (~250 keV) allowed the identification of these transitions each for ^{7}Be ground and first excited state at E_x = 0.429 MeV.

The ^{15}C structure will be analyzed in detail in the following Chapters by microscopic calculations. Besides the remarkable observation of three narrow resonances above the particle threshold, another new and important observation is represented by the interference effect between the 8.5 MeV state and the underlying non-resonant 3-body phase space, which will be investigated in Chapter 8.

The angular distributions were measured for the observed transition together with the angular distributions of the G factor, which shows a general trend to spin transfer dynamics. For the two ^{15}C bound states, in Chapter 6 the angular distributions of the cross section and G factor will be compared with the theoretical ones calculated by one-step dynamical calculations.

CHAPTER 6

THE $^{15}N(^{7}Li,^{7}Be)^{15}C$ REACTION: THEORETICAL ANALYSIS IN THE CEX-QRPA APPROACH

The theoretical analysis of the $^{15}N(^{7}Li,^{7}Be)^{15}C$ CEX reaction is discussed in detail in the present Chapter. An approach based on the Charge EXchange Quasiparticle Random Phase Approximation (CEX-QRPA) theoretical framework [Row70, Bre88, Len88] was employed to describe the structure of the observed ^{15}C strength distribution and the angular distributions of the $^{15}N(^{7}Li,^{7}Be)^{15}C$ reaction. Spectroscopic information is derived assuming a simple one-step reaction mechanism mediated by the isovector component of the effective NN-interaction $V^{(\tau)}$, which includes the tensor contribution (see Section 3.1.1). One-step microscopic calculations were performed, following the CEX-QRPA theory such as developed in refs. [Bak97, Cap04b] to describe the inelastic scattering (p,p') and (d,d') and the ($^{7}Li,^{7}Be$) CEX reaction on ^{11}B, respectively. This approach takes into account in a realistic way the state-dependent pairing field felt by the quasiparticles and an average treatment of the 2p-2h configurations, normally not considered neither in the QRPA problem nor in CEX dynamics.

The ^{15}C bound states are described in terms of correlated 1p-1h excitations with respect to the ground state of the parent nucleus ^{15}N. The results of nuclear structure calculations are directly inserted into the scattering equations to calculate the cross sections. Consistency between structure and reaction mechanism calculations is achieved through the use of the same effective NN-interaction in every step of calculations. In fact, following the semi-phenomenological approach of refs. [Bak97, Hof98], both the static mean and pairing fields derive from the residual interaction of Hofmann and Lenske [Hof98], which is also used in the QRPA and DWBA calculations. This approach, already applied to the ^{11}Be nucleus [Cap01, Cap04b], is confirmed to be well suited for light neutron-rich nuclei. In fact it succeeds in describing both ^{11}Be and ^{15}C without change of the basic parameters.

The Chapter is organized as follows: Sections 6.1 is devoted to the QRPA formalism. Sect. 6.2 gives the details of the structure calculations, with the determination of the response functions based on the RPA-Green's function method [Bak97]. The residual NN-interaction [Hof98] is described in Sect. 6.3. The results of the QRPA calculations are shown in Sect. 6.4. The dynamical DWBA calculations are described in Sect. 6.5 and their results are given in Sect. 6.6. The results of Sect. 6.4 and 6.6 are compared with the experimental data of Chapter

5. Important information is obtained on both the nuclear structure and dynamics involved in the reaction. Finally, our conclusions are stated in Sect. 6.7.

6.1 The QRPA formalism

Independent single particle models, such as the shell or Hartree-Fock (HF) ones, describe the low-energy excited states of the even-even nuclei as 1p-1h or two-quasiparticle (2-QP) excitations. The Random Phase Approximation (RPA) theory [Rin80], introducing correlations between particles and holes, constitutes the next step with respect to the mean field approaches. In this theory, a more careful description of the nuclear states is achieved in terms of correlated 1p-1h excitations, a description which also stays valid for the highly excited states. The basic idea is that a strong attractive residual interaction between particle-hole pairs will strongly lower the energy of a highly correlated state, while a repulsive interaction will have the opposite effect. This energy shift constitutes the real part of a complex quantity, called self-energy, and depends on the strength of the residual interaction and correlations. The imaginary part of the self-energy accounts for the possible broadening of the state due to the energy shift, since the decay width may change. This model practically includes weak perturbations of the mean field in the continuum.

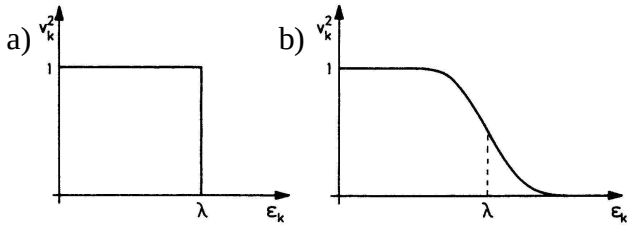

Figure 6.1. Scheme of the occupation probabilities for a) well-bound and b) weakly-bound nuclei.

The weak binding of the valence particles and the coupling with the continuum are of crucial importance for a correct description of a drip-line nucleus, such as ^{15}C. In fact (as schematized in Fig. 6.1), while for a well-bound nucleus all the states until the Fermi energy λ are occupied, for weakly-bound nuclei the Fermi surface has a significant diffuseness. This softness corresponds to an occupation probability which, for $\varepsilon_k > \lambda$, increases for the particle states and decreases for the hole ones. For these systems the equations of motion become complicated because of a more complex formalism which distinguishes between particles and holes both above and under the Fermi surface. The Quasiparticle RPA (QRPA) theory allows a treatment of the weakly-bound systems in an equivalent way. As we will see, by applying the linear Bogoliubov-Valatin transformation from the single particle to quasiparticle states, it is possible to explain the states of the weakly-bound nuclei as correlated 2-QP excitations, including at the same time both particle and hole excitations. Moreover, the QRPA theory, together with an appropriate residual interaction, allows the taking into account of the pairing correlations, which play a fundamental role in drip-line nuclei.

An RPA problem is defined by specifying the ground state system (or vacuum state) and the residual interaction. In the RPA model the Hilbert space of the excited states is truncated to include only 1p-1h excitations on the (correlated) ground state. The latter may be

described by the following Hamiltonian:

$$H_A = T + V = T + U + (V - U) = H_0 + V_{res} \tag{6.1}$$

where A is the nucleus mass number, T represents the kinetic energy and V the NN-interaction. A static mean field potential U is introduced in order to separate H in two parts: the residual particle-hole interaction $V_{res} = (V - U)$ and the mean field Hamiltonian H_0:

$$H_0 = T + U = \sum_{i=1}^{A}\left(-\frac{\hbar^2}{2m_i}\nabla_i^2 + U(r_i) \right) \tag{6.2}$$

The vacuum state $^{15}N_{GS}$ is defined as:

$$\left|0\right\rangle = \left|N_0, Z_0; GS\right\rangle \equiv \left|^{14}C_{GS} + p\right\rangle \tag{6.3}$$

where the levels of a single proton in the $^{14}C_{GS}$ are calculated assuming the proton at infinite distance (see Section 6.2.4). Starting from the single particle fermion operators $a^{+}_{jm}(p,n)$ and $\tilde{a}_{jm}(p,n) = (-1)^{j+m}\, a_{j-m}(p,n)$, the one-quasiparticle annihilation α_{jm} and creation α^{+}_{jm} operators are obtained through the linear Bogoliubov-Valatin transformation:

$$\alpha^{+}_{jm} = u_j a^{+}_{jm} - (-1)^{j+m} v_j a_{j-m} \tag{6.4a}$$

$$\alpha_{jm} = u_j a_{jm} - (-1)^{j+m} v_j a^{+}_{j-m} \tag{6.4b}$$

where u_j and v_j are the emptiness and occupation amplitudes, respectively, for the orbital with total angular momentum j, with $u_j^2 + v_j^2 = 1$. These amplitudes are determined starting from the pairing correlations in a state-dependent pairing field (see Section 6.2.5). The effects of the pairing field will be the first correlations introduced to the ground state eq. (6.3).

The 2-QP excitation operators are then constructed in the second quantisation formalism in terms of the 1-QP α_{jm} and α^{+}_{jm} operators:

$$Q^{+}_{JM}(j_n, j_p) = \sum_{m_n, m_p}\left\langle j_n m_n j_p m_p \middle| JM\right\rangle \alpha^{+}_{j_n m_n}\, \alpha^{+}_{j_p m_p} \tag{6.5}$$

A similar formula gives the 2-QP destruction operators Q_{JM}. In eq. (6.5) the α^{+}_{jm} operators describe the creation of a quasi-neutron and a quasi-proton with angular momentum j_n and j_p and magnetic quantum number m_n and m_p, respectively. Since the Q_{JM} and Q^{+}_{JM} operators describe charge exchange transitions in which a proton is transformed into a neutron or vice versa, they depends on the Clebsch-Gordan coefficients giving the angular momentum coupling, which have to satisfy the conditions $j_n + j_p = J$ and $m_n + m_p = M$. The CEX-QRPA states are obtained by applying the operator of eq. (6.5) to the vacuum eq. (6.3):

$$\left|^{15}C, JM\right\rangle = Q^{+}_{JM}(j_n, j_p)\left|^{14}C_{GS} + p\right\rangle \tag{6.6}$$

The complete operator for the CEX excitations ω^{+}_{JM} is finally obtained in the QRPA formalism considering the superposition of the Q^{+}_{JM} operator and its time reversal:

$$\omega^{+}_{JM} \equiv \sum_{j_n j_p} \left[X^{J}_{j_n j_p} Q^{+}_{JM}(j_n, j_p) - Y^{J}_{j_n j_p} (-1)^{J-M} Q_{J-M}(j_n, j_p) \right] \tag{6.7}$$

In an analogue way the destruction CEX operator ω_{JM} is constructed. The quantities X^J and Y^J represent the QRPA amplitudes for direct and time reversed exchange of such quasiparticles. These amplitudes are simply related to the emptiness u_j and occupation v_j ones and thus will be calculated from them, i.e., from the state-dependent pairing field of Sect. 6.2.5.

In the quasiparticle representation there is isospin mixing: the τ^{+}- and τ^{-}-type excitations (were τ indicates the isospin operator) are mixed as much as the softness of the Fermi surfaces increases. Therefore the action of the CEX operator ω^{+}_{JM} on the vacuum state eq. (6.3) leads to:

$$\omega^{+}_{JM} \left| {}^{14}C_{g.s.} + p \right\rangle = \left| JM;\ N_0 \pm 1,\ Z_0 \mp 1 \right\rangle = \left| JM;\ {}^{15}C,\ {}^{15}O \right\rangle \tag{6.8}$$

However, projecting on the τ^{+} subspace it is always possible to separate the two contributions in the matrix elements.

The CEX operator ω^{+}_{JM} takes into account only the 2-QP excitations. In reality, also higher order configurations (4-QP and so on) contribute to the eigenstates of the ^{15}C nucleus. Separating all these contributions from the 2-QP component and assembling them in the operator η^{+}_{JM} (orthogonal to ω^{+}_{JM}), the state operator which generates the true eigenstates is written as:

$$\Omega^{+}_{JM}(\alpha) = \sum_{a} z^{J}_{a}(E_\alpha)\, \omega^{+}_{JM}(a) + \eta^{+}_{JM}(\alpha) \tag{6.9}$$

where the summation represents the mixing of the 2-QP configurations. The spectroscopic amplitudes $z^{J}_{a}(E_\alpha)$ determine the probability to find the model states $\omega^{+}_{JM}(a)$ with eigenvalue E_a distributed over the eigenstates $\Omega^{+}_{JM}(a)$, which in general have excitation energy $E_\alpha \neq E_a$.

6.2 The CEX-QRPA structure calculations

The QRPA equations may be found in a similar way as in the RPA theory [Rin80]. They have identical form to the RPA ones but with more sophisticated A and B matrices [Rin80]. Nevertheless, the conventional RPA approach, namely to solve the eigenvalue problem by matrix diagonalization [Rin80], becomes impracticable for huge configuration spaces. When it is not required to determine with high precision features of individual states, as in the present case, a method that allows calculating reliably the energy averaged response functions is the RPA-Green's function method [Fet71].

In the approach introduced by Lenske [Len87] to the RPA-Green's function method, the RPA problem is reduced to the solution of a generalized dispersion equation of matrix form with dimension independent of size of the configuration space and determined by the number

of spin-isospin interaction channels and the dimensionality of the basis. The response functions for the one-body operators are directly calculated by solving the Dyson equation (see Section 6.2.2), without solving explicitly the RPA eigenvalue problem. The particle-hole RPA phonon vertex can be represented in separable form if the RPA transition densities are expanded into an appropriate basis. An important advantage of this method is that arbitrary particle-hole interaction of finite range can be used [Len87].

6.2.1 The nuclear response function

Starting from this Section we follow the approach of ref. [Bak97], based on the RPA-Green's function method as in ref. [Len87], to calculate the response functions via solving the Dyson equation. The transition densities for the target transitions $^{15}N \rightarrow {}^{15}C$ are then obtained. The treatment of ref. [Bak97], based on a mean field approach like the usual RPA theory, includes an average contributions of the 4-QP excitations (see Section 6.2.3) and a state-dependent pairing field (Sect. 6.2.5), usually not considered.

A practical definition of "response" of a nucleus [Bak97] is essentially the measured differential cross section for inelastic scattering normalized by the free scattering one. Assuming that all effects not directly related to intrinsic nuclear structure are negligible or have been removed from measured cross section: $\sigma^{PT} = F\,\sigma^{PN}$, where σ^{PT} is the differential cross section for the reaction between projectile P and target T, while σ^{PN} for the corresponding process in free projectile-nucleon (PN) scattering. The so defined quantity F is closely related to the nuclear response. Since F effectively represents a sum over nuclear responses in different spin-isospin channels (weighted depending on the probe), it has no meaning until the operator is specified. In this way the nuclear response depends only on nuclear structure and, once the particular channel is specified also, it is probe independent. This means that the nuclear response in a specific channel $(S,T) \equiv \alpha$ should be the same for different probes (represented by the same operator and with an appropriate normalization).

In general, the probe is defined by a function $P_\alpha(\alpha{:}1,\boldsymbol{\sigma},\boldsymbol{\tau},\boldsymbol{\sigma\tau},\ldots)$ [Bak97], characterized by a precise structure (S,T), which contains the effects of the NN-interaction and distorted wave potential. For a CEX reaction, the probe function contains only isovector operators: $P_\alpha(\alpha{:}\boldsymbol{\tau},\boldsymbol{\sigma\tau},\ldots)$. The basic hypothesis of the following discussions is that the cross section can be written as:

$$\sigma(\omega, q) = \sum_{\alpha} \left|T_\alpha(\omega, q)\right|^2 R_\alpha(\omega, q) \tag{6.10}$$

where ω and q indicate the transferred energy and momentum, respectively. Eq. (6.10) means that it is possible to separate the structure part from the dynamics one, which are represented respectively by the response function $R_\alpha(\omega,q)$ and free scattering T-matrix. The total value of the integral of the strength function $R_\alpha(\omega)$ is determined by the sum rules, depending on the specific operator P_α:

$$S_n(P_\alpha) = \int d\omega\ \omega^n\, R_\alpha(\omega, P_\alpha) \tag{6.11}$$

where n = 0, 1 represent the Non-Energy (NEWSR) and Energy (EWSR) Weighted Sum Rules, respectively. The sum rules are of great practical importance. In particular, the difference of the NEWSR for $\beta^{\pm}$ transitions lead to the well known Ikeda sum rules [Ike64], which relate the response of a nucleus to ground state properties.

The RPA nuclear response function to incoming probe P_α is precisely defined in terms of the transition matrix elements of P_α, which acts on the vacuum state $|0\rangle$:

$$R_\alpha^{RPA}(\omega, q) \equiv \sum_{N\neq 0} \left|\langle N|P_\alpha|0\rangle\right|^2 \delta(\omega - \omega_N) \tag{6.12}$$

Eq. (6.12) gives the total transition probability between the ground state $|0\rangle$ and the excited states $|N\rangle$ of energy ω_N, for a transition induced by an external field P_α. The latter, being integrated over the projectile coordinate, acts as a one-body operator in the space of the target nucleons. The EWSR, conserved in the RPA theory, relates the integral of the strength $R_\alpha^{RPA}(\omega)$ to the ground state expectation value of the double commutator of P_α with the full Hamiltonian H_A of eq. (6.1):

$$\int_0^\infty d\omega\, \omega\, R_\alpha^{RPA}(\omega, P_\alpha) = \frac{1}{2}\langle 0|\left[P_\alpha, \left[H_A, P_\alpha\right]\right]|0\rangle \tag{6.13}$$

6.2.2 The RPA-Green's function method: the Dyson equation

Rather than solving the RPA equations as an eigenvalue problem, the Dyson equation can be used to evaluate the response function $R_\alpha^{RPA}(\omega,q)$. Introducing the many-body Green function $G_{RPA}(\omega)$ of the target Hamiltonian H_A of eq. (6.1)

$$G_{RPA}(\omega) = (H_A - \omega - i\eta)^{-1} + (H_A + \omega - i\eta)^{-1} \tag{6.14}$$

eq. (6.12) may be rewritten as a ground state expectation value:

$$R_\alpha^{RPA}(\omega, q) = \frac{1}{\pi}\,\mathrm{Im}\langle 0|P_\alpha^+\, G_{RPA}(\omega)\, P_\alpha|0\rangle \tag{6.15}$$

Inserting a complete set of eigenstates $|N\rangle$ yields:

$$R_\alpha^{RPA}(\omega,q) = \frac{1}{\pi}\,\mathrm{Im}\sum_{N\neq 0}\left|\langle N|P_\alpha|0\rangle\right|^2\left[(\omega_N - \omega - i\eta)^{-1} + (\omega_N + \omega - i\eta)^{-1}\right] \tag{6.16}$$

from which, for positive ω and $\eta \to 0$, eq. (6.12) is obtained. The Green function G_{RPA} is calculated from the Dyson equation:

$$G_{RPA} = G_0 + G_0\, V_{res}\, G_{RPA} \tag{6.17}$$

where

$$G_0(\omega) = (H_0 - \omega - i\eta)^{-1} + (H_0 + \omega - i\eta)^{-1} \tag{6.18}$$

represents the Green function for the independent particle model – eq. (6.2) – which describes the uncorrelated 2-QP excitations. The solution of the Dyson equation is based on the knowledge of the G_0 propagator and the particle-hole interaction V_{res}, for which the interaction of ref. [Hof98], described in Section 6.3, is used. G_0 can be expressed in the coordinate space representation in a way suited for the description of the continuum [Shl75]:

$$G_0^{ST}(\mathbf{r},\mathbf{r}',\omega) = -\sum_h \varphi_h(\mathbf{r})\, O_{ST} \left[(H_0 + \varepsilon_h + \omega - i\eta)^{-1} + (H_0 - \varepsilon_h - \omega - i\eta)^{-1} \right] O'_{ST}\, \varphi_h(\mathbf{r}') \tag{6.19}$$

where:

$$O_{00} = 1, \quad O_{10} = \boldsymbol{\sigma}, \quad O_{01} = \boldsymbol{\tau}, \quad O_{11} = \boldsymbol{\sigma\tau} \tag{6.20}$$

The sum of eq. (6.19) is over the hole states φ_h, which correspond to all the occupied orbitals in the ground state given by single particle model. The single particle Green function (the middle factor in eq. (6.19)) may be calculated by summing over the unoccupied states φ_p of single particle excitation:

$$(H_0 + \varepsilon_h - \omega)^{-1}_{\mathbf{r},\mathbf{r}'} = \sum_p \varphi_p(\mathbf{r})\, \frac{1}{\varepsilon_p + \varepsilon_h - \omega}\, \varphi_p(\mathbf{r}') \tag{6.21}$$

In coordinate space the Dyson equation (eq. (6.17)) becomes an integral equation:

$$G^{(\alpha)}_{RPA}(\mathbf{r},\mathbf{r}',\omega) = G^{(\alpha)}_0(\mathbf{r},\mathbf{r}',\omega) + \int d\mathbf{r}_1 \int d\mathbf{r}_2\, G^{(\alpha)}_0(\mathbf{r},\mathbf{r}_1,\omega)\, V^{\alpha}_{res}(\mathbf{r}_1,\mathbf{r}_2)\, G^{(\alpha)}_{RPA}(\mathbf{r}_2,\mathbf{r}',\omega) \tag{6.22}$$

In this representation the response function is written as:

$$R^{RPA}_{\alpha}(\omega, q) = \frac{1}{\pi} \mathrm{Im} \int d\mathbf{r}' \int d\mathbf{r}\; P_{\alpha}(\mathbf{r})\; G^{(\alpha)}_{RPA}(\mathbf{r},\mathbf{r}',\omega)\; P^{*}_{\alpha}(\mathbf{r}') \tag{6.23}$$

Finally, the transition densities which will be used in the DWBA calculations are obtained for the transition in the target ($^{15}N \rightarrow {}^{15}C$):

$$\rho^{(\alpha)}_{^{15}N \rightarrow {}^{15}C}(\mathbf{r},\omega) = \frac{1}{\pi} \mathrm{Im} \frac{\int_0^{\infty} d\mathbf{r}'\, G^{(\alpha)}_{RPA}(\mathbf{r},\mathbf{r}',\omega)\, M^{*}_{\alpha}(r')}{\sqrt{\int d\omega\, R^{RPA}_{\alpha}(\omega)}} \tag{6.24}$$

where M_α denotes an auxiliary external field, used only for a computational necessity and chosen such that it accounts for the essential (S,T) properties of the probe function P_α. Indeed, since also $R_\alpha^{RPA}(\omega)$ in the denominator of eq. (6.24) is calculated using the same field, the dependence of the transition densities on M_α is only superficial.

6.2.3 The 4-QP excitations

The 4-QP excitations, not included in the 1p-1h RPA theory, are crucial for a correct description of the decay width of giant resonances. In fact the theoretical values obtained by RPA underestimate systematically the measured width, especially for heavy systems. To account for this "collisional broadening" of the RPA modes, the Hilbert space has to be extended to include both 1p-1h and 2p-2h excitations. The latter physically describe the collisions between the 1p-1h couples [Yan83, Ber83].

Because of the large number of 2p-2h excitations, a complete treatment in the enlarged 4-QP space is extremely difficult, if not numerically impossible in most cases. Therefore a number of semiempirical approximations have been developed appositely for the description of the excitation energy continuum, obtaining an average 2p-2h contribution [Bak97]. It is important to note that the equations formulated in the extended space are projected on the 1p-1h subspace, where the 2p-2h contributions are described by the matrix elements of a complex energy-dependent effective potential. In this way, the effect of the 2p-2h excitations appears as additional 1p-1h self-energy, producing an energy dependent shift and broadening of the RPA response functions and transition densities. The real and imaginary part of the matrix elements are related by a general dispersion relation [Bak97], accounting for the larger broadening effect on the more shifted structures.

It is seen that this approach does not introduce further ground state correlations. In fact, no extra strength is associated to the enlarged space, so that the final result is a state-dependent redistribution of the strength and the EWSR eq. (6.13) remains valid.

In the present case, an empirical formula was derived for the imaginary part of the 2p-2h self-energy by imposing that the broadening is zero on the ^{15}C ground state and 0.6 MeV at the energy typical for the Giant Dipole Resonance (GDR). The real part is then deduced from the dispersion relation of ref. [Bak97].

6.2.4 The mean field

To solve the Dyson equation in coordinate space, eq. (6.22), the propagator G_0 of independent particle model has to be evaluated. For this purpose, a basic description of single particle orbitals is needed. The single particle wave functions φ were obtained as eigenfunctions of a Woods-Saxon potential with nuclear, spin-orbit and Coulomb terms:

$$U(r) = V_0\, f(r) + V_{LS}\, \boldsymbol{\sigma}\cdot\mathbf{l}\, \frac{1}{r}\frac{df}{dr} + \frac{1}{2}(1-\tau_z)\, V_C(r) \tag{6.25}$$

where

$$f(r) = \left[1+\exp\frac{r-r_0A^{1/3}}{a}\right]^{-1} \tag{6.26}$$

and V_C is the Coulomb potential of a uniform sphere of radius $R_C = R_0\, A^{-1/3}$, R_0 being the radius of the central part of the potential.

The parameters of the mean field were calculated by fitting the Hartree-Fock-Bogoliubov (HFB) potential obtained for the ^{14}C nucleus. The HFB potential was derived

Table 6.1. Mean field parameters obtained by fitting the ^{14}C HFB potential. These parameters were used for the calculation of the single particle orbitals, done for protons and neutrons separately.

		Protons			Neutrons		
		U_0 [MeV]	**r_0 [fm]**	**a [fm]**	**U_0 [MeV]**	**r_0 [fm]**	**a [fm]**
V_0	(1)	-37.16	1.506	0.438	-31.39	1.479	0.424
	(2)	-23.15	0.331	0.392	-17.35	0.487	0.462
V_{LS}	(1)	59.66	1.015	0.733	33.54	1.035	0.664
	(2)	-46.57	1.001	0.815	-24.18	0.984	0.781

using a G-matrix NN-interaction [Hof98] in the Local Density Approximation (LDA), adding 3-body terms to reproduce correctly the nuclear matter properties. For a more accurate fit, two Woods-Saxon functions were used both for the central V_0 and spin-orbit V_{LS} parts of the mean field, eq. (6.26). To describe carefully the CEX reactions, a separate calculation was done for neutrons and protons. The parameters obtained from the fit are shown in Table 6.1.

The single particle wave functions were calculated solving the eigenvalue problem in the mean field for excitation energies $E_X \leq 100$ MeV and angular momenta $L \leq 6$. The levels of single proton $|^{14}C_{GS} + p\rangle$ and single neutron $|^{14}C_{GS} + n\rangle$ in the field of an inert ^{14}C core were determined separately, assuming the nucleon was at infinite distance from the core. The single particle continuum was discretized by enclosing the system in a spherical box (radius R_{box} = 40 fm). With this special technique, RPA calculations with large configurations spaces can be performed easily [Len88]. For a large R_{box} value the results are almost independent of R_{box} and the density of the states is high enough to describe possible resonances in the continuum.

6.2.5 The state-dependent pairing field

In the QRPA theory the effective particle-hole correlations are described in terms of quasiparticles interactions, which may be taken into account by a state-dependent pairing field. As advanced in Section 6.1, the emptiness and occupation amplitudes u_j and v_j – necessary to construct the 1-QP operators – are determined by pairing correlations between nucleons. In the pairing theories, like that of Bardeen-Cooper-Schieffer (BCS) describing superconductivity, these amplitudes provide the probability that a singlet even pair of particles occupies the orbital j. However the BCS pairing field is independent of the state and thus not suitable for nucleons, especially when the pairing interaction is expected to be not negligible, as in weakly-bound nuclei.

In the present model, a state-dependent pairing field is calculated with a density dependent interaction, obtained by projection of the NN-interaction of ref. [Hof98] (described in Section 6.3) to the Singlet Even particle-particle channel (S = 0, L = 0, T = 1). The strength of the pairing field used as input is G = 17.5 MeV. The occupation probabilities $|v_j|^2$ and energy shifts E_{BCS} produced by the pairing on different orbitals are shown in Table 6.2 for protons and neutrons. The dependence of E_{BCS} on the state is seen.

Table 6.2. Parameters obtained from a state-dependent pairing field with input strength G = 17.5 MeV. $|v_j|^2$ represent the occupation probabilities and E_{BCS} [MeV] the energy shifts produced by the pairing on different proton and neutron states.

	Protons					Neutrons				
n l j	$1s_{1/2}$	$1p_{3/2}$	$1p_{1/2}$	$1d_{5/2}$	$2s_{1/2}$	$1s_{1/2}$	$1p_{3/2}$	$1p_{1/2}$	$1d_{5/2}$	$2s_{1/2}$
$\|v_j\|^2$	1	1	0.707	0.032	0.015	1	1	1	0.008	0.004
E_{BCS}	20.023	10.007	0.639	7.671	9.486	24.235	10.179	3.542	3.917	4.009

6.3 The residual interaction

A realistic NN-interaction, including the tensor contribution, is used in both structure and dynamics calculations, as well as in the determination of the mean and pairing fields. In detail, it is the isovector part of the D3Y G-matrix interaction of Hofmann and Lenske [Hof98], which consists of direct and exchange terms with central (scalar and vector), rank-2 tensor and spin-orbit components. The latter has a small effect only, thus was neglected in the calculations. This interaction, dependent on the nuclear density and the charge asymmetry, is found to be well suited for light neutron-rich nuclei such as ^{11}Li and ^{19}C [Len98b, Len01] and ^{11}Be [Cap01, Cap04b].

A proper treatment of the medium effects is essential for a fully microscopic description of finite nuclei. A well proven approach to derive in-medium NN-interactions starting from the NN-interaction in free space is the Brueckner theory [Bru68]. The Brueckner G-matrix for infinite nuclear matter is then applied in the Local Density Approximation (LDA) to finite nuclei [Bru68]. However, in this way the empirical saturation properties of the nuclear matter are generally missed, at least when only 2-body correlations are included. Especially when exotic nuclei are investigated, a semi-phenomenological approach based on a microscopically derived interaction is of great advantage [Hof98].

The solutions of the Dirac-Brueckner (DB) integral equations for asymmetric matter are parametrized in terms of appropriate meson-nucleon coupling constants acting at each vertex of the in-medium NN-interaction [Len98b]. For finite nuclei, a phenomenological density dependence is supplemented to avoid the collapse of the nuclear matter at high densities [Hof98]. Density dependent vertex functions are introduced:

$$f_\gamma(\rho) = s_\gamma \left(1 + \sum_{n=1}^{N_\gamma} a_n^\gamma \, z^{n\beta} \right) \tag{6.27}$$

where $z = \rho/\rho_0$, the base exponent $\beta = 1/3$ and $\gamma = 0, \tau$ indicates isoscalar and isovector vertex functions, respectively. The scaling factors s_γ and the coefficients a^γ_n are fitted to the saturation properties of infinite symmetric nuclear matter. These allow a first ($N_\tau = 1$) and third ($N_0 = 3$) order approximation for f_τ and f_0, respectively. The vertices $f_\gamma(\rho)$ are used to

calibrate the strength of the effective potential obtained from the DB coupling constants, leaving the intrinsic momentum structure unchanged. The latter is defined by a parametrization of the M3Y G-matrix with three Yukawa functions. Their ranges are chosen to represent the long-range tail (1.414 fm) of the One Pion Exchange Potential (OPEP) and medium and short-range parts, which corresponds to σ (0.40 fm) and ω, ρ, δ (0.25 fm) meson exchange, respectively. The meson δ appears to be important in nuclear asymmetric matter because it introduces an increased isovector strength at low density [Len98b].

Let us discuss in detail the approach of ref. [Hof98]. The total HF energy of a nucleus A is given by:

$$E = T + \frac{1}{2}\left\langle \overline{V} \right\rangle \tag{6.28}$$

with kinetic and potential energy given respectively by:

$$T = \sum_{k \le A} \left\langle k \left| \frac{p^2}{2m} \right| k \right\rangle = \int d\mathbf{r}\, \frac{\hbar^2}{2m} \left[t_p(\mathbf{r}) + t_n(\mathbf{r}) \right] \tag{6.29}$$

$$\left\langle \overline{V} \right\rangle = \left[\sum_{k_1 k_2} \left\langle k_1\, k_2 \left| V \right| k_1\, k_2 \right\rangle - \left\langle k_1\, k_2 \left| V \right| k_2\, k_1 \right\rangle \right] \tag{6.30}$$

where V is a 2-body interaction, $|k\rangle$ represents single particle states and $t_q(\mathbf{r})$ is the kinetic energy density (where q = p, n denotes protons and neutrons). V may be expressed in terms of the interactions for identical (q = q') and different (q ≠ q') particles, with direct (Hartree) and exchange (Fock) contributions shown separately ($\mathbf{r}_{12} = \mathbf{r}_1 - \mathbf{r}_2 \equiv -\mathbf{s}$ is the relative coordinate):

$$\left\langle \overline{V} \right\rangle = \left\langle V^d \right\rangle + \left\langle V^e \right\rangle = \sum_{qq'} \int d\mathbf{r}_1 \int d\mathbf{r}_2 \left\{ \rho_q(\mathbf{r}_1)\rho_{q'}(\mathbf{r}_2)\, V^d_{qq'}(\mathbf{r}_{12}) + \rho_q(\mathbf{r}_1,\mathbf{r}_2)\rho_{q'}(\mathbf{r}_1,\mathbf{r}_2)\, V^e_{qq'}(\mathbf{r}_{12}) \right\} \tag{6.31}$$

The density matrices are defined in terms of the single particle wave functions Φ_k:

$$\rho_q(\mathbf{r}_1,\mathbf{r}_2) = \sum_{k\sigma} \Phi^*_k(\mathbf{r}_1,\sigma,q)\ \Phi_k(\mathbf{r}_2,\sigma,q) \tag{6.32a}$$

$$\rho_q(\mathbf{r}) = \rho_q(\mathbf{r},\mathbf{r}) \tag{6.32b}$$

Due to the Pauli principle, the exchange term is non local. Its exact treatment in the HF functional leads to a coupled system of integrodifferential equations. A convenient approach, especially for large charge asymmetry and variable density, is the Density Matrix Expansion (DME), invented by Negele and Vautherin [Neg72]. This method provide a systematic expansion of the non local exchange parts of any given finite range effective NN-interaction. The basic features of the interaction are retained, but results will obviously depend on the

expansion order. After a coordinate transformation into the center of mass reference system, the density matrix is expanded in Taylor series in terms of the one-body local density:

$$\rho\left(\mathbf{r}+\frac{\mathbf{s}}{2},\mathbf{r}-\frac{\mathbf{s}}{2}\right) = \rho_{SL}(sq_F)\ \rho(\mathbf{r}) + \frac{35}{2sq_F^3}\, j_3(sq_F)\left[\frac{1}{4}\nabla^2\rho(\mathbf{r}) - t(\mathbf{r}) + \frac{3}{5}q_F^2\rho(\mathbf{r})\right] + ... \quad (6.33)$$

where the two first terms of the series are shown. Here ρ_{SL} is the Slater density, q_F the average relative momentum between the two interacting particles, j_n the spherical Bessel function of order n, **r** and **s** are CM and relative coordinates, respectively. The variable separation is achieved with this method. If q^2_F is chosen as [Hof98]:

$$q_F^2(\mathbf{r}) = \frac{5}{3}\frac{t(\mathbf{r}) - (1/4)\nabla^2\rho(\mathbf{r})}{\rho(\mathbf{r})} \quad (6.34)$$

the second term of eq. (6.33) is cancelled and the DME reduces to the Slater approximation

$$\rho\left(\mathbf{r}+\frac{\mathbf{s}}{2},\mathbf{r}-\frac{\mathbf{s}}{2}\right) = \rho_{SL}(sq_F)\ \rho(\mathbf{r}) \quad (6.35)$$

but with a modified Fermi momentum which accounts for surface corrections. Separating the **r** and **s** coordinates and integrating on **s**, the exchange part becomes simply:

$$\left\langle V^e \right\rangle = \sum_{qq'}\int d\mathbf{r}\ \rho_q(\mathbf{r})\ \rho_{q'}(\mathbf{r})\ \tilde{V}^e_{qq'}(\mathbf{r}) \quad (6.36)$$

where $\tilde{V}^e_{qq'}(q_{Fq}, q_{Fq'}; \mathbf{r})$ is the interaction strength.

Once the pairing interaction (calculated as in Section 6.2.5) is introduced, to which the DME method can be equally well applied, the so obtained D3Y G-matrix interaction is renormalized by the in-medium vertex functions of eq. (6.27). Thus, the density dependent in-medium interaction is given by:

$$V^{*d}_\gamma(\mathbf{r}_1,\mathbf{r}_2;\rho) = g_\gamma(\mathbf{r}_1)\, V^d_\gamma(\mathbf{r}_1-\mathbf{r}_2)\, g_\gamma(\mathbf{r}_2) \quad (6.37)$$

$$V^{*e}_\gamma(\mathbf{s},\mathbf{r};\rho) = g^2_\gamma(\mathbf{r})\, V^e_\gamma(\mathbf{s}) \quad (6.38)$$

where $g_\gamma(\mathbf{r}) = g_\gamma[\rho(\mathbf{r})]$ and $g_\gamma^2 = f_\gamma(\rho)$ with $\gamma = 0, \tau$ for isoscalar and isovector components, respectively. V^d and V^e represent "bare" interactions, i.e., without in-medium effects. This approach ensures a reliable treatment of the density dependence also in the surface region (where the vertices vary rapidly), i.e., for finite nuclei. The ground state properties of the stable nuclei are well reproduced [Hof98].

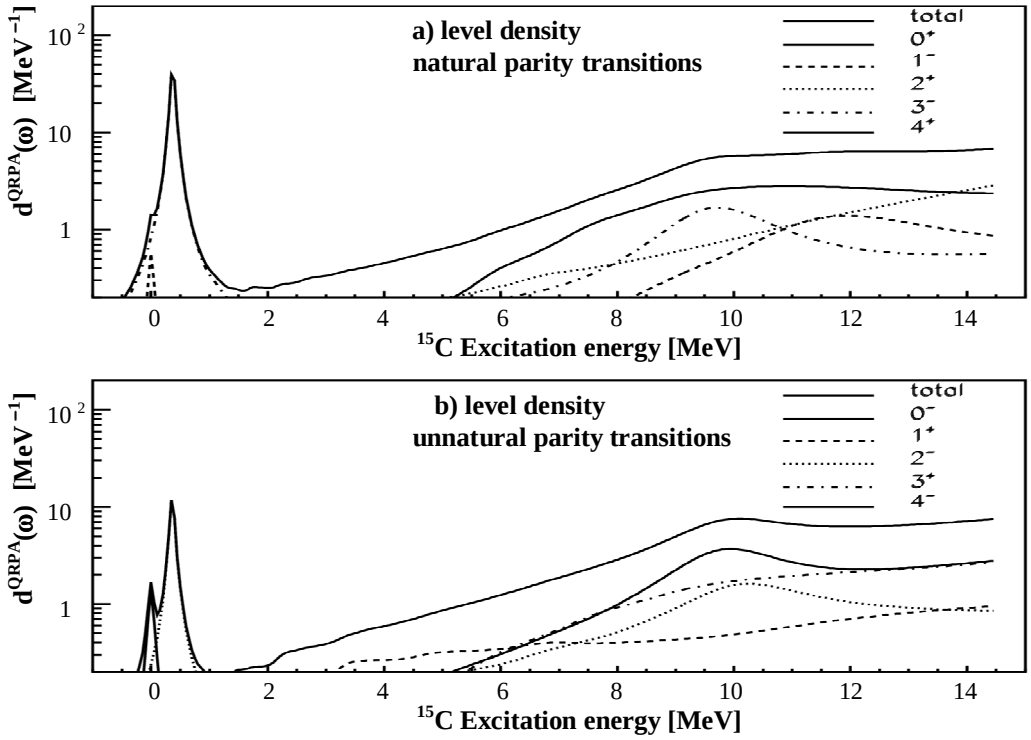

Figure 6.2. QRPA level densities for CEX transitions from $^{15}N_{GS}$ to excited states of ^{15}C. These quantities represent for each multipolarity the ratio between each response function and the respective sum rule at each energy. The bin size is 50 keV, thus the ordinate has to be divided by 20 to get the integral (6.39). a) Natural parity transitions. b) Unnatural parity transitions.

6.4 Results of the CEX-QRPA calculations

The ^{15}N ground state was calculated in the framework of the Hartree-Fock-Bogoliubov theory using the D3Y G-matrix residual interaction of ref. [Hof98]. The ^{15}C states are then described as correlated 2-QP excitations with respect to $^{15}N_{GS}$. The allowed energy range for the 2-QP excitations is up to 80 MeV. A state dependent pairing field (see Section 6.2.5) and an average treatment of the 4-QP correlations (Sect. 6.2.3) are included in the calculations. The QRPA level density distributions (per MeV) for charge exchange transitions from $^{15}N_{GS}$ to excited states of ^{15}C, calculated for $E_x \leq 15$ MeV and multipolarities from 0^+, 0^- to 4^+, 4^-, are shown in Figure 6.2. These quantities are obtained by normalizing the QRPA multipole response functions to the NEWSR of the same operator:

$$d^{QRPA}(\omega, P_\alpha) = \frac{R_\alpha^{QRPA}(\omega, P_\alpha)}{S_0(P_\alpha)}, \qquad \int d\omega \; d^{QRPA}(\omega, P_\alpha) = 1 \tag{6.39}$$

Transitions to two discrete levels of ^{15}C are observed. A first state at $E_x \sim 0$ MeV is excited by the 0^- and 1^- transitions; considering that the ^{15}N ground state has $J^\pi = 1/2^-$, this is only compatible with a final $J^\pi = 1/2^+$, which agrees with the known ^{15}C ground state J^π. The second state observed is populated by the 2^- and 3^- transitions, thus it corresponds to the $J^\pi = 5/2^+$ first excited state of ^{15}C. This result is in agreement with the known inversion between

the $1d_{5/2}$ and $2s_{1/2}$ neutron orbitals in ^{15}C (see Section 2.3.1). It is pointed out that no conditions were imposed to adjust the energies of such levels. In fact, HFB calculations without energy conditions cannot account for the inversion of single particle orbitals, which instead is reproduced by calculating the QRPA correlations. For excitation energies higher than 1.5 MeV no sharp structures are evident in the level density, rather it becomes a smooth function of the energy. The large bump at $E_x \sim 10$ MeV in the 1^-, 2^-, 3^-, 4^- transitions arises from spurious $^{15}N_{GS}$ components with $J^\pi = 3/2^+$.

The results obtained by the CEX-QRPA model – based on particle-hole degrees of freedom, not accounting for core polarization – show that this kind of approach reproduces correctly the ^{15}C level structure below 1.5 MeV excitation energy, characterized by strong single particle components, but it fails at higher excitation energies. These results (published in refs. [Orr03, Cap04]) are similar to those found in the CEX-QRPA calculations for ^{11}Be [Cap01, Cap04b], where the level structure is reproduced only up to $E_x = 2$ MeV.

It is concluded that the sharp resonances experimentally seen beyond the neutron emission threshold (see Section 5.2.2) cannot be simply connected to 1p-1h excitations and, according to the predictions of ref. [Noc03], the observed fragmentation of the strength in the ^{15}C experimental spectra is very likely produced by core-excited components of ^{15}C. As we shall see, the theoretical calculations of Chapters 7 and 8, based on the Dynamical Core Polarization (DCP) framework, will confirm these expectations, reproducing the narrow resonances seen in the continuum and achieving a deeper comprehension of the ^{15}C spectrum.

6.5 The DWBA dynamics calculations

The dynamics calculations performed for the ^{15}N(^{7}Li,^{7}Be)^{15}C reaction are described in this Section. DWBA calculations, based on the CEX-QRPA transition densities, give the cross sections for the transitions to the ^{15}C single particle states that are well reproduced by the QRPA calculations. The nuclear structure results are applied to the analysis of scattering data without further adjustment of parameters.

6.5.1 The T-matrix interaction

The effective NN-interaction used to calculate the charge exchange form factors is taken from the isovector part of the D3Y G-matrix interaction of Hofmann and Lenske [Hof98]. The full T-matrix in momentum space can be obtained at low incident energy by extrapolating the density dependent G-matrix interaction, as, e.g., in ref. [Kho93]. As in formula (3.7), the T-matrix isovector interaction consists of central (scalar and vector), spin-orbit (neglected in our case) and tensor components, each of them including direct and exchange terms:

$$t_{NN}^{(\tau)} = \underbrace{\left[t_\tau^C(r) + t_{\sigma\tau}^C(r)\ \boldsymbol{\sigma}_1 \cdot \boldsymbol{\sigma}_2\right]}_{\text{central}} + \underbrace{t_\tau^{LS}(r)\ \left(\mathbf{L}\cdot\mathbf{s}_1 + \mathbf{L}\cdot\mathbf{s}_2\right)}_{\text{spin-orbit}} + \underbrace{t_\tau^T(r)\ S_{12}}_{\text{rank-2 tensor}} \boldsymbol{\tau}_1 \cdot \boldsymbol{\tau}_2 \qquad (6.40)$$

It is remarked that we use the same interaction as in the HFB ground state and QRPA correlated excitations calculations. This assures the consistency of structure and reaction

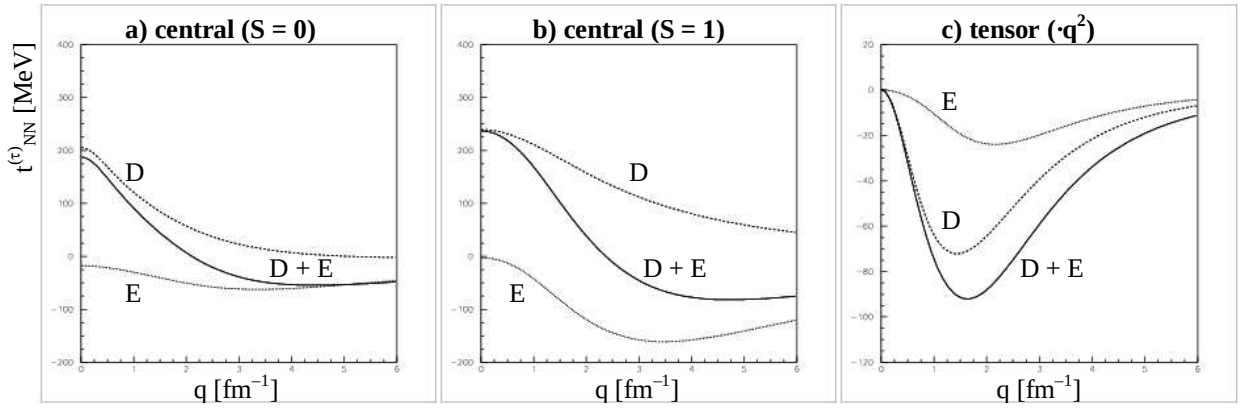

Figure 6.3. a) Central scalar, b) central vector and c) rank-2 tensor components of the isovector effective NN-interaction of eq. (6.40). The direct (D) and exchange (E) terms are separately shown, together with their sum.

calculations. The density dependence of the D3Y G-matrix gives rise to a density dependent T-matrix. The numerical calculations are simplified by using a separable LDA [Kho93, Hof98] to express this dependence. The global properties of the T-matrix interaction obtained in the various (S,T) channels are given in Table 6.3. The spin-orbit NN-interactions are neglected. For the isovector channel (S,T = 1), the central (without and with spin dependence) and tensor components are shown in momentum space in Figure 6.3, separating the direct and exchange terms. Since peripheral collisions are involved, the reaction takes place principally for linear momentum transfer q from 1 to 2 fm^{-1}. From Fig. 6.3 it is seen that, in the window of q-values considered, the tensor force cannot be neglected. The exchange terms are also important for a correct description of the interaction, especially for the central S = 1 component. However, from Table 6.3 we can see that they are more influential for isoscalar than for isovector interactions.

Table 6.3. Volume integrals for the T-matrix interaction in the various (S,T) channels at vanishing density, calculated in the (A,B) rest frame. The interaction used in the CEX form factor calculations is given by the isovector components (S, T=1).

Central (S,T) interactions [MeV · fm^3]				
(S,T)	(0,0)	(0,1)	(1,0)	(1,1)
Direct	130.1	239.3	154.1	205.2
Exchange	-838.1	62.6	-13.6	-7.1
Tensor (S,T) interactions [MeV · fm^5]				
(S,T)	(0,0)	(0,1)	(1,0)	(1,1)
Direct			-17.8	-150.2
Exchange			92.6	-31.4

6.5.2 The CEX form factors

The CEX form factor are calculated microscopically by double folding of the transition densities of the target and the projectile with the effective NN-interaction of Section 6.5.1:

$$F_{\beta\alpha}^{(\tau)}(\mathbf{r},E) = \int d\mathbf{q}\ \ \rho_{^{7}\mathrm{Li},^{7}\mathrm{Be}}(\mathbf{q})\ \ t_{NN}^{(\tau)}(\mathbf{q},E)\ \rho_{^{15}\mathrm{N},^{15}\mathrm{C}}(\mathbf{q})\ \ e^{i\mathbf{q}\cdot\mathbf{r}}/(2\pi)^3 \qquad (6.41)$$

Eq. (6.41) is the equivalent of eq. (3.4) in momentum space. The CEX-QRPA transition densities given by eq. (6.24) are used for the target transitions (^{15}N $\rightarrow$ ^{15}C). For the transitions in the projectile (^{7}Li $\rightarrow$ ^{7}Be) we use the shell model One Body Transition Densities (OBTD), calculated in ref. [Etc88] with the Cohen-Kurath [Coh65] wave functions, which are appropriate for well-bound p-shell nuclei. In fact, in our calculations the OBTD of ref. [Etc88]

$$\rho^{\mathrm{OBTD}}(^{7}\mathrm{Li}\rightarrow{}^{7}\mathrm{Be}) = \left\langle I_b\,\tau_b \left\| \left\{ a_{\rho_i}^{+}\,\tilde{a}_{\rho_j} \right\}^{J,\tau_0} \right\| I_a\,\tau_a \right\rangle \qquad (6.42)$$

are renormalized by $[(2\,J + 1)(2\,\tau_0 + 1)]^{1/2}$. In eq. (6.42) $|I_a\tau_a\rangle$ and $|I_b\tau_b\rangle$ are the single particle states respectively for $^{7}\mathrm{Li}_{GS}(J^{\pi} = 3/2^{-})$ and ^{7}Be ground or first excited state; ρ_k represents all the possible single particle states; J and τ_0 are spin and isospin transferred in the transition. We consider the transition to $^{7}\mathrm{Be}_{GS}(J^{\pi} = 3/2^{-})$ and $^{7}\mathrm{Be}_{exc}(J^{\pi} = 1/2^{-})$, for which the selection rules allow a transfer $J^{\pi} = 0^{+}$, 1^{+}, 2^{+}, 3^{+} and $J^{\pi} = 1^{+}$, 2^{+}, respectively. The energy distribution of the form factor is calculated in energy steps of 50 keV and for $E_x \leq 15$ MeV. Separate calculations are performed for each multipolarity λ resulting from the projectile and target transitions.

6.5.3 The optical potential

For the calculation of the scattering amplitudes in the DWBA framework (eq. (3.2)), the form factors (eq. (6.41)) and the distorted waves $\chi_{\alpha}^{(+)}(k_{\alpha},r)$ and $\chi_{\beta}^{(-)}(k_{\beta},r)$ in the incident α = (a, A) and exit β = (b, B) channels are needed. The choice of the optical potentials to use in the initial and final channels is important, especially because of the presence of unstable nuclei in the exit channel. For the stable ^{7}Li nucleus, low-energy optical potentials are known for elastic scattering on stable target nuclei (see, e.g., ref. [Win96]). However, empirical optical potentials for the ^{7}Be + ^{15}C channel are not known.

Therefore a double folding approach was used – for consistency also in the incident channel ^{7}Li + ^{15}N – in order to describe the elastic scattering in both channels. Since the density dependence of the elastic scattering at forward angles is small, the free NN-interaction obtained by Franey and Love at $E_{inc} \geq 50$ MeV/u [Lov81, Fra85] is used to derive the optical potential (both real and imaginary part). The isoscalar and isovector projectile and target ground state densities are folded with a complex T-matrix, which is obtained at the appropriate incident energy by spline extrapolation of the phenomenological Franey and Love potential using the value of the D3Y G-matrix of ref. [Hof98] at 0 MeV as reference. The folding is made in momentum space using the Fourier transforms of the ground state densities (with (a,A) = (^{7}Li,^{15}N) and (^{7}Be,^{15}C) in ingoing and outgoing channel, respectively):

$$U_{opt}(\mathbf{r},E) = \sum_{\tau=0,1} \int d\mathbf{q}\ \rho_a^{(\tau)}(\mathbf{q})\ t_{NN}^{(\tau)}(\mathbf{q},E)\ \rho_A^{(\tau)}(\mathbf{q})\ e^{i\mathbf{q}\cdot\mathbf{r}}/(2\pi)^3 \qquad (6.43)$$

To account for the long range contributions to the optical potential due to the coupling of the halo wave functions to the breakup channels, for ^{15}C we added a breakup term following Bonaccorso and Carstoiu [Bon02]. This reflects the larger extension into space of the ^{15}C density distribution with respect to the ^{15}N one. In the semi-classical model of ref. [Bon02], the imaginary part of the breakup potential is simply related to the properties of the halo wave function via the breakup probability. The real part is derived from the imaginary one by a dispersion relation and represents an extra polarization induced by the halo at long range. The use of the breakup term has been found to improve the agreement with the ^{11}Be experimental data [Cap04b]. Both the imaginary and real parts of this potential contribute to the calculated CEX cross sections. The properties of the full optical potential, including the breakup term in the outgoing channel, are given in Table 6.4.

Table 6.4. Total elastic cross sections σ_E [mb], volume integrals $J_{U,W}$ [MeV · fm^3] and root-mean-square radii $\langle R_{U,W}\rangle$ [fm] for the optical potential in the incident (^{7}Li + ^{15}N) and exit (^{7}Be + ^{15}C) channels. The symbols U and W indicate respectively the real and imaginary part of the potential.

^{7}Li + ^{15}N (in)					**^{7}Be + ^{15}C (out)**				
σ_E	J_U	J_W	$\langle R_U\rangle$	$\langle R_W\rangle$	σ_E	J_U	J_W	$\langle R_U\rangle$	$\langle R_W\rangle$
1574.6	-401	-334	4.03	3.79	2067.6	-386	-338	4.04	3.84

6.5.4 The CEX cross sections

The CEX cross sections of the ^{15}N(^{7}Li,^{7}Be)^{15}C reaction are obtained by DWBA calculations, performed with the HIDEX code [Len03]. The form factors of eq. (6.41) are used as input to solve the scattering equations. The one-step scattering amplitudes

$$T_{\beta\alpha}^{DWBA}(one) = \int \chi_\beta^{(-)}\, F_{\beta\alpha}^{(\tau)}\, \chi_\alpha^{(+)} d\mathbf{R} \qquad (6.44)$$

are calculated for the transitions to ^{15}C ground and first excited state. Finally, the double differential direct CEX cross sections are constructed

$$\frac{d^2\sigma}{d\Omega\ dE} = \sum_{\lambda(aA)} S_{\lambda A}(E) \frac{d\sigma_{\lambda(aA)}}{d\Omega} \qquad (6.45)$$

where the sum extends over all the transition multipolarities $\lambda(aA)$ and each reduced DWBA cross section $d\sigma_{\lambda(aA)}/d\Omega$ is weighted by the target response function per energy $S_{\lambda A}(E)$. The angular distributions have been obtained by adding the double differential cross section (6.45) at each energy step.

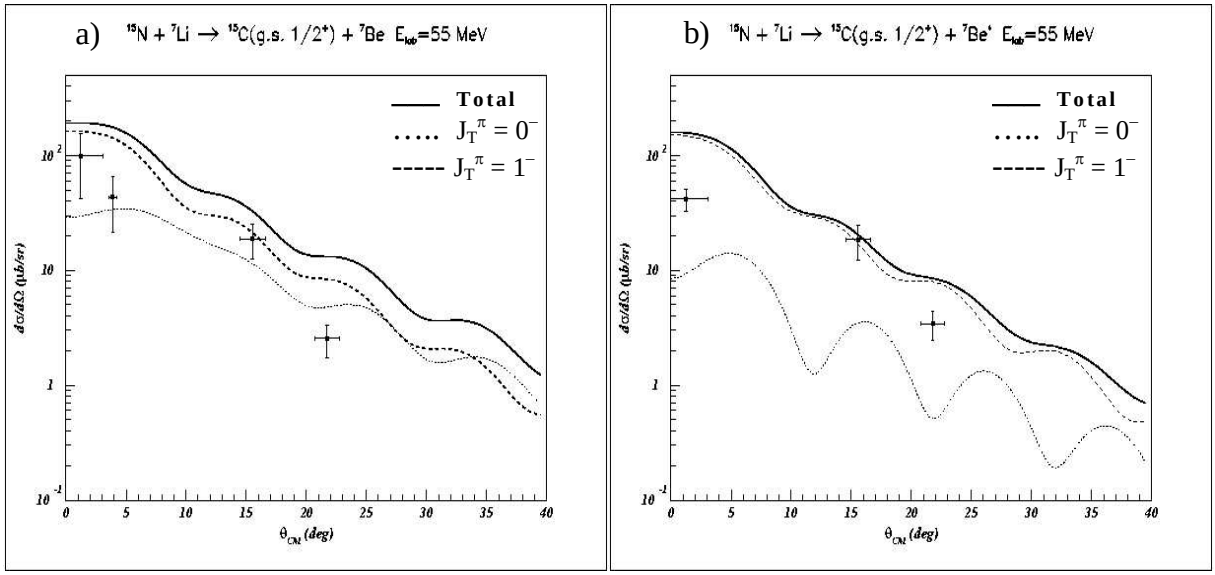

Figure 6.4. Angular distributions for the $^{15}N(^{7}Li,^{7}Be)^{15}C_{GS}$ reaction. Transition to the ^{15}C ground state a) without and b) with excitation of ^{7}Be, compared to the experimental data at θ_{lab} = 0°, 2.5°, 10° and 14°. The components from the different target transitions $J_T^\pi = 0^-$ and 1^- are shown separately, together with their incoherent sum. The calculated cross sections are not scaled.

6.6 Results of the DWBA calculations

The DWBA calculations were performed for the two bound states of ^{15}C. The angular distributions for the transition to the ^{15}C ground state are shown in Figure 6.4, for transitions without (Fig. 6.4a) and with (Fig. 6.4b) excitation of the ejectile ^{7}Be. The angular distributions for the ^{15}C first excited state are presented in Figures 6.5a and 6.5b for transitions involving $^{7}Be_{GS}$ and $^{7}Be_{exc}$, respectively. In each plot, the components of the angular distribution from the different angular momentum J_T^π transferred in the target transition are shown separately, together with their incoherent sum.

The CEX cross sections for reactions involving light nuclei are, in general, not strongly oscillatory. Even though the experimental points are few, we can see from the Figures that the behaviour of the angular distributions is quite well described and, more important, the order of magnitude of the measured cross sections is reproduced by numerical calculations without the need to introduce large renormalization. This is a noticeable result because usually large scaling factors (also of one order of magnitude) in the calculated cross sections have been used to reproduce the experimental data from the ($^{7}Li,^{7}Be$) reactions [Ban84, Coo84, Nak90b]. The close agreement is likely due to the interaction [Hof98] used in the form factor calculations, which is appropriate for light neutron-rich nuclei at low energy [Len98b, Len01, Cap04b]. This also confirms the reliability of a one-step approach, as in ref. [Cap04b].

The agreement is especially good for the ^{15}C first excited state, which is also the state more strongly populated by the ($^{7}Li,^{7}Be$) CEX reaction. This state is populated by the $J_T^\pi = 2^-$ and 3^- target transitions. Among them, from Fig. 6.5 we can see that the 2^- unnatural parity transition is dominant, both for the $^{7}Be_{GS}$ and $^{7}Be_{exc}$ cases. The different angular momentum

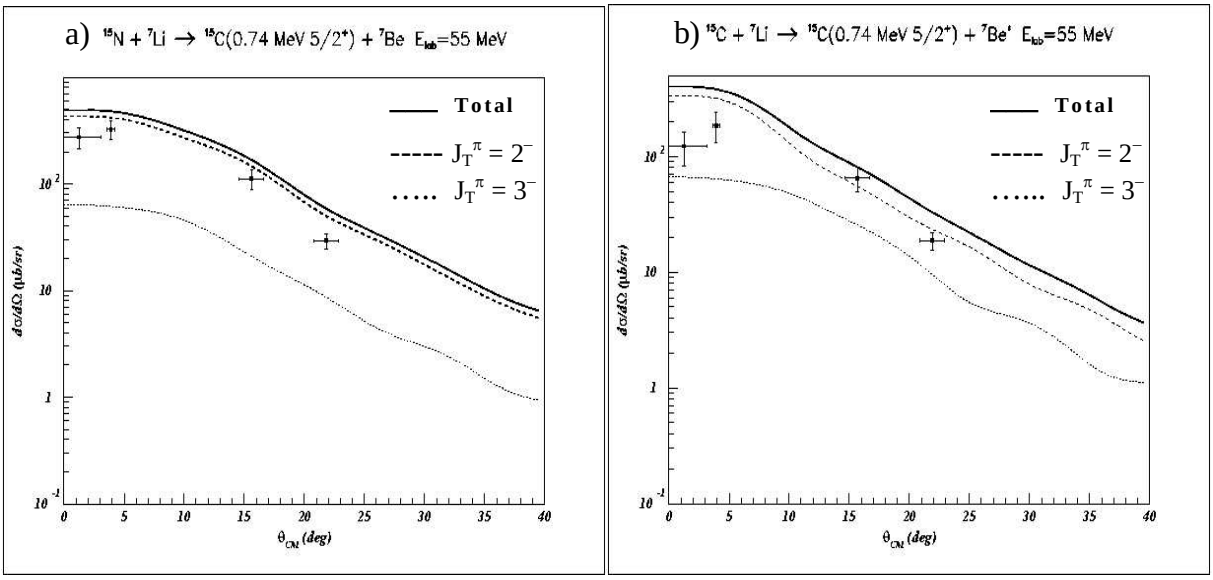

Figure 6.5. Angular distributions for the $^{15}N(^{7}Li,^{7}Be)^{15}C^*_{(5/2+)}$ reaction. Transition to the ^{15}C first excited state a) without and b) with excitation of ^{7}Be, compared to the experimental data at θ_{lab} = 0°, 2.5°, 10° and 14°. The components from the different target transitions $J_T^\pi = 2^-$ and 3^- are shown separately, together with their incoherent sum. The calculated cross sections are not scaled.

couplings J_B^π in the projectile transition $^{7}Li \rightarrow ^{7}Be$ are shown in Figure 6.7 (a and b corresponding to $^{7}Be_{GS}$ and $^{7}Be_{exc}$, respectively) for the dominant target transition $J_T^\pi = 2^-$. Also for the projectile the unnatural parity transitions (1^+ and 3^+) are prevalent, indicating a prominence of the nucleonic spin transfer process.

Concerning the excitation of the ^{15}C ground state (Fig. 6.4), this comes from the $J_T^\pi = 0^-$ and 1^- target transitions. Among them, the 1^- natural parity is dominant, also because of the weakness of the highly selective 0^- transition. The different couplings J_B^π in the projectile in correspondence with the 1^- transition are plotted in Figure 6.6 (a and b for $^{7}Be_{GS}$ and $^{7}Be_{exc}$, respectively), showing that in the projectile $J_B^\pi = 1^+$ is prevalent at small angles.

We performed two further calculations to investigate the spin transfer contribution in the 1^- transition to the ^{15}C ground state. The first calculation, shown in Figure 6.8a, accounts for the contribution of the spin-scalar components of the NN-interaction to the cross sections (i.e., all the spin-vector components are set to zero). This contribution is found to be about 4 % of the total value at 0°. Moreover the second calculation, including only the spin-vector components, is enough to reproduce the cross sections (see Fig. 6.8b). Thus the spin transfer components dominate also for transitions to the ^{15}C ground state.

Therefore we can conclude that, at the incident energy considered, there is dominance of the nucleonic spin transfer dynamics in the $^{15}N(^{7}Li,^{7}Be)^{15}C$ reaction. For this reason is fundamental to use an isovector NN-interaction mainly characterized by the spin dependent component in order to reproduce correctly the experimental data. The prevalence of spin transfer transitions at only 8 MeV/u is quite a surprising result because it is opposite to the predictions concerning the spin-isospin dependence of the free NN-interaction at low energy,

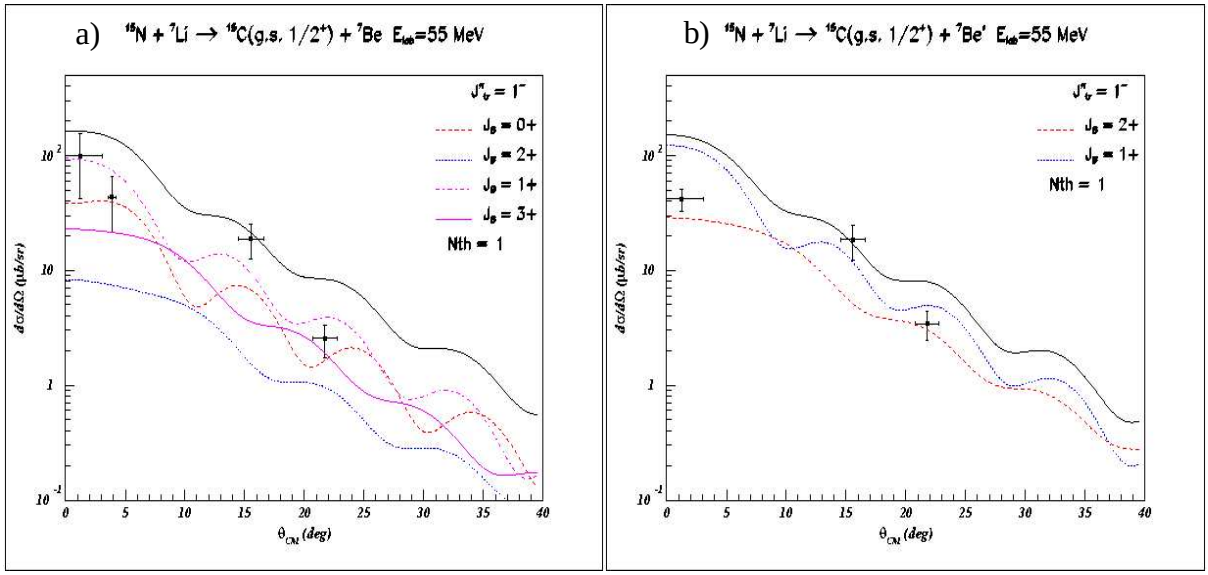

Figure 6.6. Angular distributions for the 1^- transition to the ^{15}C ground state, involving a) $^{7}Be_{GS}$ and b) $^{7}Be_{exc}$. The 1^- target transition is decomposed in terms of the different angular momentum J_B^π transferred in the projectile. Nth = 1 is the overall scaling factor.

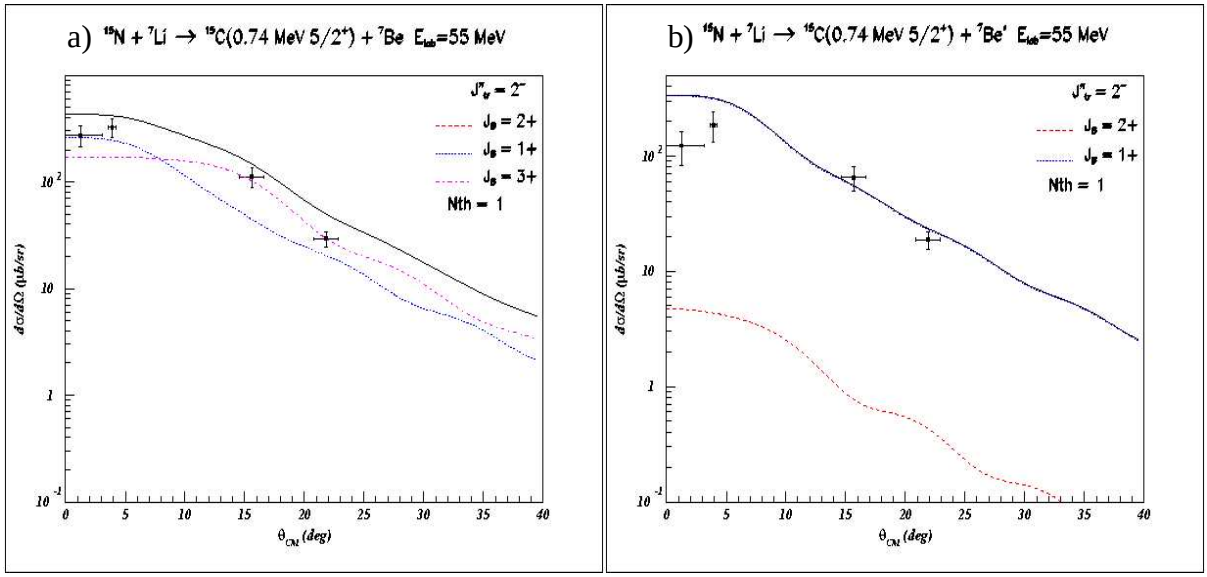

Figure 6.7. Angular distributions for the 2^- transition to the ^{15}C first excited state, involving a) $^{7}Be_{GS}$ and b) $^{7}Be_{exc}$. The 2^- target transition is decomposed in terms of the different angular momentum J_B^π transferred in the projectile. Nth = 1 is the overall scaling factor.

for which the (S,T) = (0,1) component should dominate on the (1,1) one [Tad87]. However, the predictions are about the NN-interaction in the free space, while our results concern the in-medium interaction. What we can affirm is that at about 8 MeV/u the in-medium NN-interaction depends principally on the spin component.

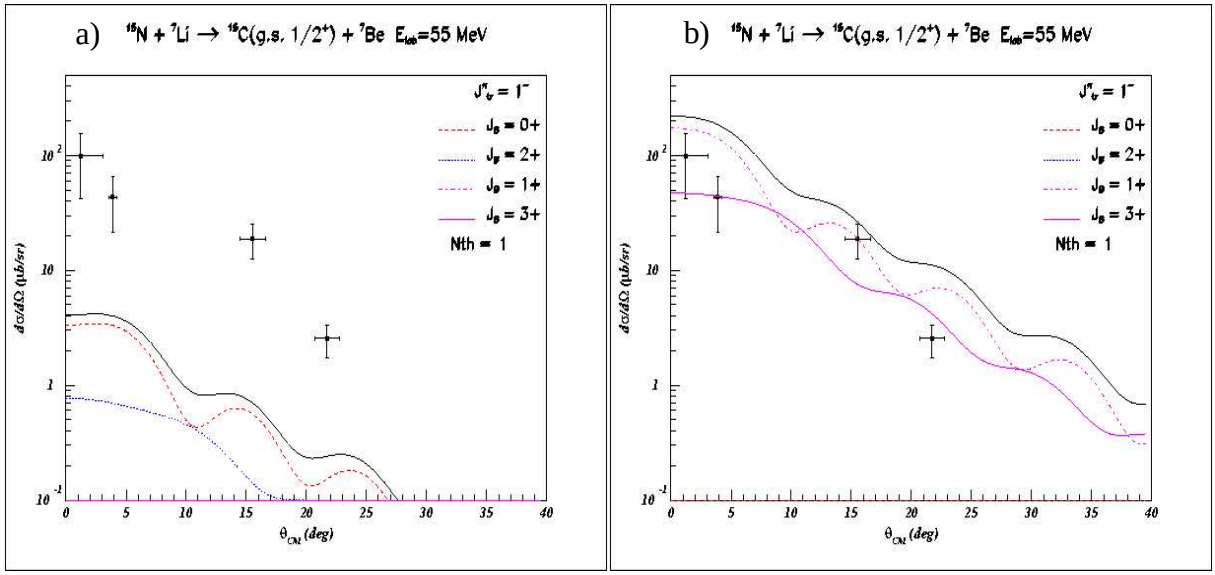

Figure 6.8. Angular distributions for the 1^- target transition to the $^{15}C_{GS}$ + $^{7}Be_{GS}$ channel. a) Calculation made with all the spin-vector (S = 1) components of the NN-interaction set to zero, showing the contribution of the spin-scalar (S = 0) components. b) Contribution of the spin-vector (S=1) components of the NN-interaction. The transferred J_B^{π} of the various transitions in the projectile are separately shown. Nth = 1 is the scaling factor.

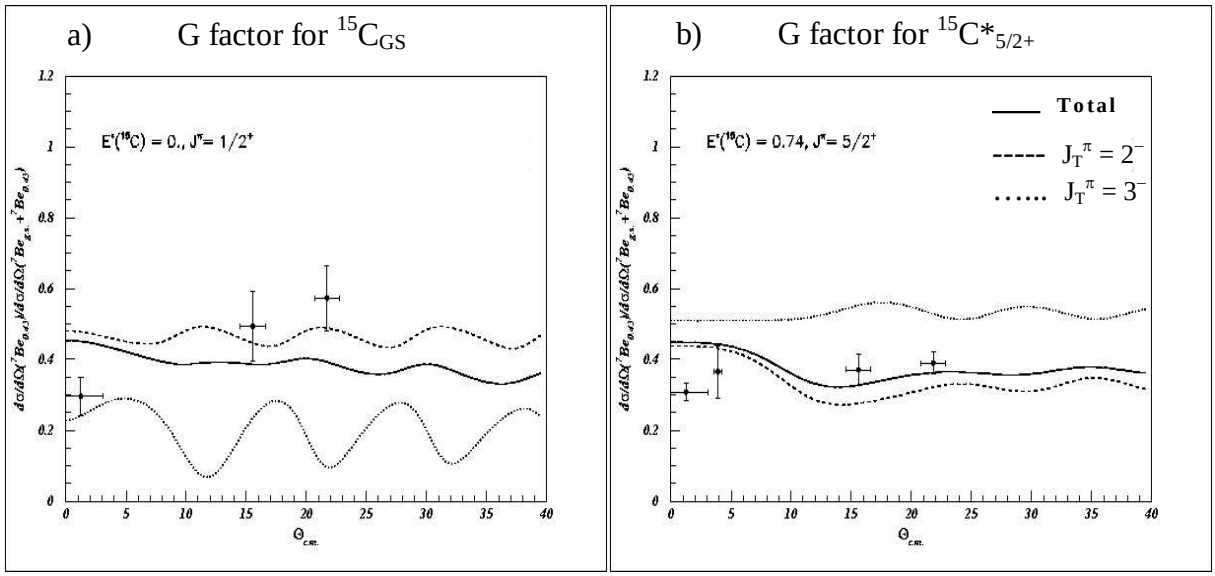

Figure 6.9. Angular distributions for the G factor relative to the ^{15}C a) ground and b) first excited state. The components due to the different target transitions J_T^{π} are separately shown.

The dominance of the spin transfer transitions is confirmed by the results for the factor G (defined in Section 3.4.1), whose angular distribution are plotted in Figure 6.9a and 6.9b relatively to the ^{15}C ground and first excited state, respectively. Being a ratio between cross sections calculated with the same optical potential, G is almost independent on the optical model and provides a test of the microscopic theory of the transition densities.

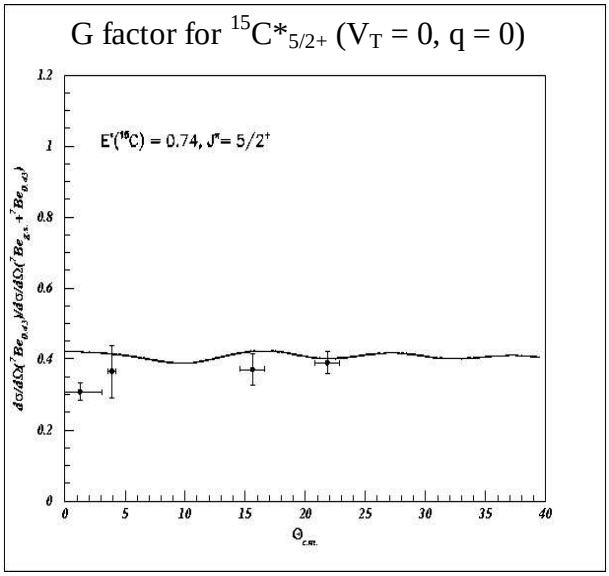

Figure 6.10. Angular distribution for the G factor relative to the ^{15}C first excited state, calculated in absence of the tensor force and imposing no momentum transfer following the method develop in refs. [Tad84, Alf98].

A not so bad agreement with the data is found for the excited state, while the few points with large errors available in the ground state case do not allow an effective comparison. However, in every case the G-value is almost constant and clearly different from zero, approaching the value of 0.46 correspondent to pure spin transfer at 0°. This indicates dominance of spin transfer dynamics.

The G-values are meaningful if the analogy between the (^{7}Li,^{7}Be) CEX reaction and the β-decay is valid. To test the reliability of the G factor in the present case, we performed a calculation in the conditions for the validity of such an analogy: the tensor component of the NN-interaction was set to zero and no momentum transfer was imposed. Following the method of refs. [Tad84, Alf98], these conditions were achieved by scaling the DWBA cross sections at θ_{lab} = 0° – calculated without tensor force – with the corresponding ones obtained by a Plane Wave (PWBA) calculation (again, without tensor force). The result is shown in Figure 6.10. The G-value at θ_{lab} = 0° is 0.42, very close to the value 0.45 of the full DWBA calculation. This supports the theoretical assumptions on the validity of the β-decay analogy and one-step process.

The approach here described was first applied to the one-neutron halo nucleus ^{11}Be [Cap01, Cap04b], giving similar results: the ^{11}Be angular distributions were described without the need to introduce large scaling factors; a dominance of unnatural parity transitions was found; the G-values at θ_{lab} = 0° indicated a spin transfer dynamics. We have consistency between the calculations in ^{11}Be and ^{15}C, in fact no parameters but the trivial (masses, charges and so on) were changed from the case of ^{11}Be.

The force of this approach consists of the use of interaction potentials determined not phenomenologically but from first principles and therefore completely general, which make the structure and reaction calculations fully consistent. For this reason the calculations reproduce well the data related both to ^{15}C and ^{11}Be without change the basic parameters.

The theoretical results shown in the present Section were published in ref. [Orr03].

6.7 Conclusions

A microscopic many-body theory for heavy-ion charge exchange reaction was presented. The approach includes direct CEX processes via the isovector NN-interaction. Nuclear structure is described microscopically calculating the CEX excitations by QRPA methods. A realistic NN-interaction [Hof98], including the tensor force, is used in every step of the calculations, assuring consistency between the structure and reaction mechanism calculations. Consistency between the calculations in ^{11}Be [Cap01, Cap04b] and ^{15}C is achieved through the use of the same parameters. Similar results are obtained in both nuclei; this strengthen our conclusions.

The CEX-QRPA approach describes very well the ^{15}C single particle strength – the ground and first excited state – and helps in extracting useful information about spin and parity for these states. The calculations reproduce also the known inversion between the $1/2^+$ and $5/2^+$ neutron orbitals. This is remarkable since no parameters were "a priori" adjusted to obtain this shell inversion. Nevertheless, the observed fragmentation of the strength at higher excitation energies cannot be explained in terms of 2-QP configurations in which the ^{14}C core is simply an inert spectator. It is clear that a more sophisticated theoretical approach is necessary, in which the quasi-particle states are coupled with the core excitations. As we will see, the DCP calculations of Chapters 7 and 8 will explain the observed fragmentation of the strength at high excitation energies. In the end, a comprehension of the ^{15}C experimental spectrum will be achieved (see Section 8.3.2).

One-step DWBA calculations based on the microscopic QRPA transition densities were performed for the two ^{15}C single particle states. A good agreement with the measured angular distributions is found. In particular, the order of magnitude of the measured cross sections for the ^{15}N(^{7}Li,^{7}Be)^{15}C reaction is reproduced without renormalization, confirming the reliability of the approach. Therefore the one-step mechanism is appropriate to describe the (^{7}Li,^{7}Be) CEX reaction at about 8 MeV/u of incident energy and for weakly bound nuclei. This is reasonable because the two-step route is strongly hindered in the (^{7}Li,^{7}Be) reaction even at low bombarding energy, due to the small overlap in the momentum space between the narrow wave functions of weakly bound states and the broad distributions of transfer operators, and due to the kinematic mismatch of the sequential transfer reaction proceeding via ^{8}Be states, which have a poor overlap in the nucleon transfer wave functions [Etc88].

A dominance of unnatural parity transitions is found and explained in terms of the spin transfer behaviour of the NN-isovector interaction at low bombarding energy. The prevalence of the unnatural parity transitions in the ^{15}N(^{7}Li,^{7}Be)^{15}C reaction and the G-values measured, together with the results concerning the ^{11}B(^{7}Li,^{7}Be)^{11}Be reaction [Cap01, Cap04], indicate a spin transfer dynamics in the low-energy charge exchange reactions. This quite surprising result is opposite to the predictions on the free NN-interaction at low energy.

Concluding, the force of the CEX-QRPA approach comes from the density dependent in-medium interaction of Hofmann and Lenske [Hof98] which, deriving from first principles, allows to treat satisfactorily the correlated 1p-1h states in different light neutron-rich nuclei without change the basic parameters.

CHAPTER 7

ANALYSIS OF THE ^{15}C STRUCTURE IN THE QRPA-DCP APPROACH

As seen in Chapter 6, theoretical calculations performed using a QRPA approach reproduce the ^{15}C single particle levels but they do not allow to explain the fragmentation of the strength observed at higher excitation energies. In the RPA-like theories the 2p-2h excitations are usually not considered or, as in Section 6.2.3, only an average treatment is included. In general, a microscopic treatment of the full 2p-2h space is not yet possible because of the very large phase space. In order to describe correctly the ^{15}C spectrum above 1.5 MeV excitation energy, it is necessary to take into account the Dynamical Core Polarization (DCP) effects. In the DCP approach, which is the subsequent step with respect to QRPA, a 2p-2h truncated space is microscopically treated: the subspace is given by the vibrational core excitations.

QRPA-DCP calculations were performed for the ^{15}C nucleus according to the Quasiparticle-Core Coupling (QPC) model [Len87]. In this model the dynamical many-body correlations in the odd-mass nuclei are described by coupling a quasiparticle to the core-excited configurations. These last are represented by correlated one particle-one hole (2-QP) core excitations and are described by the QRPA theory. The residual interaction between the one quasiparticle and core-excited configurations leads to the fragmentation of single particle or hole strengths over many eigenstates.

Some generalities about DCP are given in Section 7.1. The formulation of the QPC model is described in detail in Section 7.2. The results of the QRPA-DCP calculations for ^{15}C are shown in Section 7.3.

7.1 The core polarization

In general, the nuclear structure theories are formulated for truncated configuration spaces. In practice these truncated spaces are then projected into more limited model spaces, including the degrees of freedom of few nucleons. Usually only the valence nucleons may be excited while the more internal ones constitute an inert core, whose degrees of freedom are supposed to be frozen. The model wave functions obtained with these assumptions are not actually eigenfunctions of the true Hamiltonian and thus corrections are necessary in order to achieve a more realistic description. The core polarization represents the excitations of the

nucleons of the core owing to the motion of the active nucleons. Since the effects obtained by including states outside the model space are similar to polarization ones, the core polarization may account for the states outside the valence space. The more the initial space is enlarged, the less polarization corrections will be needed [Sat83].

Most of the work concerning DCP has been devoted to the study of odd-mass systems. In particular, as discussed in Section 1.3.2, one-nucleon halo nuclei are well suited to study the interaction between the weakly-bound valence nucleon and the even-mass core. Indeed, close to the drip lines the dynamical core polarization becomes particularly important because the core nucleus by itself may be already far off stability and thus easily polarizable. The study of these two-body systems is important also in order to describe three-body systems such as, e.g., the two-neutron halo nuclei.

There are mainly two types of theoretical approaches to describe the core polarization in one-neutron halo nuclei. The first one is based on a static deformation of the mean field, while the second considers a dynamical polarization of vibrational nature. An example of the first kind of approach is given in ref. [Nun96]. Nunes et al. used a rotational model for the core structure of the ^{11}Be, ^{13}C and ^{10}Li nuclei, in which the nuclear interaction is assumed to be the same for different states of the core (static rotor approximation). A deformed Woods-Saxon potential is used for the neutron-core interaction, where the quadrupole deformation parameter β was estimated by fitting the measured transition strengths B(E2) of the core. The calculated levels are in good agreement with the experimental ones but only in the case of low-energy states with positive parity,while the negative parity states are not well reproduced.

We will concentrate on the vibrational approach to the DCP. Bohr and Mottelson [Boh69] first investigated the single particle configurations with respect to a vibrating core by using the particle-vibration model. The odd-mass nuclear wave functions are separated into single particle and core-excited components, which are described by the collective model. The quasiparticle-phonon coupling model, introduced subsequently by Soloviev [Sol78], is a semi-microscopic approach that allows to treat also open-shell nuclei. The core excitations are calculated by QRPA methods with a schematic separable multipole-multipole interaction. Fully microscopic models using the many-body Green function theory [Fet71] were formulated by several authors and applied to describe the damping of the single particle motion [Bro63, Ham76, Ben80] and giant resonances [Jeu76, Wam82, Som83].

The above cited works study the single particle strength distributions close to the ground state (at only few MeV of excitation energy), assuming that the single particle components are given by the unperturbed eigenfunctions of a static shell model potential. This assumption corresponds to an approximation of the single particle self-energy operator by its diagonal parts only. This it is not enough if one wants to describe the strength distribution at higher excitation energies, as in the present case for ^{15}C.

The microscopic formulation of the QPC model introduced by Lenske [Len87], which will be discussed in detail in the next Section, allows a treatment also of the non-diagonal parts of the self-energy operator. The particle-core interaction will lead to an energy dependent contribution in the single particle self-energy operator, responsible for the mixing of the states with different radial quantum number n into which the single quasiparticle wave functions are expanded. The particular feature of this model is just the treatment of the 1-QP

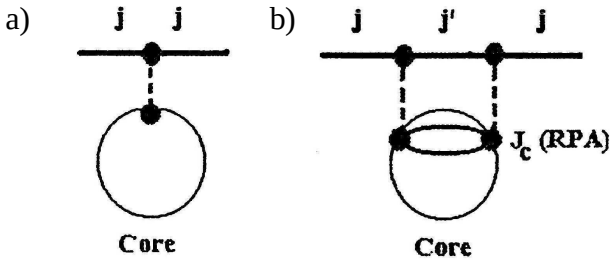

Figure 7.1. Diagramatic structure of a) mean field and b) core polarization interactions of a nucleon in a single particle state j. The interactions (meson exchange) are represented by dashed lines.

component. Recently this approach, well suited for light neutron-rich nuclei, has given interesting results [Len98b, Len01] (see Section 1.3.2 also).

7.2 The QPC model

In the various microscopic formulations [Ber83, Kre80, Sol87, Len87] of the QPC-model, the core-excited components are given by 2p-1h or 1p-2h (i.e., 3-QP) excitations. Using the QRPA formalism (Section 6.1), the 3-QP states in odd-mass nuclei are described by 1-QP states coupled to vibrational 2-QP (i.e., 1p-1h) QRPA excitations of the even-even core.

The dynamical correlations in odd-mass nuclei are treated in ref. [Len87] with a formulation of the QPC-model which accounts consistently for ground states correlations in all the steps of the theory. Particle- and hole-like excitations are treated symmetrically by including systematically the time-reversed components in QRPA notation ($\tilde{a}_{jm} = (-1)^{j+m}\, a_{j-m}$ as in Sect. 6.1). Single particle strength distributions and effective self-energies are studied with the Green function theory [Fet71]. The static self-energy (or mass operator) Σ_0 is obtained by using a basis of single particle states derived from a HFB mean field, with in addition long range particle-particle pairing correlations, as in the previous Chapter. In our case, the most important effect of pairing (introduced both in the single nucleon and core-excited parts of the odd-particle wave function) is the softening of the Fermi surface (see Figure 6.1), which influences the low-energy spectrum of the odd-mass systems. The static Σ_0 operator is supplemented by a non-static part $M(\omega)$, dependent on the frequency ω and responsible for the mixing of the single particle states from different major shells n.

The dynamical core polarization process for a nucleon in a single particle state j is shown schematically in Figure 7.1b, while Fig. 7.1a shows the corresponding mean field interaction. The dashed lines indicate the interactions (meson exchange). Core polarization leads to intermediate states (j' J_C), with a 2-QP core-excited state J_C (described by QRPA) and an 1-QP state j'. During these processes the particle may be scattered virtually into high lying orbitals with various multipolarities and excitation energies, with subsequent deexcitation back to the ground state. Assuming a spherical core nucleus, the only constraints on these 3-QP configurations are that total spin j and parity π_j must be conserved:

$$\underline{j} = \underline{j'} + \underline{J_C}; \qquad \pi_j = \pi_{j'} \cdot \pi_{J_C} \tag{7.1}$$

7.2.1 The QPC effective Hamiltonian and odd-mass wave functions

The QPC effective Hamiltonian of an odd-mass nucleus is given by:

$$H = H_{11} + V_{22} + V_{13} \tag{7.2}$$

where H_{11} is the 1-QP term, which includes the static mean field and pairing interaction and is diagonal in the 1-QP creation α^+_{jm} and annihilation α_{jm} state operators of eq. (6.4), with eigenvalues $\pm E_\mu$, respectively. Here μ = (n, *l*, j, m) denotes radial, orbital, total angular momenta and magnetic quantum numbers in the 1-QP channel. The residual interaction of eq. (7.2) consists of the two terms V_{22} and V_{13}. The first one acts on the 2-QP channel, giving the correlated 1p-1h core excitations which are described by the operators

$$\Omega^+_C \equiv \frac{1}{2}\sum_{j_1 j_2}\left[X_{j_1 j_2} Q^+_{j_1 j_2}(J_C) - Y^*_{j_1 j_2}\tilde{Q}_{j_1 j_2}(J_C)\right] \tag{7.3}$$

where the summation extends independently over the generic quasiparticle couple (j_1 j_2), which is corrected by the factor 1/2. The Ω^+_C operator is defined in terms of the 2-QP QRPA operators Q and Q^+ of eq. (6.5). The quasi-boson commutator relations valid for Q and Q^+ are assumed also for Ω^+_C. The QRPA amplitudes X and Y are state-dependent and satisfy symmetry relations. The QRPA states are solution of the equation of motion:

$$[H_{11} + V_{22}\,,\, \Omega^+_C] = E_C\, \Omega^+_C \tag{7.4}$$

The residual interaction V_{13} acts only in the odd-mass system coupling the 1-QP states $|\nu\rangle = \alpha^+_\nu |0\rangle$ to the 3-QP core-excited configurations $|(\mu\ c)_j\rangle = [\alpha^+_\mu\, \Omega^+_C]_j\, |0\rangle$, where c indicates the core quantum numbers. According to eq. (7.1), (μ c) $\equiv$ (j' J_C) are coupled to angular momentum j and carry parity $\pi(\mu\ c)_j = \pi(\mu) \cdot \pi(c)$. The 3-QP states are due to elementary excitations with energy given by the sum of the energies of 1-QP and of the unperturbed core:

$$E_{\mu c} = E_\mu + E_C \tag{7.5}$$

The definition of the core excitation operator Ω^+_C of eq. (7.3) is formally identical to those of the CEX operator ω^+_{JM} of eq. (6.8). The difference is represented by the choice of the QRPA vacuum state. Indeed, the vacuum used to calculate the CEX excitations was defined in eq. (6.3) as $|^{15}N_{GS}\rangle = |^{14}C_{GS} \otimes p\rangle$. However, in the QPC model the ^{15}C nucleus is differently described in terms of $|^{14}C \otimes n\rangle$ configurations. Thus the QRPA vacuum, above which Ω^+_C constructs correlated 2-QP core excitations, is the even-mass ground state:

$$|0\rangle \equiv |^{14}C_{GS}\rangle \tag{7.6}$$

The 3-QP configurations are given by the action of the $[\alpha^+_\mu\, \Omega^+_C]_j$ operator on the vacuum (7.6): 1-QP (neutron) is created and coupled to the ^{14}C core.

A first formula for the wave function of a generic odd mass nucleus, including in a non-trivial way many-body effects, is obtained by expanding the odd-mass wave function into the 1-QP and 3-QP configurations:

$$\left|\beta_j\right\rangle = z_\nu(\beta)\left|\nu_j\right\rangle + \sum_{\mu c} z_{\mu c}(\beta)\left|(\mu\ c)_j\right\rangle \tag{7.7}$$

where $\beta = (E_j, \pi_j)$ represents the excitation energy and parity of the odd-mass states. The 1-QP and 3-QP configurations are exactly orthogonal:

$$\left\langle 0\left|\alpha_{j\nu}\left[\alpha^{+}_{j\mu}\,\Omega^{+}_{C}\right]_j\right|0\right\rangle = 0 \tag{7.8}$$

This orthogonality condition is broken by the particle-core interaction V_{13}, which couples the 1-QP and 3-QP states. The orthogonality between the 3-QP states, valid up to order $O(|x|^2)$,

$$\left\langle 0\left|\left[\Omega_C\,\alpha_{j\nu}\right]_j\left[\alpha^{+}_{j\mu}\,\Omega^{+}_{C'}\right]_{j'}\right|0\right\rangle \approx \delta_{jj'}\,\delta_{j\mu\,j\nu}\,\delta_{J_C J_{C'}}\,\delta_{CC'} \tag{7.9}$$

is obtained with the quasi-boson approximation, in which the dynamics (and statistics) of the quasiparticle coupled to the excited core is assumed to be the same as in the ground state. Deviations from the ground state occupation probabilities are less than 10 % and become important only at high excitation energy ($E_x \geq 20$ MeV) [Len87].

7.2.2 Single particle mixing and QPC wave functions

The odd-mass wave functions of eq. (7.7) account already for important many-body aspects, but in this way the spectra may be described only at low excitation energy. A broader description of the correlation effects is obtained by including the mixing of 1-QP states from different major shells n. The major shell or energy mixing allows a study of the strength function also at higher excitation energies and, in principle, to describe the spectra over the whole energy range. The QPC-model wave functions are given by [Len87]:

$$\left|\beta_j\right\rangle = \sum_n z_n(\beta)\left|n_j\right\rangle + \sum_{\mu c} z_{\mu c}(\beta)\left|(\mu\ c)_j\right\rangle \tag{7.10}$$

New and interesting aspects of the single particle dynamics in an interacting many-body system are taken into account in eq. (7.10). The 1-QP component is expanded into a set of unperturbed single particle states of fixed orbital and total angular momentum (*l*, j) but different radial quantum number n. The sum over n represents the single particle mixing (i.e., the mixing of states with different n) induced by the frequency dependent part $M(\omega)$ of the mass operator. Since the particle-core interaction V_{13} does not conserve the single particle energy, the quantum number n is no longer good and the initial and final single particle states of the nucleon may be quite different (but with $\Delta E = \pm 2\hbar\omega$ to preserve parity). To account for these differences the core excitation process must provide a sufficiently large amount of linear momentum transfer. Therefore the energy mixing depends sensitively on the high-momentum (i.e., short-range) component of interaction.

The correlated odd-quasiparticle states of eq. (7.10) are defined in terms of the QPC excitation operators:

$$|\beta_j\rangle = \Gamma^+_\beta(j,m)\,|0\rangle \tag{7.11}$$

$$\Gamma^+_\beta(j,m) = \sum_n \left(z_{nj}(\beta)\,\alpha^+_{njm} + \tilde{z}^*_{nj}(\beta)\,\tilde{\alpha}_{njm} \right) + \sum_{\mu C} \left(z_{\mu C}(\beta)\,\left[\alpha^+_\mu\,\Omega^+_C\right]_{jm} + \tilde{z}^*_{\mu C}(\beta)\,(-1)^{j+m}\,\left[\Omega_C\,\alpha_\mu\right]_{j-m} \right) \tag{7.12}$$

The Γ^+_β operators act on the correlated QRPA ground state $|0\rangle$ of eq. (7.6). This assures consistency in the description of the core and odd-mass system. In fact, if only the core excitations are described by the use of QRPA methods and the odd-particle states are taken from uncorrelated $|BCS\rangle$ states, theoretical difficulties are found [Len87]. The difference between the QRPA and $|BCS\rangle$ vacuum states is given by admixtures of at least 4-QP configurations. Moreover, Γ^+_β contains in general contributions from the time-reversed operators of the 1-QP and 3-QP states, $\tilde{\alpha}_n$ and $[\Omega_C\,\alpha_\mu]_j$, respectively. Thus the final configuration can also be excited by annihilating 1-QP (indeed, $|0\rangle$ is no longer the vacuum for $\tilde{\alpha}_n$); besides excitations in the even-mass nucleus may also be created by annihilating virtual higher order ground state configurations. The correlated $|\beta_j\rangle$ states are orthogonal to the ground state $|0\rangle$. By analogy with the RPA theory, the stronger condition

$$\Gamma_\beta\,|0\rangle = 0 \tag{7.13}$$

may be imposed. Since eq. (7.13) implies $\langle 0|\,\Gamma^+_\beta = 0$, the orthogonality condition for the $|\beta_j\rangle$ states is expressed as:

$$\langle \gamma\ j'|\beta\ j\rangle = \langle 0|\left[\Gamma_\gamma(j'),\Gamma^+_\beta(j)\right]_+|0\rangle = \delta_{\gamma\beta}\ \delta_{jj'} \tag{7.14}$$

where the subscript + in the commutation brackets indicates anti-commutator relations. The important result of eq. (7.14) is that the Γ^+_β operators obey approximately the fermion anti-commutator rules. These will be assumed valid in the subsequent discussion. However, similar to the quasi-boson assumption for the QRPA phonons, this approximation is fulfilled only on the level of expectation values. The different components are then obtained from the state operator Γ^+_β:

$$\left[\alpha_n,\Gamma^+_\beta\right]_+ = z_n(\beta)\,; \qquad \left[\tilde{\alpha}^+_n,\Gamma^+_\beta\right]_+ = \tilde{z}^*_n(\beta) \tag{7.15a}$$

$$\left[\left[\alpha^+_\mu\,\Omega^+_C\right]^+,\Gamma^+_\beta\right]_+ = z_{\mu C}(\beta)\ ;\ \left[\left[\tilde{\Omega}_C\,\tilde{\alpha}_\mu\right]^+,\Gamma^+_\beta\right]_+ = \tilde{z}^*_{\mu C}(\beta) \tag{7.15b}$$

The normalization condition is written as:

$$\sum_n \left(|z_n(\beta)|^2 + |\tilde{z}_n(\beta)|^2 \right) + \sum_{\mu C} \left(|z_{\mu C}(\beta)|^2 + |\tilde{z}_{\mu C}(\beta)|^2 \right) = 1 \tag{7.16}$$

where the summation over n is restricted to 1-QP states with different energy but same j and π_j. The completeness relations, respectively for the 1-QP and 3-QP components, are:

$$\sum_{\beta}\left(\left|z_n(\beta)\right|^2+\left|\tilde{z}_n(\beta)\right|^2\right)=1 \tag{7.17a}$$

$$\sum_{\beta}\left(\left|z_{\mu C}(\beta)\right|^2+\left|\tilde{z}_{\mu C}(\beta)\right|^2\right)=1 \tag{7.17b}$$

where the sum includes eigenstates β with only positive (or negative) energy E_β, because E_β is positive (negative) for the positive (negative) time components.

7.2.3 Eigenvalue equation and mass operator

The stationary solutions of the eigenvalue problem defined by the Hamiltonian (7.2)

$$\left[H,\Gamma^+_\beta\right]=E_\beta\,\Gamma^+_\beta|0\rangle \tag{7.18}$$

have to be found using the QPC wave functions of eq. (7.10). In the equation of motion (7.18) E_β represents the excitation energy with respect to $|0\rangle$. By applying the anti-commutators of eq. (7.15) to eq. (7.18), a linear system of four equations is derived [Boh70]. Formally the system is equivalent to an effective Schrödinger equation for the 1-QP components, given by two coupled equations which describe completely the dynamics of the model:

$$\sum_{\nu'}\left\{\left[(E_\nu-E)\delta_{\nu\nu'}+M_{\nu\nu'}(E)\right]z_{\nu'}+M_{\nu\bar{\nu}'}(E)\,\tilde{z}^*_{\nu'}\right\}=0 \tag{7.19a}$$

$$\sum_{\nu'}\left\{\left[-(E_\nu+E)\delta_{\nu\nu'}+M_{\bar{\nu}\bar{\nu}'}(E)\right]\tilde{z}^*_{\bar{\nu}'}+M_{\bar{\nu}\nu'}(E)\,z_{\nu'}\right\}=0 \tag{7.19b}$$

where M(E) is the 1-QP energy-dependent mass operator (or dynamical self-energy) and the time reversed states are indicated by a bar. Because of the time reversal symmetry of the state operator Γ^+_β, only two of the four matrix elements of M(E) in eq. (7.19) are independent:

$$M_{\nu\nu'}(E)=-\sum_{\mu\,C}\frac{\langle\nu|V_{13}|(\mu\,C)_j\rangle\langle(\mu\,C)_j|V_{13}|\nu'\rangle}{E-E_{\mu C}}+\frac{\langle\nu\,(\mu\,C)_j|V_{13}|0\rangle\langle0|V_{13}|(\mu\,C)_j\,\nu'\rangle}{E+E_{\mu C}} \tag{7.20a}$$

$$M_{\nu\bar{\nu}'}(E)=-\sum_{\mu\,C}\frac{\langle\nu|V_{13}|(\mu\,C)_j\rangle\langle(\mu\,C)_j\,\nu'\,|V_{13}|0\rangle}{E-E_{\mu C}}+\frac{\langle\nu\,(\mu\,C)_j|V_{13}|0\rangle\langle\nu'\,|V_{13}|(\mu\,C)_j\rangle}{E+E_{\mu C}} \tag{7.20b}$$

thus the theory treats the dynamics symmetrically for both directions of propagation in time. Since M(E) vanishes at E = 0, the QPC theory guarantees that particle- and hole-type spectra are separated by an energy gap.

If the mass operator is purely diagonal the deviation of the quasiparticle strength from unity is simply given by the derivative of Σ_0 with respect to the energy, taken at the eigenvalue E_β [Fet71]. The dynamical effects of the non-diagonal self-energy M(E) on the

1-QP motion are taken into account by this extended QPC description and can be worked out by the Green function theory. The quasiparticle strength functions are derived as in Section 6.2.2 by solving the Dyson equation for the correlated 1-QP Green function. Processes of the following type are included: the quasiparticle μ is scattered on an initial core excitation vertex "off the energy shell" into an energy state $\nu \neq \mu$; it propagates and interacts repeatedly with the core until it is finally scattered back into the initial state μ.

7.2.4 Spectroscopic factors and single particle/hole wave functions

The quasiparticle approach describes in an unified way the particle and hole-type excitations, nevertheless to describe physical systems it is necessary to project the theoretical results into the hole or particle components.

The correlated single particle or hole wave functions are defined in coordinate space as:

$$\Phi_\beta^{(\pm)}(\mathbf{r}) = \frac{1}{\sqrt{S_\beta^{(\pm)}}} \sum_{n_\nu} C_\nu^{(\pm)}(\beta)\varphi_\nu(\mathbf{r}) \tag{7.21}$$

where S_β and C_ν are the spectroscopic factors and amplitudes, respectively, of the particle (+) and hole (–) wave functions Φ_β in a basis of physical nucleon states defined by the eigenstates of the static mean-field φ_ν. The summation extends only over radial states n_ν.

In order to calculate the wave functions Φ_β, the spectroscopic factors

$$S_\beta^{(\pm)} = \sum_\mu \left| C_\mu^{(\pm)}(\beta) \right|^2 \tag{7.22}$$

and the C_ν amplitudes have to be determined. In the quasiparticle representation and using the anti-commutator relations of eq. (7.15), the spectroscopic amplitudes for particle and hole channels, respectively, are evaluated as:

$$C_\mu^{(+)}(\beta) = \left\langle \beta \left| a_\mu^+ \right| 0 \right\rangle = \left\langle 0 \left| \left[\Gamma_{\beta}, a_\mu^+ \right]_+ \right| 0 \right\rangle = z_\mu^*(\beta)\, u_\mu + \tilde{z}_\mu(\beta)\, v_\mu \tag{7.23a}$$

$$C_\mu^{(-)}(\beta) = \left\langle \beta \left| \tilde{a}_\mu \right| 0 \right\rangle = \left\langle 0 \left| \left[\Gamma_{\beta}, \tilde{a}_\mu \right]_+ \right| 0 \right\rangle = -z_\mu^*(\beta)\, v_\mu + \tilde{z}_\mu(\beta)\, u_\mu \tag{7.23b}$$

where $|u_\mu|^2$ and $|v_\mu|^2$ are the emptiness and occupation probabilities of the generic state μ.The eigenvalues $E = \pm E_{\beta j}$ and the configuration amplitudes z_μ are obtained from the solution of the eigenvalue problem comprised by the DCP equation (7.19).

The sum rules are not satisfied separately in the particle and hole channels but, from the completeness relation (7.17a), a total sum rule is found to be valid for the spectroscopic factors:

$$\sum_\beta \left(S_\beta^{(+)} + S_\beta^{(-)} \right) = \sum_\mu \left(\left| u_\mu \right|^2 + \left| v_\mu \right|^2 \right) \tag{7.24}$$

where the right side corresponds to the number of basis states used in the 1-QP expansion.

7.3 Results of the QRPA-DCP calculations

QRPA-DCP calculations were performed for ^{15}C. The ^{15}C states are described microscopically by coupling the single neutron states $|1\text{-QP}\rangle = |^{14}C_{GS} \otimes n\rangle$ to the core-excited configurations $|3\text{-QP}\rangle = |^{14}C_{exc} \otimes n\rangle$, as in eq. (7.10). The core excitations are described by the QRPA theory as 2-QP excitations starting from the even-mass ground state $|^{14}C_{GS}\rangle$.

A good description of the 1-QP spectra may be obtained only by using a realistic NN-interaction and working with large configuration spaces. The D3Y G-matrix interaction of Hofmann and Lenske [Hof98] (see Section 6.3) was used in every step of the calculations; both the isoscalar and isovector parts were included. The calculations mainly consist of three steps. In the first, exactly as in Section 6.2.4, the single particle wave functions of ^{14}C were calculated in a mean field given by a superposition of two Woods-Saxon potentials, whose parameters were derived by fitting the ^{14}C HFB potential. The calculation was performed in a box with $R_{box} = 40$ fm and for $E_X \leq 100$ MeV and $L \leq 6$ (see Sect. 6.4.2 for the details).

Then, the ^{14}C single particle wave functions were used as input for QRPA calculations, which allow a study of the distributions of the collective excitations. The 0^+ ground state of the even-even ^{14}C nucleus is characterized mainly by the closure of the neutron 1p shell, with small admixture of $(sd)^2$ components: ~ 8 % for $(1d_{5/2})^2$ and ~ 1 % for $(2s_{1/2})^2$ [Cec75]. In the QRPA picture, 1p-1h excitations with respect to $^{14}C_{GS}$ are considered. Thus, e.g., low-lying negative-parity states are obtained with $(sd)^1(1p)^{-1}$ configurations, i.e., when one neutron is excited from the 1p shell to the (sd) shell. For example, the $J^\pi = 3^-, 2^-$ doublet at $E_x = 6.73$ and 7.34 MeV [Ajz91], respectively, is explainable by assuming a $(1d_{5/2})^1(1p_{1/2})^{-1}$ configuration.

The ^{14}C QRPA response functions were obtained with the Green's function method for $E_x \leq 40$ MeV and different multipolarities (from 0 to 4). The core excitations were calculated allowing 2-QP excitations up to 100 MeV. The quasiparticle energies and occupation amplitudes for ^{14}C were obtained using a BCS pairing field, dependent only on the quantum numbers transferred in the excitation of the 2-QP pair and not on the particular QRPA state, with constant strength $G_p = 23$ MeV and $G_n = 17.5$ MeV for protons and neutrons states, respectively. State dependent pairing correlations were introduced in the calculations for the $2s_{1/2}$ neutron state by redistributing the related strength between two energy levels: 90 % of the strength at the usual HFB energy (–0.626 MeV) and 10 % at a new level at –4.0 MeV.

The QRPA electromagnetic response functions are shown in Figures 7.2 and 7.3 for natural and unnatural parity states of ^{14}C, respectively. The low-lying excited states of ^{14}C (with E_x between 6 and 8 MeV [Ajz91]) in general give rise to peaks with very low intensity: e.g., the ^{14}C first excited state ($J^\pi = 1^-$) at $E_x = 6.09$ MeV is found in the 1^- QRPA spectrum as an extremely weak peak at 6.04 MeV, corresponding to $(2s_{1/2})^1(1p_{1/2})^{-1}$ and $(1d_{5/2})^1(1p_{3/2})^{-1}$ configurations. The major part of the 2-QP strength is found at higher excitation energy and corresponds to more excited 2-QP configurations, which might be associated to higher energy ^{14}C states [Ajz91]. However, it is pointed out that the QRPA strength distributions do not include all the possible collective states. In fact, the QRPA approach can reproduce only 1p-1h configurations, thus highly collective states are not expected in the QRPA spectra.

The last step regards the DCP calculations, whose input is the calculated single particle and core-excited wave functions. The occupation probabilities $|v_j|^2$ of the single proton and

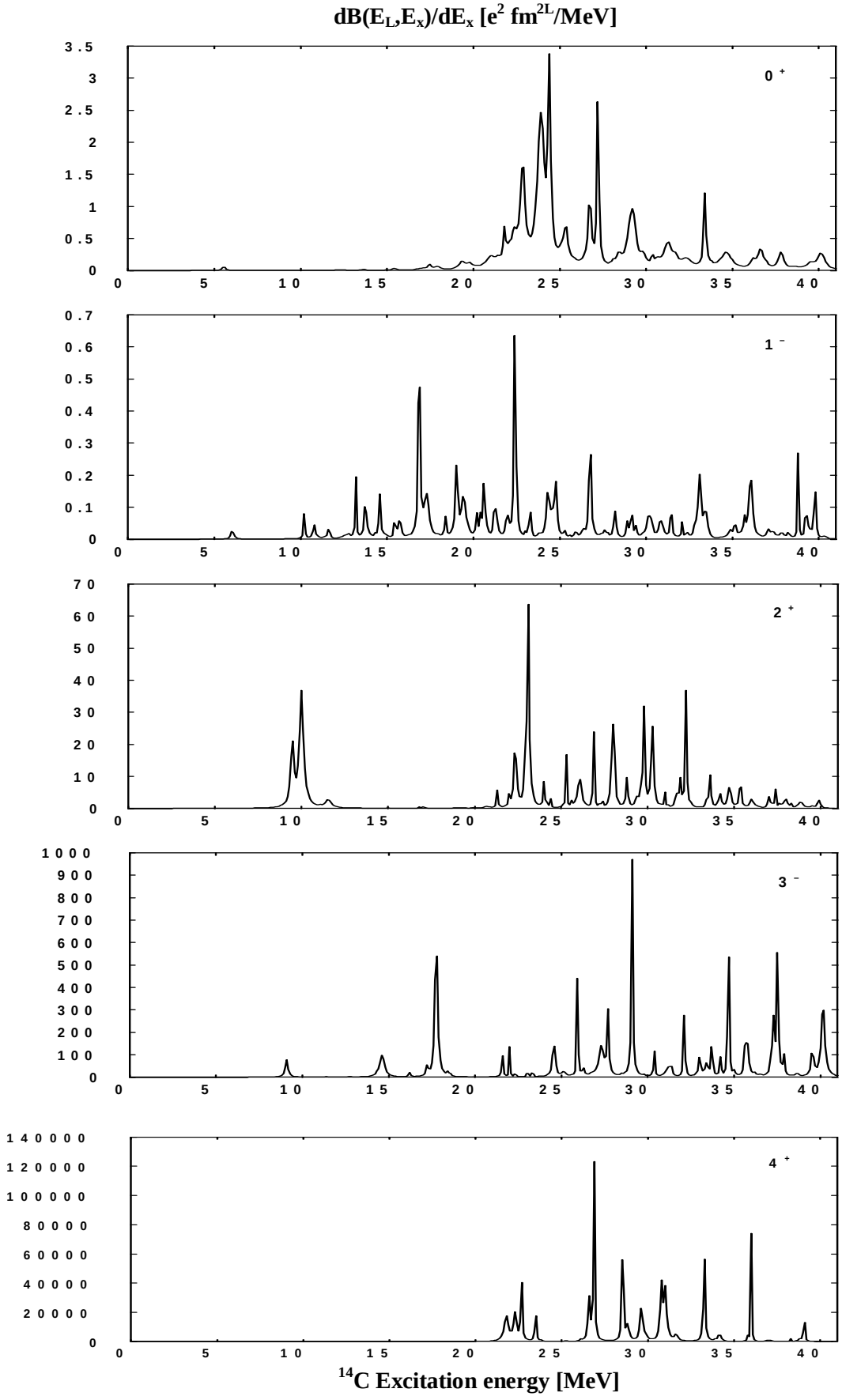

Figure 7.2. QRPA electromagnetic response functions for ^{14}C natural parity states.

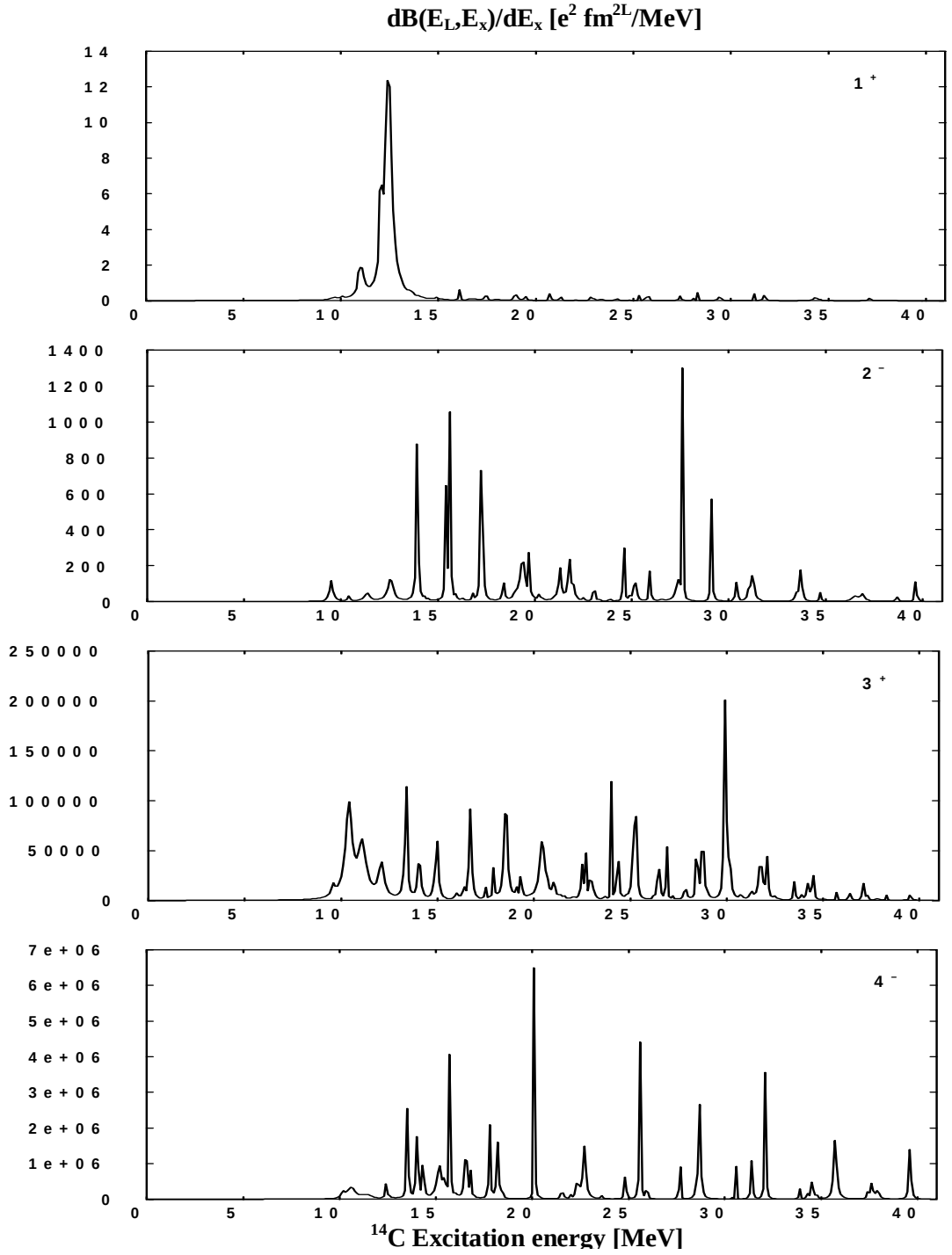

Figure 7.3. QRPA electromagnetic response functions for ^{14}C unnatural parity states.

single neutron states E_j in the ^{14}C core are shown in Table 7.1. They were calculated by use of a state dependent pairing field with G = 30 MeV, obtained as in Section 6.2.5. The DCP eigenvalues and eigenfunctions $|\beta_j\rangle$ were calculated by solving the effective 1-QP Scrödinger equation (7.19). The 1-QP response functions for ^{15}C were obtained from the resolution of the Dyson equation (see Section 6.2.2). Finally, the spectroscopic factors (eq. (7.22)) may be determined and it is possible to pass from the quasiparticle to the single particle or hole representations, corresponding to ^{15}C and ^{13}C, respectively.

Table 7.1. Occupation probabilities $|v_j|^2$ for the single particle states E_j in ^{14}C, calculated with a state dependent pairing field (see Section 6.2.5).

	Protons		Neutrons	
n l j	**E_j [MeV]**	**$\|v_j\|^2$**	**E_j [MeV]**	**$\|v_j\|^2$**
$1s_{1/2}$	-27.020	1	-24.902	1
$1p_{3/2}$	-20.831	1	-14.814	1
$1p_{1/2}$	-10.848	0.018	-8.176	1
$1d_{5/2}$	-3.193	0.005	-0.719	0.016
$2s_{1/2}$	-1.367	0.003	-0.626	0.008

Table 7.2. Range of values of the radial quantum number n which, for each state (*l*,j), are included in the 1-QP expansion into major shell components.

l j	$s_{1/2}$	$d_{5/2}$	$d_{3/2}$	$p_{3/2}$	$p_{1/2}$	$f_{7/2}$	$f_{5/2}$	$g_{9/2}$	$g_{7/2}$
n_i	1	1	1	1	1	1	1	1	1
n_f	10	10	6	4	4	3	3	3	3

The DCP response functions were calculated for the s, d, p, f and g ^{15}C strengths, as listed in Table 7.2, and for 1-QP energies up to 15 MeV. The major shells which, for each state (*l*,j), contributes to the 1-QP expansion are those with radial quantum number n from n_i to n_f (see Table 7.2). The 1-QP states of Table 7.2 are coupled to the core excitations to construct the 3-QP states. The 3-QP components are fully taken into account by allowing QRPA core excitations up to 25 MeV and including core states with J_C^π from 0^+, 1^- to 4^+, 4^-. The ^{15}C response functions are shown in Figure 7.4 with the ^{15}C excitation energy scale, which is obtained from the 1-QP energy scale by subtracting the ground state energy.

The intense peaks at $E_x \sim 0$ MeV in Figures 7.4a and b correspond to the $2s_{1/2}$ ground and $1d_{5/2}$ first excited ^{15}C state, respectively. Strong fragmentation of the ^{15}C strength is found in the $s_{1/2}$ (Fig. 7.4a), $d_{5/2}$ (Fig. 7.4b) and $d_{3/2}$ (red line in Fig. 7.4c) strengths, in the energy region $E_x \sim$ from 5 to 11 MeV. Large bumps are observed in the remaining strength functions (Fig. 7.4c and d), where the $f_{7/2}$ and $f_{5/2}$ strengths are found to be identical and the same occurs for the $g_{9/2}$ and $g_{7/2}$ ones.

The results of the QRPA-DCP calculations foresee fragmentation of the $s_{1/2}$, $d_{5/2}$ and $d_{3/2}$ ^{15}C strengths. Therefore the fragmentation of the ^{15}C strength observed in the experimental spectra in the region $E_x \sim$ from 6 to 9 MeV (see Section 5.2.2.) may be explained in terms of dynamical core polarization. In the light of these results, the narrow resonances seen in the ^{15}C continuum may be interpreted as BSEC (Sect. 2.2) with low spin (possible J^π: $1/2^+$, $3/2^+$ or $5/2^+$). The present results confirm the predictions obtained by similar calculations [Noc03].

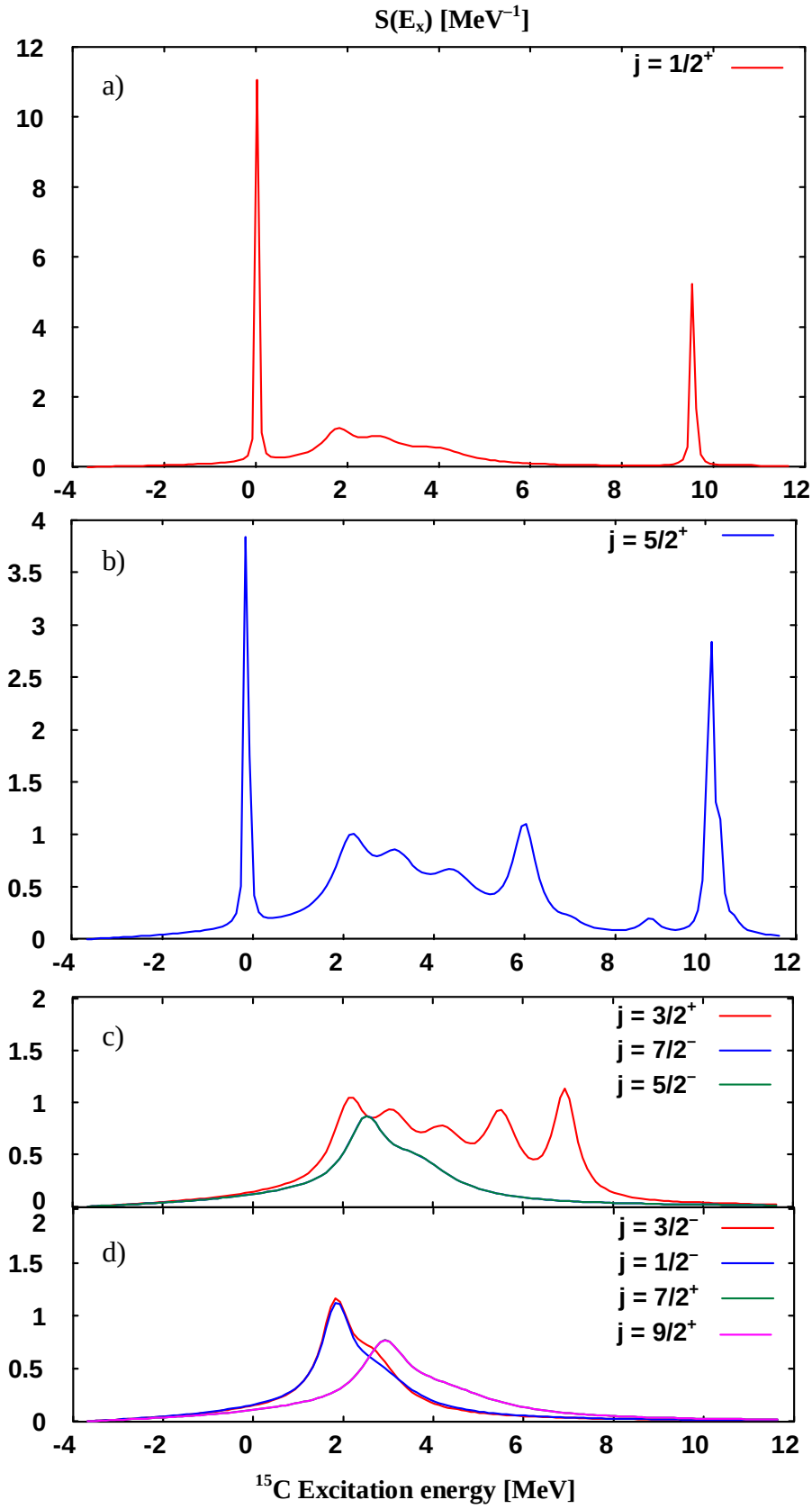

Figure 7.4. DCP response functions for ^{15}C, calculated according to the QPC-model, for the a) $s_{1/2}$; b) $d_{5/2}$; c) $d_{3/2}$, $f_{7/2}$, $f_{5/2}$; d) $p_{3/2}$, $p_{1/2}$, $g_{9/2}$ and $g_{7/2}$ strengths. The bin size is 100 keV.

The strength fragmentation over various eigenstates is a consequence of dynamical many-body effects, included in the adopted microscopic formulation of the QPC model [Len87]. This approach, in which the quasiparticle states are coupled with the QRPA core excitations by the residual interaction, allows a description of the single particle strength distributions also at high excitation energies.

Moreover, it is confirmed to be suitable for light neutron-rich nuclei, where the dynamical core polarization is expected to be enhanced owing to the softer core. Once it was established that the ^{15}C narrow continuum states may be described as BSEC excitations, line shape calculations based on the QPC-model could be performed, as described in Chapter 8, where we consider for the first time the effects of the BSEC phenomenon in unstable neutron-rich nuclei.

CHAPTER 8

RESONANCE LINE SHAPE IN LIGHT NEUTRON-RICH NUCLEI

The work presented in this Chapter takes its origin from the new experimental observation discussed in Chapter 5, concerning the possible interference between the 3-body phase space continuum and the 8.5 MeV BSEC (see Sections 5.2.3 and 7.3). This work gets inspiration from the Baur and Lenske article [Bau77], in which the Fano interference [Fan61] is analysed in the case of the (p,p') inelastic scattering of nucleons on nuclei.

In a preliminary step, in Sect. 5.2 the 8.5 MeV peak has been fitted by simply assuming a Gaussian shape, but in general interference phenomena give rise to typically asymmetric structures in the spectra with a non-trivial energy dependence. Besides, rather than the position of the unperturbed level, a "modified" resonance energy is experimentally accessible. In fact the position, width and shape of a resonance may be affected by the presence of other resonances or continuous backgrounds. This is due to the configuration interactions shifting the position of the peak and/or altering the shape, which then might deviate considerably from the Gaussian or Breit-Wigner forms, often used to fit the data. Configuration interaction may be regarded as a core effect, which takes place in the outer region of the core [Fan61].

To show the generality of this subject and the interest of various fields of the physics in it, in Section 8.1 a historical background about the Fano interference is given, together with the basic points of the Fano's original approach. The theoretical model used to investigate the resonance line shape in light neutron-rich nuclei is described in Section 8.2. The results of calculations are reported and discussed in Section 8.3. The ^{15}C results are compared with the experimental spectra of Chapter 5 (see 8.3.2). With the purpose of a systematic study of the interference effects in the C-isotopes, results for ^{17}C and ^{19}C are presented (see 8.3.4). A summary is given in Section 8.4. This work will be object of next publications.

8.1 Fano interference

The first theory of these interference effects was developed by Fano in the 1960's when studying the inelastic scattering of electrons on atoms exciting autoionized states [Fan61]. Fano interference consists of the quantum-mechanical interaction between discrete and continuous states, leading to characteristically asymmetric peaks in the spectra. In the original work of Fano [Fan61] explicit results were derived for the following cases: one resonance

interacting with one continuum, one discrete level interacting with two or more continua, and a set of discrete levels coupled with one continuum. In particular, Fano found that the coupling of a discrete autoionized state with a continuum leads to an asymmetric line shape in the spectra of the electrons, which may be characterized by one real parameter q (the Fano's parameter). Fano applied his theory to the perturbation of a Rydberg series of discrete levels, giving the position and intensity shifts produced in the series by the interaction with a level of another configuration. Also the possible connection with the nuclear theory of resonance scattering was indicated.

Fano interference is an universal phenomenon, which has been observed in many different areas of physics. A theoretical framework was developed in a series of papers by Feshbach [Fes58, Fes62, Fes67], giving an unified description of the nuclear reaction theory and considering also overlapping resonances. Several authors have extended Fano's model to include the case of many resonances coupled to many continua, principally regarding atomic physics phenomena. In detail, Mies [Mie68] included the inelastic couplings between the continuum states and examined the effects of overlapping resonances for the atomic photoabsorption and electron diatomic molecule scattering. Starace [Sta72] enlarged the theory for the photoabsorption, showing how to construct the prediagonalized states which Fano and Mies assumed at the outset and deriving the total photoabsorption cross section as a sum of the partial ones. Later, Bhatia and Themkin [Bha84] unified the Fano and Feshbach approaches and gave a derivation of Fano's results using the projection-operator formalism. They also included the interaction between discrete resonances, leading to energy-dependent line shape parameters. Connerade and Lane [Con88] extended the work of Mies, analysing many interesting effects associated with interactions between the resonances.

Recently, Ligterink considered the case of many resonances and one continuum, applying the Fano theory to the analysis of the hadronic resonances of the ρ-meson in the two-pion decay of the τ-lepton. The resonance shape is described through the coupling of the ρ-meson resonance to the pionic continuum; the matrix elements of the Hamiltonian are fitted by the data [Lig02]. Finally, in solid-state physics, Glutsch derived a compact formula for the optical absorption coefficient of the Fano model in the general case of many resonances coupled with many continua. His calculations [Glu02] are entirely based upon a simple matrix algebra, without the need to involve the scattering theory.

8.1.1 Fano's original approach

Fano developed [Fan61] an analysis for atomic resonances based on a general Hamiltonian for such systems. This Hamiltonian can be diagonalized exactly, therefore yielding direct relations between its parameters and the data.

Let us examine the simplest case of a discrete configuration $|\varphi\rangle$ interacting with a continuum of states $|\psi_{E'}\rangle$. Assuming that $|\varphi\rangle$ and $|\psi_{E'}\rangle$ diagonalize separate submatrices of the total Hamiltonian H,

$$\langle\varphi|H|\varphi\rangle = E_{\varphi} \tag{8.1}$$

$$\langle\psi_{E''}|H|\psi_{E'}\rangle = E'\delta(E''-E') \tag{8.2}$$

the task is to introduce the off-diagonal terms which couple the two configurations:

$$\langle \psi_{E'} | H | \varphi \rangle = V_{E'} \tag{8.3}$$

Each energy value E within the range of E' is an eigenvalue of the energy matrix (8.1, 8.2, 8.3) to be diagonalized. The exact total wave function $|\Psi_E\rangle$, eigenvector of the full Hamiltonian H, is a linear combination of the two sets $|\varphi\rangle$ and $|\psi_{E'}\rangle$:

$$\Psi_E = a\varphi + \int dE' \, b_E \psi_{E'} \tag{8.4}$$

where the coefficients a and $b_{E'}$, which are functions of E, are determined as solutions of the system of equations pertaining to the energy matrix:

$$E_\varphi \, a + \int dE' \, V^*_{E'} \, b_{E'} = E \, a \tag{8.5}$$

$$V_{E'} \, a + E' \, b_{E'} = E \, b_{E'} \tag{8.6}$$

The diagonalization of the matrix is achieved by solving system (8.5, 8.6). This system is exactly solved using the Dirac's procedure of introducing into eq. (8.5) the formal solution [eq. (8.7)] of eq. (8.6):

$$b_{E'} = \left[\frac{1}{E - E'} + z(E)\delta (E - E') \right] V_{E'} \, a \tag{8.7}$$

thus, from eq. (8.5), it is possible to determine z(E) as:

$$z(E) = \frac{E - E_\varphi - F(E)}{|V_E|^2} \tag{8.8}$$

where

$$F(E) = P \left[\int dE' \frac{|V_{E'}|^2}{E - E'} \right] \tag{8.9}$$

and P indicates the principal part of the integral. The phase shift due to configuration interaction of the continuum $|\psi_{E'}\rangle$ with the single discrete state $|\varphi\rangle$ is defined as:

$$\Delta = - \arctan[\pi / z(E)] \tag{8.10}$$

and it varies swiftly by $\sim\pi$ as E traverses an interval $\sim|V_E|^2$ (index of the configuration interaction strength) about the "resonance" at $E = E_\varphi + F$. The quantity F represents thus a shift of the resonance position with respect to the unperturbed resonance energy E_φ .

The coefficient a, which factors out from (8.5), is determined by normalization as:

$$|a(E)|^2 = \frac{|V_E|^2}{\left[E - E_\varphi - F(E) \right]^2 + \pi^2 |V_E|^4} \tag{8.11}$$

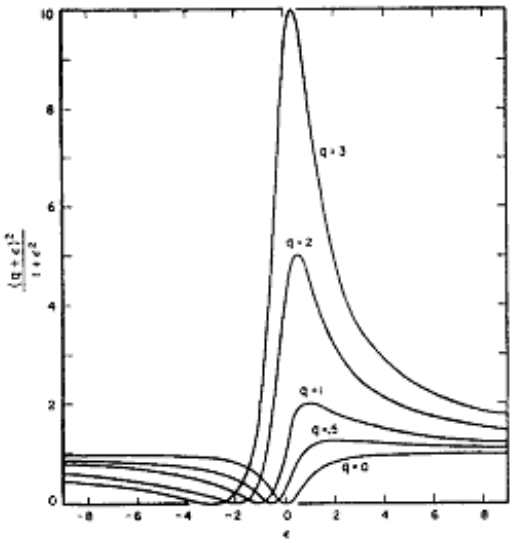

0

Figure 8.1. General line shape of isolated autoionizing resonance in a flat continuum for different values of the Fano's parameter q, according to the formula (8.12) taken from the classic paper of Fano [Fan61].

This result shows that the discrete state $|\varphi\rangle$ is "diluted" by the configuration interaction throughout a band of actual stationary states $|\Psi_E\rangle$, whose profile is represented by a resonance curve with half-width $\Gamma/2 = \pi|V_E|^2$ which reduces to a Breit-Wigner form if the coupling function V_E is a constant.

A study of the excitation probability of the stationary state $|\Psi_E\rangle$ is interesting. Independently from the excitation mechanism, this probability may be represented as the squared matrix element of a suitable transition operator T between $|\Psi_E\rangle$ and an initial state $|i\rangle$. The ratio of the transition probability $\left|\langle\Psi_E|T|i\rangle\right|^2$ to the probability $\left|\langle\psi_E|T|i\rangle\right|^2$ of transition to the unperturbed continuum is represented by a single family of curves, according to the Fano's famous result:

$$\frac{\left|\langle\Psi_E|T|i\rangle\right|^2}{\left|\langle\psi_E|T|i\rangle\right|^2} = \frac{(q+\varepsilon)^2}{1+\varepsilon^2} \tag{8.12}$$

which is valid for an isolated line in a "flat" continuum, that is a background with a constant phase shift δ. Eq. (8.12) is a function of the reduced energy ε and of the Fano's parameter $q = \cot\delta$:

$$\varepsilon = -\cot\Delta = \frac{\pi|V_E|^2}{E - E_\varphi - F(E)} \tag{8.13}$$

$$q = \frac{\langle\Phi|T|i\rangle}{\pi\, V_E^*\langle\psi_E|T|i\rangle} \tag{8.14}$$

where $|\Phi\rangle$ indicates the state $|\varphi\rangle$ modified by an admixture of continuum states:

$$\Phi = \varphi + P\left[\int dE' \frac{V_E \psi_{E'}}{E - E'}\right] \tag{8.15}$$

The shape of the resonance depends on the mode of excitation because q involves the probability of excitation to the continuum, therefore depending also on the initial state $|i\rangle$. Thus the profile q can be varied by varying the initial state, while the resonance width remains constant.

In Figure 8.1 the curve (8.12) is plotted as function of ε and for different q values. The two contributions to $\langle \Psi_E | T | i \rangle$, $\langle \Phi | T | i \rangle$ and $\langle \psi_E | T | i \rangle$, interfere with opposite phase on the two sides of the resonance, giving the characteristic line shapes of Figure 8.1. In particular, the asymmetric peak lies adjacent to a minimum in the cross section, indicating that the transition probability vanishes on one side of the resonance. The profile shape is perfectly symmetric only for q = 0, while for $q \to \pm\infty$ the quasi-Lorentzian limit is recovered.

When two or more continua are present, Fano showed that one should expect to observe an excitation spectrum of the type in Figure 8.1 superposed on a smooth background, thus the cross section should not drop to zero, even with ideal resolution.

8.1.2 Fano interference in nuclear physics

In nuclear physics Fano interference is often described in terms of the interaction of open and closed channels. Using the projection-operator formalism it is possible to obtain a Schrödinger equation for the open channel part, eliminating the closed channel configurations [Fes58, Fes62, Fes67]. By analysing the structure of the effective Hamiltonian for the open channels, Feshbach obtained the various aspects of reaction theory. The effective Hamiltonian consists of a part which varies slowly with energy – responsible for the direct reactions, for potential scattering and "single particle" giant resonances – and a rapidly varying part which gives rise to the narrow compound nuclear resonances of Breit-Wigner form, closely associated with the bound state wave functions of the closed channels.

The Fano model is exactly solvable, but the calculation, which is based on an eigenvalue problem, sometimes may be intricate. The typical approach in atomic physics is to expand the BSEC wave functions into a basis of electron Hartree-Fock (HF) wave functions, to put the matrix elements calculated in that basis together with the continuum ones into a large matrix and to solve the resulting eigenvalue problem, using matrix algebra without involving the scattering theory. Instead we used a different, but equivalent, method which follows and extends the approach of refs. [Bau75, Bau77] developed in the 1970's, namely to solve directly the coupled channels problem in the coordinate space. This coupled channels model gives rise to a interfering resonance through the coupling of the single particle continuum to a BSEC.

In detail, in ref. [Bau75] this method was applied to the study of the resonance line shape in the (d,p) stripping reactions into the continuum, while in ref. [Bau77] it was employed to study the line shape in the (p,p') inelastic scattering. Different assumptions about the radial shape of the coupling term have been made, the main are: a constant Volume Coupling potential in the interior region (model VC); a Surface peaked Coupling in the form of a δ-interaction (model SC); or both cases. Analytical solutions can be obtained for the coupled channels problem. The wave functions obtained with the models VC and SC, although identical in the exterior region ($r > R_0$ = potential radius) by definition, differ considerably in the interior region, as shown in Fig. 8.2.

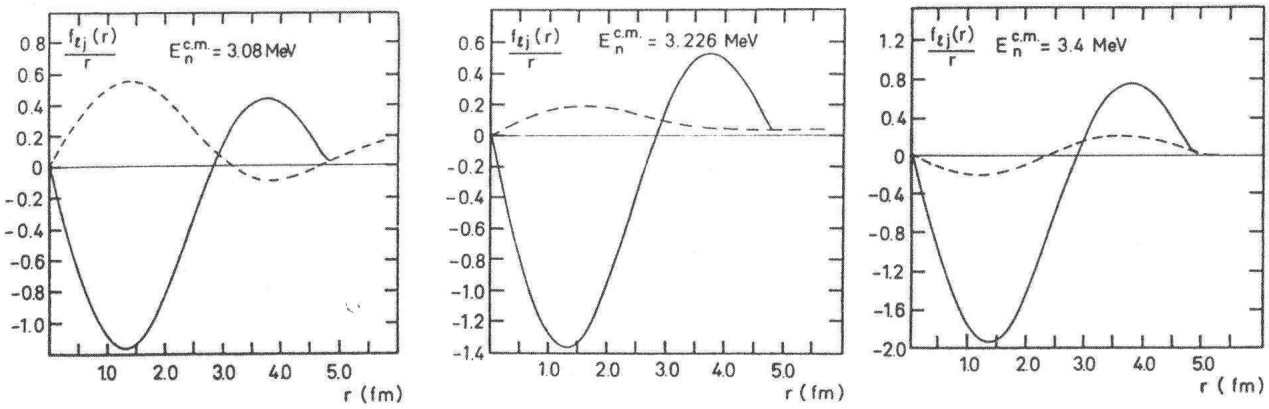

Figure 8.2. Comparison of the neutron wave functions of model VC (dashed lines) and model SC (continuous line) for three different neutron energies [Bau75].

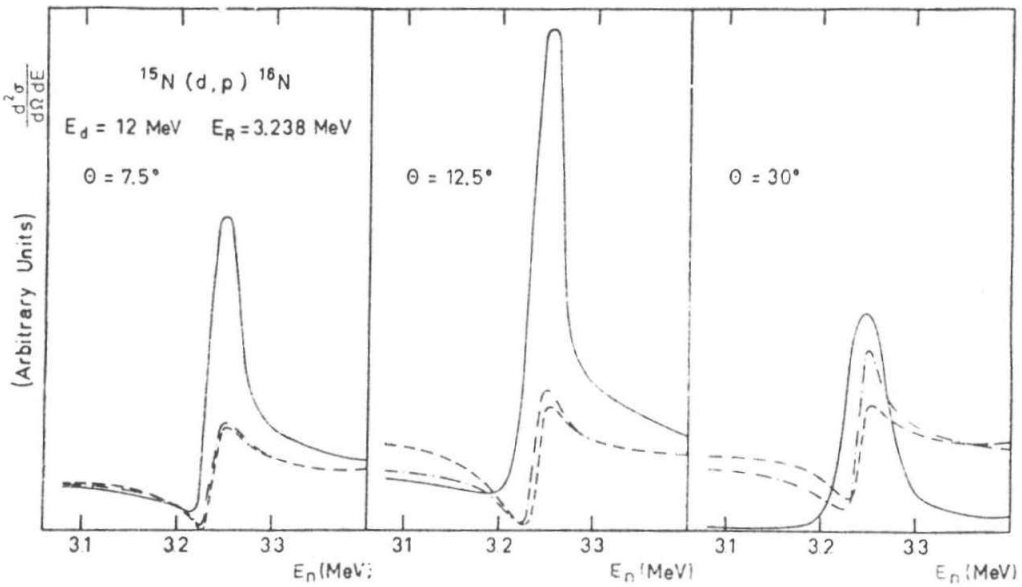

Figure 8.3. Calculation for the $^{15}N(d,p)^{16}N$ continuum stripping spectrum. Three different curves are shown: model VC (dashed line), model SC (continuous line) and a calculation with a cut-off for $r < R_0$ (dashed-dotted line) [Bau75].

This means that the resonance energy, width and background phase shift are not sensitive to the inner part of the wave function. An obvious improvement might be to use Woods-Saxon type potentials. However, in that case it is expected that the strong model dependence persists [Bau75]. With the general assumption of a Breit-Wigner shape for the unperturbed resonance, the typical interference pattern shown in Figure 8.3 was found by calculations for the $^{15}N(d,p)^{16}N$ stripping reaction. The resonance shape tends to become symmetric with increasing proton scattering angle, especially in the case of the model SC. The difference between the model VC and the calculation with a cut-off for $r < R_0$ becomes larger with increasing proton scattering angle because the influence of the interior region increases. However, for $^{208}Pb(d,p)^{209}Pb$ (unbound) at an energy close to the Coulomb barrier, the contributions from the interior are modest: the interior wave functions of the resonance for the different models have the same shape and are nearly equal [Bau75].

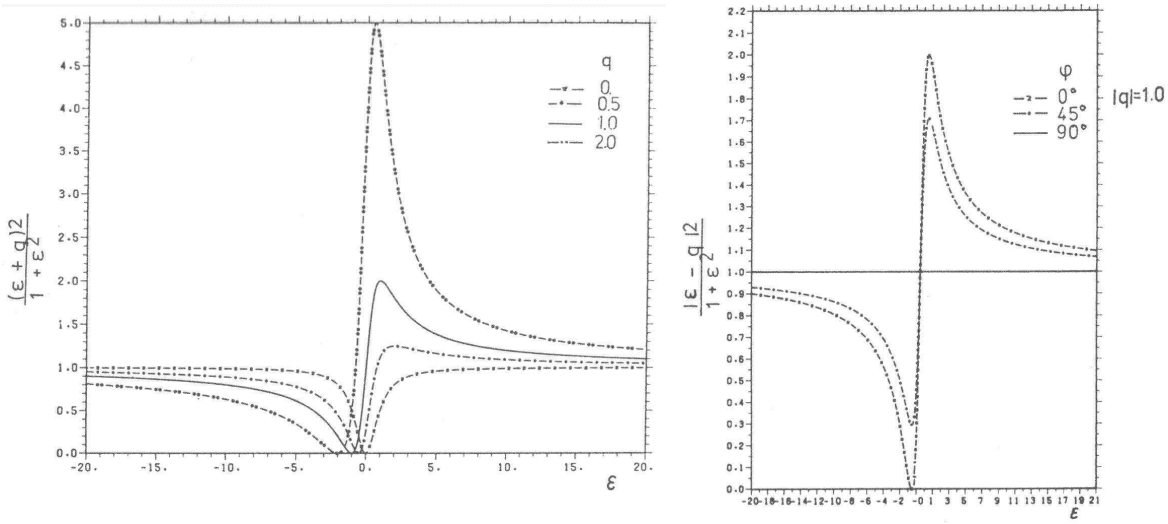

Figure 8.4. Comparison of the line shapes with real and complex line shape parameter q. Left: The shape for different real values of q. Right: The line shape for complex $q = |q|\, e^{i\varphi}$ with $|q| = 1$ and various phase φ [Bau77].

In the case of the (p,p') inelastic scattering [Bau77], the asymmetric resonances arising from the coupling of the single particle continuum to the BSEC of Breit-Wigner form have a characteristic interference pattern with an energy dependence more complicated than a simple Breit-Wigner function. Assuming a direct excitation process and including the distortion for the projectile wave function (DWBA), the simple Fano formula (8.12) has to be generalized, named replaced by one with a complex Fano's parameter. In Fig. 8.4 the comparison of the line shapes with real and complex q is shown [Bau77]. The main consequence of a complex q is the prediction of a specific evolution of the line shape as a function of the scattering angle.

8.2 Theoretical approach

A theoretical model to investigate the resonances and their line shapes in the low-energy continuum has been developed, on the basis of the Quasiparticle-Core Coupling (QPC) model (see Sect. 7.2 and ref. [Len87]). The model extends the previous work of refs. [Bau77, Fuc80], by incorporating information from HFB and QRPA calculations for potentials, single particle and excitation energies and transition probabilities, respectively. Two components are considered: the single particle continuum and the resonances, which in absence of a continuum are discrete eigenstates. A general Hamiltonian couples the continuum to the set of discrete states that are orthogonal with respect to each other.

Let us recall some general concepts already discussed in Section 7.2. In our model we consider the QPC effective Hamiltonian, which has the form:

$$H = \begin{pmatrix} H_{11} & V_{13} \\ V_{31} & H_{33} \end{pmatrix} \tag{8.16}$$

where H_{11} represents the Hamiltonian operator acting on the one-quasiparticle (1-QP) components, describing the single particle motion of the valence neutron with respect to the inert core, and defines the basis of single particle states. H_{33} acts on the 3-QP components,

chosen as correlated one particle-one hole (i.e., 2-QP) core excitations – described below in terms of quasi-particle RPA (QRPA) theory – to which 1-QP states are coupled. The residual interaction V_{13}, acting between the two above-mentioned channels, leads to the coupling between the 1-QP states and the 3-QP core-excited configurations. The eigenstates $|\beta_J\rangle$ of the full Hamiltonian H, i.e., (H – E) $|\beta_J\rangle$ = 0, will be therefore a superposition of the two components of 1-QP $|n_J\rangle$ and 3-QP $|(j' J_C)_J\rangle$, respectively without and with core excitation:

$$|\beta_J\rangle = \sum_n z_n |n_J\rangle + \sum_{j' J_C} z_{j' J_C} |(j' J_C)_J\rangle \tag{8.17}$$

where the total spin $\underline{J}$ and parity π_J must be conserved: $\underline{J} = \underline{j'} + \underline{J_C}$; $\pi_J = \pi_{j'} \cdot \pi_{J_C}$; and $\underline{j'}$ and $\underline{J_C}$ indicate the spin of the 1-QP valence and the 2-QP core-excited state, respectively. The first term includes a superposition of radial wave functions with nodes n because in an interacting system the radial quantum numbers n are no longer conserved. The core excitations in the second term are described by QRPA states with energy E_C.

Projecting the Schrödinger equation onto the 1-QP and 3-QP channels and integrating out the core degrees of freedom, the following set of coupled equations is obtained:

$$\left(h_{n_j} - \varepsilon_1\right) z_n + \sum_{j' J_C} z_{j' J_C} \langle n_J | V_{13} | (j' J_C)_J \rangle = 0 \tag{8.18a}$$

$$\left(h_{j' J_C} - \varepsilon_2\right) z_{j' J_C} + \sum_n z_n \langle (j' J_C)_J | V_{13} | n_J \rangle = 0 \tag{8.18b}$$

describing the change of single particle motion under the influence of the particle-core interaction V_{13} which induces (inelastic) rescattering of a nucleon on the core nucleus. In equations (8.18), h_{nj} and $h_{j'Jc}$ are the effective single particle Hamiltonians with respect to the ground state and the core excited states, respectively. The single particle energies are related by $\varepsilon_2 = \varepsilon_1 - E_C$, where $\varepsilon_1 = E - E_0$ is the ground state single particle (HFB) energy and E_C is the excitation energy of the core state. Negative ε_1 values correspond to the bound single particle states, while $\varepsilon_1 > 0$ corresponds to the 1-QP continuum. The BSEC (see Sect. 2.2), considered bound core-excited states, are represented by negative ε_2 values although their total energy E_3 is positive, i.e., they are immersed into the single particle continuum.

8.2.1 Two channels model

For our purposes, we prefer to work out a set of coupled differential equations, which give directly the radial wave function and the scattering phase shifts as a function of the energy. Here, we use a simplified but realistic model, chosen for the sake of a transparent presentation of the essential aspects of bound-continuum interactions. We consider only two channels, the first representing the single particle continuum ($\varepsilon_1 > 0$) and the second corresponding to a bound core-excited configuration ($\varepsilon_2 < 0$). As done in refs. [Bau75, Bau77] we use square well potentials for the channel potentials U_1 and U_2:

$$U_i(r) = \begin{cases} -U_i & r \le R_0 \\ 0 & r > R_0 \end{cases} \quad i = 1, 2; \;\; U_i > 0 \tag{8.19}$$

where R_0 is the model nuclear radius. A similar choice is made for the coupling form factors $F_{Jc}(r) = \langle 0|V_{13}|J_C\rangle$ within the core, which are assumed to be constant following the VC model:

$$F_{J_C}(r) = \begin{cases} F_{0c} > 0 & r \le R_0 \\ 0 & r > R_0 \end{cases} \tag{8.20}$$

that is, for $r > R_0$ the radial equations are decoupled. The depths $U_{1,2}$ and the radius R_0 are determined from HFB calculations [Len04].

The choice of step-potentials (U_1, U_2) for both channels and also for the coupling potential V_{13} between them leads to a spherically symmetric problem with known analytic solutions. The radial coupled equations in matrix form for the single particle wave functions with respect to the ground and the core excited state, respectively, are obtained with the assumptions (8.19) and (8.20) from equations (8.18):

$$\left[\frac{d^2}{dr^2} - \frac{l(l+1)}{r^2}\right]\begin{pmatrix} u_{1,l}(r) \\ u_{2,l}(r) \end{pmatrix} = \frac{2m}{\hbar^2}\begin{pmatrix} U_1(r) - \varepsilon_1 & V_{13}(r) \\ V_{13}(r) & U_2(r) - \varepsilon_2 \end{pmatrix}\begin{pmatrix} u_{1,l}(r) \\ u_{2,l}(r) \end{pmatrix} \tag{8.21}$$

where $u_{i,l}(r)$ are the radial wave functions for the two channels (i = 1, 2). We treat the case where the BSEC and the scattering channel carry the same angular momentum *l*.

Posing $K_i^2 = 2m(\varepsilon_i + U_i)/\hbar^2$ in the internal region ($r < R_0$), $K_i^2 = 2m\varepsilon_i/\hbar^2 \equiv k_i^2$ in the external region ($r > R_0$) and $W = 2mV_{13}/\hbar^2$, m being the reduced mass between neutron and core, we can rewrite the system of coupled equations as:

$$\left[\frac{d^2}{dr^2} - \frac{l(l+1)}{r^2} + K_1^2\right] u_{1,l}(r) - W\, u_{2,l}(r) = 0 \tag{8.22a}$$

$$\left[\frac{d^2}{dr^2} - \frac{l(l+1)}{r^2} + K_2^2\right] u_{2,l}(r) - W\, u_{1,l}(r) = 0 \tag{8.22b}$$

As known from Potential Scattering Theory (see, e.g., [Joa75]) in the particular case of square well potentials the solutions for $r < R_0$, regular at the origin, are expressed in terms of spherical Bessel functions $j_l(kr)$, while for $r > R_0$ in terms of spherical Hankel functions $h_l(kr)$.

For $r < R_0$ we find, respectively, for the open and closed channel wave functions:

$$u_{1,l}(r) = b_1\left[a_{11} j_l(Q_+ r)\right] + b_2\left[a_{12} j_l(Q_- r)\right] \tag{8.23a}$$

$$u_{2,l}(r) = b_1\left[a_{21} j_l(Q_+ r)\right] + b_2\left[a_{22} j_l(Q_- r)\right] \tag{8.23b}$$

The energy matrix of system (8.22) constitute a 2x2 square matrix. Solving the related eigenvalue problem

$$\begin{pmatrix} K_1^2 - Q_\pm^2 & -W \\ -W & K_2^2 - Q_\pm^2 \end{pmatrix}\begin{pmatrix} a_{1j} \\ a_{2j} \end{pmatrix} = 0 \qquad j = 1, 2 \tag{8.24}$$

we can determine the eigenvalues $Q_\pm^2$ and the eigenvectors with coefficients a_{ij} as:

$$Q_{\pm}^2 = \tfrac{1}{2}\left\{\left(K_1^2 + K_2^2\right) \pm \left[\left(K_1^2 - K_2^2\right)^2 + 4W^2\right]^{1/2}\right\} \tag{8.25}$$

$$a_{21}/a_{11} = \left(K_1^2 - Q_+^2\right)/W \tag{8.26a}$$

$$a_{12}/a_{22} = \left(K_2^2 - Q_-^2\right)/W \tag{8.26b}$$

where the a_{ij} have to be normalized: $a_{1j}^2 + a_{2j}^2 = 1$ for j = 1, 2. It is possible to show that in the absence of interaction (W = 0) we obtain: $Q_+ = K_1$, $Q_- = K_2$ and

$$\begin{pmatrix} a_{11} \\ a_{21} \end{pmatrix} = \begin{pmatrix} 1 \\ 0 \end{pmatrix} \qquad \begin{pmatrix} a_{12} \\ a_{22} \end{pmatrix} = \begin{pmatrix} 0 \\ 1 \end{pmatrix} \tag{8.27}$$

thus the wave functions are simply the decoupled Bessel functions of the two channels:

$$u_{1,l}(r) = b_1\ j_l(K_1 r) \tag{8.28a}$$

$$u_{2,l}(r) = b_2\ j_l(K_2 r) \tag{8.28b}$$

Now let us consider the external region $r > R_0$. The corresponding solutions are:

$$u_{1,l}(r) = j_l(k_1 r) + C_{11}\ h_l(k_1 r) \tag{8.29a}$$

$$u_{2,l}(r) = C_{12}\ h_l(k_2 r) \tag{8.29b}$$

where the $h_l(k_2 r)$ of the second channel reduces is exponentially decaying because $k_2 = i\kappa_2$ is purely imaginary due to the negative value of ε_2. From equations (8.23) and (8.29) we have the four unknowns b_1, b_2, C_{11} and C_{12} to determinate; obviously they – and the coefficients a_{ij} also – are all functions of the energy, this dependence is not indicated explicitly for brevity. Imposing the matching conditions, that is the boundary conditions that both $u_{i,l}(r)$ and $du_{i,l}(r)/dr$ be continuous at $r = R_0$, allows to determine the coefficients b_1, b_2, C_{11} and C_{12} and thus the wave functions.

Moreover the knowledge of the elements of the scattering matrix S

$$S_{ij} = e^{2i\delta_{ij}(k)} = \eta_{ij}\, e^{2i\alpha_{ij}(k)} \tag{8.30}$$

where the elastic scattering phase shifts $\delta_{ij}(k) = \alpha_{ij}(k) + i\,\beta_{ij}(k)$ and $\eta_{ij}(k) = e^{-2\beta_{ij}(k)}$, defined by the asymptotic form (8.29) of the radial wave functions

$$C_{ij} = \frac{S_{ij} - 1}{2i} \tag{8.31}$$

enables one to obtain and the partial wave elastic cross sections $\sigma_i(k)$ (for a spin-less particle):

$$\sigma_i(k) = \frac{4\pi}{k_i^2}(2l+1)\left|C_{ii}(k)\right|^2 = \frac{4\pi}{k_i^2}(2l+1)\sin^2\delta_{ii}(k) \tag{8.32}$$

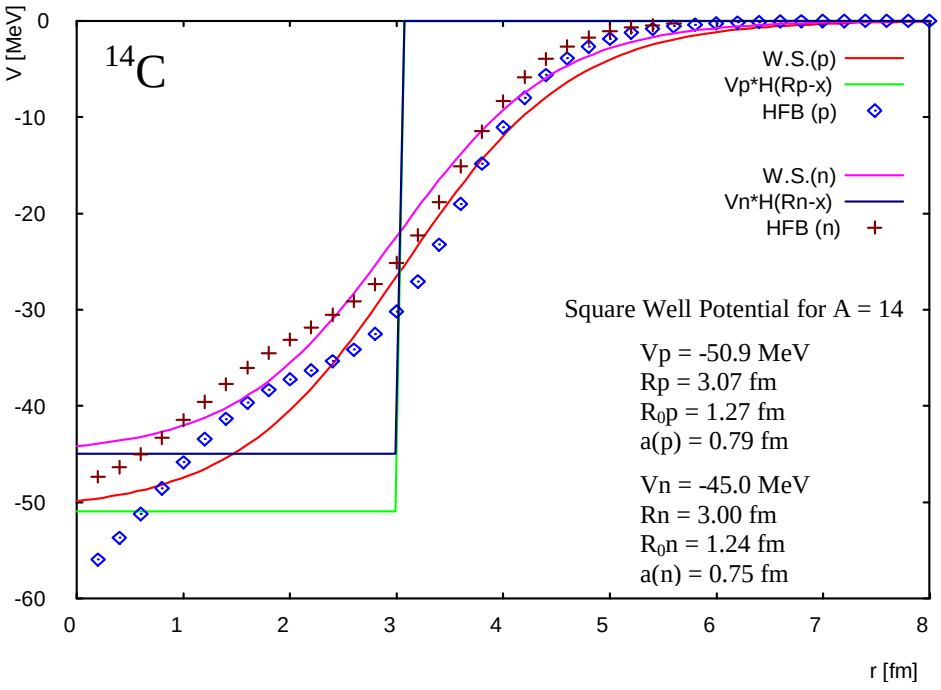

Figure 8.5. Example of the results of the HFB calculations for a ^{14}C core. The HFB potential is separately calculated for proton (p) and neutron (n). Then it is fitted using a Woods-Saxon (W.S.) potential. The parameters of this fit give the square well potential, which is used in the line shape calculations.

8.3 Model calculations

Our main purpose in the calculations is to study the effects which can occur when resonance and continuum overlap. Here, we need in particular the scattering matrix elements in the open channel. One could in principle develop a formula which clarifies the cross section dependence on the interaction V_{13}. However, it would be so complicated and absolutely not trivial to derive and exhibit, due to the fact that this dependence is contained in the internal radial wave functions through both $Q_{\pm}$ and the coefficients a_{ij} of equations (8.23). Thus it is more convenient to calculate numerically the cross section in the open channel, σ_{11}, and then to assess the quantitative importance of such a dependence by comparing the results in the two cases $V_{13} \neq 0$ and $V_{13} = 0$. This is done in Section 8.3.1 in the case of the ^{15}C nucleus, considering one core-excited state.

To perform the calculations, the potentials U_1, U_2 and the potential range R_0 have been taken from Hartree-Fock-Bogoliubov (HFB) calculations by adjusting their values such that single particle energies and root-mean-square radii of the single neutron states in the various core systems (^{14}C, ^{16}C and ^{18}C, respectively for ^{15}C, ^{17}C and ^{19}C) are reproduced. Precisely, U_1, representing the ground state potential, has been made state dependent by fitting independently the experimental (if available) or HFB single particle energies ε_{HFB}. On the contrary, U_2 is taken to be state independent by fixing strength and radius from the HFB mean-field potential as described in Figure 8.5. In order to have a consistent description, R_0 has been optimised with the purpose to reduce to only few MeV the variation of U_1 for a same HFB state in the different core nuclei. The parameters utilized for the HFB fit and the so determined potentials and radii are reported in Table 8.1. Finally, the particle-core

Table 8.1. Adopted HFB radii R_0 [fm] and potentials U_1, U_2 [MeV]. For each core nucleus the HFB energies ε_{HFB} [MeV] used for the fit of U_1 are reported together with the obtained U_1 values. When available, the experimental values – taken from refs. ([a])=[Ajz91], ([b])=[Til93], ([c])=[Til95] – are used; they account, e.g., for the known shell inversion in the ^{15}C ground state.

	n + ^{14}C		**n + ^{16}C**		**n + ^{18}C**	
HFB values	**R_0**	**U_2**	**R_0**	**U_2**	**R_0**	**U_2**
	3.1332	-45	3.1498	-46	3.1449	-46
HFB level	**ε_{HFB}**	**U_1**	**ε_{HFB}**	**U_1**	**ε_{HFB}**	**U_1**
$1s_{1/2}$	-31.867	-46.538	-32.798	-47.299	-33.709	-48.228
$1p_{3/2}$	-15.365	-44.257	-15.748	-44.232	-16.336	-44.847
$1p_{1/2}$	-8.939	-36.236	-9.854	-36.953	-10.923	-38.225
$1d_{5/2}$	-0.478([a])	-46.498	-0.728([b])	-46.033	-1.845	-47.589
$2s_{1/2}$	-1.218([a])	-54.747	-0.433([b])	-51.706	-0.160([c])	-50.506

interaction strength $F_{0c} \sim V_{13}$ has been left as a free parameter but using constraints from experimental or QRPA transition probabilities.

Subsequently, for the calculation of σ_{11} for the different core-excited states, the interaction V_{13} has been fixed to 15 MeV and it has been weighted for each core state E_C. In detail, to weight the interaction V_{13} in the case of a ^{14}C core, the experimental collective deformation amplitudes β from the scalar-isoscalar (S=0, T=0) transitions in ^{14}C(α,α') [Ajz91] have been used. For ^{16}C [Til93] and ^{18}C [Til95], however, no experimental amplitudes are available, thus theoretical amplitudes β_{QRPA} have been calculated for the (S=0, T=0) transitions using a QRPA code. The β_{QRPA} are determined from the QRPA transition probabilities, representing the response for excitations due to the microscopic QRPA fields. Precisely, β_{QRPA} is deduced from the reduced transition probability $B(T_\lambda^{S,T})$ as:

$$\beta_\lambda^2 = \frac{B(T_\lambda^{S,T})}{< r^\lambda >^2} \tag{8.33}$$

where $T_\lambda^{S,T}$ is the multipolar transition operator and λ indicates the multipolarity.

The energies E_C of the core states included in the calculations and the corresponding β-amplitudes are reported in Table 8.2. Only natural parity core states are considered due to the nature of the (S=0, T=0) transitions. Core states with low β ($\sim 10^{-3}$) have been neglected because they gives only a shapeless background. For ^{18}C only the first excited state at E_C = 1.620 MeV is known [Til95], the other reported levels have been calculated with the QRPA code. An example of a calculation of the β_{QRPA} amplitudes for the ^{16}C states is shown in

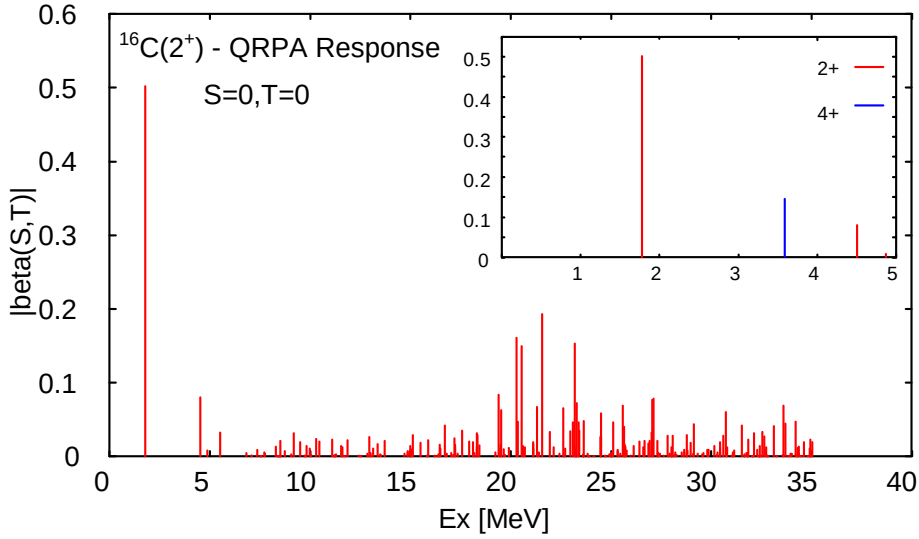

Figure 8.6. Density β_{QRPA} amplitude (S = 0, T = 0) for the ^{16}C states, calculated by the QRPA code. Main plot: β_{QRPA} for the 2^+ states. Inset: Detail of the 2^+ and 4^+ components, which constitute the values used in the line shape calculations with a ^{16}C core.

Table 8.2. Characteristics of the core-excited states included in the calculation of σ_{11}: spin and parity J^π, energies E_C in [MeV] and β-amplitudes. The experimental values are taken from refs. ([a])=[Ajz91], ([b])=[Til93] and ([c])=[Til95]. (*) indicates theoretical values obtained from QRPA calculations.

^{14}C ([a])			**^{16}C ([b])**			**^{18}C (*)**		
J^π	**E_C**	**β**	**J^π**	**E_C**	**β**	**J^π**	**E_C**	**β**
1^-	6.094	0.224	2^+	1.766	0.502(*)	2^+([c])	1.620([c])	0.420
3^-	6.728	0.397	2^+	3.986	0.080(*)	4^+	2.967	0.123
2^+	7.012	0.293	4^+	4.142	0.145(*)	2^+	3.313	0.058
2^+	8.317	0.221				1^-	5.502	0.055

Figure 8.6. In the main plot β_{QRPA} (S=0, T=0) of the 2^+ states is reported with respect to the ^{16}C excitation energy. The first two lines give the β_{QRPA} values adopted for the two 2^+ states at E_C = 1.766, 3.986 MeV (see Table 8.2). Indeed, we are interested in core-excited states at low excitation energy, corresponding to the low energy BSEC, while the strength in the region E_C ~ from 20 to 25 MeV corresponds to the giant resonances. In the inset the region between 0 and 5 MeV is shown in detail, together with β_{QRPA} for the 4^+ component (adopted value for the 4^+ state at E_C = 4.142 MeV).

8.3.1 Results of the line shape calculations

The results of the line shape calculations are given in this Section, considering for example the ^{15}C nucleus. The results concerning one core-excited state, the ^{14}C state at E_C = 8.317 MeV, are shown in detail for each step of the calculations, comparing them in the two cases $V_{13} \neq 0$ and $V_{13} = 0$. All the plots of this Section refer to the E_C = 8.317 MeV core state.

The wave functions of the two channel $u_{1,l}(r)$ and $u_{2,l}(r)$ are reported, respectively, in Figures 8.7 and 8.8 for $l = 0$, in Fig. 8.9 and 8.10 for $l = 1$, in Fig. 8.11 and 8.12 for $l = 2$. For each channel, the real and imaginary parts of the wave function are plotted separately, comparing them with the corresponding ones in absence of interaction ($V_{13} = 0$). The wave functions are determined with continuity. The absence of discontinuities between the internal ($r < R_0$) and external ($r > R_0$) regions is an useful test of the goodness of the matching. Comparing the $V_{13} \neq 0$ and $V_{13} = 0$ (decoupled Bessel function) cases for channel 1 and $l = 0$, we can see from Figure 8.7 that there are only small differences in the internal region, while for $r > R_0$ the two wave functions are almost the same. For $l = 1$ (Fig. 8.9) the wave functions are practically identical, so no resonances are expected in the p-wave. The influence of the interaction is evident in the d-wave ($l = 2$, Fig. 8.11), where the wave function is slightly shifted for $r > R_0$ with respect to the one with $V_{13} = 0$.

Regarding the second channel (Fig. 8.8, 8.10, 8.12), the wave functions $u_{2,l}(r)$ have the correct behaviour, that is the exponential decay for $r > R_0$ due to the negative ε_2 value. Besides, $u_{2,l}(r)$ is always zero when $V_{13} = 0$ (from the matching in this case $b_2 = 0$ and $C_{12} = 0$). This is due to the fact that equations (8.22) are solved under the boundary condition that the ground state channel (channel 1) is the one with incoming plane waves, i.e., the one which is populated initially, independently of the interaction V_{13}. The core-excited channel is populated only through the residual interaction, which diverts part of the flux into the (asymptotically) closed BSEC channel before scattering back into the open elastic channel. Thus, all that is observed in channel 2 for $V_{13} \neq 0$ is caused by the presence of the interaction. A second class of solutions, corresponding to $\varepsilon_2 > 0$ and not considered in the present case, describes the opposite situation in which the incoming flux is carried by the core-excited channel and the ground state channel has only outgoing waves.

In general [Joa75] for reaction processes (absorption without emission) together with the elastic scattering (always present) the phase shift δ is complex with Im $[\delta] = \beta > 0$ and thus $0 \leq \eta < 1$, while for pure elastic scattering δ is a real quantity and $\eta = e^{-2\beta} = 1$. The partial wave amplitudes C_{ij} are directly related to the T-matrix elements: $C_{ij} = T_{ij}/(2i)$. The $|C_{11}|$ calculated in the open channel in the two cases with and without interaction are shown in Fig. 8.13 and 8.14, respectively. Some small effect is present in the s-wave component (Fig. 8.13a), while the p-wave one remains practically unaffected (Fig. 8.13b). Strong interference effects are present in the d-wave (Fig. 8.14a). The real and imaginary parts of C_{11} for $l = 2$ are separately shown in Fig. 8.14b; the imaginary part is found to be correctly positive, as expected for $0 \leq \eta_{11} \leq 1$. The elements of the scattering matrix S are given by $S_{ij} = T_{ij} + 1 = 2i\, C_{ij} + 1$. As long as the second channel is closed, the S-matrix S_{11} is unitary with inelasticity $\eta_{11} = |S_{11}| = 1$. In Fig. 8.15 the modulus η_{11} is plotted for s-, p- and d-waves, in comparison with the $V_{13} = 0$ case in which $\eta_{11} = 1$ always. The $V_{13} \neq 0$ term is responsible for the strong deviations of η_{11} from the constant value 1, producing a very narrow peak in the d-wave.

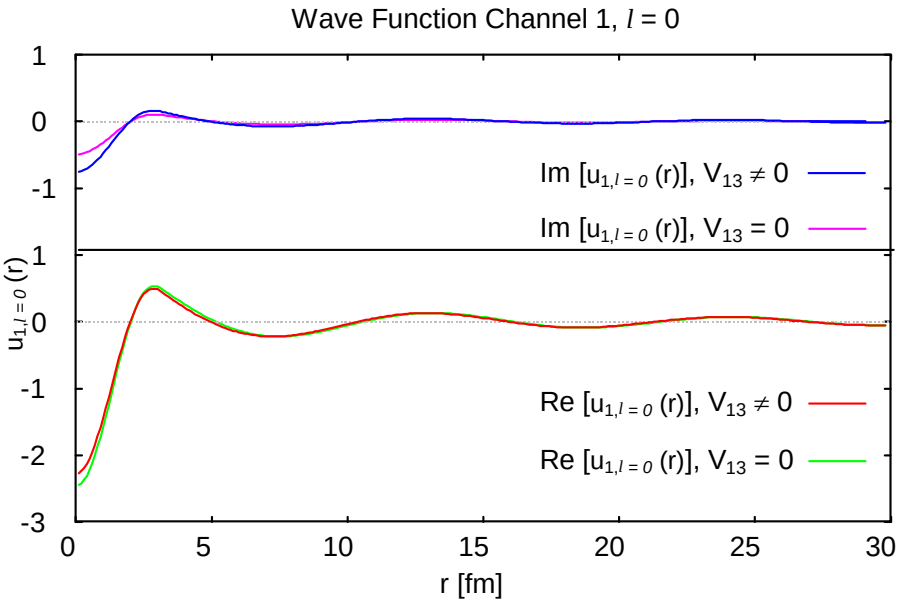

Figure 8.7. Calculated ^{15}C wave function of the first channel for $l = 0$. Imaginary and real parts are compared in the two cases with and without interaction V_{13}.

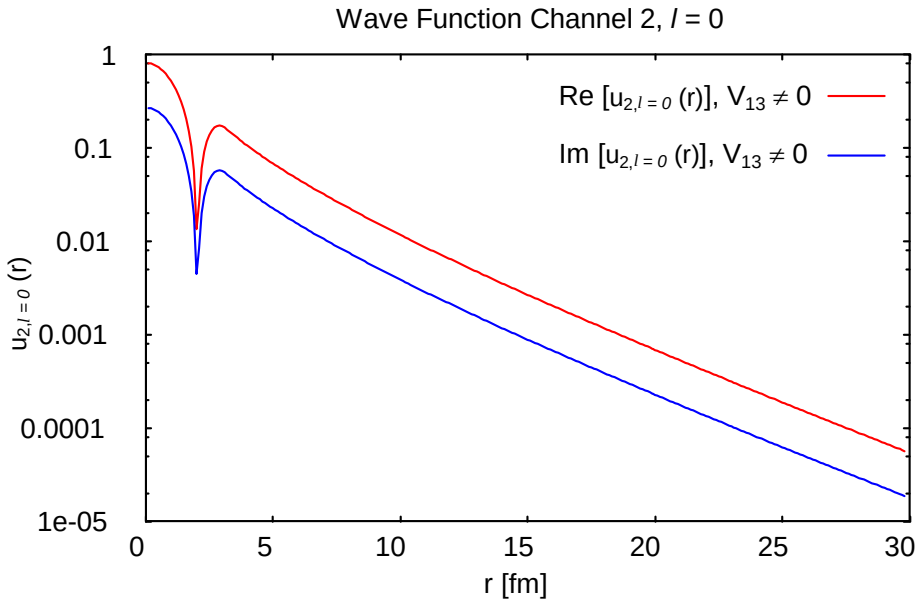

Figure 8.8. Calculated ^{15}C wave function of the second channel for $l = 0$. The imaginary and real parts are zero in the case without interaction ($V_{13} = 0$).

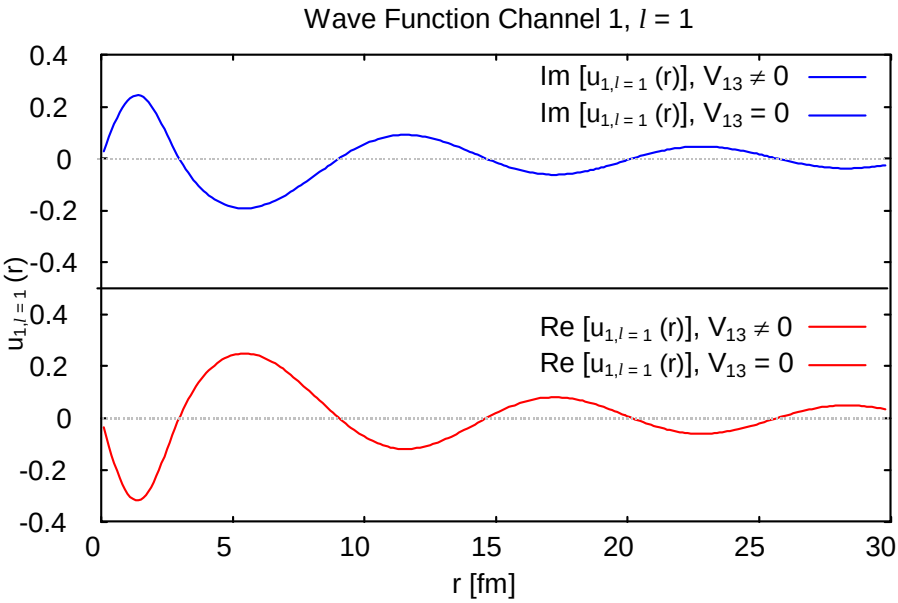

Figure 8.9. Calculated ^{15}C wave function of the first channel for l = 1. The wave functions (both imaginary and real part) are identical in the two cases with and without interaction V_{13}.

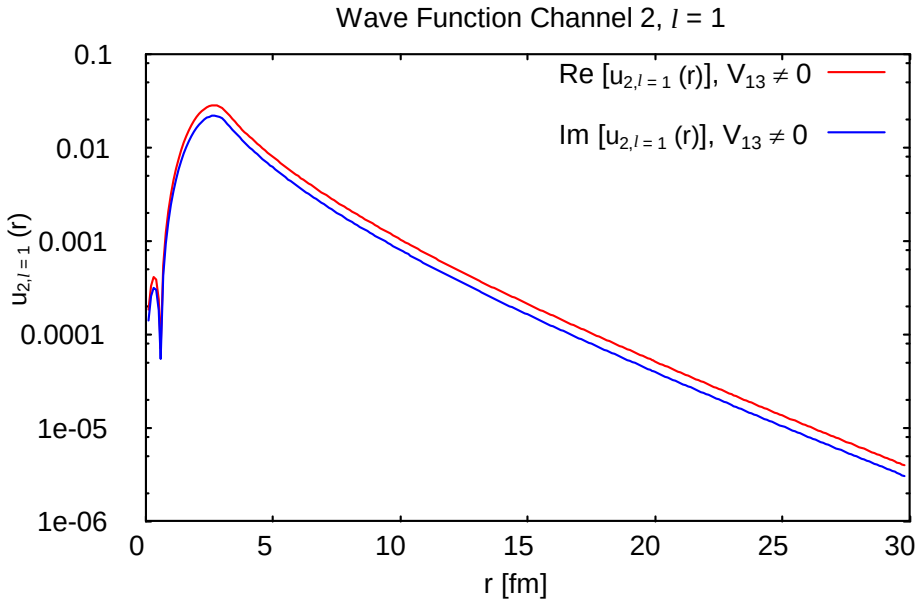

Figure 8.10. Calculated ^{15}C wave function of the second channel for l = 1. The imaginary and real parts are zero in the case without interaction (V_{13} = 0).

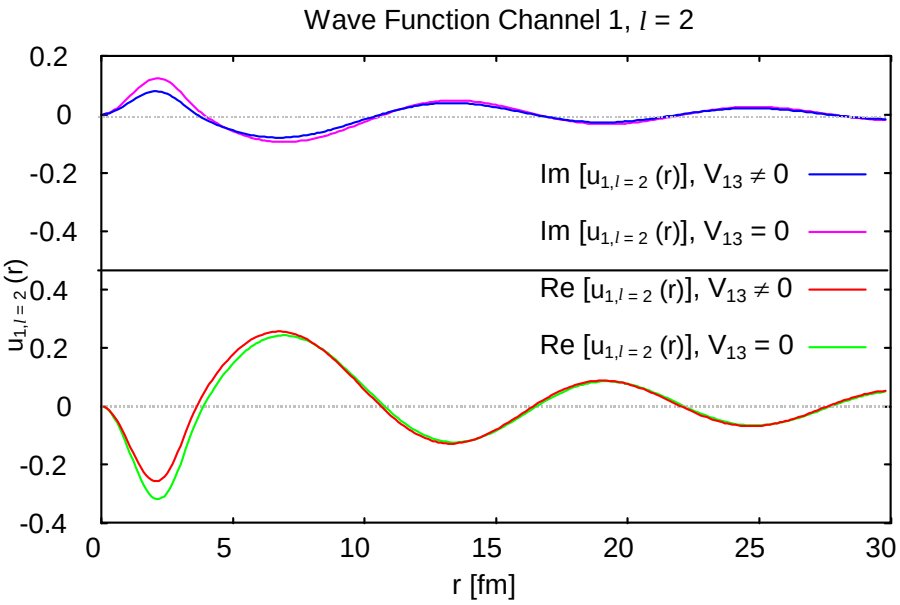

Figure 8.11. Calculated ^{15}C wave function of the first channel for $l = 2$. Imaginary and real parts are compared in the two cases with and without interaction V_{13}.

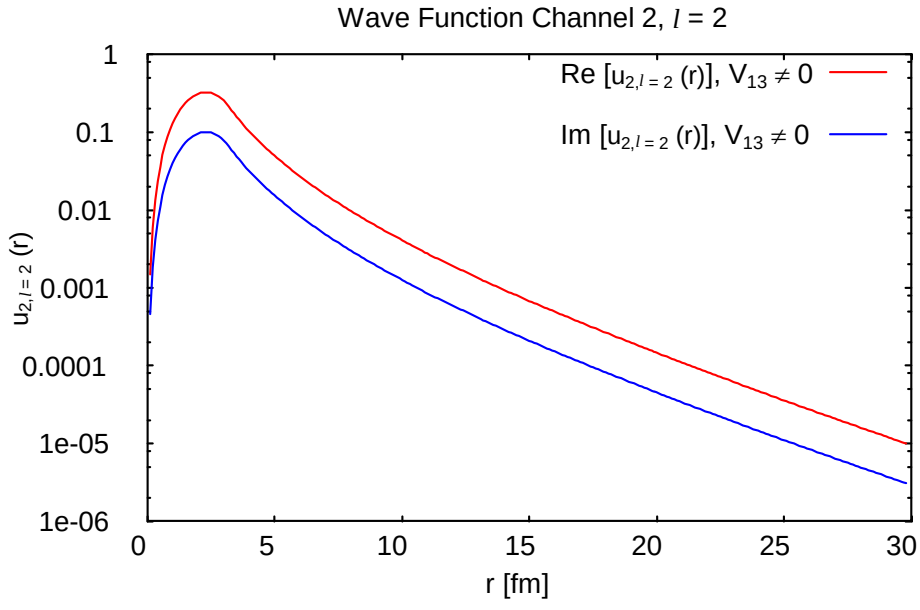

Figure 8.12. Calculated ^{15}C wave function of the second channel for $l = 2$. The imaginary and real parts are zero in the case without interaction ($V_{13} = 0$).

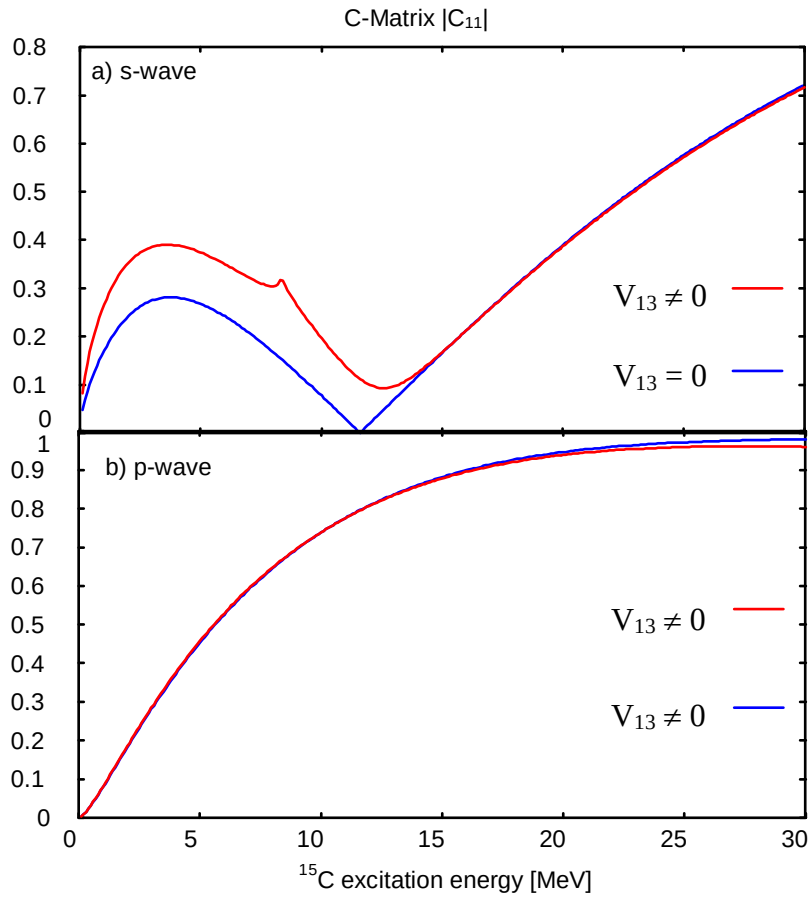

Figure 8.13. Calculated partial wave amplitude $|C_{11}|$ in the two cases with and without interaction V_{13}. a) s-wave (l = 0). b) p-wave (l = 1).

The phase shift δ displays the influence of the interaction. Usually a positive δ indicates an attractive interaction; conversely a negative δ corresponds to a repulsive one [Joa75]. δ = δ(ε), i.e., it is a function of the energy and may change sign as the energy is changed: for example, in the NN-interaction case δ is positive at low energy and becomes negative at high energy. This behaviour reflects the existence of a repulsive core in the nuclear force. Nevertheless V_{13} is a non-diagonal interaction and then the simple rules of the Potential Scattering Theory do not apply to it. In fact, the sign of V_{13} is not influential because it enters quadratically into the eigenmomenta Q_+ and Q_- of eq. (8.25).

In our case the phase shift is real because the flux of particles is a conserved quantity. Indeed, even though the residual interaction diverts part of the flux into the core-excited channel, afterwards this flux scatters back into the open elastic channel. In general, a sharp variation of the phase shift is index of the presence of a resonance. The calculated phase shift δ_{11} is shown in Figure 8.16 for s-, p- and d-waves in the two cases $V_{13} \neq 0$ and $V_{13} = 0$. No large difference is seen in the s-wave and δ_{11} for the p-wave remains unchanged. On the contrary, a very prominent variation is observed in the d-wave. Thus this confirms that we can expect a resonance for l = 2.

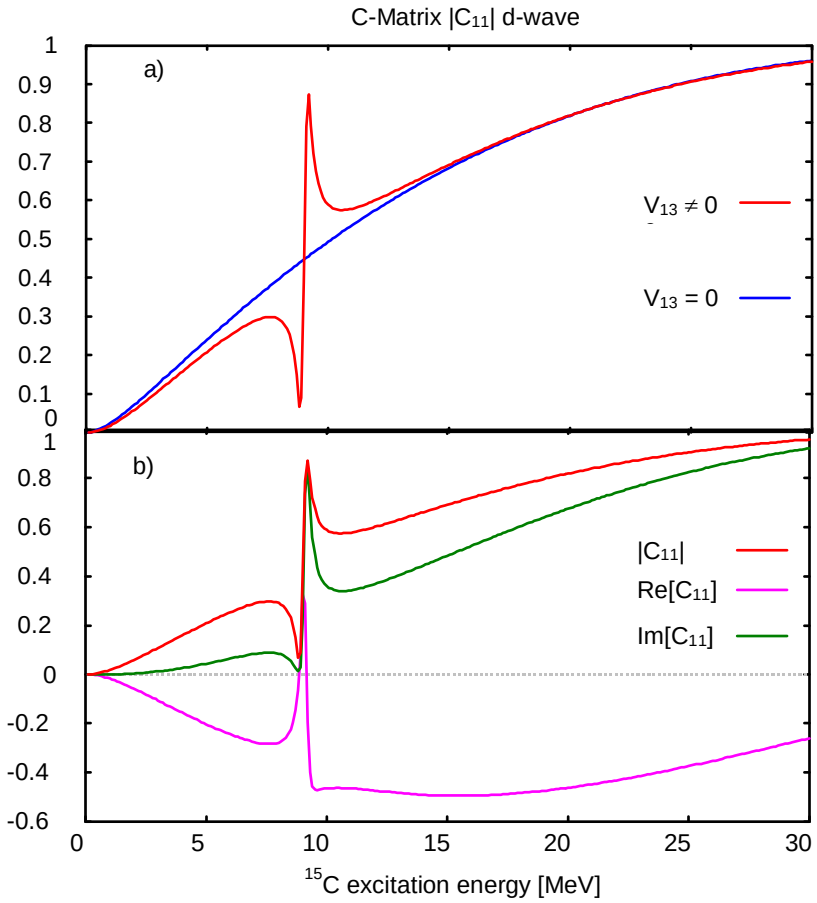

Figure 8.14. Calculated partial wave amplitude $|C_{11}|$ for the d-wave (l = 2). a) Comparison between the calculations with and without interaction V_{13}. b) Real and imaginary parts of C_{11} for l = 2 and $V_{13} \neq 0$.

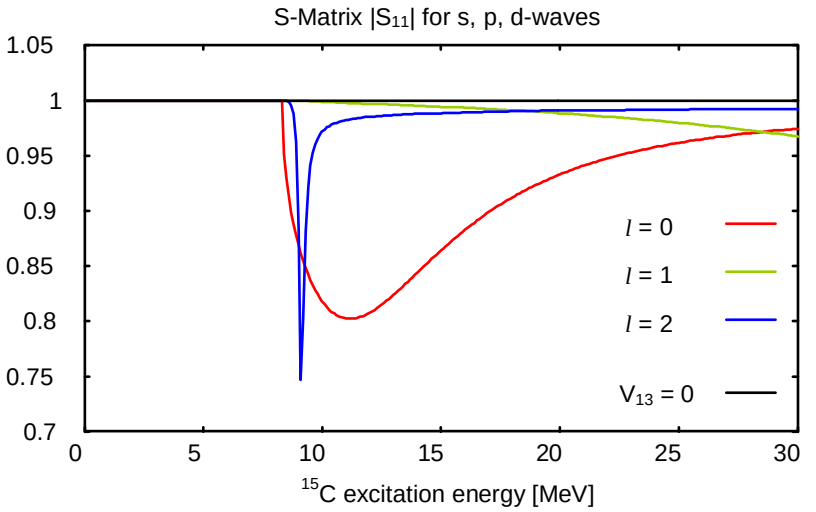

Figure 8.15. Calculated scattering matrix element $|S_{11}|$ for s-, p- and d-waves. Also the V_{13} = 0 case is plotted for comparison: for each l-value $|S_{11}|$ = 1 always.

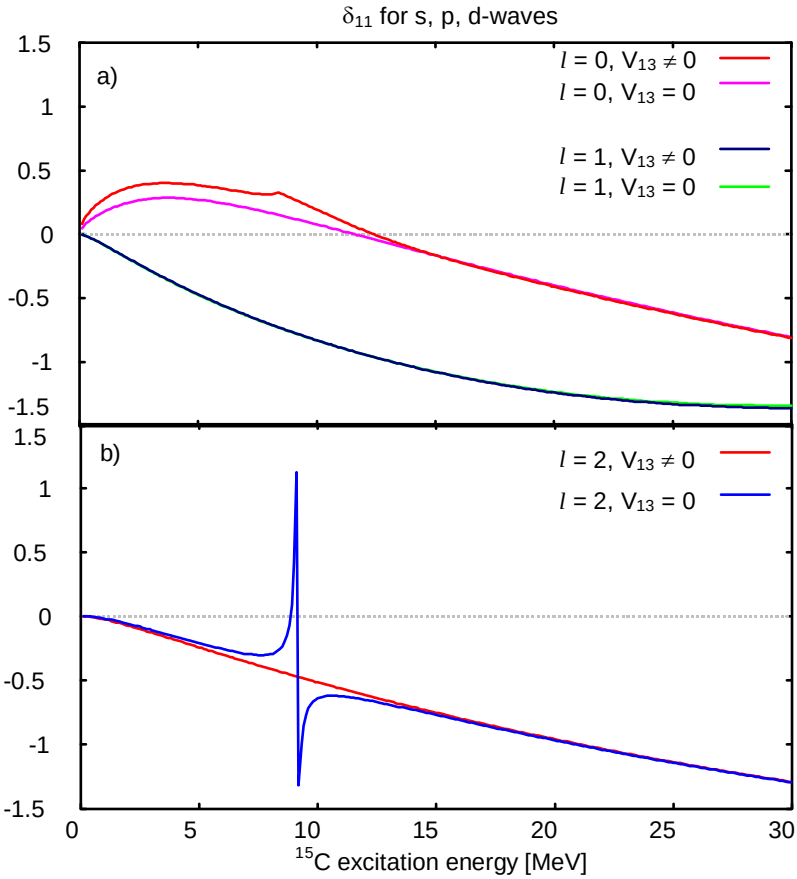

Figure 8.16. Calculated phase shift δ_{11}: a) s- (l = 0) and p- (l = 1) waves. b) d-wave (l = 2). For each l-value, δ_{11} is plotted in the two cases $V_{13} \neq 0$ and $V_{13} = 0$.

The partial wave cross sections σ_{11} of elastic scattering between neutron and core have been calculated for a range between 0 and 30 MeV of excitation energy. In Figure 8.17a the interference pattern related to the core-excited state E_C = 8.317 MeV is shown in detail for s-, p- and d-waves. Whereas the s- and p-wave cross sections are smooth functions of the energy, constituting only a continuous background, a narrow and asymmetric peak is evident in the d-wave cross section. The appearance of this peak illustrates how a discrete level may be modified by the interference with a continuous background.

In Figure 8.17b a calculation is shown for the same ^{14}C state at E_C = 8.317 MeV with exactly the same parameters of the previous one of Fig. 8.17a, but in which the interaction V_{13} is set to zero. While the shape of the s- and p-wave cross sections is almost unchanged, here the d-wave cross section appears without any structure. This comparison between Figures 8.17a and 8.17b confirms that the peculiar resonance line shape seen in the d-wave arises from the interference term due to V_{13} which couples the 1-QP and 3-QP channels, that is producing a resonant state by coupling the single particle continuum to the closed core-excited channel. The two contributions interfere with opposite relative phase on the two sides of the resonance, changing from destructive interference on the low-energy side to

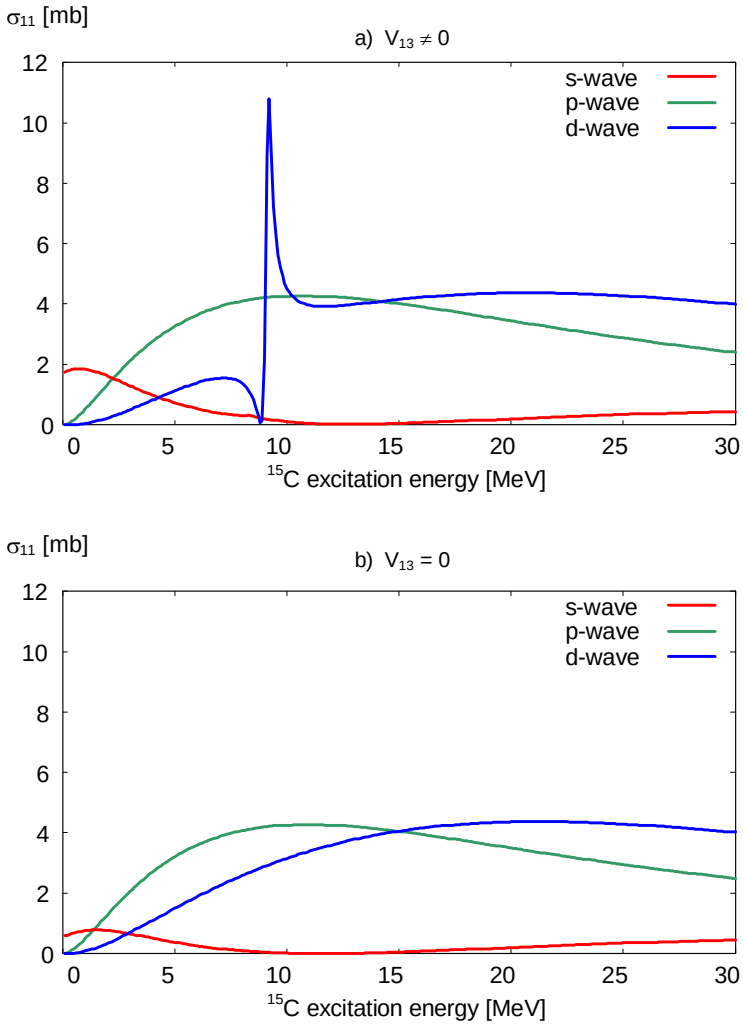

Figure 8.17. a) Calculated ^{15}C elastic cross section σ_{11} related to the core-excited state E_C = 8.317 MeV for s-, p- and d-waves. b) As above but with interaction V_{13} = 0.

constructive interference on the high-energy side of the resonance. Practically, the interaction V_{13} acts by shifting part of the low-energy strength to the BSEC, the cross section vanishes on the left side of the peak and is maximal on the right side. Instead, for energies away from the resonance, the non resonant background is the only significant contribution to the cross section. Of course, from an experimental point of view, a complete cancellation of the cross section may be not observed because of insufficient resolution or additional background contributions. However, the observed asymmetry of the 8.5 MeV peak in the ^{15}C spectra of Chapter 5 shows that the effect of the interference is not altogether obscured in the data.

These results, obtained for the core-excited state E_C = 8.317 MeV, are an example of the interference effects predicted by the coupled channels model, which give rise to a resonance through the coupling of the single particle continuum to a BSEC. The coupling is due to a non-diagonal interaction. Similar results are obtained for other core-excited states (as shown in Section 8.3.2) and the ^{17}C and ^{19}C nuclei (see Section 8.3.4).

8.3.2 Final results for ^{15}C

The main interest is to reproduce the ^{15}C spectrum in the region between about 6 and 10 MeV, where three narrow resonances in the continuum have been experimentally observed (see Sect. 5.2, also published in refs. [Orr03, Cap04]). On the basis of the results of the microscopic DCP calculations of Chapter 7 and ref. [Noc03], these resonances are interpreted as BSEC, therefore the present approach may be applied.

The final results of the calculations for ^{15}C are presented in this Section. Whereas obviously the experimental results include all the (incoherent) background contributions due to all the other *l*-values, here we only consider the results of calculations for the resonant *l*-value because the other contributions are only slowly varying in the resonance region (see, e.g., Fig. 8.17). Besides, we consider all the different core-excited states reported in Table 8.2.

In Figure 8.18a the calculated elastic cross section σ_{11} for the d-wave – the one contributing to the resonance – is plotted with respect to the ^{15}C excitation energy. For comparison, the experimental spectrum in counts taken at $\theta_{lab} = 14°$ is plotted in the region of interest in Figure 8.18b. The core states included in the calculations are: E_C (J^π) = 6.094 (1^-), 6.728 (3^-), 7.012 (2^+), 8.317 (2^+) MeV, and the coupling to each of them was determined by weighting the form factors F_{13} according to the experimental β-values reported in Table 8.2. An interference pattern similar to that in Figure 8.17a is obtained for every σ_{11} calculated for the ^{14}C states. The total σ_{11} has been then calulated by summing the individual contributions of all the above-mentioned core excitations. In the theoretical cross section (Fig. 8.18a) three narrow resonances are evident in the energy region between 6 and 10 MeV of ^{15}C excitation energy, with the noticeable result that the three BSEC structures seen experimentally (Fig. 8.18b and Chapter 5) are reproduced in the observed energy region. The theoretical levels are observed at E_x = 7.15, 8.48, 9.26 MeV, while the experimental ones are at E_x = (6.77 ± 0.06, 7.30 ± 0.06, 8.50 ± 0.06) MeV. In our calculations the "energy-shift" term E_0 has been not included, which has been used in other works to shift a resonance to the desired position [Bau77, Bau75]. Introducing an additional average shift E_0 = 0.77 MeV, the theoretical peaks are shifted to E_x = 6.38, 7.71, 8.49 MeV. Without overemphasizing the results of our schematic model calculations, the qualitative agreement between these values and the experimental ones is surprisingly good. Some differences may arise from the not easy determination of the centroids because of the asymmetry induced by the interference.

Moreover, it is important to underline that we are calculating elastic scattering cross sections, while the experimental data were obtained using the (^{7}Li,^{7}Be) CEX reaction. The present calculations simulate the rescattering of the neutron after production on the residual target nucleus, but reaction dynamics are not included. Since the population of the states depends on the reaction dynamics, we cannot compare the magnitudes directly with the experimental CEX cross sections of Sect. 5.3 and ref. [Orr03], or the peak intensities between Figs. 8.18a and 8.18b. However, we can compare on a qualitative level the results of our structure calculations and the experimental spectra. Keeping in mind these constraints and the schematic nature of the calculations, the global agreement with the data is very good. In fact, with our simple model it is possible to reproduce the interference pattern seen in the line shape and we are able to explain the existence of the three experimental measured narrow resonances in the continuum, even lying in the observed energy region. Hence, the model

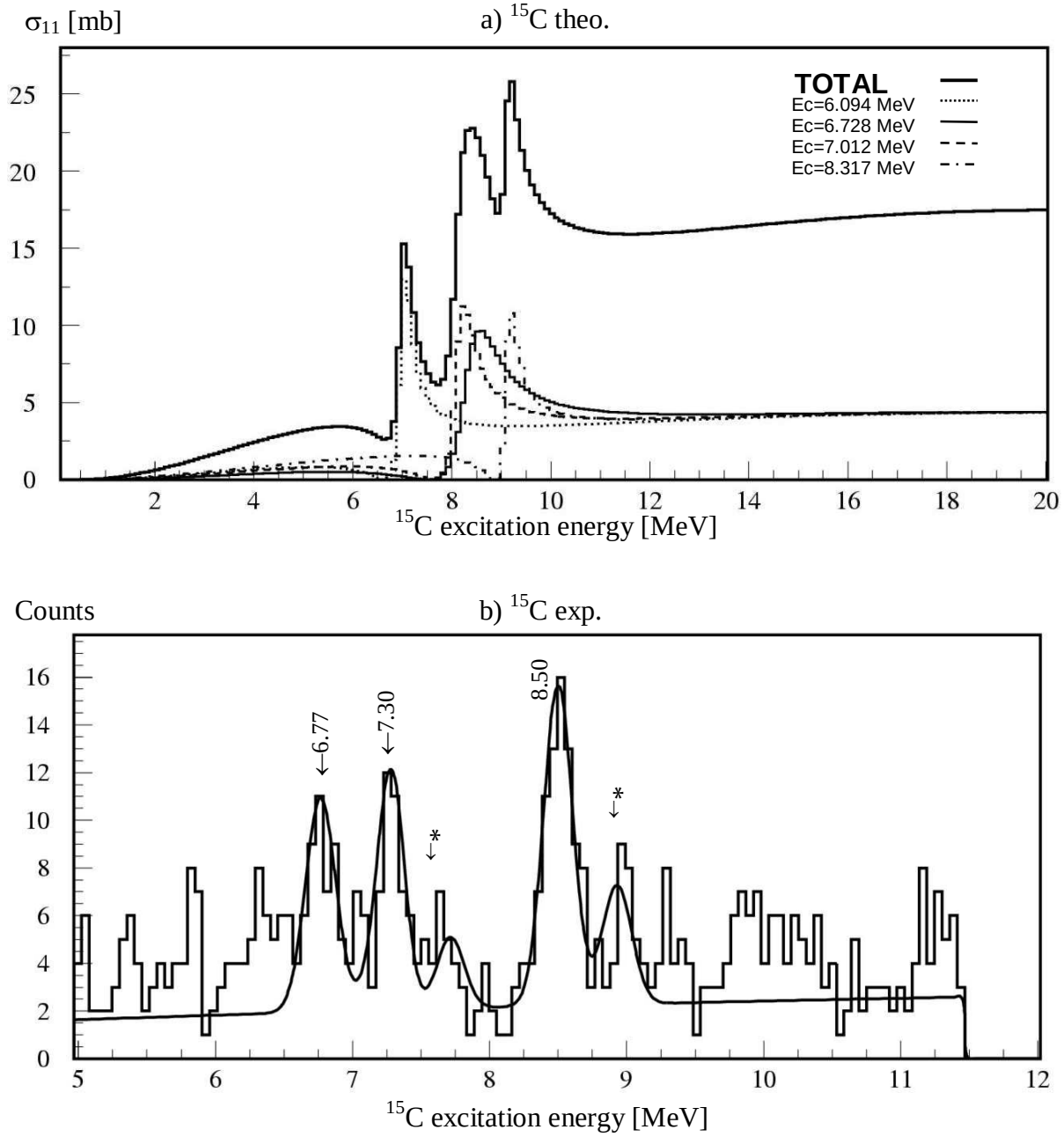

Figure 8.18. a) Calculated elastic cross section σ_{11} for the d-wave plotted with respect to the ^{15}C excitation energy. Core states included in the calculations: E_C (J^π) = 6.094 (1^-), 6.728 (3^-), 7.012 (2^+), 8.317 (2^+) MeV. b) Measured excitation energy spectrum for the ^{15}N(^{7}Li,^{7}Be)^{15}C reaction at E_{inc} = 55 MeV and θ_{lab} = 14°. Peaks marked with an asterisk are associated to the excitation of ^{7}Be at 0.429 MeV. The continuous line is the sum of the background (the ^{15}N(^{7}Li,n^{7}Be)^{14}C 3-body phase space) and the Gaussians used to fit the peaks (see Sect. 5.2).

does account for the essential physics aspects contained in the observed data. In order to compare quantitatively with the measured cross sections, dynamical DWBA calculations are under development, on the basis of the CEX-QRPA calculations of Chapter 6. The DCP wave functions obtained with the present model will be the starting point for the CEX-DCP calculations, in which the effects of the CEX transition operator and the optical potential will be included. This will ultimately allow to determine a theoretical CEX cross section to be compared with the experimental one of ref. [Orr03] and Sect. 5.3.

8.3.3 Discussion

As discussed in Section 2.1.2, the ^{15}C narrow resonances were also observed in the ^{9}Be(^{7}Li,p)^{15}C reaction [Gar74], which proceeds through an intermediate compound system and therefore is less selective than the ^{14}C(d,p) stripping reaction [Gos75] or than the present (^{7}Li,^{7}Be) CEX reaction. In ref. [Gar74] the narrow widths of the ^{15}C unbound states were considered as indication of hindrance for neutron emission. It was further speculated that this may result either from a reduced penetrability, because of the high angular momentum of the neutron in the n + $^{14}C_{GS}$ configuration, or from structure configurations having a small overlap with n + $^{14}C_{GS}$ (i.e., core-excited configurations). Following the first hypothesis, they suggested high spins J^{π} for the ^{15}C unbound states (see Table 5.2). Also in ref. [Boh03] high J^{π} values are proposed for two among such states, on the basis of a comparison with the particle-hole structure of the related ^{14}C states (see Section 2.1.3).

Nevertheless, the hypothesis of high spin has not been definitively proved and in both cases it was based on qualitative arguments only. On the contrary, microscopic calculations based on the QRPA-DCP approach (see Chapter 7 and ref. [Noc03]) show dominant core excited configurations for the $s_{1/2}$, $d_{3/2}$ and $d_{5/2}$ strengths in the energy region of interest. These results strongly support the interpretation based on DCP states with low angular momentum. Besides, the results of the line shape calculations indicate that the interference between the BSEC structures and the single particle continuum happens for l = 2, i.e., when the neutron is in the d-wave with respect to the core. This is perfectly compatible with the low J^{π} values obtained by DCP calculations.

Moreover, in our case the ^{15}C BSEC are obtained by the CEX reaction (see Chapter 3) and thus how the high spin states are populated remains to be explained. In fact, the transfer of a large amount of angular momentum by the CEX mechanism is improbable, especially at forward angles [Alf98, Cap04b]. The more detailed CEX-DCP calculations will permit to investigate spin and parity of the ^{15}C BSEC.

8.3.4 Results for ^{17}C and ^{19}C

An enhancement of BSEC structures is expected close to the neutron drip line due to the softer core and the increased polarizability of the system. The quadrupole polarizability increases, related to the presence of low-energy 2^{+} core states, whose energy decreases with increasing mass. In particular, a strong enhancement of BSEC excitations is predicted in the low-energy continuum of the carbon isotopes with increasing the neutron number, in connection with the decrease of the first 2^{+} core state from E_x = 4.44 MeV in ^{12}C to E_x = 1.77 MeV in ^{16}C and E_x = 1.62 MeV in ^{18}C [Cor01, Len01]. These arguments show the importance of a systematic study of such effects for carbon isotopes. Thus the calculations have been performed not only for ^{15}C (S_n = 1.218 MeV) but also for the more exotic ^{17}C (S_n = 0.73 MeV) and ^{19}C (S_n = 0.16 MeV) nuclei.

The partial wave elastic cross sections σ_{11} have been calculated for a range between 0 and 30 MeV of excitation energy. The calculated σ_{11} (s-, p- and d-waves) for ^{17}C – considering, e.g., the core-excited state at E_C = 3.986 MeV – are shown in Fig. 8.19. The σ_{11}

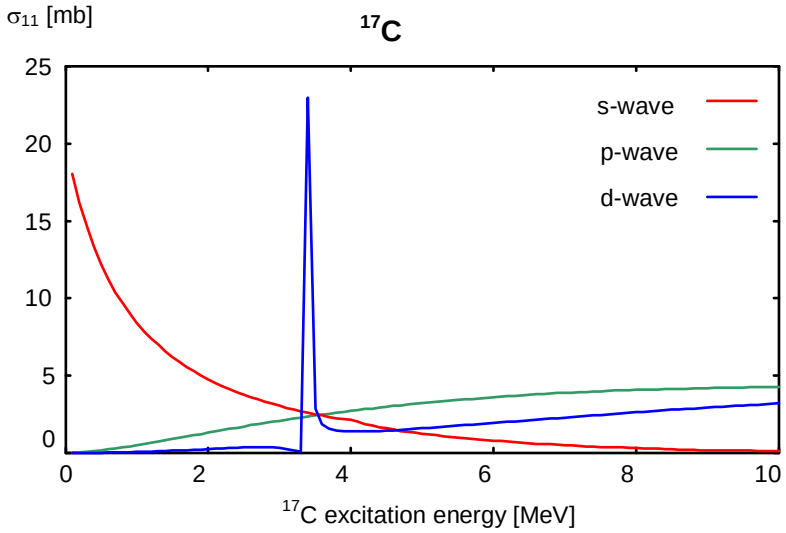

Figure 8.19. Calculated ^{17}C elastic cross section σ_{11} related to the core-excited state E_C = 3.986 MeV for s-, p- and d-waves. A pronounced resonance line shape is evident in the d-wave.

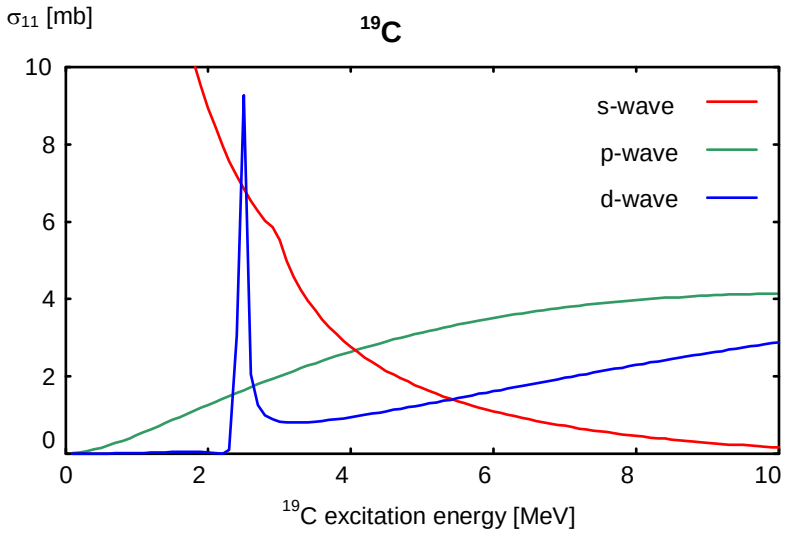

Figure 8.20. Calculated ^{19}C elastic cross section σ_{11} related to the core-excited state E_C = 2.967 MeV for s-, p- and d-waves. A pronounced resonance line shape appears in the d-wave.

of Figure 8.20 are calculated for ^{19}C and the core state E_C = 2.967 MeV. Similar to the case of ^{15}C, for ^{17}C and ^{19}C the interference pattern also develops in the d-wave.

The final results of the calculations for the ^{17}C and ^{19}C nuclei are shown in Figures 8.21 and 8.22, respectively. These results have been obtained using the potential parameters given in Table 8.1. For the ^{17}C calculations the core-excited states which contribute are: E_C (J^π) = 1.766 (2^+), 3.986 (2^+), 4.142 (4^+) MeV. The core states included in the calculations for ^{19}C are: E_C (J^π) = 1.620 (2^+), 2.967 (4^+), 3.313 (2^+), 5.502 (1^-) MeV; among them E_C = 1.620 MeV is the only experimentally known excitation, and the others are taken from QRPA calculations. Each core state has been weighted according to the β_{QRPA}-values (see Table 8.2). As already mentioned, we consider only natural parity core states with the β order of

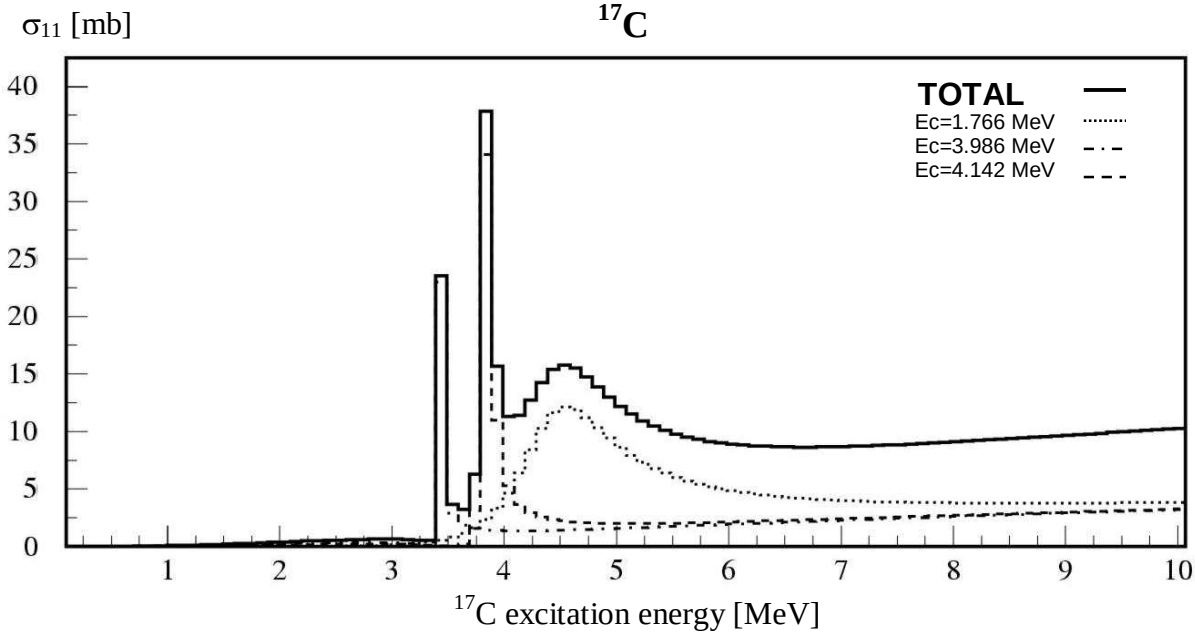

Figure 8.21. ^{17}C: calculated elastic cross section σ_{11} for the d-wave plotted with respect to the ^{17}C excitation energy. Core states included in the calculations: E_C (J^π) = 1.766 (2^+), 3.986 (2^+), 4.142 (4^+) MeV.

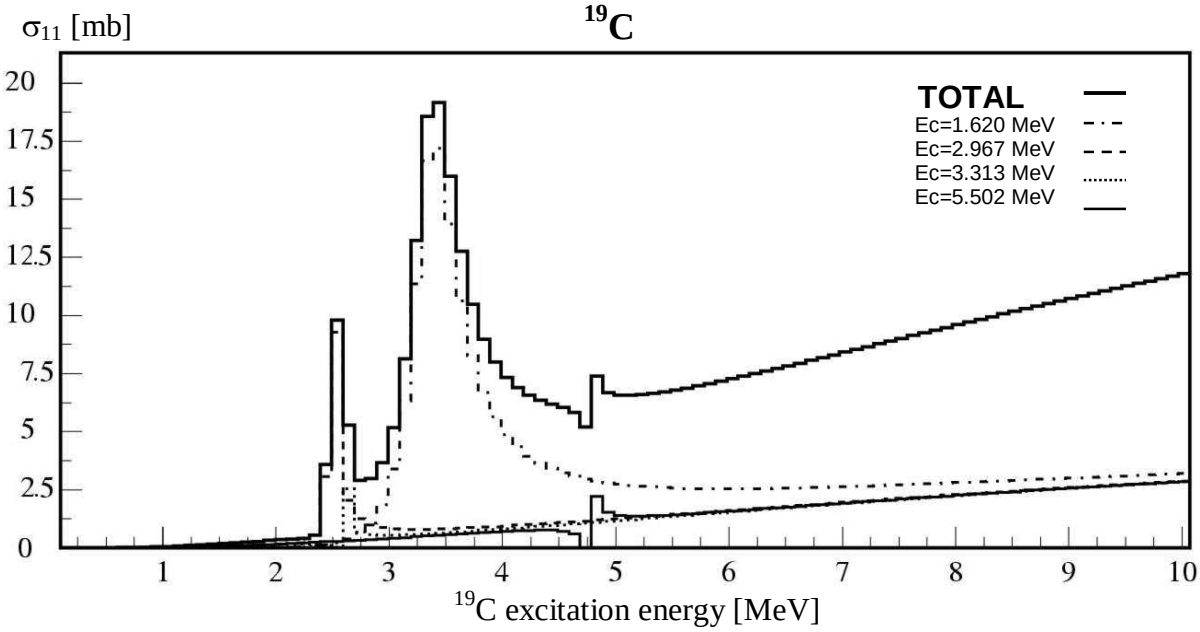

Figure 8.22. ^{19}C: calculated elastic cross section σ_{11} for the d-wave plotted with respect to the ^{19}C excitation energy. Core states included in the calculations: E_C (J^π) = 1.620 (2^+), 2.967 (4^+), 3.313 (2^+), 5.502 (1^-) MeV.

magnitude greater than ~ 10^{-3}. The total d-wave cross sections σ_{11} of Figures 8.21 and 8.22 have been obtained by a sum of the individual core contributions, in the same way as for ^{15}C in Section 8.3.2. Regarding ^{17}C, three BSEC are obtained at E_x = 3.44, 3.85, 4.59 MeV (Fig. 8.21). For ^{19}C (Fig. 8.22) three states in the continuum are evident at E_x = 2.55, 3.46, 4.86

MeV. Unfortunately, at the moment for the ^{17}C and ^{19}C nuclei experimental spectra are not available to compare with our theoretical results.

By analysing systematically the interference effect in ^{15}C (Fig. 8.18a), ^{17}C and ^{19}C, we can see that the interference shape is similar: all the individual peaks are asymmetric, interfering destructively on their low energy side. The energy E_C of the core state influences the position of the BSEC, while the intensity of the coupling (β V_{13}) acts on the strength of the peak. In fact, a clear correlation between the value of E_C and the position of the related BSEC is observed. This is obvious by comparing states in a given nucleus, e.g., in ^{16}C with E_C = 3.986, 4.142 MeV leading to the BSEC E_x = 3.44, 3.85 MeV respectively in ^{17}C. Correspondingly, from a comparison of different nuclei we find, for example, from ^{18}C with E_C = 5.502 MeV a state at E_x = 4.86 MeV in ^{19}C, while E_C = 6.094 MeV in ^{14}C gives rise to a ^{15}C state at E_x = 7.15 MeV. Altogether, we observe a progressive lowering of the BSEC energies going from ^{15}C to ^{17}C and ^{19}C due to the decreasing energies of the respective core spectra. Therefore, we expect to observe the BSEC at progressively lower energies with increasing neutron excess. Concerning the interaction, core states with greater β – and thus greater coupling strength (β V_{13}) – correspond to more intense BSEC.

However, there is some exception to these findings. As an illustration, let us consider the following case, a BSEC, obtained from the core states with the strongest interaction (see Table 8.2) in the various nuclei: in ^{15}C from E_C = 6.728 MeV (β = 0.397), in ^{17}C from E_C = 1.766 MeV (β = 0.502) and in ^{19}C from E_C = 1.620 MeV (β = 0.420). We see from Figure 8.18 to Fig. 8.21 and 8.22 that, over the chain of nuclei, the state considered becomes broader and appears at higher energy than the other BSEC which are originated from core states with higher E_C. Thus, when the interaction becomes too strong the peak tends to be broaden and to shift to higher excitation energy.

The relation between E_C and the peak position is independent on spin and parity of the involved core state because the model calculations are insensitive to the $J_C^{\pi c}$ values, which enter only indirectly because of the determination of the β-amplitudes from the QRPA calculations. Besides, the cross sections are independent of the j of the valence neutron. Indeed, in general for a particle with spin s = 1/2 the cross sections are weighted by a factor (2j + 1)/(2s + 1) rather than (2l + 1) as in formula (8.32). However, since for the moment we do not include spin-orbit potentials in the calculations, the C-matrix elements C(l,j) ≡ C(l) and therefore the cross sections only depend on the orbital l. Hence, our cross section should be considered as representing averages over j = l + 1/2 and j = l – 1/2.

8.4 Summary

The theoretical approach here described provides an explanation of the resonance line shape in the light neutron-rich nuclei as an effect of the interference between the 1-QP and 3-QP components. A simple model was chosen in order to allow analytic solutions. Results of model calculations for the ^{15}C, ^{17}C and ^{19}C nuclei show a pronounced interference pattern in the d-wave elastic cross section, which is due to the coupling term V_{13} between the single particle continuum and the resonant state. The interference of the two contributions cancels the cross section on the left side of the resonance producing a typically asymmetric line shape.

The results for ^{15}C are compared with the experimental spectra of Section 5.2. The global agreement is very good, in fact the present model reproduces qualitatively both the interference pattern seen in the line shape and all the experimentally observed narrow continuum states in ^{15}C. The theoretical resonance energies are very close to the measured ones. In the light of these results, together with those of the QRPA-DCP calculations (see Chapter 7), these resonances are described as BSEC with low angular momentum (possible J^{π} values: $1/2^{+}$, $3/2^{+}$ or $5/2^{+}$) and interference in the d-wave.

Interfering BSEC are theoretically obtained in the ^{15}C, ^{17}C and ^{19}C nuclei and described as the result of interactions between the ground state and core-excited configurations. From the systematic comparison of the results, the energy E_C of the core state influences the position of the BSEC, giving a lower position for lower E_C. Moreover, a greater coupling strength (β V_{13}) corresponds to a more intense BSEC. However, if the interaction is too strong the peak appears at higher excitation energy with a larger width.

Therefore going towards the neutron drip line a progressive decrease of the BSEC energies is expected, owing to the lowering of the corresponding E_C from ^{15}C to ^{17}C and ^{19}C. An interesting aspect, also of astrophysical importance, is that the BSEC phenomena leads to a change of the level density close to the continuum threshold. Hence, neutron capture processes will be affected which, in turn, might influence astrophysical reaction rates and nuclear life times. The increase of the level density beyond the typically assumed level of states in a potential will also affect the thermodynamical properties of exotic nuclei.

The interference effect, hypothesized starting from the experimental observation in the ^{15}C peak at E_x = 8.5 MeV, turns out to be a rather general phenomenon. Indeed, the results of the calculations foresee such an effect (more o less marked) for the states in the continuum of different carbon isotopes. However, from an experimental point of view, the interference is not easily observable if the resonance is not well isolated as the 8.5 MeV peak. Although similar interferences have been previously seen (see, e.g., refs. [Bau75, Bau77] and refs. therein), it is underlined that this is the first time that such an effect is experimentally observed in a CEX reaction. Such an observation is very important also because the interference pattern is a strong experimental signature of the existence of BSEC. Moreover, the theoretical model presented in this Chapter is the first which explores the interference effects due to the BSEC in unstable neutron-rich nuclei.

Further improvements are in progress in order to extend the model, such as to develop multi-channel calculations including at the same time the different core-excited states, in this way reproducing the interaction of a set of discrete levels with a single continuous background. In addition, the DCP wave functions obtained constitutes the starting point for the development of dynamical CEX-DCP calculations, which will allow to determine a theoretical CEX cross section to be compared with the experimental one (Sect. 5.3 and ref. [Orr03]) and to investigate J^{π} of the ^{15}C BSEC.

CONCLUSIONS

A general discussion of the physical scenario involving light drip-line nuclei has been given in the first Chapters, considering both the theoretical and experimental aspects. My main interest was in the structural properties and reaction mechanisms of light neutron-rich nuclei, concerning in particular the ^{15}C nucleus.

The ^{15}N(^{7}Li,^{7}Be)^{15}C charge exchange reaction at 55 MeV incident energy was used to investigate the ^{15}C energy levels. Experimental spectra were measured at θ_{lab} = 0°, 2.5°, 8°, 10°, 14°. The gas target was crucial to overcome the difficulties encountered previously with a solid melamine target. The energy resolution (~ 250 keV) allowed the identification of the transitions corresponding to the ^{7}Be ground and first excited state at E_x = 0.429 MeV. The ^{15}C ground and the excited states at E_x = 0.77, 6.77, 7.30, 8.50 MeV were experimentally observed, together with a structure at E_x = 6.4 MeV which likely included contributions from several closely spaced ^{15}C levels. The angular distributions were measured for the transitions observed together with the angular distributions of the G factor [Jän96], which depends on the ratio of the cross sections related to the two ^{7}Be states (see Section 3.4.1). The values of G at 0° shows a general trend to spin transfer dynamics.

In the ^{15}C spectrum three narrow resonances are observed above the particle threshold (S_n = 1.218 MeV). In particular, a new observation is the suppression of counts immediately before the 8.5 MeV peak, most likely produced by the interference between the 8.5 MeV state and the non-resonant 3-body phase space. Although similar interferences have been previously observed, this is the first time that such an effect is experimentally seen in a CEX reaction.

A microscopic many-body theory for heavy-ion charge exchange reaction was used in order to analyze the ^{15}C structure and the (^{7}Li,^{7}Be) dynamics. The CEX-QRPA approach describes the ^{15}C states as correlated 2-QP excitations with respect to the HFB $^{15}N_{GS}$. A state dependent pairing field and an average treatment of the 4-QP correlations are included in the calculations. A realistic residual interaction [Hof98], dependent on the nuclear density and charge asymmetry and including the tensor force, is used in every step of calculations, assuring consistency between the structure and reaction mechanism calculations.

The CEX-QRPA calculations describe well the ^{15}C single particle levels (ground and first excited state), giving useful information about their spin and parity and reproducing also the known inversion between the $1/2^+$ and $5/2^+$ neutron orbitals. It is underlined that no parameters were “a priori” adjusted to obtain this inversion. Nevertheless, the fragmentation of the strength observed in the experiment spectra at higher excitation energies is not reproduced. Thus the higher excitation region cannot be explained in terms of configurations in which the valence neutron is coupled to an inert ^{14}C core; the core-excited components have to be taken into account.

The CEX-QRPA transition densities are used in the one-step DWBA calculations performed for the two bound states of ^{15}C. A rather good agreement with the measured angular distributions is found. In particular, the order of magnitude of the cross sections is reproduced without the need to introduce large renormalization, which usually are necessary in order to reproduce the experimental data from the (^{7}Li,^{7}Be) reactions. This also confirms the reliability of a one-step approach. A prevalence of the unnatural parity transitions is found in the ^{15}N(^{7}Li,^{7}Be)^{15}C reaction and this, together with the measured G-values, indicates a prominence of spin transfer process.

Similar results are found with the same approach for the ^{11}Be nucleus [Cap04b] and, since the same basic parameters are used for both the ^{15}C and ^{11}Be calculations, this strengthen our conclusions. The one-step mechanism seems appropriate to describe the (^{7}Li,^{7}Be) CEX reaction at about 8 MeV/u incident energy when weakly-bound nuclei are populated. The dominance of the spin transfer dynamics at only 8 MeV/u is quite a surprising result because it is opposite to the predictions concerning the spin-isospin dependence of the free NN-interaction at low energy [Tad87]. However, our results concern the spin component of the in-medium NN-interaction.

A more sophisticated theoretical approach, accounting for DCP effects, is necessary in order to explain the ^{15}C structure above the neutron emission threshold. In the QPC model the ^{15}C states are described microscopically by coupling the single neutron states to the 3-QP core-excited configurations. The latter are calculated with QRPA methods as 2-QP excitations starting from $^{14}C_{GS}$. Again, the residual interaction of ref. [Hof98] is used in the calculations. Strong fragmentation is found in the $s_{1/2}$, $d_{5/2}$ and $d_{3/2}$ ^{15}C strengths in the region E_x ~ from 5 to 11 MeV, while large bumps are observed in the remaining strength functions. Therefore the fragmentation seen in the experimental spectra for E_x ~ from 6 to 9 MeV may be explained as arising from dynamical core polarization. In the light of the QRPA-DCP results, the narrow resonances seen in the ^{15}C continuum may be interpreted as BSEC with low spin.

In the last Chapter a theoretical approach based on the QPC model is presented and used to investigate the resonances and their line shapes in the low-energy continuum of light neutron-rich nuclei. The results of the calculations for the ^{15}C, ^{17}C and ^{19}C nuclei show a pronounced interference pattern in the d-wave elastic cross section. This asymmetric line shape is produced by the interference of the 1-QP and 3-QP components, which are coupled by the residual interaction.

The results for ^{15}C are compared with experimental data, showing a very good global agreement: the present model reproduces qualitatively both the interference pattern seen in the line shape of the 8.5 MeV peak and all the narrow states experimentally observed in the ^{15}C continuum. The theoretical resonance energies are very close to the measured ones. Without overemphasizing these results, the model accounts for the essential physics aspects observed in the data. This model is the first which studies the interference effects between a single particle continuum and a BSEC in weakly-bound nuclei.

From the systematic comparison of the results in ^{15}C, ^{17}C and ^{19}C, the energy E_C of the core state influences the position of the BSEC: going towards more neutron-rich nuclei a progressive decrease of the BSEC energies is expected owing to the lowering of the

corresponding E_C. Greater coupling strength corresponds to more intense BSEC, but if the interaction is too strong the peak appears at higher excitation energy with a larger width. The interference effect, hypothesized as starting from the experimental observation in ^{15}C, turns out to be a rather general phenomenon. Indeed, the results of the calculations predict such an effect (more or less marked) for the states in the continuum of different carbon isotopes. Thus the observation of an interference pattern in these nuclei may be considered an experimental signature of the BSEC.

Room is left for further improvements, such as the development of multi-channel calculations including at the same time the different core-excited states, in this way reproducing the interaction of a set of discrete levels with a single continuous background. In addition, the DCP wave functions obtained with the present model are the starting point for the development of dynamical CEX-DCP calculations, in which the effects of the CEX transition operator and the optical potential will be included. This will ultimately allow the determination of a theoretical CEX cross section to be compared with the experimental one.

In my opinion, exotic nuclear physics is a very intriguing branch of modern physics. The recent development of the radioactive beam facilities has opened new perspectives in the investigation of the peculiar properties of drip-line nuclei. The exploration of the extreme regions of the mass table is just at the beginning and much remains to discover.

ACNOWLEDGEMENTS

The three years devoted to my Ph.D. and to the work described in this thesis were a wonderful period of my life, rich of experiences which I will never forget.

My first thought is for my tutor, Prof. Angelo Cunsolo, who has given me the exciting opportunity to work in his Group. I thank him very much, not only for the constant cure he had on my research activity, for his great competence and precious teachings, but also for his moral qualities, which make pleasant the daily work from the human side too.

I am also very grateful to Prof. Horst Lenske, an extraordinary person from both the professional and human point of view. I heartily thank him for his fundamental collaboration, for the constant attemption on my studies and, above all, for giving me the chance to work with him. His theachings and the exciting scientific discussions are invaluable to me. My stay in Giessen was an extremely important experience and I enjoyed very much to work with him.

Special thanks to Dr. Francesco Cappuzzello and Dr. John Winfield, for the stimulating discussion and the useful suggestions, for their great expertise and availability. I would like also to thank the other colleagues of my research Group, Prof. Nino Foti, Chiara Nociforo, Alberto Lazzaro and Maria Allia, for the pleasant time spent working together.

I thank the Coordinator of the Ph.D. course, Prof. A. Insolia, and the Director of the LNS, Prof. E. Migneco, also including all the people who helped me both at the Physics Department and at the LNS.

Finally, my gratitude is for who, more than whoever, supported and encouraged me: my Family and Maurizio.

Sonja Orrigo

BIBLIOGRAPHY

[Ajz68] F.Ajzenberg-Selove, *Nucl. Phys.* A **114**(1968)1.

[Ajz86] F.Ajzenberg-Selove, *Nucl. Phys.* A **449**(1986)1.

[Ajz91] F.Ajzenberg-Selove, *Nucl. Phys.* A **523**(1991)1 and refs. therein.

[Alf98] W.P.Alford and B.M.Spicer, *Adv. in Nucl. Phys.* **24**, Plenum, New York (1998)1, edited by J.W.Negele and E.Vogt.

[Alk02] J.Al-Khalili@surrey.ac.uk, Univ. Surrey, UK, (2002); *The Euroschool Lectures on Physics with Exotic Beams*, Vol. I, *Lect. Notes Phys.* **651**, Edited by J.Al-Khalili and E.Roeckl, Springer, Berlin Heidelberg (2004).

[And70] J.D.Anderson, C.Wong and V.A.Madsen, *Phys. Rev. Lett.* **24**(1970)1074.

[Ann90] R.Anne et al., *Phys. Lett.* B **250**(1990)19.

[Arn86] E.Arnold, Ph.D. thesis, University of Mainz (1986).

[Arn87] E.Arnold, J.Bonn, R.Gegenwart, W.Neu, R.Neugart, E.W.Otten, G.Ulm, K.Wendt and ISOLDE Collaboration, *Phys. Lett.* B **197**(1987)311.

[Aud93] G.Audi, A.H.Wapstra and M.Dedieu, *Nucl. Phys.* A **565**(1993)193 and refs. therein.

[Aud97] G.Audi and A.H.Wapstra, *Nucl. Phys.* A **624**(1997)1.

[Aum00] T.Aumann et al., *Phys. Rev. Lett.* **84**(2000)35.

[Aus94] S.M.Austin, N.Anantaraman and W.G.Love, *Phys. Rev. Lett.* **73**(1994)30.

[Aut70] D.L.Auton, *Nucl. Phys.* A **157**(1970)305.

[Bak97] F.T.Baker, L.Bimbot, C.Djalali, C.Glashausser, H.Lenske, W.G.Love, M.Morlet, E.Tomasi-Gustafsson, J.Van De Wiele, J.Wambach and A.Willis, *Phys. Rep.* **289**(1997)235.

[Bal73] G.C.Ball, G.J.Costa, W.G.Davies, J.S.Forster, J.C.Hardy and A.B.McDonald, *Phys. Rev. Lett.* **31**(1973)395.

[Ban84] J.Bang, F.A.Gareev, S.A.Goncharov and G.S.Kasacha, *Nucl. Phys.* A **429**(1984)330.

[Bau75] G.Baur, F.Rösel and D.Trautmann, *Nucl. Phys.* A **252**(1975)77.

[Bau77] G.Baur and H.Lenske, *Nucl. Phys.* A **282**(1977)201.

[Bau86] G.Baur, C.A.Bertulani and H.Rebel, *Nucl. Phys.* A **458**(1986)188.

[Bau98] T.Baumann et al., *Phys. Lett.* B **439**(1998)256.

[Baz95] D.Bazin, B.A.Brown, J.Brown, M.Fauerbach, H.Hellström, S.E.Hirzebruch, J.H.Kelley, R.A.Kryger, D.J.Morrissey, R.Pfaff, C.F.Powell, B.M.Sherrill and M.Thoennessen, *Phys. Rev. Lett.* **74**(1995)3569.

[Baz98] D.Bazin, W.Benenson, B.A.Brown, J.Brown, B.Davids, M.Fauerbach, P.G.Hansen, P.Mantica, D.J.Morrissey, C.F.Powell, B.M.Sherrill, M.Steiner, *Phys. Rev.* C **57**(1998)2156.

[Ben80] V.Benard and N.Van Giai, *Nucl. Phys.* A **348**(1980)75.

[Ber83] G.F.Bertsch, P.Bortignon and R.Broglia, *Rev. Mod. Phys.* **55**(1983)287.

[Ber92] C.A.Bertulani and K.W.McVoy, *Phys. Rev.* C **46**(1992)2638.

[Bha84] A.K.Bhatia and A.Temkin, *Phys. Rev.* A **29**(1984)1895.

[Boh69] A.Bohr and B.Mottelson, *Nuclear Structure* **1**-**2**, Benjamin, New York, (1969-1970).

[Boh78] H.G.Bohlen and W.vonOertzen, *Z. Phys.* A **285**(1978)371.

[Boh88] H.G.Bohlen, *Nucl. Phys.* A **488**(1988)89.

[Boh03] H.G.Bohlen, R.Kalpakchieva, B.Gebauer, S.M.Grimes, H.Lenske, K.P.Lieb, T.N.Massey, M.Milin, W.von Oertzen, Ch.Schulz, T.Kokalova, S.Torilov and S.Thummerer, *Phys. Rev.* C **68**(2003)054606.

[Bon02] A.Bonaccorso and F.Carstoiu, *Nucl. Phys.* A **706**(2002)322.

[Bre88] C.Brendel, P.vonNeumann-Cosel, A.Richter, G.Schrieder, H.Lenske, H.H.Wolter, J.Carter and D.Schüll, *Nucl. Phys.* A **477**(1988)162.

[Bro63] G.E.Brown, J.H.Gunn and P.Gould, *Nucl. Phys.* A **46**(1963)598.

[Bru68] K.A.Brueckner, J.R.Buchler, S.Jorna and R.J.Lombard, *Phys. Rev.* **171**(1968)1188.

[Cap01] F.Cappuzzello et al., *Phys. Lett.* B **516**(2001)21; F.Cappuzzello, Ph.D. thesis, University of Catania (1999).

[Cap04] F.Cappuzzello, S.E.A.Orrigo, A.Cunsolo, H.Lenske, M.C.Allia, D.Beaumel, S.Fortier, A.Foti, A.Lazzaro, C.Nociforo and J.S.Winfield, *Europhys. Lett.* **65**/6(2004)766.

[Cap04b] F.Cappuzzello, H.Lenske, A.Cunsolo, D.Beaumel, S.Fortier, A.Foti, A.Lazzaro, C.Nociforo, S.E.A.Orrigo and J.S.Winfield, *Nucl. Phys.* A **739**/1-2(2004)30.

[Cat02] W.Catford, Catkin version 2.00, Univ. Surrey, www.surrey-ac.uk/~pg/catford (2002).

[Cec75] F.E. Cecil, J.R.Shepard, R.E.Anderson, R.J.Peterson and P.Kaczkowski, *Nucl. Phys.* A **255**(1975)243.

[Cel91] A.Celler et al., *Phys. Rev.* C **43**(1991)639.

[Cho93] W.T.Chou, E. K.Warburton and B.A.Brown, *Phys. Rev.* C **47**(1993)163.

[Chu00] L.V.Chulkov et al., *Nucl. Phys.* A **674**(2000)330.

[Cla68] D.D.Clayton, *Principles of Stellar Evolution and Nucleosynthesis*, Univ. of Chicago Press (1968).

[Cob97] A.Cobis., A.S.Jensen. and D.V.Fedorov, *J. Phys.* G **23**(1997)401.

[Coh65] S.Cohen and D.Kurath, *Nucl. Phys.* A **73**(1965)1.

[Coo84] J.Cook and K.W.Kemper, *Phys. Rev.* C **30**(1984)1538.

[Con88] J.P.Connerade and A.M.Lane, *Rep. on Progr. in Phys.* **51**(1988)1439.

[Cor01] D.Cortina-Gil et al., *Eur. Phys. J* A **10**(2001)49.

[Cun02a] A.Cunsolo, F.Cappuzzello, A.Foti, A.Lazzaro, A.L.Melita, C.Nociforo, V.Shchepunov and J.S.Winfield, *Nucl. Instr. and Meth.* A **481**(2002)48.

[Cun02b] A.Cunsolo, F.Cappuzzello, A.Foti, A.Lazzaro, A.L.Melita, C.Nociforo, V.Shchepunov and J.S.Winfield, *Nucl. Instr. and Meth.* A **484**(2002)56.

[Cun02c] A.Cunsolo, F.Cappuzzello, A.Foti, P.Gangnant, A.Lazzaro, J.F.Libin, A.L.Melita, W.Mittig, C.Nociforo, S.E.A.Orrigo, P.Roussel-Chomaz, C.Spitaels and J.S.Winfield, *Nucl. Instr. and Meth.* A **495**(2002)216.

[Dar85] S.E.Darden, G.Murillo and S.Sen, *Phys. Rev.* C **32**(1985)1764.

[Dev87] H.DeVries, C.W.DeJager and C.DeVries, *At. Data Nucl. Tables* **36**(1987)495.

[Dev88] J.V.deVries, D.Doornhof, C.W.deJager, R.P.Singhal, S.Salem, G.A.Peterson and R.S.Hicks, *Phys. Lett.* B **205**(1988)22.

[Dob96] J.Dobaczewski, W.Nazarewicz, T.R.Werner, J.F.Berger, C.R.Chinn and J.Dechargé, *Phys. Rev.* C **53**(1996)2809.

[Dod85] A.C.Dodd, N.M.Clarke, J.Coopersmith, R.J.Griffiths, K.I.Pearce, B.Stanley and J.Cook, *J. Phys.* G **11**(1985)1035.

[Eck89] F.J.Eckle, H.Lenske, G.Eckle, G.Graw, R.Hertenberger, H.Kader, F.Merz, H.Nann, P.Schiemenz and H.H.Wolter, *Phys. Rev.* C **39**(1989)1662.

[Eck90] F.J.Eckle, H.Lenske, G.Eckle, G.Graw, R.Hertenberger, H.Kader, H.J.Maier, F.Merz, H.Nann, P.Schiemenz, and H.H.Wolter, *Nucl. Phys.* A **506**(1990)159.

[Eml98] H.Emiling, *J. Physics G: Nucl. Part. Phys.* **24**(1998)1561.

[Etc88] A.Etchegoyen, M.C.Etchegoyen, E.D.Izquierdo, D.Abriola, D.E.Di Gregorio, J.O. Fernández Niello, A.M.J.Ferrero, S.Gil, A.O.Macchiavelli, A.J.Pacheco and J.E.Testoni, *Phys. Rev.* C **38**(1988)2124.

[Fan61] U.Fano, *Phys. Rev.* **124**(1961)1866.

[Fan00] D.Q.Fang et al., *Phys. Rev.* C **61**(2000)064311.

[Fed93] D.V.Fedorov, A.S.Jensen and K.Riisager, *Phys. Lett.* B **312**(1993)1.

[Fed94] D.V.Fedorov, A.S.Jensen and K.Riisager, *Phys. Rev.* C **50**(1994)2372.

[Fes58] H.Feshbach, *Ann. of Phys.* **5**(1958)357.

[Fes62] H.Feshbach, *Ann. of Phys.* **19**(1962)287.

[Fes67] H.Feshbach, *Ann. of Phys.* **43**(1967)410.

[Fet71] A.L.Fetter and J.D.Walecka, *Quantum Theory of Many-Particle System*, Mc Graw-Hill, New York (1971).

[Fra85] M.A.Franey and W.G.Love, *Phys. Rev.* C **31**(1985)488.

[Fuc80] H.Fuchs, J.A.Nolen, G.J.Wagner, H.Lenske and G.Baur, *Nucl. Phys.* A **343**(1980)133.

[Gar74] J.D.Garret, F.Ajzenberg-Selove and H.G.Bingham, *Phys. Rev.* C **10**(1974)1730.

[Gla87] C.Glashausser, K.Jones, F.T.Baker, L.Bimbot, H.Esbensen, R.W.Fergerson, A.Green, S.Nanda and R.D.Smith, *Phys. Rev. Lett.* **58**(1987)2404.

[Glu02] S.Glutsch, *Phys. Rev.* B **66**(2002)075310.

[Gos73] J.D.Goss, A.A.Rollefson, C.P.Browne, R.A.Blue and H.R.Weller, *Phys. Rev.* C **8**(1973)514.

[Gos75] J.D.Goss, P.L.Jolivette, C.P.Browne, S.E.Darden, H.R.Weller and R.A.Blue, *Phys. Rev.* C **12**(1975)1730.

[Ham76] I.Hamamoto and P.Siemens, *Nucl. Phys.* A **269**(1976)199.

[Han87] P.G.Hansen and B.Jonson, *Europhys. Lett.* **4**(1987)409.

[Han93] P.G.Hansen *Nucl. Phys.* A **553**(1993)89.

[Han95] P.G.Hansen, A.S.Jensen and B.Jonson, *Annu. Rev. Nucl. Part. Sci.* **45**(1995)591 and refs. therein.

[Han96] P.G.Hansen, *Phys. Rev. Lett.* **77**(1996)1016.

[Hey99] K.Heyde, *Basic Ideas and Concepts in Nuclear Physics*, edited by D.F.Brewer, IOP Publishing, Bristol and Philadelphia (1999).

[Ike92] K.Ikeda, *Nucl. Phys.* A **538**(1992)355.

[Ike64] K.Ikeda, *Prog. Theor. Phys.* **31**(1964)434.

[Jah78] R.Jahn, D.P.Stahel, G. J.Wozniak, R.J.deMeijer and J.Cerny, *Phys. Rev.* C **18**(1978)9.

[Jän96] J.Jänecke, T.Annakkage, G.P.A.Berg, B.A.Brown, J.A.Brown, G.Crawley, S.Danczyk, M.Fujiwara, D.J.Mercer, K.Pham, D.A.Roberts, J.Stasko, J.S.Winfield and G.H.Yoo, *Phys. Rev.* C **54**(1996)1070.

[Jen00] A.S.Jensen and K.Riisager, *Phys. Lett.* B **480**(2000)39.

[Jeu76] J.P.Jeukeunne, A.Lejeune and C.Mahaux, *Phys. Rep.* **C** 25(1976)83.

[Joa75] See, e.g., C.J.Joachain, *Quantum Collision Theory*, American Elsevier Pub. Co. (1975), cap.4.

[Jon95] B.Jonson, *Nucl. Phys.* A **583**(1995)733.

[Kel96] J.H.Kelley et al., *Phys. Rev. Lett.* **77**(1996)5020.

[Kho93] D.T.Khoa, W.vonOertzen, *Phys. Lett.* B **304**(1993)8.

[Kob88] T.Kobayashi, O.Yamakawa, K.Omata, K.Sugimoto, T.Shimoda, N.Takahashi and I.Tanihata, *Phys. Rev. Lett.* **60**(1988)2599.

[Kre80] S.Krewald and J.Speth, *Phys. Rev. Lett.* **45**(1980)417.

[Len87] H.Lenske, *Habilitationsschrift*, University of Munich, 1987 (unpublished); C.Nociforo and H.Lenske, in preparation.

[Len88] H.Lenske, *Nucl. Phys.* A **482**(1988)343.

[Len89] H.Lenske, *Nucl. Phys.* A **495**(1989)127.

[Len89b] H.Lenske, H.H.Wolter and H.G.Bohlen, *Phys. Rev. Lett.* **62**(1989)1457.

[Len98] H.Lenske and G.Schrieder, *Eur. Phys. J* **2**(1998)41.

[Len98b] H.Lenske, *J. Phys. G: Nucl. Part. Phys.* **24**(1998)1429.

[Len01] H.Lenske, F.Hofmann and C.M.Keil, *Jour. Progr. Part. Nucl. Phys.* **46**(2001)187.

[Len03] H.Lenske, HIDEX3-3 code, private communication.

[Len04] H.Lenske, C.M.Keil and N.Tsoneva, *Progr. Part. Nucl. Phys.* **53**(2004)153.

[Lig02] N.E.Ligterink, *PiN Newslett.* **16**(2002)400, e-archive: nucl-th/0203054(2002).

[Loh81] B.Lohmann and E.Weingold, *Phys. Lett.* A **86**(1981)139.

[Lov81] W.G.Love and M.A. Franey, *Phys. Rev.* C **24**(1981)1073.

[Mad01] V.Maddalena et al., *Nucl. Phys.* A **682**(2001)332c.

[Mah69] C.Mahaux and H.A.Weidenmüller, *Shell Model Approach to Nuclear Reactions*, North-Holland, Amsterdam (1969).

[Mar96] F.M.Marqués et al., *Phys. Lett.* B **381**(1996)407.

[Mie68] F.H.Mies, *Phys. Rev.* **175**(1968)164.

[Mil83] D.J.Millener, J.W.Olness, E.K.Warburton and S.S.Hanna, *Phys. Rev.* C **28**(1983)497.

[Min92] MINUIT, Function Minimization and Error Analysis, CERN Program Library Long Writeup D506, version 92.1 (1992).

[Mit87] W.Mittig, J.M.Chouvel, ZhanWenLong, L.Bianchi, A.Cunsolo, B.Fernandez, A.Foti, J.Gastebois, A.Gillibert, C.Grégoire, Y.Schutz and C.Stephan, *Phys. Rev. Lett.* **59**(1987)1889.

[Moo59] W.E.Moore and J.N.McGruer, *Bull. Am. Phys. Soc.* **4**(1959)17.

[Mur94] G.Murillo, S.Sen and S.E.Darden, *Nucl. Phys.* A **579**(1994)125.

[Nak90] S.Nakayama, T.Yamagata, K.Yuasa, M.Tanaka, H.G.Bohlen, H.Lenske, H.H.Wolter, M.Inoue, T.Itahashi and H.Ogata, *Nucl. Phys.* A **507**(1990)515.

[Nak90b] S.Nakayama, T.Yamagata, K.Yuasa, M.Tanaka, M.Inoue, T.Itahashi and H.Ogata, *Phys. Lett.* B **246**(1990)342.

[Nak91] S.Nakayama, T.Yamagata, M.Tanaka, M.Inoue, K.Yuasa, T.Itahashi, H.Ogata, N.Koori and K.Shima, *Phys. Rev. Lett.* **67**(1991)1082.

[Nak99] S.Nakayama et al., *Phys. Rev.* C **60**(1999)047303.

[Nav99] A.Navin, T.Aumann, D.Bazin, B.A.Brown, T.Glasmacher, P.G.Hansen, R.W.Ibbotson, V.Maddalena, B.M.Sherrill, J.A.Tostevin and J.Yurkon, *Proceedings of*

Experimental Nuclear Physics in Europe (ENPE 99), Seville 1999, AIP Conf. Proc. No. 495 (AIP, New York, 1999), p.309.

[Naz96] W.Nazarewicz, B.Sherrill, I.Tanihata and P.VanDuppen, *Nucl. Phys. News* **6**(1996)17.

[Neg72] J.W.Negele and D.Wauterin, *Phys. Rev.* C **5**(1972)1472.

[Nie98] E.Nielsen, D.V.Fedorov and A.S.Jensen, *J. Phys.* B **31**(1998)4085.

[Noc03] C.Nociforo, F.Cappuzzello, A.Cunsolo, S.Fortier, A.Foti, A.Lazzaro, H.Lenske, S.E.A.Orrigo and J.S.Winfield, Proc. XXXVII Zakopane School of Physics *Trends in Nuclear Physics*, Zakopane, Poland, 2002, *Acta Phys. Polonica* B **34**(2003)2387; C.Nociforo, Ph.D. thesis, University of Catania (2001).

[Nun96] F.M.Nunes, I.J.Thompson and R.C.Johnson, *Nucl. Phys.* A **596**(1996)171.

[Oer88] W.vonOertzen, *Nucl. Phys.* A **482**(1988)357.

[Ohl65] G.G.Ohlsen, *Nucl. Instr. and Meth.* **37**(1965)240.

[Orr92] N.A.Orr, N.Anantaraman, S.M.Austin, C.A.Bertulani, K.Hanold, J.H.Kelley, D.J.Morrissey, B.M.Sherrill, G.A.Souliotis, M.Thoennessen, J.S.Winfield and J.A.Winger, *Phys. Rev. Lett.* **69**(1992)2050.

[Orr01] S.E.A.Orrigo, Laurea dissertation, University of Catania (2001).

[Orr03] S.E.A.Orrigo, M.C.Allia, D.Beaumel, F.Cappuzzello, A.Cunsolo, S.Fortier, A.Foti, A.Lazzaro, H.Lenske, C.Nociforo and J.S.Winfield, Proceeding "*10th International Conference on Nuclear Reaction Mechanisms*", Villa Monastero, Varenna, Italy, 9-13/06/2003, edited by E. Gadioli, Ricerca Scientifica ed Educazione Permanente (2003), Supplemento n.122, p.147.

[Ost92] F.Osterfeld, *Rev. Mod. Phys.* **64**(1992)491.

[Oza94] A.Ozawa, T.Kobayashi, H.Sato, D.Hirata, I.Tanihata, O.Yamakawa, K.Omata, K.Sugimoto, D.Olson, W.Christie and H.Wieman, *Phys. Lett.* B **334**(1994)18.

[Oza95] A.Ozawa et al., *Nucl. Phys.* A **583**(1995)807.

[Oza96] A.Ozawa, I.Tanihata, T.Kobayashi, Y.Sugahara, O.Yamakawa, K.Omata, K.Sugimoto, D.Olson, W.Christie and H.Wieman, *Nucl. Phys.* A **608**(1996)63.

[Oza01] A.Ozawa et al., *Nucl. Phys.* A **691**(2001)599.

[Par00] Yu.L.Parfenova, M.V.Zhukov and J.S.Vaagen, *Phys. Rev.* C **62**(2000)044602.

[Rid97] D.Ridikas, M.H.Smedberg, J.S.Vaagen and M.V.Zhukov, *Europhys. Lett.* **37**(1997)385.

[Rii92] K.Riisager, A.S.Jensen and P.Moller, *Nucl. Phys.* A **548**(1992)393.

[Rii00] K.Riisager, D.V.Fedorov and A.S.Jensen, *Eurphys. Lett.* **49**(2000)547.

[Rin80] P.Ring and P.Schuck, *The Nuclear Many-Body Problem*, Springer (1980).

[Rol88] C.Rolfs and W.S.Rodney, *Cauldrons in the Cosmos*, Univ. of Chicago Press (1988).

[Row70] D.J.Rowe, *Nuclear Collective Motion*, Methuen, London (1970).

[Sai89] M.G.Saint-Laurent et al., *Z. Phys.* A **332**(1989)457.

[Sak93] S.B.Sakuta, A.A.Ogloblin, O.Ya.Osadchy, Yu.A.Glukhov, S.N.Ershov, F.A.Gareev and J.S.Vaagen, *Europhys. Lett.* **22**(1993)511.

[Sat83] G.R.Satchler, *Direct Nuclear Reaction*, Oxford Science Publication (1983).

[Sau00] E.Sauvan et al., *Phys. Lett.* B **491**(2000)1.

[Ser47] R.Serber, *Phys. Rev.* **72**(1947)1008.

[Shl75] S.Shlomo and G.F.Bertsch, *Nucl. Phys.* A **234**(1975)507.

[Sil59] E.A.Silverstein, *Nucl. Instr. and Meth.* **4**(1959)53.

[Sim99] H.Simon et al., *Phys. Rev. Lett.* **83**(1999)496.

[Sin83] R.P.Singhal, J.Dubach, R.S.Hicks, R.A.Lindgren, B.Parker and G.A.Peterson, *Phys. Rev.* C **28**(1983)513.

[Sol78] V.G.Soloview, *Sov. J. Part. Nucl.* **9**(1978)810.

[Sol87] V.G.Soloview, *Prog. Part. Nucl. Phys.* **19**(1987)107.

[Som83] H.M.Sommermann, K.F.Ratcliff and T.T.S.Kuo, *Nucl. Phys.* A **406**(1983)109.

[Spe67] J.E.Spencer and H.A.Enge, *Nucl. Instr. and Meth.* **49**(1967)181.

[Sri00] J.Ziegler, SRIM 2000, version 39, Srim (PC version only) Copyright: International Business Machines Corporation (1998).

[Sta72] A.F.Starace, *Phys. Rev.* B **5**(1972)1773.

[Tad84] T.N.Taddeucci, T.A.Carey, C.Gaarde, J.Larsen, C.D.Goodman, D.J.Horen, T.Masterson, J.Rapaport, T.P.Welch and E.Sugarbaker, *Phys. Rev. Lett.* **52**(1984)1960.

[Tad87] T.N.Taddeucci, C.A.Goulding, T.A.Carey, R.C.Byrd, C.D.Goodman, C.Gaarde, J.Larsen, D.Horen, J.Rapaport and E.Sugarbaker, *Nucl. Phys.* A **469**(1987)125.

[Tan85] I.Tanihata, H.Hamagaki, O.Hashimoto, Y.Shida, N.Yoshikawa, K.Sugimoto, O.Yamakawa, T.Kobayashi and N.Takahashi, *Phys. Rev. Lett.* **55**(1985)2676.

[Tan88] I.Tanihata, T.Kobayashi, O.Yamakawa, S.Shimoura, K.Ekuni, K.Sugimoto, N.Takahashi, T.Shimoda and H.Sato, *Phys. Lett.* B **206**(1988)592.

[Tan88b] I.Tanihata, *Nucl. Phys.* A **488**(1988)113.

[Tan90] I.Tanihata, *Nucl. Phys.* A **520**(1990)411.

[Tan91] I.Tanihata, *Nucl. Phys.* A **522**(1991)275.

[Tan92] I.Tanihata, T.Kobayashi, T.Suzuki, K.Yoshida, S.Shimoura, K.Sugimoto, K.Matsuta, T.Minamisono, W.Christie D.Olson and H.Wieman *Phys. Lett.* B **287**(1992)307.

[Tan96] I.Tanihata, *J. Phys. G.* **22**(1996)157.

[Til93] D.R.Tilley, H.R.Weller and C.M.Cheves, *Nucl. Phys.* A **564**(1993)1 and refs. therein.

[Til95] D.R.Tilley, H.R.Weller, C.M.Cheves and R.M.Chasteler, *Nucl. Phys.* A **595**(1995)1 and refs. therein.

[Tru83] S.Truong and H.T.Fortune, *Phys. Rev.* C **28**(1983)977.

[Wam82] J.Wambach,V.K.Mishra and L.Chu-Hsia, *Nucl. Phys.* A **380**(1982)285.

[War92] E.K.Warburton and B.A.Brown, *Phys. Rev.* C **46**(1992)923.

[Win86] J.S.Winfield, N.Anantaraman, S.M.Austin, L.H.Harwood, J.van der Plicht, H.L.Wu and A.F.Zeller, *Phys. Rev.* C **33**(1986)1333.

[Win96] J.S.Winfield, D.Beaumel, S.Galès, H.Laurent, I.Lhenry, J.M.Maison, G.M.Crawley, S.Danczyk, S.E.Hirzebruch, J.C.Staško and T.Suomijärvi, *Phys. Rev.* C **54**(1996)125.

[Win97] J.S.Winfield, W.N.Catford and N.A.Orr, *Nucl. Instr. and Meth.* A **396**(1997)147.

[Win01] J.S.Winfield et al., *Nucl. Phys.* A **683**(2001)48.

[Yan83] C.Yannouleas, M.Dworzecka and J.J.Griffin, *Nucl. Phys.* A **397**(1983)239.

[Zho97] R.Zhongzhou, C.Baoqiu, M.Zhongyu and X.Gongou, *Z. Phys.* A **357**(1997)137.

[Zin97] M.Zinser et al., *Nucl. Phys.* A **619**(1997)151.